



Exsolved Perovskite Systems Applied for the Production of Syngas via Chemical Looping Methane Reforming

Leonidas Bekris

A thesis submitted for the degree of Doctor of Philosophy (PhD) in
Chemical Engineering at Newcastle University

SCHOOL OF ENGINEERING

December 2021

Abstract

The development of materials with tailorable properties that will lead to tuneable performance has always been key for the advancement of catalytic and energy technologies. Challenging transformations like that of methane to syngas at low temperatures introduce multiple challenges for both material and process. Due to methane's slow activation kinetics traditional processes and materials lack efficiency. To address this, attractive alternative technologies like Chemical Looping have been designed. In this, mixing of fuel and oxidant is eliminated and oxygen exchange between the reactant streams is facilitated via an oxygen carrier material (OCM) which is cycled between them. This allows for side reaction elimination, leading to a safer process in which potentially increased conversions and higher selectivity can be achieved. However, material design for such a process remains a challenge since an OCM should tackle all problems associated with a catalytic process that also involves methane activation such as: particle agglomeration and carbon deposition, while exhibiting excellent oxygen storage and exchange ability that will allow the material to perform reliably under repeated redox cycling. An emerging concept for material design promising to address these limitations is redox exsolution. According to this, nanoparticles with tuneable characteristics can be grown on the surface of oxide supports, exhibiting high resistance to agglomeration and carbon deposition owing to their socketed and strained nature.

In this study the exsolution concept is employed and evolved for the design of perovskite systems with active particles present not only on their surface but for the first time, also in their bulk. The produced materials are decorated throughout with self-strained highly active nanoparticles and exhibit enhanced oxygen transport and storage capabilities. The systems are employed for the activation of methane while their structural and compositional changes are investigated *in situ* and operando via synchrotron X-ray. They manage to activate methane at lower temperatures than state of the art systems, exhibiting high selectivity to syngas while minimizing agglomeration and carbon deposition. It is demonstrated that submerged, redox-active nanoparticles work synergistically with their surface exsolved counterparts and can be actively involved in driving redox transformations. The system's micro-structural and nano-structural characteristics are tuned and their pivotal role on the system's performance is investigated. The insight gained on exo- endo- systems is used to produce an even more reactive against methane system that successfully activates methane while maintaining high selectivity at even lower temperatures, proving that the techniques developed can be applied for the application-driven design of tailored materials. The produced systems are employed for long term cycling for Chemical Looping methane partial oxidation, exhibiting steady and selective performance showcasing their robustness. The insights gained in this study demonstrate the capabilities and provide insight on this new class of composite material which will enable the rational design of such systems for a plethora of catalytic and energy applications.

Acknowledgements

I would like to start by thanking my supervisors Dr Evangelos Papaioannou and Prof. Ian Metcalfe for their guidance and support throughout my PhD. For the opportunities they gave me to learn, travel, meet and collaborate with inspiring people and present my work at conferences around the world. Also, my advisors Dr Kalliopi Kousi and Dr Dragos Neagu for their mentoring, guidance and help throughout the years.

Thanks to Dr Dragos Neagu for introducing me to the world of exsolved perovskite materials and to Dr Kelly Kousi for expanding my horizons in the world of catalysis. Both have been an integral part of this journey sharing their knowledge, assisting with data interpretation and more importantly always being there to discuss.

Many thanks to old and new members of the Matcore group: Dr Greg Much, Dr Maria Kazakli, Dr Liam McNeil, Dr Chris de Leeuwe, Stephen Johnston, Selim Ungut, Alex Martinez, Reinaldo Pereira, Daniel Telford and to collaborators and master students that I had the pleasure to work with through the years for the great conversations and good times in and out of the lab.

I would like to acknowledge the contribution of Dr Dragos Neagu for carrying out the Voronoi Tessellation and corresponding particle analysis, the sequential Rietveld refinement of operando synchrotron data and for the creation of selected 3D figures. Dr Kelly Kousi for the synthesis of NiAl_2O_3 , TEM sessions and her work with collaborators at Imperial College who provided the XPS measurements and analysis. Their contribution is acknowledged in relevant points within text.

I acknowledge the support of the European Synchrotron Radiation Facility (ESRF) and thank Dr Catherine Dejoie for her help during setup and data acquisition at beamline ID22. Dr Budhika Mendis and Durham University Microscopy Facility for access to the SEM and TEM facilities used in this study. Finally, thanks to the team of collaborators at Imperial College: Dr Eleonora Cali, Dr Gwilherm Kerherve and Prof David Payne for the XPS measurements and analysis.

Thanks to EPSRC for making this project possible with their funding via their award for doctoral training.

Finally, I would like to thank my family for their endless support throughout my studies.

List of publications

This thesis is based on several publications which are cited throughout.

Published papers on which this thesis was based on:

Kousi, K., Neagu, D., Bekris, L., Papaioannou, E.I. & Metcalfe, I.S. (2020) Endogenous Nanoparticles Strain Perovskite Host Lattice Providing Oxygen Capacity and Driving Oxygen Exchange and CH₄ Conversion to Syngas. *Angewandte Chemie - International Edition*. 59 (6), 2510–2519.

Kousi, K., Neagu, D., Bekris, L., Cali, E., Kerherve, G., Papaioannou, E.I., Payne, D.J. & Metcalfe, I.S. (2020) Low temperature methane conversion with perovskite-supported: exo / endo - particles. *Journal of Materials Chemistry A*. 8 (25), 12406–12417.

Published papers from collaboration during the course of this PhD:

Otto, S.K., Kousi, K., Neagu, D., Bekris, L., Janek, J. & Metcalfe, I.S. (2019) Exsolved Nickel Nanoparticles Acting as Oxygen Storage Reservoirs and Active Sites for Redox CH₄ Conversion. *ACS Applied Energy Materials*. 2 (10), 7288–7298.

Papers in preparation stemming from results presented this thesis:

Bekris, L., Kousi, K., Neagu, D., Papaioannou, E.I. & Metcalfe, I.S. Methane Activation with Submerged Particles: Deconvolution of Microstructural and Nanostructural Effects on Activity and Selectivity.

Table of Contents

Abstract.....	II
Acknowledgements.....	IV
List of publications	V
Table of Contents.....	VI
List of Figures	X
Nomenclature	XVIII
1 Introduction	1
1.1 Research background	1
1.2 Exsolved perovskite oxide systems	2
1.2.1 Perovskite structure and tailorability	2
1.2.2 Nonstoichiometry in perovskite oxides	4
1.2.3 The self-regeneration concept.....	6
1.2.4 The exsolution concept.....	7
1.3 Hydrogen and syngas production	12
1.3.1 Steam reforming of hydrocarbons.....	13
1.3.2 Partial Oxidation of Hydrocarbons.....	15
1.3.3 Coal Gasification.....	15
1.3.4 H ₂ from renewable sources	16
1.4 Chemical looping for H ₂ production.....	17
1.4.1 Concept overview and applications	17
1.4.2 Chemical looping reforming.....	20
1.4.3 Steam reforming with chemical looping combustion.....	20
1.4.4 Autothermal chemical looping reforming	21
1.4.5 Chemical looping reforming of methane	22
1.5 Chemical looping materials for H ₂ production	24
1.5.1 Oxygen carrying materials requirements	24
1.5.2 Metal oxides as oxygen carrying materials.....	24
1.5.3 Perovskite oxides as oxygen carrying materials	26
1.6 Aim and objectives of the thesis	27

1.7	Thesis outline	28
	References	29
2	Experimental.....	35
2.1	Introduction	36
2.2	Material preparation and processing	37
2.2.1	Modified Solid state synthesis.....	37
2.2.2	Pellet processing.....	39
2.2.3	Sample pre-treatment	40
2.2.4	Pechini sol-gel method	40
2.3	Characterisation methods and techniques.....	40
2.3.1	Powder X-ray diffraction	40
2.3.2	Synchrotron In situ and operando XRD at ESRF	42
2.3.3	Scanning electron microscopy.....	44
2.3.4	Transmission electron microscopy	46
2.3.5	Thermogravimetric analysis	47
2.4	Experimental setups	47
2.4.1	Mini reactor setup for temperature programmed experiments	47
2.4.2	Automated fixed bed Integral reactor system	48
2.4.3	Gas analysis.....	50
2.5	Experimental procedures.....	51
2.5.1	Temperature programmed reduction	51
2.5.2	Temperature programmed oxidation	52
2.5.3	Chemical looping cycling experiments	52
2.6	Data processing.....	52
2.6.1	Gas analysis data	52
2.6.2	XRD data analysis and Rietveld refinement	54
2.6.3	Image analysis.....	54
	References	54
3	Development and investigation of a system with exo-/ endo- nanoparticles for the conversion of methane to syngas.....	56
3.1	Introduction	57
3.2	Developing a perovskite system with endogenous nanoparticles.....	58
3.3	Controlling material strain and oxygen exchange by controlling the release of endoparticles	66

3.4	Further increase of strain through reversible oxygen incorporation	70
3.5	Employing an exsolved system with endo- exo- nanoparticles for methane activation 72	
3.6	Operando mechanistic insight of methane conversion with an exo/endo- exsolved system	76
3.7	Operando mechanistic insight of methane conversion via chemical looping partial oxidation with an exo/endo- exsolved system	78
3.8	Application of the developed exo/endo- exsolved system as an oxygen carrier for the partial oxidation of methane via chemical looping	81
3.9	Conclusions.....	85
	References.....	85
4	Deconvolution of the effect of micro- and nano-structure on the performance of exsolved perovskite systems with exo-/endo- particles.....	90
4.1	Introduction.....	91
4.2	Probing the effect of endo- nanoparticles on activity	91
4.3	Deconvoluting the role of surface nanoparticles on the material's activity.....	97
4.4	Elucidation of the effect of microstructural modification on the system's performance.....	100
4.5	Conclusions.....	109
	References.....	109
5	Development and testing of and exsolved perovskite system with exo/ endo- nanoparticles for low temperature methane activation	112
5.1	Introduction.....	113
5.2	Design and exsolution of $\text{La}_{0.7}\text{Ce}_{0.1}\text{Co}_{0.3}\text{Ni}_{0.1}\text{Ti}_{0.6}\text{O}_{3-\delta}$	113
5.3	Employment of the system for methane activation	119
5.4	Activity enhancement by microstructural modification	124
5.5	Application of the system as an OCM for the conversion of methane via Chemical Looping.....	127
5.6	Conclusions.....	128
	References.....	129
6	Conclusions	133
6.1	Conclusions.....	134
	References.....	136
7	Future work.....	138
7.1	Investigation of emergent material properties stemming from strain.....	139

7.2	Further studying of exoparticle involvement on the activation process and their synergistic relationship with endoparticles.....	140
7.3	Investigation of exsolved exo-/ endo- bimetallic particle systems with varying alloying particle composition.....	141
7.4	Increasing the reactivity of exo-/ endo- particle systems by modifying exoparticle characteristics.....	142
	References.....	142
	Appendix A.....	144

List of Figures

Figure 1.1 The ideal perovskite structure (ABO₃) as observed in SrTiO₃. Two perspectives presented: (a) with a focus on the unit cell and cation coordination number and (b) focusing on the BO ₆ octahedra (Neagu & Irvine, 2013).	3
Figure 1.2 Cases of nonstoichiometry in perovskites and corresponding examples based on SrTiO₃ with different dopants (Neagu & Irvine, 2013).	5
Figure 1.3 Schematic representation of redox exsolution. a) Visualisation of B-site exsolution where upon reduction the doped catalytically active species that have been doped on the B-site of the perovskite lattice as cations (yellow squares), exsolve as nanoparticles on the outer surface and b) processes taking place for exsolution to occur (Kousi et al., 2021).	7
Figure 1.4 The role of perovskite nonstoichiometry in exsolution. Exsolution from a) an initially A-site deficient, O-stoichiometric perovskite, and b) an A-site-stoichiometric, O-excess perovskite treated at the same conditions (Neagu et al., 2013a).	8
Figure 1.5 Schematic representation of B-site exsolution from an A-site deficient perovskites. The O, B and A sites are depicted as silver, yellow/grey and dark grey spheres, respectively. The A-site vacancy is represented by the hashed light red circle (Neagu et al., 2013a).	9
Figure 1.6 The role of perovskite surface stoichiometry in exsolution. SEM micrographs illustrating the difference in particle exsolution on a A-site-deficient, O-stoichiometric La _{0.52} Sr _{0.28} Ni _{0.06} Ti _{0.94} O ₃ . a) and b) Difference in nanoparticle exsolution on the native and cleaved surface. b) Preferential partial exsolution on the terraced native surface of the perovskite (Neagu et al., 2013b).	10
Figure 1.7 The aligned and socketed nature of exsolved nanoparticles. a and b) Exsolved particle–perovskite support interface. a) TEM micrograph of an exsolved Ni particle; scale bar, 10 nm. b) TEM micrograph detail of the metal–perovskite interface; scale bars, 1 nm. c) Illustration of particle-support interface for deposited and exsolved particles. d) Three-dimensional AFM of particle sockets (Neagu et al., 2015).	11
Figure 1.8 Anti-coking ability of exsolved particles. a) Ni particles created by infiltration on La _{0.4} Sr _{0.4} TiO ₃ after coking test, exhibiting extensive carbon fibre growth; scale bars, 1 mm. b) Schematic of carbon fibre growth mechanisms. c) Ni particles formed by exsolution from La _{0.52} Sr _{0.28} Ni _{0.06} Ti _{0.94} O ₃ , after coking test, exhibiting limited carbon fibre growth; scale bars, 0.5 mm (overview); 100nm (detail). e) False colour micrograph of the sample presented in c (Neagu et al., 2015).	12
Figure 1.9 Block diagram of the steam methane reforming process for hydrogen production (Goswami et al., 2003).	14
Figure 1.10 Block diagram of the partial oxidation process for hydrogen production (Goswami et al., 2003).	15
Figure 1.11 Pathways for hydrogen production from biomass. Storage intermediates are shown in boxes (Milne et al., 2002).	16
Figure 1.12: Schematic representation water decomposition by electrolysis (Goswami et al., 2003).	17

Figure 1.13 Schematic representation of the chemical looping process performed in two separate reactors between which the OCM is circulated. The OCM is reduced in the Fuel reactor and oxidized in the Air reactor.	19
Figure 1.14 Schematic representation of the chemical looping process performed in one reactor that is operated periodically. The reducing and oxidizing streams are run counter-currently.	20
Figure 1.15 Schematics representation of a steam reforming process combined with CLC (Luo et al., 2018).	21
Figure 1.16 Schematic representation of the CLR(a) process (Luo et al., 2018).	22
Figure 1.17: Schematic representation of the CLMR process for hydrogen and syngas production in a (a) two and a (b) three reactor system (Luo et al., 2018).	23
Figure 2.1 Flow chart and pictures of the modified solid state synthesis route.	38
Figure 2.2 SEM micrographs of the Glassy carbon spherical powder, 0.4-1.2 micron, type 1.	39
Figure 2.3: Diffraction of X-rays from the lattice planes of a crystalline material (Hubschen et al., 2016).	41
Figure 2.4 Components of a typical powder diffractometer (photo courtesy of Malvern-PANalytical B.V.).	42
Figure 2.5 Photographs from ESRF. a) Reactor system set up at ESRF. b) Capillaries loaded with powdered samples used for room temperature scans.	44
Figure 2.6 Schematic of a typical Scanning Electron Microscope (SEM) (Zhou & Lin, 2007).	45
Figure 2.7 Schematic representation of the different signals produced by electron-specimen interactions and regions within the specimen where the signals are generated (Image courtesy of ThermoFisher Scientific).	46
Figure 2.8: Flow diagram of the mini-reactor setup.	48
Figure 2.9: Flow diagram of the automated fixed bed integral reactor system.	50
Figure 2.10 Simplified layout of a mass spectrometer (Flowers et al., 2015).	51
Figure 3.1 Models of systems with particles with different levels of immersion. a) Deposited, surface-exsolved and submerged-exsolved particles as produced by different preparation techniques. b) Model of the proposed composite system with exo-/endo- nanoparticles (Kousi, Neagu, Bekris, et al., 2020).	58
Figure 3.2 SEM micrographs of powdered $\text{La}_{0.8}\text{Ce}_{0.1}\text{Ni}_{0.4}\text{Ti}_{0.6}\text{O}_3$. (a) Powder grains after sieving with a particle size of 80-160 μm , (b) Detail of the surface of the powder presented in (a) and (c) Powder surface decorated with exsolved Ni nanoparticles.	59
Figure 3.3 Room temperature Synchrotron XRD patterns and SEM micrographs of the synthesised $\text{La}_{0.8}\text{Ce}_{0.1}\text{Ni}_{0.4}\text{Ti}_{0.6}\text{O}_3$. a) XRD patterns of the systems in as-prepared state (grey) and post exsolution at 1000 °C for 10 h in 5% H_2/Ar atmosphere (navy). b) and c) SEM images of the surface of the system: (b) Before exsolution and (c) after exsolution.	59
Figure 3.4 SEM and TEM images of the $\text{La}_{0.8}\text{Ce}_{0.1}\text{Ni}_{0.4}\text{Ti}_{0.6}\text{O}_3$ system. (a) Surface of the perovskite after exsolution (b) Cross section of a near surface area of the perovskite after exsolution with endo- and exo- particles visible. Line added to highlight the edge between surface and bulk. (c) TEM image of the bulk in near surface region before exsolution (d)-(e) TEM images of the bulk after exsolution in near surface (d) and only bulk region (e) where embedded nanoparticles are visible (f) TEM images of the perovskite lattice before (left) and	

after exsolution (right) with lattice models superimposed illustrating the expansion of the perovskite unit cell after endoparticle formation (Kousi, Neagu, Bekris, et al., 2020). 61

Figure 3.5 **Investigation of surface (exo-) and bulk (endo-) exsolved particles. a)** Cross-section SEM revealing exo- and endo- particles and their differences in size and population **b)** Measurement of particles on the surface and bulk in near-surface region **(c)-(d)** Voronoi tessellation of the perovskite based on the proximity of exsolved particles. SEM images with Voronoi diagrams superimposed of a **(c)** near-surface region with both endo- and exo-particles are visible **(d)** bulk region containing only endoparticles **e)** Deconvoluted Ni metal peak from the synchrotron XRD diffractogram presented in Figure 3.3 into the contributing surface and bulk particles via Rietveld refinement **f)** Ni metal particle size distribution of **(a)** calculated via image analysis. **g)** Domain size distribution calculated by image analysis on the Voronoi diagram in **(d)** (Kousi, Neagu, Bekris, et al., 2020). 63

Figure 3.6 **Rietveld refinement of the fresh (a,b) and reduced-exsolved (c,d) samples.** For **(a)** $wR = 17\%$ and **(c)** $wR=18\%$ (Appendix A) (Kousi, Neagu, Bekris, et al., 2020). 65

Figure 3.7: **SEM micrographs of samples reduced at 900 °C for 0, 10 and 30 h and at 1000 °C for 10 h. (a)-(d)** Overview of surface exsolved particles, **(e)** View of the surface and bulk of the sample reduced at 900 °C for 0 h where endoparticles did not form **(f)-(h):** Submerged nanoparticles with superimposed Voronoi tessellation of their spatial arrangement of the samples presented in **b, c** and **d** (Kousi, Neagu, Bekris, et al., 2020). 67

Figure 3.8: **Controlling bulk exsolution, strain and oxygen capacity and exchange. a)** Synchrotron XRD diffractograms of samples reduced at 900 °C for 0 h (dark grey), 10 h (dark blue) and 30 h (blue) and at 1000 °C for 10 h (light blue). **b)** Detail of the diffractogram presented in **(a)**, focusing on the Ni peak and corresponding total (surface and bulk) Ni content (wt.%) calculated via Rietveld refinement. **c)** Parallel axes plot for the systems presented in **(a)** for the Ni metal content at the surface (Ni_s , wt.%) and in the bulk (Ni_b , wt.%) both calculated via Rietveld refinement of the data from **(a)**, oxygen capacity (ζ_G , mol O per mol of perovskite), time constant of oxygen exchange calculated by fitting the data shown in **(d)** with a logistic function (Eq. 3.8) (τ , h^{-1}), ratio of the average endoparticle diameter (s) and average interparticle distance between endoparticles (d), average endoparticle diameter (s , nm) and average distance between neighbouring bulk particles (d , nm, Figure 3.7). **d)** Oxygen uptake from the oxidation experiment via TGA and corresponding oxygen capacity (mol O per mol of perovskite) as a function of time, up to a temperature of 600 °C, for the samples presented in **(a)**. **e)** Arrhenius plot corresponding to the data presented in **(d)** and calculated activation energy for oxygen transport (Kousi, Neagu, Bekris, et al., 2020). 69

Figure 3.9 **Increasing strain levels to unlock oxygen ion exchange. a)** Synchrotron XRD data acquired during the temperature programmed oxidation of a system with submerged nanoparticles presented in 3D plot as a function of diffraction angle, time, and scan number. **b)** XRD data from **(a)** presented in a 2D plot as a function of diffraction angle, time, and corresponding temperature. **c)** O_2 (%) consumption during experiment **(a)**. **d-e)** structural information calculated from **(a)** by Rietveld refinement showing: **d)** Ni metal content and $rABO_3$ microstrain (relative to the initial, reduced state value) as a function of time and temperature and **e)** Unit cell parameter of the Ni metal and $rABO_3$ phase as a function of time and temperature (Kousi, Neagu, Bekris, et al., 2020). 71

Figure 3.10 **Structure and surface of the system post increasing strain via oxygen incorporation by a temperature programmed oxidation experiment.** a) Room temperature synchrotron XRD diffractograms of the system before (navy) and after (yellow) the TPO showing the change in the Ni and perovskite peaks while the La_2TlO_5 remains unchanged. b) SEM image of a cross section of the sample after the TPO c) TEM image and detail of the sample after post oxidation highlighting the crystallographic alignment between perovskite host and a NiO endoparticle. The dotted line follows the perovskite-particle interface. 72

Figure 3.11 **Room temperature synchrotron XRD diffractogram of Ni/Al₂O₃ before (Fresh) and after (Tested) being employed for the activation of methane.** 73

Figure 3.12 **Employing a system with exo-/endo- particles for the activation of methane.** a) Methane consumption as a function of temperature (MTPR) for various systems (150 mg of sample tested): Ni/Al₂O₃ (grey) (SSA ~ 100 m²/ g), system with exo-/endo- exsolved particles, Ni-rABO₃ (navy) (SSA ~ 1 m²/ g) containing nanoparticles exsolved on the surface and in the bulk, and P1 and P2 (black), representing a sample with only surface particles and one with only bulk particles (all surface particles were removed via etching), respectively. (b) Selectivity to carbon containing products corresponding to the experiment described in (a). c) Carbon containing products produced during the experiment described in (a). d) SEM image of the surface of the exsolved sample after the experiment described in (a), e) Room temperature XRD data for Ni-rABO₃ at different stages: fresh (reduced/exsolved), post oxidation (before testing) and after testing for CH₄ activation in the TPR experiment described in (a)..... 74

Figure 3.13 **Carbon deposition after the MTPR experiment described above, measured by temperature programmed oxidation of Ni/rABO₃ (Navy) and Ni/Al₂O₃ (Grey).** a) CO₂ produced during the oxidation of the deposited carbon as a function of temperature, revealing the amount and type of carbon. b) Quantified released carbon from the two systems (Kousi, Neagu, Bekris, et al., 2020)..... 76

Figure 3.14 **Operando insight into the mechanism of methane conversion with a system with exo-/endo-nanoparticles.** a) Synchrotron XRD data of the system acquired during the temperature programmed reduction under 5% CH₄ in 2D, as a function of diffraction angle, time and corresponding temperature (presented in (c)); the plot is aligned with (b) and (c). b) CH₄ conversion to H₂, CO₂, CO products during the TPR experiment described in (a). c) NiO content and perovskite unit cell parameter calculated by Rietveld refinement of the data presented in (a) and plotted as a function of time (presented in (a)) and temperature. d) XRD data of (a) presented in 3D showcasing the transition of NiO to Ni during the TPR experiment described in (a). e) Schematic of the methane conversion mechanism corresponding to the stages identified during the experiment described in (a) (Kousi, Neagu, Bekris, et al., 2020). 78

Figure 3.16 **Operando insight into the mechanism of methane conversion via chemical looping partial oxidation with a system with exo-/endo-nanoparticles.** a) Synchrotron XRD pattern of the system in operando under cycling between redox feeds of 5% CH₄ and 5% O₂ at 650 °C. b) Composition of reactants (CH₄ and O₂) and products (H₂, CO, CO₂) obtained by gas analysis at the outlet during cycling experiment described in (a) and microstrain of rABO₃ during cycling calculated from Rietveld refinement, c) Calculated Ni and NiO wt% and rABO₃ unit cell during cycling, d) SEM micrographs of the micro- and nano- structure of the sample post cycling (Kousi, Neagu, Bekris, et al., 2020). 80

Figure 3.16 **La_{0.8}Sr_{0.2}MnO₃ (LSM821) employed for the conversion of methane.** a) Methane consumption and b) selectivity to carbon products against temperature. Sample microstructure c) before testing and d) after testing. 81

Figure 3.17 **Survey of Chemical looping partial oxidations cycling conditions.** Conversion (left axis) and selectivity (right axis) as a function of cycle number, using an endo-/exo- particle system at different temperatures and flow rates. 150 mg of sample were used and cycled between 5% CH₄/He and 5% O₂/He (Kousi, Neagu, Bekris, et al., 2020)..... 82

Figure 3.18 **Long term stability test of a system with exo/endo-particles employed for the conversion of methane via chemical looping partial oxidation at 570 °C using 300 mg of sample, over 130 cycles.** a) Conversion of reactants and b) product selectivity as a function of cycle number..... 83

Figure 3.20 **Long-term cycling of a system with exo-/endo- particles for the conversion of methane via Chemical Looping partial oxidation using 300 mg of sample, over 130 cycles.** a) CH₄ conversion and selectivity to CO against cycle number. b) Difference in consumption of reactants and selectivity to all products between cycles 25, 75 and 130, c) Selectivity to carbon products against cycle number. d-f) SEM micrographs of the micro- and nano- structure of the sample post 130 cycles, d) Microstructure of the sample intact, e) exoparticles and f) endoparticles preserved post 130 cycles with the nanoparticles preserved. Particle size distribution before (g) and after (f) cycling in their oxidized state (Kousi, Neagu, Bekris, et al., 2020). 84

Figure 4.1 **Systems with gradually increasing endoparticle content.** (a)-(d) 3D models of systems with increasing nanoparticle content in the bulk. (b)-(h) Corresponding SEM micrographs of the surface and bulk of the systems illustrated in (a)-(d). Gradual release of nanoparticles in the bulk was achieved by reducing the La_{0.8}Ce_{0.1}Ni_{0.4}Ti_{0.6}O₃ perovskite in 5% H₂/Ar atmosphere: at 900 °C for 0 h (a, e, grey), 10 h (b, f, teal) and 30 h (c, g, light blue) and at 1000 °C for 10 h (d, h, navy blue). 92

Figure 4.2 **Structure and characteristics of the developed exo-/ endo- systems with progressively higher endoparticle content presented in Figure 4.1.** a) Room temperature synchrotron X-ray patterns of the systems after reduction in different conditions. b) XRD pattern detail of the Ni peak evolution from (a) as the extent of exsolution in the bulk increases. c) Extent of exsolution expressed as increasing exsolved Ni (wt%) content from the quantification of the Ni peak presented in b via Rietveld refinement. d) Average size of exo- and endo- nanoparticles. 94

Figure 4.3 **Activity of endo-/exo- systems with progressively higher endoparticle content against methane.** Methane conversion and selectivity to syngas as a function of temperature. 96

Figure 4.4 **Removal of exoparticles by chemical etching.** (a)-(b) SEM images of a sample with exo- and endo- exsolved particles a) before and b) after removal of surface particles by chemical etching while particles in the bulk remain intact. c) Synchrotron XRD diffractograms of the samples before (Reduced) and after (Etched) etching, d) Detail of the Ni peak from (c) illustrating the absence of a sharp tip on the diffractogram of the etched sample..... 98

Figure 4.5 **Systems designed for deconvoluting the effect of exo-particles on activity.** (a) 3D models of systems with their surface nanoparticles gradually removed while the ones in the bulk remain intact. System with all exoparticles (navy blue) present, system with all exoparticles

removed (grey), system with few exoparticles removed (light blue) and systems with all exoparticles removed but etched to the point where endoparticles are exposed on the surface (teal) (b) Corresponding SEM micrographs of the model systems illustrated in (a).....	99
Figure 4.6 Involvement of exoparticles on the activity of systems with exo-/ endo- particles. Methane activation profiles of the systems presented in Figure 4.5.	100
Figure 4.7 Surface exsolution on exo/endo- particle perovskite systems with different porosity. a) Overview of a dense perovskite system with pore surfaces exhibiting limited exsolution highlighted, b) Overview of a perovskite system with high porosity where pore surfaces are dominant, showcasing the difference between exoparticle characteristics exsolved on native (A-site rich) and cleaved surfaces (A-site deficient).....	102
Figure 4.8 Exo/endo- particle exsolved systems with varying porosities. a) Overviews of perovskite grains with increasing porosity. b) Morphology of the surface the systems presented in (a) with pores occupying larger percentage of the materials surface area as porosity increases.....	103
Figure 4.9 Exsolved particle characteristics in different regions of an exo/endo- particle system. Endoparticles exsolved in the Bulk (navy blue) and exoparticles exsolved on a cleaved surface (black) and on a native surface (teal).	104
Figure 4.10 Comparison of exoparticle exsolution between samples with different porosities. Increasing magnification from left to right. a) Sample with low porosity exhibiting uniform exsolution across its surface and large grain size. b) Highly porous sample with smaller grains and non-uniform exsolution across its surface, which consists of areas with extremely high and extremely low particle population.	105
Figure 4.11 Characteristics of exo/endo- particle systems with increasing porosity. Quantification of a) Exoparticle population and grain size, b) Ni atoms exsolved on the surface and exoparticle size.	106
Figure 4.12 Elucidation of microstructural modification effects on the performance of systems with exo/ endo- nanoparticles. Methane activation profiles of exo/ endo- particle systems with increasing relative porosity.	107
Figure 4.13 Effect of microstructural modifications on product selectivity. a) Methane conversion and product selectivity of systems with increasing relative porosity. b) Schematic of the conversion of methane to products. (c) Variation of CO/CO ₂ and H ₂ /CO ratios as a result of microstructural modification.	108
Figure 5.1 Room temperature synchrotron XRD patterns of the synthesized exo/endo- systems in as-prepared, reduced (exsolved) and oxidised stage. XRD patterns of the newly synthesised La _{0.7} Ce _{0.1} Ni _{0.1} Co _{0.3} Ti _{0.6} O _{3-δ} (LCCNT) system (blue) compared to those of the La _{0.8} Ce _{0.1} Ni _{0.4} Ti _{0.6} O _{3-δ} (LCNT) system (grey) in as prepared (a), reduced (b) and oxidised stage (c).....	114
Figure 5.2 SEM micrographs of La_{0.7}Ce_{0.1}Co_{0.3}Ni_{0.1}Ti_{0.6}O_{3-δ} (LCCNT). a) Overview of the sample grains (80-160 μm), b) overview and c) detail of the surface of the perovskite post reduction (exsolution) in 5% H ₂ / Ar atmosphere at 1000 °C for 10 h, d) cross-section view after exsolution revealing exo- and endo- particles and their different characteristics.....	116
Figure 5.3 Phase analysis via Rietveld refinement of the synthesised exo/endo- systems. Room temperature synchrotron XRD patterns of a) LCCNT (blue) and b) LCNT (grey) in as-prepared, reduced and oxidised states.....	117

Figure 5.4 **Examination of the nanostructure of the Co and Ni-based samples via TEM.** a) Detail of a surface particle embedded in the perovskite matrix b) Overview of the perovskite matrix with exo- and endo- nanoparticles. c) Moire patterns, characteristic of the samples' morphology and FFT pattern. STEM images and corresponding EDX map of d) Reduced LCNT sample with mapping indicating the Ni exsolved particles. e) Reduced LCCNT sample demonstrating the presence of CoNi particles f) Oxidised LCCNT sample with a bimetallic particle with both Co and Ni components on the surface and demonstration of the socket in oxidised form by EDX mapping (Kousi, Neagu, Bekris, Cali, et al., 2020). 118

Figure 5.5 **Employment of the LCCNT system for the activation of methane.** a) Consumption of methane and conversion to products (CO, CO₂ and H₂) for LCCNT, LCNT and Ni/Al₂O₃. b) X-ray diffraction patterns of LCCNT and LCNT. c) Calculated oxygen capacity of the two exsolved samples via the experiments described in a and Rietveld refinement. d) Temperature programmed oxidation experiment (TPO) following the activation experiment described in a. e) Carbon deposition calculated by integration of the curves resulting from the TPO experiment presented in d (Kousi, Neagu, Bekris, Cali, et al., 2020). 120

Figure 5.6 **SEM micrographs of tested samples.** a) SEM images of LCCNT, also representative of LCNT (hence LC(C)NT), before and after testing and after the carbon oxidation experiment after testing. b) Image of the Ni/Al₂O₃ sample after testing illustrating extensive carbon fibre formation on the surface of the sample (Kousi, Neagu, Bekris, Cali, et al., 2020). 122

Figure 5.7 **Surface analysis of the Ni and the Co-based exo/endo-particle systems via XPS.** Core level XPS spectra for LCNT of a. Ti b. Ce c. La d. O₂. Core level XPS spectra for LCCNT of e. Ti f. Ce g. La d. O₂. i. Core level XPS spectra of Ni for the as-prepared (unexsolved), reduced (exsolved), oxidised and tested LCNT system. j. Core level XPS spectra of Co for the as-prepared (unexsolved), reduced(exsolved), oxidised and tested LCCNT system (Kousi, Neagu, Bekris, Cali, et al., 2020). 123

Figure 5.8 **Microstructural modification of the LCCNT exo/endo-particle system.** a) Overview of the sample before (blue) and after (teal) porosity enhancement. b) Particle size analysis of the exoparticles for the systems described in a. 125

Figure 5.9 **Employing the microstructurally modified LCCNT system for methane conversion.** a) Conversion of methane to syngas against temperature by the microstructurally modified (teal) and unmodified (blue) LCCNT systems. b) X-ray diffraction patterns revealing the change in microstructure and in turn nanostructure between the systems tested in a. c) Oxygen capacity of the two LCCNT systems calculated via refinement and the TPR experiment presented in a. 126

Figure 5.10 **Application of the pLCCNT exo/endo-particle system as OCM for the low temperature conversion of methane via Chemical Looping.** a) Conversion of methane and selectivity to carbon products (CO and CO₂) through cycling b) Outlet gas composition over time in the 10th cycle c. 20th cycle d. and 30th cycle e. SEM images of the surface of pLCCNT after the cycling experiment presented in a (Kousi, Neagu, Bekris, Cali, et al., 2020). 128

Figure 7.1 **Flow diagram of the automated fixed bed and pellet reactor characterisation system.** 139

Figure 7.2 **Preliminary results of LCNT exo/ endo- systems in pellet form with increasing exoparticle content employed for the activation of methane.** Unpolished (grey) pellet with exoparticle formation suppressed, and systems with one surface (1S, light blue) and two

surfaces (2S, navy blue) polished with gradually increasing exoparticle content while endoparticle content remains unchanged.141

Nomenclature

\bar{x}	Conversion
f_x	Weight fraction of x species calculated via Rietveld refinement
N_x	Moles of gas x [mol]
ζ_x	Oxygen capacity of x [moles of O per moles of perovskite]
ΔH	Enthalpy change [kJ mol ⁻¹]
AR	Air Reactor
BFP	Back flow preventer
c	Carbon deposition [mg _{carbon} /g _{sample}]
CCS	Carbon Capture and Storage
CL	Chemical Looping
CLC	Chemical Looping Combustion
CLMR	Chemical Looping Methane Reforming
CLMR	Chemical Looping Methane Reforming
CLPO	Chemical Looping Partial Oxidation
CLR	Chemical Looping Reforming
CLR(a)	Autothermal Chemical Looping Reforming
CL-SMR	Chemical Looping-Steam Methane Reforming
CLWGS	Chemical Looping Water Gas Shift
C_x	Conversion of gas x
d	Lattice spacing [nm]
d	Average interparticle distance [nm]
EDX	Energy Dispersive X-ray Spectroscopy
FR	Fuel Reactor
HW	Water delivery system
LCCNT	La _{0.7} Ce _{0.1} Co _{0.3} Ni _{0.1} Ti _{0.6} O _{3-δ}
LCNT	La _{0.8} Ce _{0.1} Ni _{0.4} Ti _{0.6} O _{3-δ}
LSF731	La _{0.7} Sr _{0.3} FeO _{3-δ}
LSM821	La _{0.8} Sr _{0.2} MnO ₃
m	Sample mass [g]
Me	Metal
MPD	Multipurpose diffractometer
MS	Mass spectrometer
M_x	Molar mass of gas x
n	Extend of diffraction
Ni _B	Ni metal content in the bulk [wt.%]
Ni _S	Ni metal content at the surface [wt.%]
NO _x	Nitrogen Oxides
OCM	Oxygen Carrying Material
P	Particle population [particles μm ⁻²]
PI	Pressure Indicator
PI	Pressure indicator

pLCCNT	Porous $\text{La}_{0.7}\text{Ce}_{0.1}\text{Co}_{0.3}\text{Ni}_{0.1}\text{Ti}_{0.6}\text{O}_{3-\delta}$
POX	Partial Oxidation
PSA	Pressure Swing Adsorption
r	Ionic radius
RT	Room Temperature
s	Average nanoparticle diameter [nm]
SEM	Scanning Electron Microscopy
SI	Solid Intermediate(s)
SMR	Steam Methane Reforming
SR	Steam Reforming
SR-CLC	Steam Reforming integrated with Chemical Looping Combustion
S_x	Selectivity of gas x
T	Temperature [K]
TEM	Transmission Electron Microscopy
tf	Tolerance factor
TGA	Thermo-gravimetric analysis
TPO	Temperature Programmed Oxidation
TPR	Temperature Programmed Reduction
WGS	Water Gas Shift
wR	Weighted residual [%]
XPS	X-ray photoelectron spectroscopy
XRD	X-ray Diffraction
δ	Deviation from stoichiometry
δ_{lim}	Concentration limit
θ	Angle of the diffracted beam [°]
λ	Wavelength [nm]
τ	Time constant [h^{-1}]
$p\text{O}_2$	Partial pressure of oxygen
γ	Mole fraction [mol/mol]

1 Introduction

1.1 Research background

One of the major technological challenges facing humanity is providing an abundant, safe, and clean renewable energy source. Hydrogen's potentially high energy efficiency combined with its low generation of pollutants have made it a promising energy vector, which is expected to contribute significantly towards the transition to a Net Zero economy. Reaching Net Zero greenhouse gas emissions by 2050 poses a major challenge that requires action across many economic sectors. When it comes to energy, hydrogen has an important role to play in replacing fossil fuels, as when it is used as fuel, it does not produce any carbon dioxide. Recent scientific and technological interest in hydrogen as an energy carrier and potential transportation fuel has sparked a resurgence in the hydrogen value chain. Additionally, hydrogen is a very important raw material, used in numerous industrial processes such as: petroleum refining, ammonia production (Haber - Bosch process) and hydrogenation of fats in the food industry. Although elemental hydrogen is the most abundant element in the universe, it is not abundant on Earth. In order for hydrogen to be utilized extensively in a sustainable future energy infrastructure to address global energy issues, a number of significant obstacles must be overcome. It is necessary to develop low-carbon, low-polluting, and less expensive methods for producing hydrogen in order to reap the full environmental benefits of it as an energy carrier. Higher energy density hydrogen storage systems, as well as more energy efficient and cost-effective purification and delivery methods, also require scientific advancements.

There are many routes to hydrogen production with the most dominant technology being steam reforming of hydrocarbons (Hafizi et al., 2016b). Currently, almost half of the hydrogen produced globally is via steam reforming of natural gas (Kalamaras and Efstathiou, 2013). The Steam Methane Reforming (SMR), is a well-established process based on the reforming of natural gas with steam, to produce synthesis gas, a mixture of H_2 and CO. However, SMR is an energy intensive process, with the reaction being endothermic and requiring downstream refinement of the products (Tang et al., 2015). Through this process, H_2 production is accompanied by the emission of large quantities of CO_2 , which is another main disadvantage of the steam reforming. For CO_2 separation, additional energy and equipment is needed and even with that, 100% CO_2 capture cannot be achieved (Luo et al., 2018). As a result, research focus has shifted to the development of processes that can offer high yields of pure hydrogen with reduced requirements for separation.

In view of the development of an intensified process for hydrogen production, there has been an increasing interest in chemical looping (CL). Chemical Looping is an attractive alternative to SMR that offers hydrogen/syngas production with high purity and process efficiency. In a chemical looping process, the oxygen needed for the redox reactions is provided by an oxygen carrier material (OCM). A carbonaceous fuel is used to reduce the OCM, which is then re-oxidised by water towards the production of hydrogen or syngas. This is performed in a cyclic manner. One of the main advantages of this process is that the two reactant streams exchange

oxygen only through the OCM. This way, the reactants never come in contact and side reactions are eliminated, all adding to a process that can achieve higher hydrogen conversions without the need of an expensive separation unit.

It needs to be emphasized though, that efficient operation of any chemical looping process strongly depends on the selection of the suitable OCM (Hafizi et al., 2016b; Voitic and Hacker, 2016). The process imposes extremely demanding operating conditions and stringent requirements to the material (Nalbandian & Zaspalis, 2015). Transition metal oxides have been employed as OCMs but suffer from limitations such as: degradation in long term cycling, due to metal particle agglomeration and sintering, limited oxygen capacity, coke deposition and poor activation towards reactants (Dueso et al., 2015). Aiming to overcome these limitations, research interest now lies in the development of novel materials for chemical looping reforming that will exhibit high reactivity and durability. To achieve this, several design approaches have been employed, although tackling problems like particle agglomeration and poisoning especially under cycling remains a challenge.

A wide number of supported materials have been studied during the past decades which mainly include metal oxides, such as NiO and Fe₂O₃, supported on different inert substrates, such as Al₂O₃ and TiO₂ (Nalbandian & Zaspalis, 2015). Among these, Ni-based systems have been the ones studied the most owing to nickel's their high performance against methane. Perovskite oxides have also gained popularity as OCM supports showing promising results, with systems like La_{0.7}Sr_{0.3}FeO_{3-δ} (LSF731) system exhibiting good stability under cycling and resistance to carbon deposition in Chemical Looping Water Gas Shift (Murugan et al., 2011a).

Perovskite supported systems have recently become even more attractive for wide range of demanding technologies, including chemical looping, after the introduction of the exsolution concept. In this, the active metal oxides are doped in the B-site of the perovskite lattice, and upon reduction, emerge on the surface as fine, anchored, metal nanoparticles with tuneable characteristics. Via redox exsolution it is possible to develop complex nanostructures via a single step process with the supported nanoparticles exhibiting high stability, resistance to poisoning and agglomeration and enhanced activity on a plethora of applications (Neagu et al., 2013a).

Aiming to tackle the above challenges and to exploit the potential of exsolved systems and chemical looping, in this study, exsolved materials are developed, characterised and tested for the conversion of methane via chemical looping. The insight gained allows for the demonstration of the exsolved materials' enhanced performance as catalysts and oxygen carriers for methane conversion, while also showcasing the potential of their applicability in various technologies and other fields of research.

1.2 Exsolved perovskite oxide systems

1.2.1 *Perovskite structure and tailorability*

Discovered by Gustav Rose and named after mineralogist Count Lev Aleksevich von Perovski, perovskite materials were first described as a mineral having the composition of CaTiO₃ (Tanaka & Misono, 2001). Since then, perovskite oxides and their derived structures have been studied extensively and even described as 'one of the most important geologic compounds'

owning to their highly stable structure which also has the capacity to accommodate a wide range of cations offering a high degree of versatility (X. Zhu et al., 2018). This has made them an attractive candidate for various processes and transformations that require tuneable materials that can perform under harsh conditions.

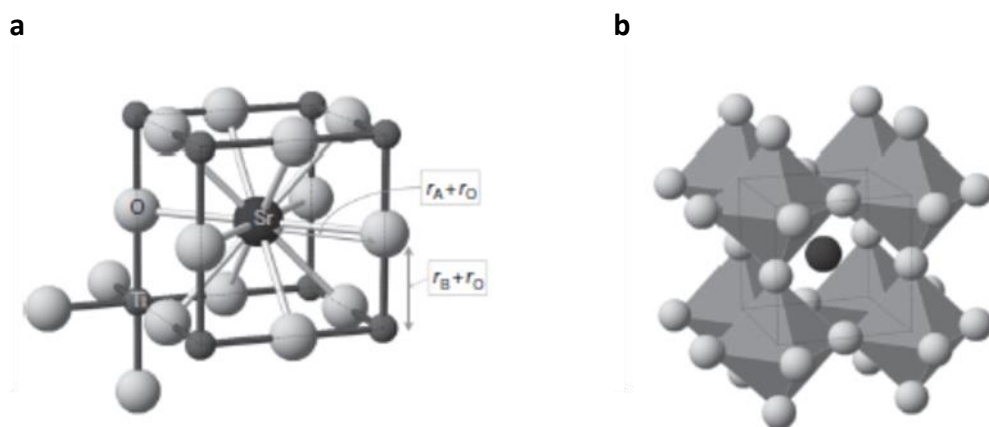


Figure 1.1 **The ideal perovskite structure (ABO₃) as observed in SrTiO₃**. Two perspectives presented: (a) with a focus on the unit cell and cation coordination number and (b) focusing on the BO₆ octahedra (Neagu & Irvine, 2013).

Perovskite oxides are complex oxides with the general chemical formula ABO₃, where generally A is an alkali and/or alkaline earth/rare earth metal and B is a transition element from the transition series or from the main groups III, IV or V of the periodic table (Sarshar et al., 2011). The ideal cubic perovskite structure as exhibited by SrTiO₃ (**Error! Reference source not found.**), space group $Pm\bar{3}m-O_h^1$, can be visualised in two ways. In the first one, the A-site cation in twelve-fold coordination is occupying the centre of the cubic cell while the B cations in 6-fold coordination occupy the corners, with the oxygen anions lying at the midpoint of the edges (Figure 1.1a). Alternatively, the A-site cation is visualised at the centre of the cuboctahedra formed by eight BO₆ octahedra, with the B-site cations located in the in the corner surrounded by an octahedron of oxygen anions (Figure 1.1b) (Peña & Fierro, 2001).

However, defects are commonly observed in the structure due to oxygen deficiency. Consequently, the general chemical formula is modified taking into account these defects, to ABO_{3-δ}, where δ expresses the oxygen deficiency (Protasova & Snijkers, 2016). Additionally, the stability of the cubic structure depends greatly on the ion size; hence the size requirements are quite strict. The relationship between the radii of the different ions in an ideal perovskite unit cell of an ideal perovskite can be derived from Figure 1.1a and expressed as:

$$r_A + r_O = \sqrt{2}(r_B + r_O) \quad (\text{Eq. 1.1})$$

where r_A , r_B and r_O are the ionic radii of A-site, B-site and oxygen ions, respectively.

However, perovskite formation is possible even if Equation 1.1 is not satisfied. In view of this, Goldschmidt (Goldschmidt, 1926) introduced the tolerance factor (tf) in order to predict the feasibility of creating a perovskite structure based on the geometric relationship of ionic radii:

$$tf = \frac{r_A + r_O}{\sqrt{2}(r_B + r_O)} \quad (\text{Eq. 1.2})$$

According to Equation 1.2, for an ideal perovskite structure $tf \approx 1$, while a stable perovskite structure can still form when $0.8 \leq tf \leq 1$ even though some lattice distortion will be present as a result of the tilting of BO_6 octahedra and lowering of symmetry (Tanaka & Misono, 2001; Travis et al., 2016). If $tf > 1$, the A-site cations are too big thus potentially hindering the formation of a stable perovskite. On the other hand, when $tf < 0.8$, alternative structure formation may occur due to the A-site cations being not big enough to fill the perovskite structure (Travis et al., 2016). This level of flexibility, allows the perovskite framework to accommodate and stabilise close to 90% of the metallic species found in the periodic table (Lin & Hohn, 2014). So, with slight buckling and distortion, several distorted versions of the perovskite can be produced (Tiwari et al., 2016). This way the perovskite structure can allow the incorporation of various metal cations at different valence states within the perovskite matrix as long as these fit the size constraints of the A and B sites. The A cation of the perovskite lattice is responsible for the thermal resistance, while the transition metals located at the B-site are responsible for the catalytic activity. In addition, both A and B cations can play an important role in the stability of the perovskite structure as well as the reactivity and selectivity of lattice oxygen during the oxidation of CH_4 (Tang et al., 2015). Taking advantage of this, the material can be tailored in order to achieve required properties (Murugan et al., 2011a).

Additionally, partial substitution of the A-site and/or B-site cations with small amounts of other elements is possible, which can lead to more intricate perovskite chemistries with the general formula of $\text{A}_{1-x}\text{A}'_x\text{B}_{1-y}\text{B}'_y\text{O}_3$ (Jiang et al., 2014; Moradi et al., 2012; Peña & Fierro, 2001; Rioseco et al., 2010). According to the electroneutrality principle, such substitutions can result into the changes of the oxidation state of the metal cations as well as the vacancies on either A-, B- or oxygen sites (non-stoichiometry) (Keav et al., 2014; J. Zhu et al., 2014).

1.2.2 Nonstoichiometry in perovskite oxides

Nonstoichiometric perovskites are perovskites with a structure that deviates from the ideal ABO_3 . As described above, perovskites are able to accommodate defects in their structure and depending on the nature of these defects, accommodation can occur through various mechanisms (Neagu & Irvine, 2013). The type and level of these defects can be caused/ controlled by doping or substituting cations in the perovskite matrix with ones of different size (as briefly described above) and ones that are of similar size but exhibit different oxidation states. This increase/ decrease of charge in the perovskite structure must be compensated according to the electroneutrality principle and perovskites with intricate chemistry can be produced as exemplified in Figure 1.2.

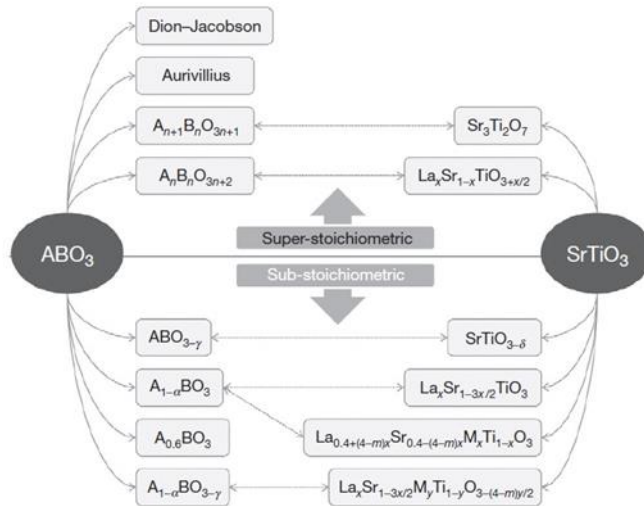


Figure 1.2 Cases of nonstoichiometry in perovskites and corresponding examples based on SrTiO₃ with different dopants (Neagu & Irvine, 2013).

In theory, nonstoichiometry can be observed individually or simultaneously on all A, B and oxygen sites. However, due to the strong interactions between the B and oxygen ions which share the BO₆ octahedra, nonstoichiometry on the B- sites is more difficult to occur than on the A and oxygen sites (Goodenough, 2004). Examples of B- site deficient compositions do exist, such as the hexagonal perovskite series with the general formula of A_nB_{n-1}O_{3n}, but usually the B-site cations are stoichiometric (Trolliard et al., 2004). On the contrary, there is a wide range of perovskite systems exhibiting a plethora of combinations of A and/ or oxygen deficiency. Based on the type of the nonstoichiometry, perovskites can be classified as super-stoichiometric and sub-stoichiometric, as presented in Figure 1.2. In this, the different possible nonstoichiometric systems are exemplified by SrTiO₃ and their deviation from the stoichiometric composition where the oxidation states of Sr and Ti are +2 and +4, respectively. Partial substitution of the Sr²⁺ cations with La⁺³, will require for the excess charge to be compensated and this can happen in a different manner. If extra oxygen is incorporated, oxygen excess stoichiometry is observed, and the resulting perovskite is La_xSr_{1-x}TiO_{3+x/2}. Alternatively, A-site vacancies can form, resulting into an A-site deficient perovskite with the formula La_xSr_{1-3x/2}TiO₃. Partial decrease of the oxidation state of the B-site can also occur. Provided that the lower oxidation state is stable, by reducing the system, perovskites with the formula of La_xSr_{1-x}Ti_{x+1}Ti_{1-x}O₃ can be produced. In the case of B-site cation substitution (Ti₄₊ with M_{m+}, m≠4), a perovskite with oxygen nonstoichiometry with the formula SrM_xTi_{1-x}O_{3-(4-m)(x/2)} can be formed. In this, if m < 4 oxygen vacancies will be formed and if m > 4, oxygen interstitials will be formed. If both A and B site cation substitution occurs, depending on the nature of M and the concentration of vacancies, perovskites of the La_xSr_{1-3x/2}M_yTi_{1-y}O_{3-(4-m)(y/2)} type will be generated. Finally, charge compensation can also happen between the A and B sites, which will lead to perovskite structures with A site deficiency and oxygen stoichiometry (La_{0.4+(4-m)x}Sr_{0.4-(4-m)x}M_xTi_{1-x}O₃).

The tailorable composition, possibility to partly substitute the A and B site cations and the ability of the lattice to accommodate nonstoichiometry, has made perovskite systems attractive for their application in array of technologies. Through careful design it is possible to produce systems with enhanced performance (Tanaka & Misono, 2001). In view of this, perovskites have been studied extensively for a plethora of applications (Sun et al., 2021). The

above are an integral part of this study as well, as upon tailoring the systems' composition and nonstoichiometry and then exposing them to reducing conditions, metal exsolution from the B-site is possible.

Due to their versatile and unique structural and compositional capabilities, perovskite oxides have found application in a wide range of energy-related technologies. Their ability to accommodate a wide arrange of dopants in the anionic and cationic sites, their mixed ion and electron conductivity properties and their tailorable bulk and surface have brought them to the forefront of research of several fields. Here, the focus will be on exsolved perovskite systems and their applications in heterogenous catalysis and chemical looping where their additional ability to accommodate oxygen non-stoichiometry has led to a plethora of articles and reviews specifically focusing on their application as oxygen carrier for chemical looping processes (X. Zhu et al., 2018). Nevertheless, several reviews have been published on their applications in fields like solar cells (Kim et al., 2020; Suresh Kumar & Chandra Babu Naidu, 2021), photovoltaics (Jena et al., 2019), electrochemistry (Hwang et al., 2017; Irvine et al., 2021; Sun et al., 2021), photocatalysis (Irvine et al., 2021; Kanhere & Chen, 2014; Peña & Fierro, 2001; W. Wang et al., 2015), sensors (Shellaiah & Sun, 2020), solid oxide cells (Irvine et al., 2021; Sunarso et al., 2017) and the reader is referred to them and the ever-growing literature for more information.

1.2.3 *The self-regeneration concept*

For years, research on perovskite catalysts was mostly focused on the selection and doping of transition metals on the B-site (Guo et al., 2015; Pecchi et al., 2011; Tanaka & Misono, 2001; Z. Wang et al., 2018) since this is where most of the system's catalytic activity stems from (Chen et al., 2015; Tanaka & Misono, 2001), while the A-site cations have an indirect influence in overall performance. This changed when Nishihate et al. proposed the concept of self-generation of metals from perovskites (Nishihata Y et al., 2002). According to this, particle agglomeration could be addressed by enabling the regeneration of particles via periodical redox cycling of the perovskite system. In the report, Pd nanoparticles on $\text{LaFe}_{0.57}\text{Co}_{0.38}\text{Pd}_{0.05}\text{O}_3$ would oxidise under oxidising conditions and re-dissolve as ions in the perovskite lattice. When then exposed to reducing condition, the ions would be able to re-emerge as on the surface as metallic nanoparticles. These types of systems were referred to as 'intelligent catalysts' owing to their ability of self-regenerating their metal nanoparticles. Additionally, they were found to exhibit higher thermal stability than traditional Al_2O_3 supported catalysts which was attributed to the nanoparticle's ability to suppress agglomeration due to their ability to reversible dissolve and re-emerge in/ from the perovskite lattice (Nishihata Y et al., 2002). Tanaka et al. reported that such Pd/perovskite systems also exhibited higher activity than the Pd supported on Al_2O_3 equivalents with the same loading, further claiming that such perovskite systems can potentially reduce the use of noble metals in catalysis (Tanaka et al., 2004). Adding to the investigation of self-generating systems, later works from Tanaka et al. exemplified that the concept could be successfully employed for the production of systems with metals other than Pd, such as Rh and Pt which showed promising performance applied for automotive emissions control (Tanaka, Taniguchi, et al., 2006; Tanaka, Uenishi, et al., 2006). However, Katz et al. reported that re-generation of Pd nanoparticles on the surface was limited with only a small amount of Pd being able to segregate out of the surface to form nanoparticles upon reduction (Katz et al., 2011, 2012). Additionally, this small amount of Pd was found to be just a few nanometres below the surface of the perovskite host rather than

diffused in the lattice (Katz et al., 2011), while noble metals were found to remain submerged in the bulk of the perovskite (Katz et al., 2012).

In view of the above, coupled with the fact that early research on self-generating systems focused on stoichiometric compositions and limited amount of cations, only a few metals were found capable to actually diffuse through the lattice leading to metal particle formation (namely Ni²⁺, Pd⁴⁺, Rh⁴⁺ and Ru²⁺) (Bierschenk et al., 2011; Madsen et al., 2007; Tanaka, Uenishi, et al., 2006) mostly in the bulk (Katz et al., 2011, 2012) and the process was through to be dependent on the reducibility of the metals. As a result, the self-regeneration concept stopped being attractive for the design of active catalytic systems.

1.2.4 The exsolution concept

Redox exsolution is one of the latest approaches for the creation of materials with supported nanoparticles. Through this method it is possible to develop complex nanostructures via a single step process with the supported nanoparticles exhibiting high stability, resistance to poisoning and agglomeration and enhanced activity on a plethora of applications (Neagu et al., 2013a). In this, through reduction in different atmospheres, metal particles of controlled size are enabled to emerge at the surface of an oxide support (Neagu et al., 2017). Thus, through redox exsolution, the catalytically active transition metals, which in oxidizing conditions are embedded on the B-site of perovskite oxides, can be exsolved on the surface as metal particles (Figure 1.3) (Neagu et al., 2015).

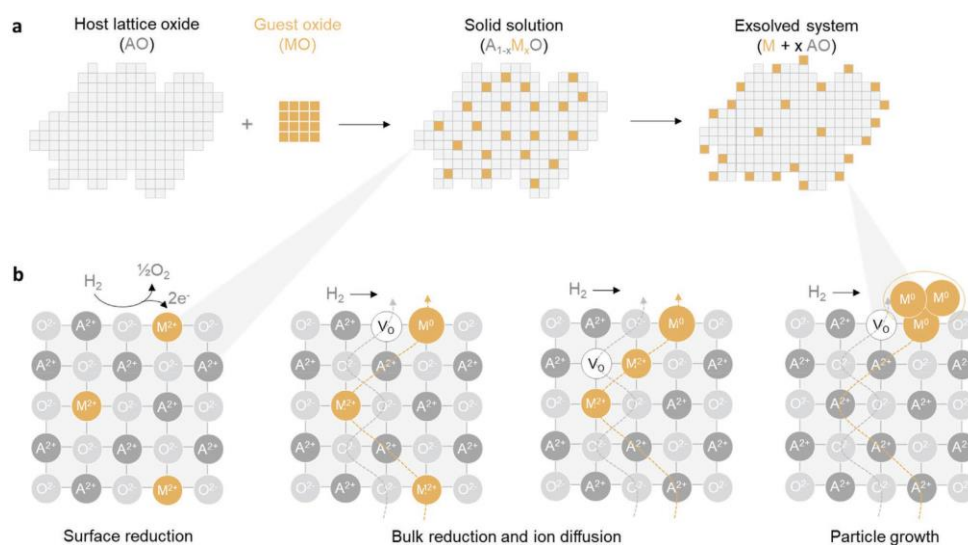
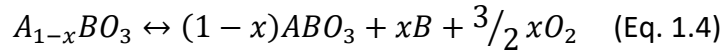
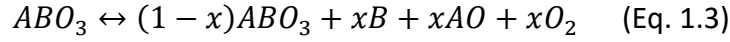


Figure 1.3 **Schematic representation of redox exsolution.** a) Visualisation of B-site exsolution where upon reduction the doped catalytically active species that have been doped on the B-site of the perovskite lattice as cations (yellow squares), exsolve as nanoparticles on the outer surface and b) processes taking place for exsolution to occur (Kousi et al., 2021).

As discussed above, in the original concept of self-regeneration, stoichiometric perovskite oxides (ABO₃) were studied. In this, for the exsolution of x moles of metal from the B-site, x moles of AO oxide will form (Eq. 1.3). Post oxidation, particle redissolution in the lattice would be facilitated by the AO phase reacting with the oxidised particles to form the initial perovskite (Eq. 1.3). However, for an A-site deficient perovskite containing x moles of A-site vacancies (A_{1-x}BO₃), up to x moles of metal would be possible to exsolve from the B-site without AO

formation (Eq. 1.4). Given that in most conditions only a limited fraction of x of the B-site dopant is exsolvable, if sufficient A-site deficiency is present ($x \geq 0.1$), AO oxide formation upon exsolution is less likely, promoting this way the formation of a stable residual perovskite instead. Additionally, this will suppress particle redissolution to the lattice upon oxidation which can lead to irreversibly exsolved particles.



Neagu et al. (Neagu et al., 2013b), proposed the idea that by controlling non-stoichiometry it is possible to produce perovskites which, upon reduction, have surfaces decorated by high populations of anchored metal nanoparticles. They supported this by demonstrating that B-site exsolution is more prone to happen in A-site deficient perovskites rather than in the oxygen excess ones (Figure 1.4). Based on the principle described above, exsolution occurs when in the presence of A-site vacancies (x), the oxygen vacancy concentration, caused through reduction, surpasses a concentration limit (δ_{lim}) destabilizing the perovskite lattice triggering spontaneous exsolution from the B-site in an effort to re-establish stoichiometry of the perovskite lattice (Eq. 1.5) (Neagu et al., 2015). Thus, A-site deficiency serves as the driving force that triggers B-site exsolution which has the capacity to enable the production of a wide range of nanoparticle compositions, including metals previously thought to not be possible to exsolve due to their low reducibility (Neagu et al., 2013b). Additionally, since the residual perovskite formed is stable, this type of redox exsolution differs from the self-regeneration concept, as it is irreversible.

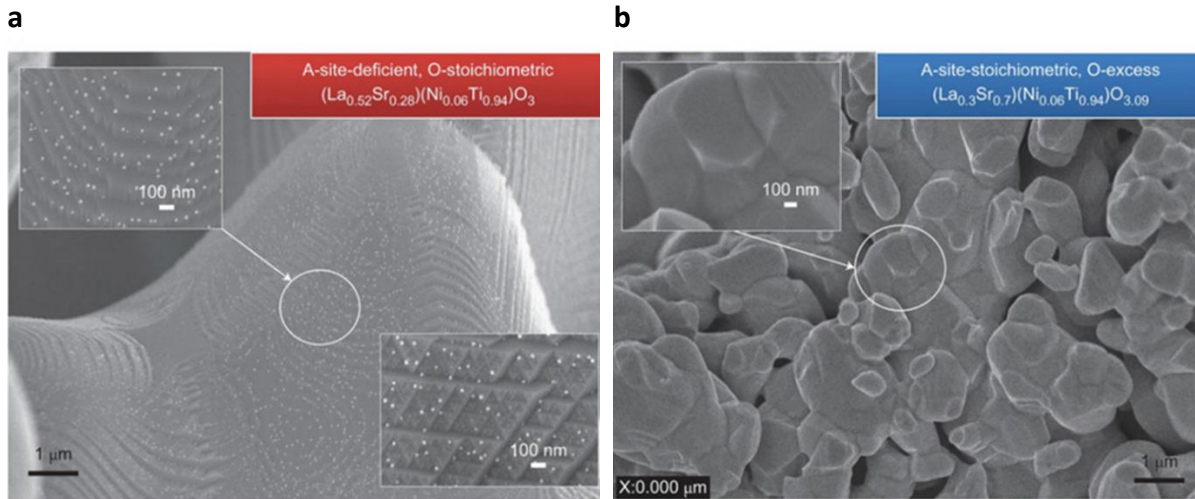
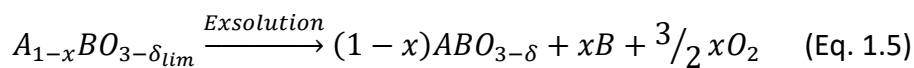


Figure 1.4 **The role of perovskite nonstoichiometry in exsolution.** Exsolution from a) an initially A-site deficient, O-stoichiometric perovskite, and b) an A-site-stoichiometric, O-excess perovskite treated at the same conditions (Neagu et al., 2013a).



The process of exsolution from an A-site deficient perovskite is presented in (Figure 1.5). The perovskite can also be visualised as B-site rich since both A and oxygen sites exhibit deficiency and due to this oxygen can easily be stripped from the unit cell that hosts the A-site vacancy.

As a result, the B-site are prone to exsolution as this dissociation is causing the BO_n to segregate out of the perovskite structure. Upon further reduction of the perovskite, the segregated BO_n site is stripped by the remaining oxygen causing it to exsolve (B).

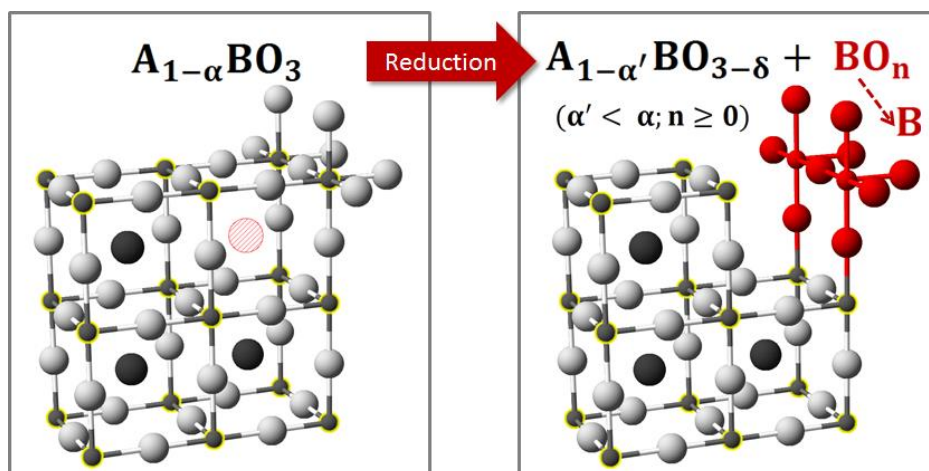


Figure 1.5 **Schematic representation of B-site exsolution from an A-site deficient perovskites.** The O, B and A sites are depicted as silver, yellow/grey and dark grey spheres, respectively. The A-site vacancy is represented by the hashed light red circle (Neagu et al., 2013a).

Due to exsolution's close relationship with stoichiometry, the morphology and topical stoichiometry of the surface of the perovskite also plays an integral role. As the perovskite is treated in oxidising conditions during its synthesis (sintering) the outer surface of the resulting composition (native surface) has been found to develop a different stoichiometry from the bulk. The native surface has been reported to develop A-site enrichment where the surface stoichiometry exhibits a higher A/B ratio compared to the targeted composition stoichiometry (Jalili et al., 2011; Lee et al., 2013). This can occur even if the nominal stoichiometry of the perovskite is A-site deficient (Neagu et al., 2015) and can have major implications on exsolution. Since A-site and oxygen deficiency is necessary in order to destabilise the lattice and trigger exsolution, nanoparticle formation is suppressed on native surfaces (Figure 1.6). Additionally, some perovskite native surfaces are terraced and B-site exsolution will occur preferentially on the edges of the terraces where stoichiometry is more favourable (Figure 1.6b), proof of spatial inhomogeneity on even native surfaces themselves (Neagu et al., 2015). On the other hand, exsolution on the bulk surface of the perovskite, which is exposed by cleaving through the perovskite grains, appears homogenous with high populations of uniformly dispersed nanoparticles, owing to its nominal A-site deficient stoichiometry (Neagu et al., 2015). Therefore, by tuning the perovskite's stoichiometry and taking advantage of the particular chemistry of its surfaces, systems with different exsolution can be developed. This close relationship between surface stoichiometry and exsolution is an important part of this study and is discussed in more detail in Chapter 4.

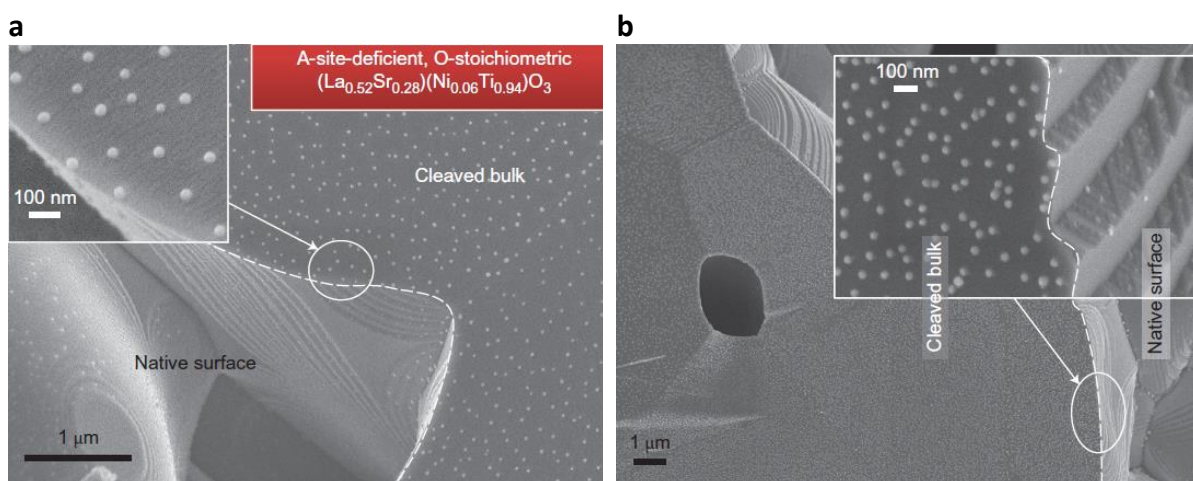


Figure 1.6 The role of perovskite surface stoichiometry in exsolution. SEM micrographs illustrating the difference in particle exsolution on a A-site-deficient, O-stoichiometric $\text{La}_{0.52}\text{Sr}_{0.28}\text{Ni}_{0.06}\text{Ti}_{0.94}\text{O}_3$. a) and b) Difference in nanoparticle exsolution on the native and cleaved surface. b) Preferential partial exsolution on the terraced native surface of the perovskite (Neagu et al., 2013b).

Nanoparticle-host systems formed via redox exsolution have exhibited numerous enhanced properties owing to the particle's unique characteristics which stem by the fact that they grow from within the support lattice. Exsolution offers a high level of control over the particles characteristics such as size, distribution, shape and population allowing for the design of highly tailorable systems with features that can greatly enhance their activity and selectivity (Myung et al., 2016; Neagu et al., 2013b). The socketed nature or anchorage of the exsolved nanoparticles is of particular importance, as they are partially embedded in the support phase while remaining crystallographically aligned (Figure 1.7) (Neagu et al., 2015). Exsolved particles have been reported to be partially socketed with up to ~30% of the particle being submerged in the perovskite host (Figure 1.7c, d). The alignment and deep anchorage result in a strong interaction between particle and support thus leading to a combination of unique properties (Chambers et al., 2013; Neagu et al., 2015), which systems prepared with traditional deposition techniques do not possess (Figure 1.7d).

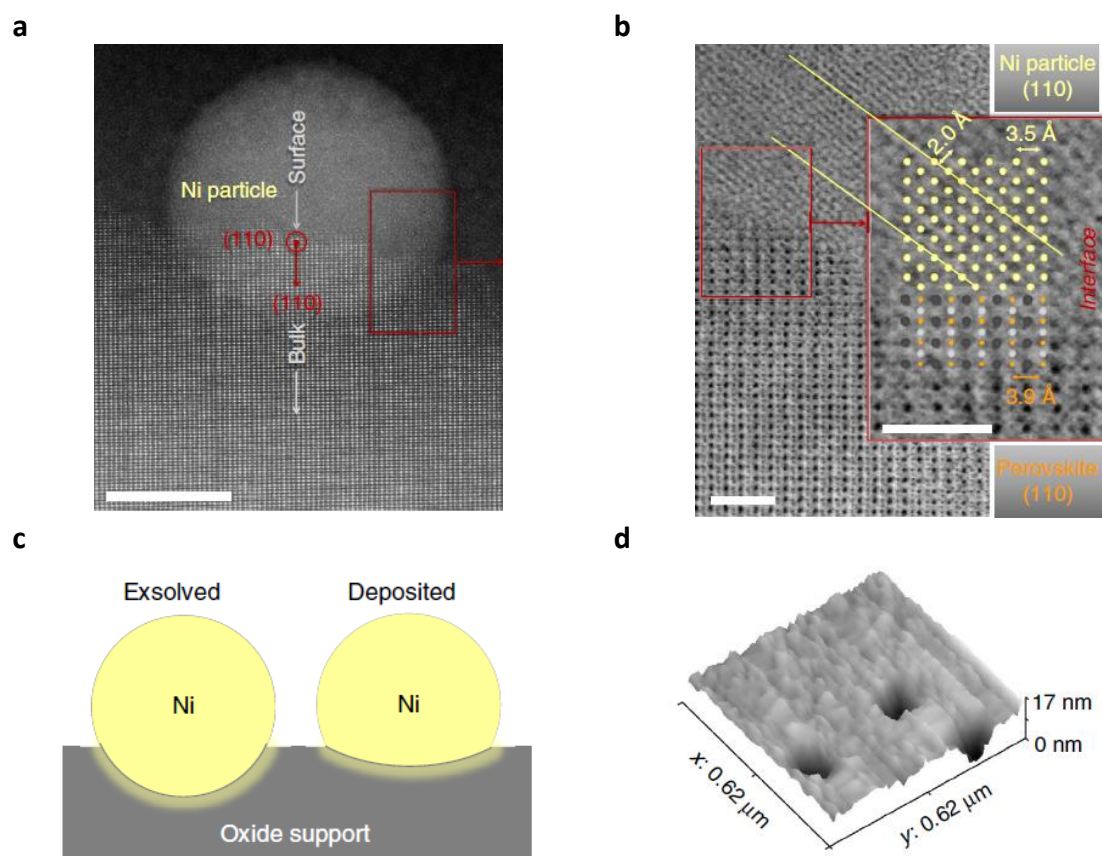


Figure 1.7 **The aligned and socketed nature of exsolved nanoparticles. a and b) Exsolved particle–perovskite support interface.** a) TEM micrograph of an exsolved Ni particle; scale bar, 10 nm. b) TEM micrograph detail of the metal–perovskite interface; scale bars, 1 nm. c) Illustration of particle–support interface for deposited and exsolved particles. d) Three-dimensional AFM of particle sockets (Neagu et al., 2015).

Correspondingly, particles produced via exsolution have been reported to exhibit enhanced stability against agglomeration and resistance to poisoning mechanisms, such as coke formation, due to the combination of socketing and alignment (Neagu et al., 2015, 2017). This is presented in Figure 1.8a, c, d where a deposited nanoparticle system is covered in carbon fibres after being exposed to a 20% CH₄ atmosphere, while an exsolved system only exhibits minimal amounts of carbon on its surface after being treated in the same conditions. The strong particle–host interaction in the exsolved system suppresses carbon fibre mechanisms such as tip-growth which would lead to carbon fibre formation and uplifting of the particle out of the support. Instead, only a small amount of carbon is formed if any, and even this is following a base growth mechanism which leaves the nanoparticle still attached to the support (Figure 1.8b). Additional research on the resistance of exsolved systems to other types of poisoning, has also found them to be tolerant to sulphur poisoning. Papaioannou et al. found that exsolved systems exhibit a higher tolerance to poisoning from sulphur versus deposited ones and although loss of activity did occur, this was able to be recovered once sulphur was removed from the reactant gas (Papaioannou et al., 2019). This makes exsolved systems attractive for a plethora of challenging transformations in harsh conditions like CLMR.

Furthermore, exsolved particle systems have exhibited superior activity to that of deposited systems attributed to the strain imposed to the nanoparticles due to their socketing (Han et al., 2019). Since strain has been reported to unlock multiple material properties, this opens the possibility for further tailoring the materials performance via strain engineering possibly improving the system's thermal, ion, magnetic, thermal transport, catalytic activity and magnetic properties (Kousi et al., 2020).

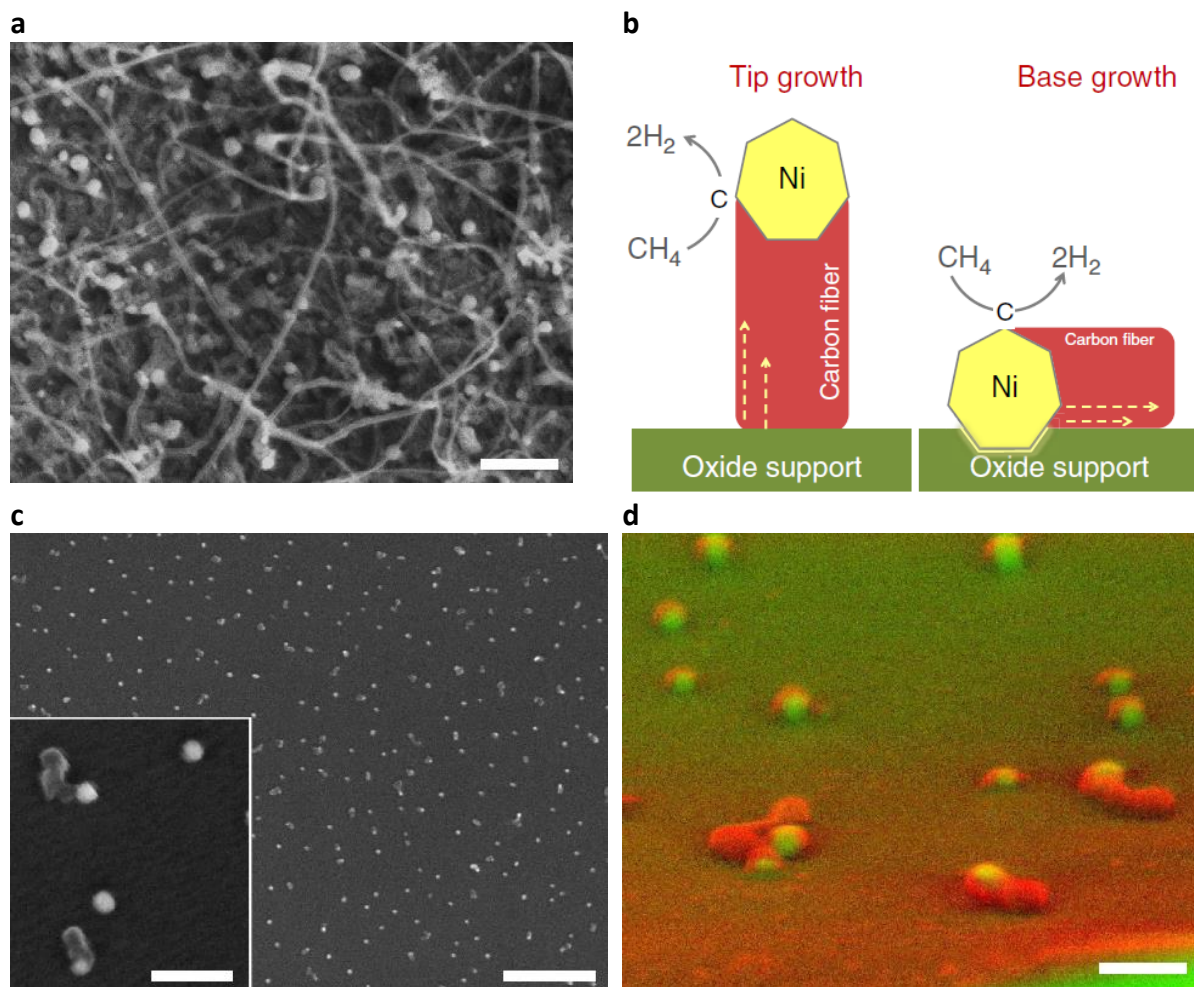


Figure 1.8 **Anti-coking ability of exsolved particles.** a) Ni particles created by infiltration on $La_{0.4}Sr_{0.4}TiO_3$ after coking test, exhibiting extensive carbon fibre growth; scale bars, 1 mm. b) Schematic of carbon fibre growth mechanisms. c) Ni particles formed by exsolution from $La_{0.52}Sr_{0.28}Ni_{0.06}Ti_{0.94}O_3$, after coking test, exhibiting limited carbon fibre growth; scale bars, 0.5 mm (overview); 100nm (detail). e) False colour micrograph of the sample presented in c (Neagu et al., 2015).

1.3 Hydrogen and syngas production

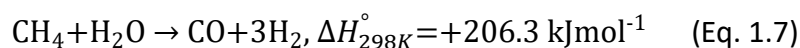
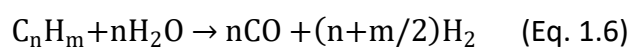
Reports have shown a rise in hydrogen demand which has been demonstrated by the increase of its annual production and consumption (Hafizi et al., 2016b). Indicatively the annual production of hydrogen has been estimated to reach 55 million tons and its consumption is projected to increase by 6% (Kalamaras and Efstathiou, 2013). Hence, the development of efficient processes that will make hydrogen readily available and lower production cost which, at the moment is still high, has been the focus of many researchers (Luo et al., 2018).

There are many routes to hydrogen production through both renewable and non-renewable sources, the main of which are: natural gas, coal, oil, biomass and water. However, large scale hydrogen production has been dominated by fossil fuels, with the most significant and well-established technology being steam reforming of hydrocarbons (Hafizi et al., 2016b). Currently, almost 50% of the hydrogen produced globally is via steam reforming of natural gas, while about 30% comes from oil/naphtha reforming, 18% from coal gasification, 3.9% from water electrolysis, and 0.1% from other sources (Kalamaras and Efstathiou, 2013). Natural gas (methane) has been selected as the main feedstock for hydrogen production through reforming, mainly because of its low cost and, when compared to other hydrocarbons, its lower emissions of airborne pollutants and greenhouse gases. Apart from steam methane reforming, partial oxidation, auto-thermal reforming, and CO₂ reforming are the primary processes considered for large scale methane conversion into hydrogen (Hafizi et al., 2016b). A brief review of the main established technologies for hydrogen/ syngas production follows.

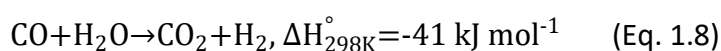
1.3.1 Steam reforming of hydrocarbons

Steam reforming of natural gas or steam methane reforming (SMR) is one of the most developed and well-established commercial technologies. The main steps of the process include: feed stock purification, steam reforming, high-temperature shift reactor, low-temperature shift reactor followed by a pressure swing adsorption unit for purification of the produced hydrogen (Luo et al., 2018). A block diagram of the SMR process is presented in Figure 1.9.

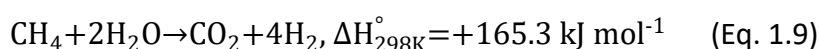
In order to protect the catalyst from corrosion, the feedstock must pass through a desulfurization process prior to entering the reformer, since even small amounts of sulphur are enough to poison the catalyst. Following that, the feedstock consisting of light hydrocarbons (Eq. 1.6), methane in SMR (Eq. 1.7), is catalytically reformed with steam at high temperatures (700 °C to 925 °C) to produce syngas (Eq. 1.6). Syngas is a mixture of hydrogen (H₂) and carbon monoxide (CO). The heat required for the reaction, is supplied to the reformer by the combustion of part of the natural gas or the purge gas from the pressure-swing adsorption (PSA) in a furnace (Goswami et al., 2003; Luo et al., 2018).



The produced syngas is then cooled and then shifted in the water-gas shift reactors, where carbon monoxide reacts with steam to produce H₂ and carbon dioxide (CO₂), increasing hydrogen yield and decreasing CO concentration in the stream (Eq. 1.8).



And the overall reaction of the SMR (Eq. 1.9):



Finally, the mixture of CO₂ and H₂ is sent to a gas purifier where the separation of hydrogen from CO₂ takes place via pressure swing absorption. Overall, SMR produces hydrogen with a purity of 96-98% and with operating efficiencies ranging from 65-75% (Goswami et al., 2003).

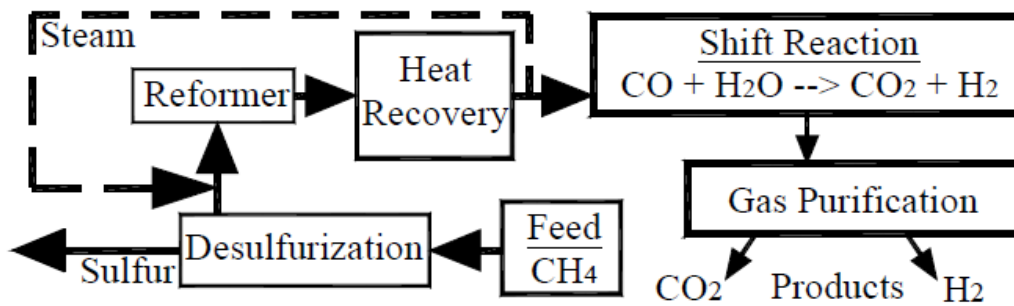
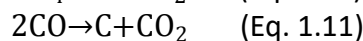
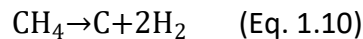


Figure 1.9 Block diagram of the steam methane reforming process for hydrogen production (Goswami et al., 2003).

Due to the combustion of fossil fuels, in order to provide the heat to the reformer, by-products of this are carbon monoxide and carbon dioxide. The most common catalysts used is nickel. However, catalyst utilization of the process can be poor, since the rate-limiting parameter is the heat transfer coefficient of the internal tube wall of the reformer tubes. Hence, great care should be taken when loading the tubes.

Additionally, carbon deposition through methane decomposition (Eq. 1.10) and the Boudouard reaction on the Ni catalyst (Eq. 1.11) occurs during the process. This leads to material degradation and can cause other severe operational trouble (ie: reactor blockage), thus it's very important to be avoided (Luo et al., 2018).

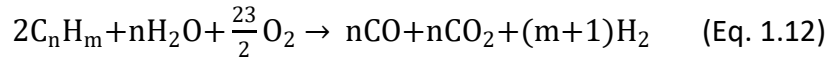


The WGS reaction (Eq. 1.8) is usually carried out in two fixed bed adiabatic reactors, connected in series with a cooler between them. The first reactor operates at higher temperatures with a Fe/Cr catalyst, while the second operates at lower temperatures employing a Cu/Zn/Al catalyst with a purpose to increase the possible equilibrium conversion of CO as the WGS reaction is exothermic. In order to capture CO₂ and purify the H₂ produced, PSA and amine absorption can be used. Chemical adsorption is usually met in older plants while modern hydrogen plants apply PSA. PSA separates hydrogen from the other components with high efficiency, producing higher quality hydrogen (99.999%) against the one obtained through the scrubbing systems (95-98%). However, these processes increase the total investment costs and decrease the thermal efficiency of the SMR process (Luo et al., 2018).

It is projected that the cost of hydrogen generation will increase by almost 22% if carbon capture and storage (CCS) system is added. Therefore, although the SMR process is the dominant process for hydrogen generation, it's also a very complex, multi-step, and energy intensive process, with variable parameters, like the heat transfer coefficient of the reformer tubes that limit the efficiency of the process. Additionally, H₂ production is accompanied by the emission of large quantities of CO₂, which is the main disadvantage of the steam reforming. For CO₂ separation, additional energy and equipment is needed and even with that, 100% CO₂ capture cannot be achieved (Luo et al., 2018).

1.3.2 Partial Oxidation of Hydrocarbons

Partial oxidation of hydrocarbons is an exothermic reaction that uses oxygen and superheated steam at moderately high pressure with or without a catalyst, depending on the feedstock, for conversion of (heavy) hydrocarbon feedstocks into a mixture of syngas and CO₂ (Eq. 1.12) (Goswami et al., 2003; Kothari et al., 2008). A block diagram of the POX process can be seen in Figure 1.10.



The energy required for the process is provided through the combustion of part of the feedstock. The process is capable of handling all kinds of gaseous and liquid hydrocarbon fuels and due to that, it's attractive for processing high-boiling and high-sulphur raw materials (i.e.: heavy oil and petroleum refinery residual oil) (Kothari et al., 2008). Control over the quantity of O₂ and water vapour required for the reactions is very important. Similar to the SMR, in order to increase the H₂ content, the mixture of H₂, CO and CO₂ is subjected to the water gas shift reaction (Eq. 1.8), towards the formation of H₂ and CO₂. The overall process efficiency lies at about 50%. The main disadvantage of the POX process is that CO and CO₂ are emitted and the need for an air separation unit that is required for supplying pure oxygen to the process in order to prevent the release of nitrous oxide. The addition of this unit increases the capital cost of the plant and consequently the overall cost of the produced hydrogen (Goswami et al., 2003).

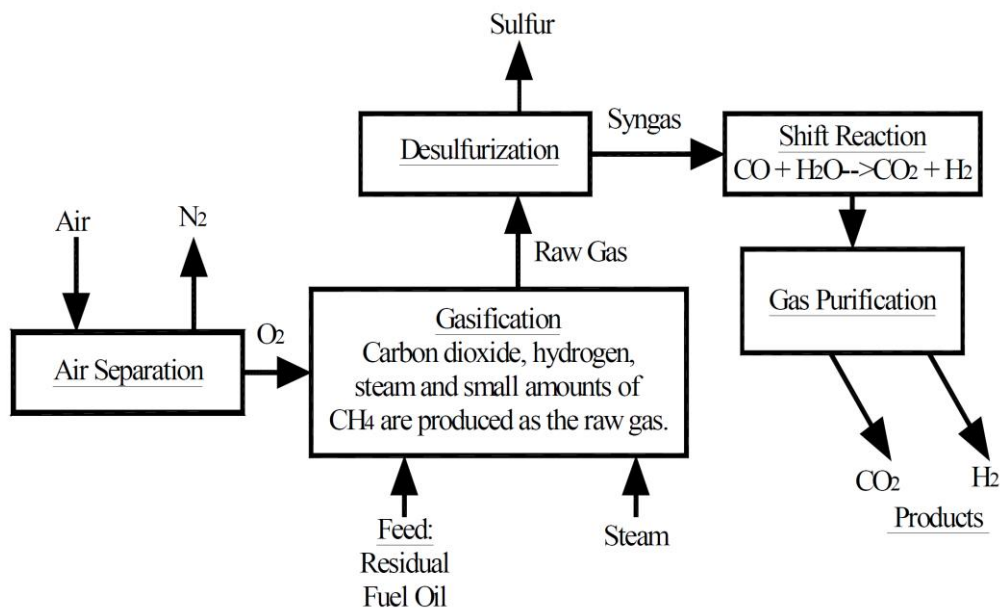
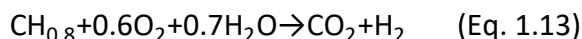


Figure 1.10 Block diagram of the partial oxidation process for hydrogen production (Goswami et al., 2003).

1.3.3 Coal Gasification

The gasification process shares similarities with the partial oxidation process, with its reaction mechanisms resembling with those of the partial oxidation of heavy oils, but it takes place at much higher temperatures (1100-1300 °C) and is capable of using a wide range of solid feed

stocks such as: coal, heavy refinery residuals and biomass. The main reaction for the gasification of coal is:



The process allows the utilisation of a wide range of fuel options from coal, which is the most abundant fossil fuel, to low-grade coal types. In the gasification process, the feedstock in a dry or slurry form is subjected to elevated temperature and pressure conditions in an oxygen-depleted environment. This leads to the conversion of the carbonaceous fuel into a mixture of gas, which mainly consist of carbon monoxide and hydrogen. After that the inorganic materials present in the feed are removed in the form of molten slag from the bottom of the reactor (Goswami et al., 2003). CO_2 is the largest emission from the systems. More details on the two major methods used for the production of hydrogen from coal: the synthane process and the CO_2 acceptor process can be found in literature (Kothari et al., 2008). At the moment there are two coal gasification processes that are commercially established: the Koppers-Totzek process, which operates at atmospheric pressure, and the Texaco process (Goswami et al., 2003).

1.3.4 H_2 from renewable sources

Hydrogen can also be produced from biomass resources such as: agricultural residues (corn stover, wheat and rice straw), forest residues (trees and leaves), industrial wastes (sugarcane bagasse, citrus peel and milling residues) and energy crops (tall grasses and fast-growing trees) (Goswami et al., 2003). Given the options, biomass is the most versatile non-fossil energy resource and as a result it has attracted a lot of research.

Biomass can be converted to hydrogen through many routes, including the methods described for the conversion of fossil fuels. These routes are summarized in Figure 1.11 and will not be covered here. The reader is referred to literature for more information on the topic (Milne et al., 2002).

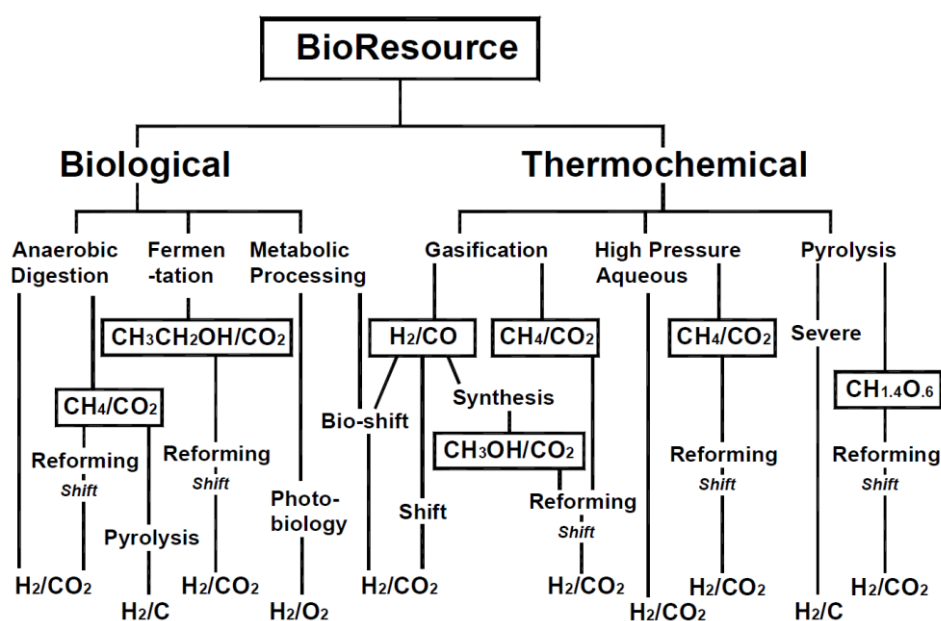


Figure 1.11 Pathways for hydrogen production from biomass. Storage intermediates are shown in boxes (Milne et al., 2002).

When electricity passes through a media, it has the ability to split the media into its elements. With the water acting as the medium, through electrolysis, can be split to hydrogen and oxygen. Water decomposition by electrolysis can be described by two partial reactions that take place at two electrodes that are separated by an ion-conducting electrolyte (Figure 1.12). Hydrogen is produced at the cathode and oxygen at the anode. An ion-conducting separator (diaphragm) is used to separate the two chambers, so that the two gasses will not mix (Goswami et al., 2003). The interest in electrolysis rises because it doesn't rely on fossil fuels and has the ability to produce high purity hydrogen with low to zero CO₂ emissions. Carbon dioxide is only emitted when electrolysis is employed within power plants that use fossil fuels to generate the required electricity (Kothari et al., 2008).

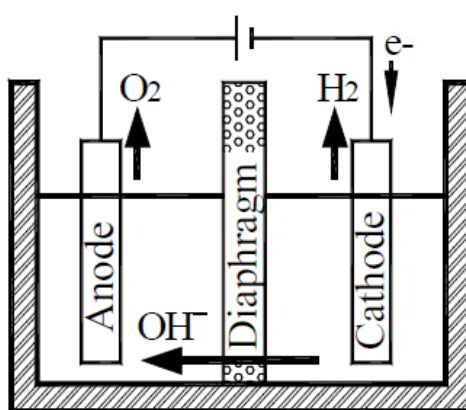


Figure 1.12: **Schematic representation water decomposition by electrolysis** (Goswami et al., 2003).

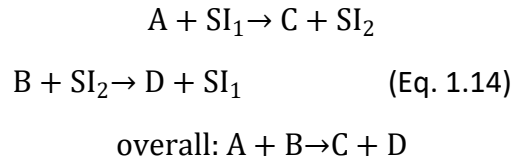
Hydrogen can also be generated from renewable energy sources such as water, wind and solar, leading to a considerable reduction or zeroing of the production CO₂ emissions. In the case of electrolysis being carried out with electricity produced from wind and solar energy could have the process has the potential to be CO₂ neutral. Therefore, many processes have been developed for hydrogen production through various non-hydrocarbon routes. These processes are not going to be discussed here and the reader is referred to (Goswami et al., 2003; Kothari et al., 2008) for more information.

1.4 Chemical looping for H₂ production

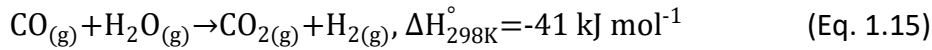
1.4.1 *Concept overview and applications*

In view of the need for the development of an intensified process for hydrogen production, there has been an increasing interest in chemical looping. Chemical looping (CL) has the ability to convert carbonaceous fuels to desired products, such as syngas/hydrogen or heat/electricity, combined with carbon capture without significant loss of efficiency or additional cost (Hafizi et al., 2016; Luo et al., 2018)

Chemical looping can be defined as a process where a reaction (e.g., $A+B\rightarrow C+D$) is divided into multiple subreactions which are carried out divided in time and or/space (Eq. 1.14). The sub-reactions are linked through solid intermediate (SI), such as metal oxides, that is circulated between the reactors, with the SIs being reduced and oxidized in a cyclic fashion through the progress of the sub-reactions (Moghtaderi, 2012).

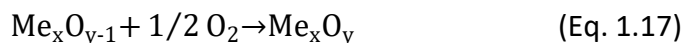


Historically, the chemical looping concept for large scale generation of hydrogen was first introduced as the “steam-iron” process by Howard Lane and his co-workers. In this process CO was used as a reducing agent to reduce iron oxide, which then was re-oxidized by H₂O producing H₂. H₂O splitting over metal Fe results in oxidation of the Fe to Fe₃O₄ producing H₂. The Fe₃O₄ is then reduced back to metal by CO closing the cycle (Murugan et al., 2011b; Voitic & Hacker, 2016). The overall process is the water-gas shift (WGS) reaction:



The main advantage of the Chemical looping concept is that the concept can be applied for many different well-established processes and optimised so that the energy losses of the overall process are reduced, while allowing inherent separation of undesired products (e.g., CO₂), that are generated from side-reactions, yielding an overall efficient, economical, and low-emission process. Indeed, chemical looping, especially during the last decade, has been employed in a wide range of processes. These processes include chemical looping gasification and chemical looping reforming (pre-combustion capture of CO₂), chemical looping combustion (CLC; in situ capture of CO₂), sorbent chemical looping (post-combustion capture of CO₂), chemical looping air separation for oxygen supply in oxy-fuel and integrated gasification combined cycle operations, and chemical looping removal of ventilation air methane in mining operations (Moghtaderi, 2012)

A typical chemical looping process is chemical looping combustion (CLC) which is a combustion process, used for heat and power generation. In CLC, two reactors, an air reactor (AR) and a fuel reactor (FR), are used, and, between them, an oxygen carrier (metal oxide) is cycled transferring oxygen from air to the fuel, avoiding direct contact between the two (Fig. 6). In the FR, the metal oxide is reduced by the fuel, and the fuel is oxidized to CO₂ and H₂O through Eq. 1.16. In the AR, the metal oxide is oxidized to its initial state with O₂ through Eq. 1.17. Because fuel and air are separated in CLC, the combustion products of CO₂ and H₂O are not diluted with nitrogen. This way it is possible to obtain almost pure CO₂ simply by condensing the H₂O without spending any extra energy for separation. Other benefits include a large elimination of NO_x emission and high thermal efficiency (Luo et al., 2018; Protasova & Snijkers, 2016).



The application of the chemical looping technology for hydrogen production shares the same general principles with CLC, with the main difference that the target products are hydrogen and/or synthesis gas instead of heat. In a typical chemical looping process for hydrogen production, the oxygen needed for oxidation reactions is provided by a solid oxygen carrier, thus avoiding inserting gas phase oxygen in the feed. A carbonaceous fuel is used to reduce the oxygen carrying material (OCM) which is then re-oxidised by water, towards the production of hydrogen. This is performed in a cyclic manner (Dueso et al., 2015). The OCMs can be simple transition metal oxides or complex metal-based composite materials. One of the main advantages of this process is that the two-reactant streams (water and carbonaceous fuel) exchange oxygen only through the OCM. That way, the two streams never come in contact, oxygen is exchanged only through the OCM and side reactions are eliminated, all adding to a process that can achieve higher hydrogen conversions without the need of an expensive separation step. The reduction and oxidation stages can either be carried out in two separate reactors between which the OCM is circulated (Figure 1.13) or in one reactor that is operated periodically (Figure 1.14).

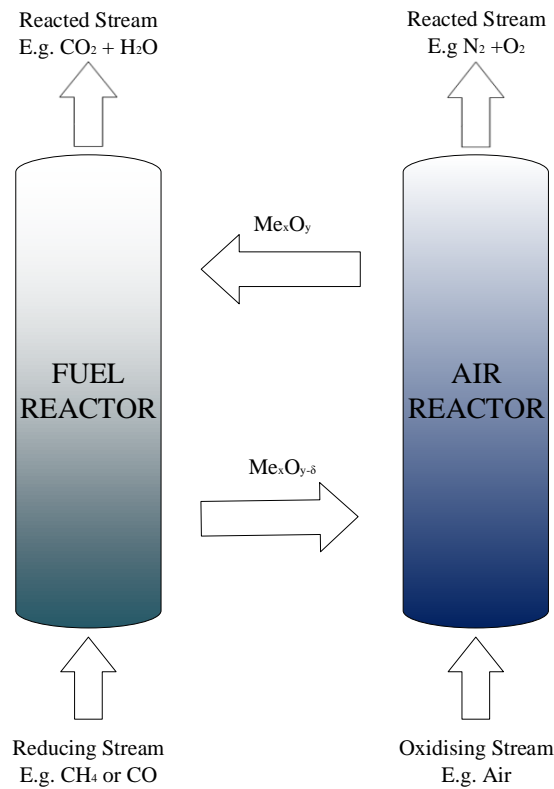


Figure 1.13 **Schematic representation of the chemical looping process performed in two separate reactors between which the OCM is circulated.** The OCM is reduced in the Fuel reactor and oxidized in the Air reactor.

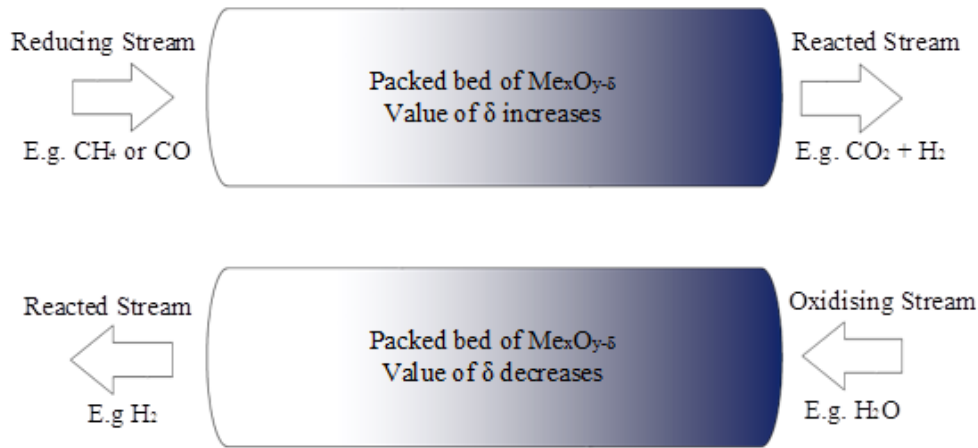


Figure 1.14 **Schematic representation of the chemical looping process performed in one reactor that is operated periodically.** The reducing and oxidizing streams are run counter-currently.

1.4.2 Chemical looping reforming

When the chemical looping concept is applied on reforming processes, the resulting technologies can be divided in three main categories, based on their principles and characteristics. The first is steam reforming with chemical looping combustion (CLR), also called Steam reforming integrated with chemical looping combustion (SR-CLC), the second autothermal chemical looping reforming (CLR(a)) and the third chemical looping reforming of methane (CLMR or CLRM), also called chemical looping steam methane reforming (CL-SMR) or two step methane reforming (Luo et al., 2018).

1.4.3 Steam reforming with chemical looping combustion

This process is a combination of the conventional steam reforming process and CLC. The steam reforming reactions take place inside tubes that are filled with a suitable catalyst and work at elevated pressures, but instead of being located inside a reformer, as in the conventional process, they are either placed directly in the fuel reactor, or in a fluidized bed heat exchanger of a CLC system (Figure 1.15). This way, the heat required for the reformer tubes is provided by the oxygen carrier particles from the AR and not by direct firing outside of the tubes. The gas produced from the steam reforming reactions, (a mixture of CH_4 , CO_2 , CO and H_2) is used as the feed gas to the fuel reactor. The product of the AR is depleted air, and from the FR is a mixture of CO_2 and H_2O . Pure CO_2 can be easily obtained by removing the H_2O from the stream through condensation (Luo et al., 2018). Advantages of this process over the conventional SMR include: almost 100% CO_2 capturing can be achieved by separating H_2O in the flue gas of the FR through condensation, higher heat-transfer coefficient can be obtained for the outside of the tubes in the fluidized bed than in a furnace, which is very important for the reforming process, since low heat transfer coefficient of the tubes is the limiting step, and thermal NO_x formation is avoided because the temperature in the AR is relatively low. Additionally, because steam reforming takes place in elevated pressure, the power consumption for compression of produced H_2 is reduced. The main problems faced are erosion of the reformer

tubes inside the reactors due to their exposure to the high temperatures of the reformer or the harsh environment of the fluidized bed reactor. Also, the WGS and PSA units required downstream, increase investment and product costs (Luo et al., 2018).

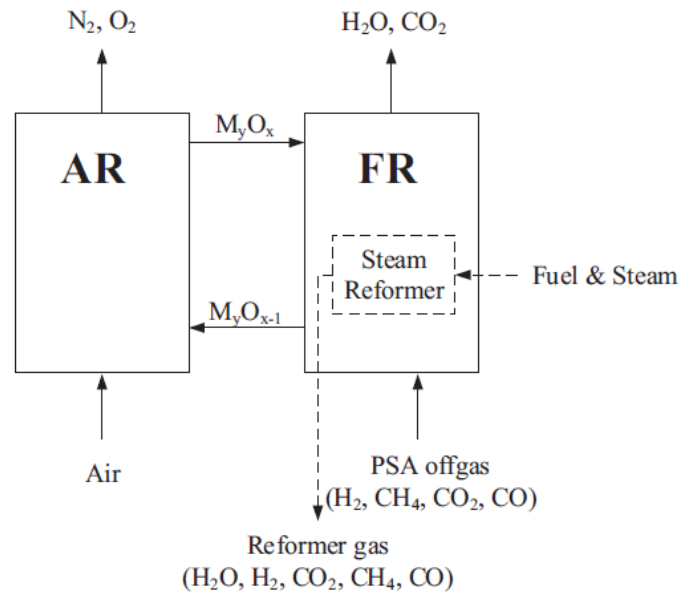


Figure 1.15 Schematics representation of a steam reforming process combined with CLC (Luo et al., 2018).

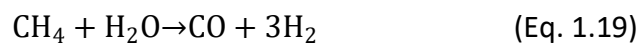
1.4.4 Autothermal chemical looping reforming

Autothermal chemical looping reforming (CLR(a)), shares the same basic principles with CLC with the difference that the target product is not heat but synthesis gas (H_2 and CO). A schematic representation of the CLR(a) process is provided in Figure 1.16. To achieve that, the air to fuel ratio is kept low to prevent the carbonaceous fuel from being fully oxidized to CO_2 and H_2O . The reacted stream that exits the FR mainly consists of CO and H_2 , with trace amounts of CO_2 and H_2O . A WGS reactor is employed downstream the reformer in order to maximize hydrogen production. This is followed by a PSA or ammine adsorption unit that is used for the separation of H_2 from CO_2 (Luo et al., 2018)

Direct partial oxidation of CH_4 with the metal oxide:



Heterogeneous steam reforming and CO shift:



Internal combustion:

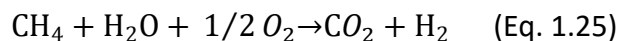




In the AR the metal oxide is re-oxidized by air:



The overall reaction of the CLR(a):



As can be understood from the above reactions, practically CLR(a) in its simplest form can be described as a combination of the partial oxidation and steam reforming processes. The partial oxidation process is exothermic, but the steam reforming process is highly endothermic, so it's important that the ratio of the reforming process to the partial oxidation process be kept low in order to maintain an exothermic overall status (Luo et al., 2018).

Advantages of the CLR(a) process include: attractive process for the production of syngas for methanol production and Fischer-Tropsch synthesis, as the syngas produced has the required H_2/CO ratio of 2, elimination of the need for external combustion for heat generation for the reforming process, CO_2 emissions from external combustion are eliminated, less steam and catalyst required per unit of fuel feed, high heat transfer in the fluidised bed and no thermal NO_x formation (Luo et al., 2018).

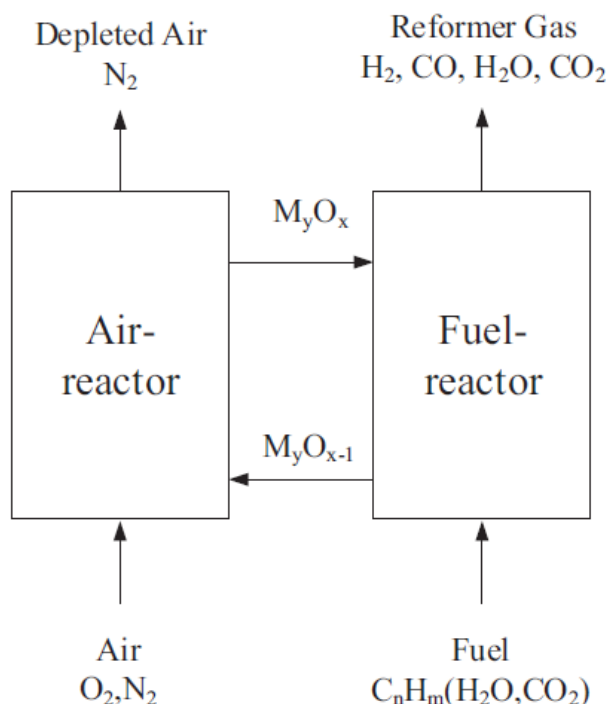
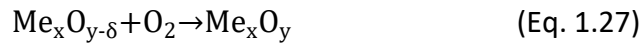
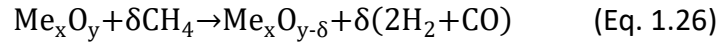


Figure 1.16 Schematic representation of the CLR(a) process (Luo et al., 2018).

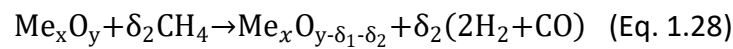
1.4.5 Chemical looping reforming of methane

CLMR is a very attractive technology because it enables the production of pure hydrogen and syngas separately and simultaneously. In the CLMR, methane is partially oxidized by the OCM

in the FR producing syngas, and the reduced OCM is then re-oxidized by water (steam) in the steam reactor (SR), simultaneously producing hydrogen. An AR can be added to the system for the complete re-oxidation of the unreacted OCM (Figure 1.17) (Luo et al., 2018). CLMR can be described by the following reactions. Methane and steam are not mixed at any point of the process, meaning that the gas purification problem that is faced in the conventional SMR process can be avoided. (Protasova and Snijkers, 2016)



Where Me, Me_xO_y and $\text{Me}_x\text{O}_{y-\delta}$ correspond to the OCM in its metal, oxidized, and partially reduced state, respectively. In a three reactor setup (Figure 1.17b) the material can be described as having two different reduction rates (δ_1 and δ_2), and the system's reactions:



What makes the CLMR process attractive is the fact that it enables the simultaneous production of syngas and hydrogen. Pure hydrogen can be obtained from the SR simply by condensing the water that is present in the stream, without any additional gas treatment (Luo et al., 2018). WGS can be employed downstream the FR in order to increase overall H_2 conversion.

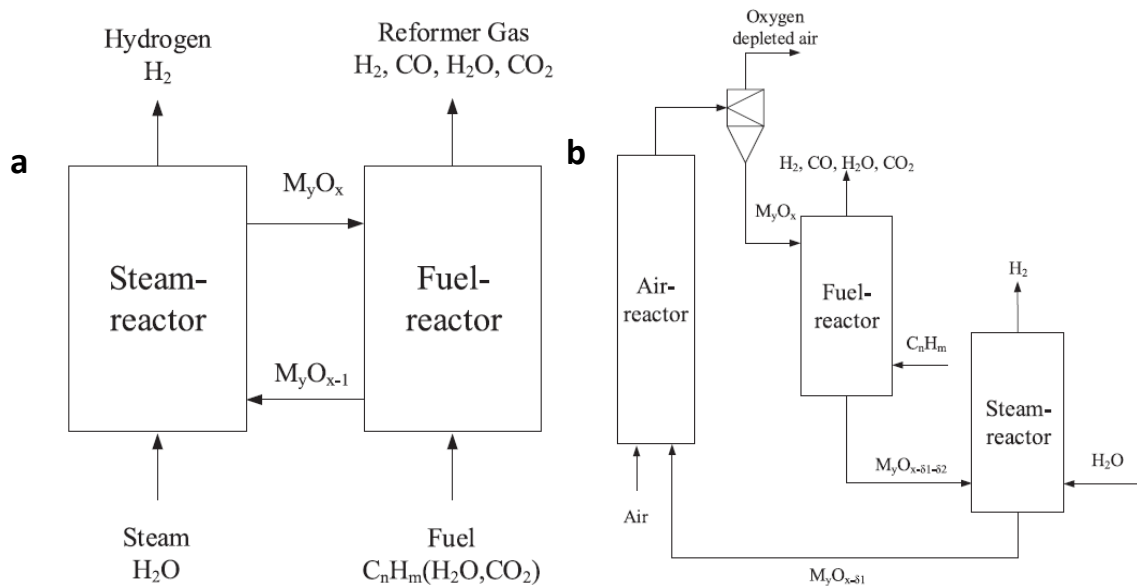
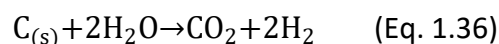
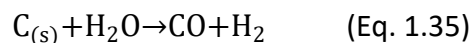
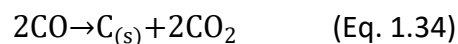
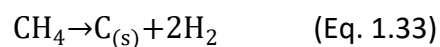
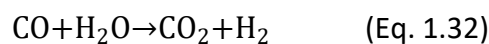


Figure 1.17: Schematic representation of the CLMR process for hydrogen and syngas production in a (a) two and a (b) three reactor system (Luo et al., 2018).

It should be noted that besides reactions 1.21 and 1.22 that describe the process, in reality the two steps are more complex with multiple reactions, besides steam methane reforming (Eq. 1.31), taking place. The water gas shift (Eq. 1.32), solid carbon formation from CH₄ cracking (Eq. 1.33), and the Boudouard reaction (Eq. 1.34), are the main side reactions occurring during the reduction stage. During the oxidation step the deposited solid carbon can also react with water towards the formation of CO (Eq. 1.30) and CO₂ (Eq. 1.36). The Boudouard reaction (Eq. 1.34) is kinetically limited below 600 °C and has low equilibrium conversions above 800 °C while carbon deposition from cracking (Eq. 1.33) is not limited thermodynamically (Murugan et al., 2011b).



Hence, although the process is less complex than the conventional SMR and has less limitations, still process conditions need to be optimized and OCMs that exhibit high resistance to coking are of great interest.

1.5 Chemical looping materials for H₂ production

1.5.1 Oxygen carrying materials requirements

As its name states, the oxygen carrier functions as a ‘vehicle’ responsible for the transportation of oxygen between the two reacting streams. Efficient operation of a chemical looping process is strongly dependent on the selection of the suitable OCM (Hafizi et al., 2016b; Voitic and Hacker, 2016). As a result, researchers have focused on optimizing the OCMs either by synthesizing new materials and experimenting with different compositions or by modifying the particle structure (Voitic and Hacker, 2016).

Key properties of an oxygen carrying material namely are high oxygen capacity, high reactivity towards the reactants (e.g. high methane activation for CLMR), high reactivity towards the reduction and oxidation reactions, high stability under long-term redox cycling and high resistance to carbon deposition. Other factors that should also be taken into consideration include mechanical and thermal properties, material and production cost and environmentally friendly characteristics (Adanez et al., 2012; Voitic and Hacker, 2016).

1.5.2 Metal oxides as oxygen carrying materials

Because of their demonstrated high catalytic activity in several processes (i.e., Ni catalyst use in SMR), transition metal oxides such as Fe, Ni, Cu, Co and Mn have been employed as OCMs exhibiting good activity, but when used alone, suffer from loss of stability under repeated oxidation/reduction due to metal particle agglomeration and sintering (Bohn et al., 2010; Dueso et al., 2015; Murugan et al., 2011a). The necessary phase changes that a transition

metal oxide has to go through during the process, cause the lattice parameter to change which creates stress in the material, leading to its eventual fragmentation. In addition, due to the low oxidation kinetics of steam, the reactivity of OCM towards water splitting is a critical issue. Aiming to overcome these limitations, research focused on improving the OCM, either by adding a support structure to the material or by additives (Dueso et al., 2015). Components such as ZrO_2 , TiO_2 , SiO_2 and Al_2O_3 have been employed as supports in order to improve the mechanical and chemical properties.

Iron-based oxygen carriers have been found to be among the best candidates for hydrogen production (Luo et al., 2018), mainly due to their low susceptibility to carbon and their strong resistance to agglomeration, both important attributes for an OCM (Tang et al., 2015). However, Fe-based OCMs suffer from weak redox characteristics and low oxygen transfer capacity, as well as the low reactivity towards methane (Tang et al., 2015). Many Fe-based materials have been developed, synthesized and tested during the past years. Different preparation methods and metal contents of metal oxide have been investigated. In most cases, in order to compensate for the low oxygen transport capability of the metal oxide, materials with high contents of Fe_2O_3 (higher than 60 wt%), were used (Adanez et al., 2012). Al_2O_3 , $MgAl_2O_4$, SiO_2 , ZrO_2 and TiO_2 have been investigated as supports with alumina being the most successful, exhibiting a positive effect on the oxygen transport capacity of the oxygen-carrier as described by (Alberto Abad et al., 2007). In general, supported Fe-based materials exhibited improved performance and good reactivity, especially in the CL-WGS, with the exception of the Fe_2O_3/SiO_2 system, whose reactivity was found to decrease under cycling due to the formation of unreactive iron silicates (Adanez et al., 2012). In addition, Fe-based OCs have been found to have the best performance for water splitting, among other transition metals. However, H_2 production with steam by Fe is thermodynamically limited, requiring the Fe phase to be as fully reduced as possible, while it is difficult for Fe to be completely oxidized beyond Fe_3O_4 by steam (Tang et al. 2015).

Mn-based materials have also attracted attention, aiming to overcome the limitations of iron compounds, as the oxygen transport capacity of Mn ions is higher than that of Fe ions (Adanez et al., 2012). Mn-based OCMs are attractive due to their high oxygen capacity, their toxic-free nature and low cost (Tang et al., 2015). Pure manganese oxide has shown low reactivity towards methane and when supported in inert materials, such as Al_2O_3 , $MgAl_2O_4$, SiO_2 and TiO_2 , is forming irreversible unreactive phases. Good reactivity was achieved for Mn-based OCMs supported in ZrO_2 towards syngas, but reactivity with methane was found to be low (Adanez et al., 2012). With ZrO_2 as support, the OCM exhibited good reactivity and stability over cycling. However, due to phase transformation between Mn species and ZrO_2 , cracks were formed within the OCM (Tang et al., 2015). Agglomeration of particles was also observed. Aiming to overcome these problems MgO , CaO , or CeO_2 were employed as stabilizing agents for ZrO_2 , but all failed to increase the reactivity of Mn (Tang et al., 2015).

Because of Ni's established high reactivity and selectivity, demonstrated by its commercial use in SMR, Ni-based oxygen-carriers are among the most extensively researched materials (Adanez et al., 2012; Luo et al., 2017; Tang et al., 2015). Ni based OCMs have shown high performance (Protasova and Snijkers, 2016), but pure NiO particles have exhibited low

reaction rates because of their low porosity (Adanez et al., 2012) and since they are oxidized at relatively higher oxygen partial pressures, are considered problematic in oxidation by steam. In addition, the high cost and toxic nature of Ni, as well as the rapid catalyst deactivation caused by carbon deposition and metal sintering problems, make the development of Ni-based OCMs a challenge (Tang et al., 2015). Different preparation methods and different supports have been employed aiming to improve the stability of Ni-based OCMs, both having great effect on performance. The effect of different support materials such as La_2O_3 , CeO_2 and Al_2O_3 has been investigated. Supports may affect the dispersion of NiO, giving it resistance against sintering, can limit carbon deposition and affect the oxygen mobility enhancing the reducibility of the OCM. In addition, Ni-support interactions may increase the material's overall catalytic activity. Al_2O_3 supported NiO has exhibited high reactivity towards different gaseous fuels, little to no agglomeration problems, low attrition rates and low susceptibility to carbon deposition when employed in CLC (Tang et al., 2015). However, partial transformation of NiO into NiAl_2O_4 , which has poor reactivity, inhibits the reduction of NiO/ Al_2O_3 , requiring materials to be synthesized with high NiO loadings (60 wt. % - 80 wt. %) in order to increase reactivity.

Fe-, Ni-, Cu-, Ce-, Co- and Mn-based oxygen carriers synthesised by different methods and supported on different materials, have been tested extensively in several chemical looping systems. All are feasible candidate OCMs, however limitations such as: low reactivity of Fe, Mn and Co; low melting points and high agglomeration for Cu; and toxicity concern for Ni make their development a challenge. The reader is referred to the extensive reviews published on the development of OCMs for more information (Adanez et al., 2012; Luo et al., 2018; Protasova and Snijkers, 2016; Tang et al., 2015).

The interest now lies in creating materials that will exhibit better properties than the traditional metal oxide systems. As a result, complex metal oxides, such as perovskite oxides, have been the focus of research, aiming to minimize carbon deposition, increase reactivity and/or stability of the particles, improve conversions, improve mechanical strength and decrease attrition, decrease preparation costs, minimize the use of toxic metals (Adanez et al., 2012).

1.5.3 Perovskite oxides as oxygen carrying materials

Perovskite oxides are complex oxides with the general chemical formula ABO_3 , where generally A is an alkali and/or alkaline earth/rare earth metal and B is a transition element from the transition series or from the main groups III, IV or V of the periodic table (Sarshar et al., 2011). The ideal cubic perovskite structure has the B cation in 6-fold coordination, surrounded by an octahedron of anions, and the A cation in 12-fold cuboctahedral coordination. However, defects are commonly observed in the structure due to oxygen deficiency. Consequently, the general chemical formula is modified taking into account these defects, to $\text{ABO}_{3-\delta}$, where δ expresses the oxygen deficiency (Protasova and Snijkers, 2016). The stability of the cubic structure depends greatly on the ion size; hence the size requirements are quite strict. So, with slight buckling and distortion, several distorted versions of the perovskite can be produced (Tiwari et al., 2016). That way the perovskite structure can allow the incorporation of various metal cations at different valence states

within the perovskite matrix as long as these fit the size constraints of the A and B sites. The A cation of the perovskite lattice is responsible for the thermal resistance, while the transition metals located at the B-site are responsible for the catalytic activity. In addition, both A and B cations can play an important role in the stability of the perovskite structure as well as the reactivity and selectivity of lattice oxygen during the oxidation of CH₄ (Tang et al., 2015). Taking advantage of this, the material can be tailored in order to achieve required properties (Murugan et al., 2011a).

Due to their high stability under cycling, good mechanical properties, high oxygen mobility and tailorability, perovskites have been suggested as promising candidate OCMs (Murugan et al., 2011b; Protasova and Snijkers, 2016). During reduction and oxidation, only small structural changes occur in most cases, depending on partial pressure of oxygen (pO_2) and temperature (T), thus fast redox kinetics and high reversibility are possible (Vieta et al., 2016). That way, the perovskite matrix can allow fast oxygen transport to the active metal oxide clusters while preventing agglomeration (Dueso et al., 2015). The perovskite itself does not require a high oxygen capacity since this capacity is provided by the metal oxide, rather it's expected to act as an oxygen transfer pathway to access metal oxide and provide mechanical strength. The composite material is expected to combine the benefits of both materials individually, i.e. the high oxygen capacity of the metal oxide and the stability and oxygen transport properties of the perovskite (Dueso et al., 2015). More information on the employment of perovskites as OCMs in chemical looping can be found in the works of ((Nalbandian & Zaspalis, 2015, Luo et al., 2018; Protasova and Snijkers, 2016).

Among many perovskite systems, LaFeO₃ has exhibited excellent characteristics such as: high oxygen mobility and capability of hosting large concentrations of vacancies in the structure at elevated reaction temperatures, making it a promising OCM (Tang et al., 2015). Of particular interest is the La_{0.7}Sr_{0.3}FeO_{3-δ} (LSF731) system as it has exhibited good stability under cycling and resistance to carbon deposition (Murugan et al., 2011a). Also, through the work of Dueso et al. (Dueso et al., 2015) who embedded iron oxide within the matrix of the same system higher hydrogen production was observed than that expected from a simple combination of the iron oxide and LSF731 alone, indicating a synergetic effect between the iron oxide clusters and the supporting LSF731. Other works on similar perovskite systems, like that of Galinsky et al. (Galinsky et al., 2013) who prepared an OCM containing 60 wt% iron oxide supported on La_{0.8}Sr_{0.2}FeO₃ showed that the reactivity of the oxygen carrier was enhanced by 5–70 times compared to that of the conventional TiO₂-, Al₂O₃- or YSZ supported materials. Further optimization of the system's performance can be achieved by partial substitution of the B site by aliovalent transition metal cations, which can lead to an increase in catalytic activity due to synergistic valence changes and non-stoichiometry related defects in the lattice.

Based on the promising performance of perovskite oxide systems as OCMs combined with the novel approach of redox exsolution, here exsolved systems are designed, tested and employed in order to tackle methane activation.

1.6 Aim and objectives of the thesis

In light of the potential of exsolved materials and the Chemical Looping concept as well as the challenges currently faced, as presented above, the aim of this thesis is to explore the

development and application of exsolved perovskite systems as catalysts and oxygen carriers for the conversion of methane.

The study revolves around material design, synthesis, and testing, as well as developing an understanding of the material properties in relation to structure and composition. In view of the above the objectives of the project are outlined below:

To design an exsolved perovskite system suitable for methane activation and employ exsolved materials for carrying out this transformation for the first time.

Explore and attempt to advance the exsolution concept in order to develop an exsolved perovskite system with enhanced functionalities that will allow it to successfully perform as a catalyst and oxygen carrier for the activation of methane.

Employ a combination of techniques for the study of the developed systems aiming to uncover arising material properties and gain insight on their reactivity.

Prove the material's applicability and robustness by employing it for methane conversion while monitoring its performance under reaction conditions and comparing it to state-of-the-art materials.

Proceed with the investigation of the characteristics of the developed system and attempt to deconvolute the effect different components of the system have on its performance. Aim to provide insight on how the tuneable nature of exsolved materials can be utilised for their rational design.

Use the insight gained and methods introduced for developing and tailoring an even more active exsolved system as proof of concept. Showcase this way the potential for the improvement and wider application of both the exsolved systems and the chemical looping process.

1.7 Thesis outline

Chapter 1 Introduction. The field of study where this thesis fits in is introduced. The problems that need to be tackled in the field are discussed and a short review of previous research relevant to the thesis is presented.

Chapter 2 Experimental. Summarises the main techniques and methods employed for the preparation, analysis and testing of the developed materials. The experimental apparatuses used throughout this study and the fundamentals of data analysis are also introduced.

Chapter 3 Development and investigation of a system with exo-/ endo- nanoparticles for the conversion of methane to syngas. Describes the method developed for the creation of exsolved perovskites systems with exo-/endo- nanoparticles. The developed systems are studied via various *ex-* and *in-situ* techniques uncovering their emergent properties and where they are stemming from. The system's enhanced performance is showcased by employing it as a catalyst and OCM for the conversion of methane and comparing its performance with a state-of-the-art system.

Chapter 4 Deconvolution of the effect of micro- and nano-structure on the performance of exsolved perovskite systems with exo-/endo- particles. Focuses on the deconvolution of the effect that different components of the system have on activity. Systems with different surface and bulk characteristics are strategically prepared and tested aiming to unmask the effect of changes on the systems characteristics, exsolution, activity against methane and product selectivity.

Chapter 5 Development and testing of an exsolved system with exo- endo- particles for low temperature methane reforming. The insight gained from the previous chapters is utilised for the development of an exo-/ endo- system with enhanced performance. The system's composition is optimised for the activation of methane as is its microstructural characteristics. This leads to the proof of concept that the methodology developed in this study can be applied for a wide range of applications leading to the development of high performing materials suitable for their employment in Chemical Looping and other technologies.

Chapter 6 Future work. Ideas and preliminary results of future projects stemming from this study are discussed.

Chapter 7 Conclusions. The main findings of this thesis are summarised.

References

- Bierschenk, D. M., Potter-Nelson, E., Hoel, C., Liao, Y., Marks, L., Poepelmeier, K. R., & Barnett, S. A. (2011). Pd-substituted (La,Sr)CrO_{3-δ}-Ce_{0.9}Gd_{0.1}O_{2-δ} solid oxide fuel cell anodes exhibiting regenerative behavior. *Journal of Power Sources*, *196*(6), 3089–3094. <https://doi.org/https://doi.org/10.1016/j.jpowsour.2010.12.050>
- Chambers, S. A., Gu, M., Sushko, P. V, Yang, H., Wang, C., & Browning, N. D. (2013). Ultralow Contact Resistance at an Epitaxial Metal/Oxide Heterojunction Through Interstitial Site Doping. *Advanced Materials*, *25*(29), 4001–4005. <https://doi.org/https://doi.org/10.1002/adma.201301030>
- Chen, D., Chen, C., Baiyee, Z. M., Shao, Z., & Ciucci, F. (2015). Nonstoichiometric Oxides as Low-Cost and Highly-Efficient Oxygen Reduction/Evolution Catalysts for Low-Temperature Electrochemical Devices. *Chemical Reviews*, *115*(18), 9869–9921. <https://doi.org/10.1021/acs.chemrev.5b00073>
- Dueso, C., Thompson, C., & Metcalfe, I. (2015). High-stability, high-capacity oxygen carriers: Iron oxide-perovskite composite materials for hydrogen production by chemical looping. *Applied Energy*, *157*, 382–390. <https://doi.org/10.1016/j.apenergy.2015.05.062>
- Goldschmidt, V. M. (1926). Die Gesetze der Krystallochemie. *Naturwissenschaften*, *14*(21), 477–485. <https://doi.org/10.1177/089686089501500104>
- Goodenough, J. B. (2004). Electronic and ionic transport properties and other physical aspects of perovskites. *Reports on Progress in Physics*, *67*(11), 1915–1993. <https://doi.org/10.1088/0034-4885/67/11/R01>
- Goswami, D. Y., Goel, S. T. M. N., & Ingley, H. A. (Skip). (2003). A review of hydrogen production technologies. *Fuel Cell Science, Engineering and Technology*, 61–74.

- Guo, S., Wu, H., Puleo, F., & Liotta, L. F. (2015). B-site metal (Pd, Pt, Ag, Cu, Zn, Ni) promoted $\text{La}_{1-x}\text{Sr}_x\text{Co}_{1-y}\text{Fe}_y\text{O}_{3-\delta}$ perovskite oxides as cathodes for IT-SOFCs. *Catalysts*, *5*(1), 366–391. <https://doi.org/10.3390/catal5010366>
- Hafizi, A., Rahimpour, M. R., & Hassanajili, S. (2016). Hydrogen production by chemical looping steam reforming of methane over Mg promoted iron oxygen carrier: Optimization using design of experiments. *Journal of the Taiwan Institute of Chemical Engineers*, *62*, 140–149. <https://doi.org/10.1016/j.jtice.2016.01.023>
- Han, H., Park, J., Nam, S. Y., Kim, K. J., Choi, G. M., Parkin, S. S. P., Jang, H. M., & Irvine, J. T. S. (2019). Lattice strain-enhanced exsolution of nanoparticles in thin films. *Nature Communications*, *10*(1), 1–8. <https://doi.org/10.1038/s41467-019-09395-4>
- Hwang, J., Rao, R. R., Giordano, L., Katayama, Y., Yu, Y., & Shao-Horn, Y. (2017). Perovskites in catalysis and electrocatalysis. *Science*, *358*(6364), 751–756. <https://doi.org/10.1126/science.aam7092>
- Irvine, J., Rupp, J. L. M., Liu, G., Xu, X., Haile, S., Qian, X., Snyder, A., Freer, R., Ekren, D., Skinner, S., Celikbilek, O., Chen, S., Tao, S., Shin, T. H., O'Hayre, R., Huang, J., Duan, C., Papac, M., Li, S., ... Martín, S. G. (2021). Roadmap on inorganic perovskites for energy applications. *JPhys Energy*, *3*(3). <https://doi.org/10.1088/2515-7655/abff18>
- Jalili, H., Han, J. W., Kuru, Y., Cai, Z., & Yildiz, B. (2011). New insights into the strain coupling to surface chemistry, electronic structure, and reactivity of $\text{La}_{0.7}\text{Sr}_{0.3}\text{MnO}_3$. *Journal of Physical Chemistry Letters*, *2*(7), 801–807. <https://doi.org/10.1021/jz200160b>
- Jena, A. K., Kulkarni, A., & Miyasaka, T. (2019). Halide Perovskite Photovoltaics: Background, Status, and Future Prospects. *Chemical Reviews*, *119*(5), 3036–3103. <https://doi.org/10.1021/acs.chemrev.8b00539>
- Jiang, B., Cheng, H., Luo, L., Lu, X., Zhang, N., & Liu, J. (2014). Oxygen permeation and phase structure properties of partially A-site substituted $\text{BaCo}_{0.7}\text{Fe}_{0.225}\text{Ta}_{0.075}\text{O}_{3-\delta}$ perovskites. *Journal of Energy Chemistry*, *23*(2), 164–170. [https://doi.org/10.1016/S2095-4956\(14\)60131-5](https://doi.org/10.1016/S2095-4956(14)60131-5)
- Kanhere, P., & Chen, Z. (2014). A review on visible light active perovskite-based photocatalysts. *Molecules*, *19*(12), 19995–20022. <https://doi.org/10.3390/molecules191219995>
- Katz, M. B., Graham, G. W., Duan, Y., Liu, H., Adamo, C., Schlom, D. G., & Pan, X. (2011). Self-regeneration of Pd-LaFeO₃ catalysts: New insight from atomic-resolution electron microscopy. *Journal of the American Chemical Society*, *133*(45), 18090–18093. <https://doi.org/10.1021/ja2082284>
- Katz, M. B., Zhang, S., Duan, Y., Wang, H., Fang, M., Zhang, K., Li, B., Graham, G. W., & Pan, X. (2012). Reversible precipitation/dissolution of precious-metal clusters in perovskite-based catalyst materials: Bulk versus surface re-dispersion. *Journal of Catalysis*, *293*, 145–148. <https://doi.org/10.1016/j.jcat.2012.06.017>
- Keav, S., Matam, S. K., Ferri, D., & Weidenkaff, A. (2014). Structured perovskite-based catalysts and their application as Three-Way Catalytic converters-a review. *Catalysts*, *4*(3), 226–255. <https://doi.org/10.3390/catal4030226>

- Kim, J. Y., Lee, J. W., Jung, H. S., Shin, H., & Park, N. G. (2020). High-Efficiency Perovskite Solar Cells. *Chemical Reviews*, *120*(15), 7867–7918. <https://doi.org/10.1021/acs.chemrev.0c00107>
- Kothari, R., Buddhi, D., & Sawhney, R. L. (2008). Comparison of environmental and economic aspects of various hydrogen production methods. *Renewable and Sustainable Energy Reviews*, *12*(2), 553–563. <https://doi.org/10.1016/j.rser.2006.07.012>
- Kousi, K., Neagu, D., Bekris, L., Papaioannou, E. I., & Metcalfe, I. S. (2020). Endogenous Nanoparticles Strain Perovskite Host Lattice Providing Oxygen Capacity and Driving Oxygen Exchange and CH₄ Conversion to Syngas. *Angewandte Chemie - International Edition*, *59*(6), 2510–2519. <https://doi.org/10.1002/anie.201915140>
- Kousi, K., Tang, C., Metcalfe, I. S., & Neagu, D. (2021). Emergence and Future of Exsolved Materials. *Small*, *17*(21). <https://doi.org/10.1002/smll.202006479>
- Lee, W., Han, J. W., Chen, Y., Cai, Z., & Yildiz, B. (2013). Cation size mismatch and charge interactions drive dopant segregation at the surfaces of manganite perovskites. *Journal of the American Chemical Society*, *135*(21), 7909–7925. <https://doi.org/10.1021/ja3125349>
- Lin, Y. C., & Hohn, K. L. (2014). Perovskite Catalysts-A Special issue on versatile oxide catalysts. *Catalysts*, *4*(3), 305–306. <https://doi.org/10.3390/catal4030305>
- Luo, M., Yi, Y., Wang, S., Wang, Z., Du, M., Pan, J., & Wang, Q. (2018). Review of hydrogen production using chemical-looping technology. *Renewable and Sustainable Energy Reviews*, *81*(June 2017), 3186–3214. <https://doi.org/10.1016/j.rser.2017.07.007>
- Madsen, B. D., Kobsiriphat, W., Wang, Y., Marks, L. D., & Barnett, S. (2007). SOFC Anode Performance Enhancement through Precipitation of Nanoscale Catalysts. *ECS Transactions*, *7*(1), 1339. <https://doi.org/10.1149/1.2729237>
- Milne, T. A., Elam, C. C., & Evans, R. J. (2002). Hydrogen from biomass: state of the art and research challenges. *Other Information: PBD: 1 Feb 2002*, Medium: ED; Size: 82 pages. <https://doi.org/10.2172/792221>
- Moghtaderi, B. (2012). Review of the recent chemical looping process developments for novel energy and fuel applications. *Energy and Fuels*, *26*(1), 15–40. <https://doi.org/10.1021/ef201303d>
- Moradi, G. R., Khosravian, F., & Rahmzadeh, M. (2012). Effects of partial substitution of Ni by Cu in LaNiO₃ perovskite catalyst for dry methane reforming. *Chinese Journal of Catalysis*, *33*(4–6), 797–801. [https://doi.org/10.1016/S1872-2067\(11\)60378-1](https://doi.org/10.1016/S1872-2067(11)60378-1)
- Murugan, A., Thursfield, A., & Metcalfe, I. S. (2011a). A chemical looping process for hydrogen production using iron-containing perovskites. *Energy & Environmental Science*, *4*(11), 4639. <https://doi.org/10.1039/c1ee02142g>
- Murugan, A., Thursfield, A., & Metcalfe, I. S. (2011b). A chemical looping process for hydrogen production using iron-containing perovskites. *Energy & Environmental Science*, *4*(11), 4639. <https://doi.org/10.1039/c1ee02142g>

- Myung, J. H., Neagu, D., Miller, D. N., & Irvine, J. T. S. (2016). Switching on electrocatalytic activity in solid oxide cells. *Nature*, *537*(7621), 528–531. <https://doi.org/10.1038/nature19090>
- Nalbandian, L., & Zaspalis, V. (2015). Perovskites as Oxygen Carrier-Transport Materials for Hydrogen and Carbon Monoxide Production by Chemical Looping Processes. In *Perovskites and Related Mixed Oxides: Concepts and Applications* (pp. 839–862). <https://doi.org/10.1002/9783527686605.ch37>
- Neagu, D., & Irvine, J. T. S. (2013). Perovskite Defect Chemistry as Exemplified by Strontium Titanate. In *Comprehensive Inorganic Chemistry II (Second Edition): From Elements to Applications* (Vol. 4). Elsevier Ltd. <https://doi.org/10.1016/B978-0-08-097774-4.00421-6>
- Neagu, D., Oh, T. S., Miller, D. N., Ménard, H., Bukhari, S. M., Gamble, S. R., Gorte, R. J., Vohs, J. M., & Irvine, J. T. S. (2015). Nano-socketed nickel particles with enhanced coking resistance grown in situ by redox exsolution. *Nature Communications*, *6*. <https://doi.org/10.1038/ncomms9120>
- Neagu, D., Papaioannou, E. I., Ramli, W. K. W., Miller, D. N., Murdoch, B. J., Ménard, H., Umar, A., Barlow, A. J., Cumpson, P. J., Irvine, J. T. S., & Metcalfe, I. S. (2017). Demonstration of chemistry at a point through restructuring and catalytic activation at anchored nanoparticles. *Nature Communications*, *8*(1), 1855. <https://doi.org/10.1038/s41467-017-01880-y>
- Neagu, D., Tsekouras, G., Miller, D. N., Ménard, H., & Irvine, J. T. S. (2013a). In situ growth of nanoparticles through control of non-stoichiometry. *Nature Chemistry*, *5*(11), 916–923. <https://doi.org/10.1038/nchem.1773>
- Neagu, D., Tsekouras, G., Miller, D. N., Ménard, H., & Irvine, J. T. S. (2013b). In situ growth of nanoparticles through control of non-stoichiometry. *Nature Chemistry*, *5*(11), 916–923. <https://doi.org/10.1038/nchem.1773>
- Nishihata Y, Mizuki J, Akao T, Tanaka H, Uenishi M, Kimura M, Okamoto T, & Hamada N. (2002). Self-regeneration of a Pd-perovskite catalyst for automotive emissions control. *Nature*, *418*(6894), 164–167. <https://doi.org/10.1038/nature00875.1>
- Papaioannou, E. I., Neagu, D., Ramli, W. K. W., Irvine, J. T. S., & Metcalfe, I. S. (2019). Sulfur-Tolerant, Exsolved Fe–Ni Alloy Nanoparticles for CO Oxidation. *Topics in Catalysis*, *62*(17–20), 1149–1156. <https://doi.org/10.1007/s11244-018-1053-8>
- Pecchi, G., Jiliberto, M. G., Delgado, E. J., Cadús, L. E., & Fierro, J. L. G. (2011). Effect of B-site cation on the catalytic activity of La_{1-x}CaxBO₃ (B=Fe, Ni) perovskite-type oxides for toluene combustion. *Journal of Chemical Technology & Biotechnology*, *86*(8), 1001–1124. <https://doi.org/DOI 10.1002/jctb.2611>
- Peña, M. A., & Fierro, J. L. G. (2001). Chemical structures and performance of perovskite oxides. *Chemical Reviews*, *101*(7), 1981–2017. <https://doi.org/10.1021/cr980129f>
- Protasova, L., & Snijkers, F. (2016). Recent developments in oxygen carrier materials for hydrogen production via chemical looping processes. *Fuel*, *181*, 75–93. <https://doi.org/10.1016/j.fuel.2016.04.110>

- Rioseco, F., Radovic, L., García, X., Gordon, A., & Pecchi, G. (2010). Effect of Ag addition on the thermal stability and catalytic properties of LaFeO₃ perovskite. *Journal of the Chilean Chemical Society*, 55(1), 44–49. <https://doi.org/10.4067/S0717-97072010000100011>
- Sarshar, Z., Kleitz, F., & Kaliaguine, S. (2011). Novel oxygen carriers for chemical looping combustion: La_{1-x}Ce_xBO₃ (B = Co, Mn) perovskites synthesized by reactive grinding and nanocasting. *Energy & Environmental Science*, 4(10), 4258. <https://doi.org/10.1039/c1ee01716k>
- Shellaiah, M., & Sun, K. W. (2020). Review on Sensing Applications of Perovskite Nanomaterials. *Chemosensors*, 8(3), 55. <https://doi.org/10.3390/chemosensors8030055>
- Sun, C., Alonso, J. A., & Bian, J. (2021). Recent Advances in Perovskite-Type Oxides for Energy Conversion and Storage Applications. In *Advanced Energy Materials* (Vol. 11, Issue 2). <https://doi.org/10.1002/aenm.202000459>
- Sunarso, J., Hashim, S. S., Zhu, N., & Zhou, W. (2017). Perovskite oxides applications in high temperature oxygen separation, solid oxide fuel cell and membrane reactor: A review. *Progress in Energy and Combustion Science*, 61, 57–77. <https://doi.org/10.1016/j.pecs.2017.03.003>
- Suresh Kumar, N., & Chandra Babu Naidu, K. (2021). A review on perovskite solar cells (PSCs), materials and applications. *Journal of Materiomics*, 7(5), 940–956. <https://doi.org/10.1016/j.jmat.2021.04.002>
- Tanaka, H., & Misono, M. (2001). Advances in designing perovskite catalysts. *Current Opinion in Solid State and Materials Science*, 5(5), 381–387. [https://doi.org/10.1016/S1359-0286\(01\)00035-3](https://doi.org/10.1016/S1359-0286(01)00035-3)
- Tanaka, H., Taniguchi, M., Kajita, N., Uenishi, M., Tan, I., Sato, N., Narita, K., & Kimura, M. (2004). Design of the intelligent catalyst for Japan ULEV standard. *Topics in Catalysis*, 30–31(July), 389–396. <https://doi.org/10.1023/b:toca.0000029780.70319.36>
- Tanaka, H., Taniguchi, M., Uenishi, M., Kajita, N., Tan, I., Nishihata, Y., Mizuki, J., Narita, K., Kimura, M., & Kaneko, K. (2006). Self-regenerating Rh- and Pt-based perovskite catalysts for automotive-emissions control. *Angewandte Chemie - International Edition*, 45(36), 5998–6002. <https://doi.org/10.1002/anie.200503938>
- Tanaka, H., Uenishi, M., Taniguchi, M., Tan, I., Narita, K., Kimura, M., Kaneko, K., Nishihata, Y., & Mizuki, J. (2006). The intelligent catalyst having the self-regenerative function of Pd, Rh and Pt for automotive emissions control. *Catalysis Today*, 117(1–3), 321–328. <https://doi.org/10.1016/j.cattod.2006.05.029>
- Tang, M., Xu, L., & Fan, M. (2015). Progress in oxygen carrier development of methane-based chemical-looping reforming: A review. *Applied Energy*, 151, 143–156. <https://doi.org/10.1016/j.apenergy.2015.04.017>
- Tiwari, A., Gerhardt, R. A., & Szutkowska, M. (2016). *Advanced Ceramic Materials*. Wiley.
- Travis, W., Glover, E. N. K., Bronstein, H., Scanlon, D. O., & Palgrave, R. G. (2016). On the

application of the tolerance factor to inorganic and hybrid halide perovskites: A revised system. *Chemical Science*, 7(7), 4548–4556. <https://doi.org/10.1039/c5sc04845a>

Trolliard, G., Ténèze, N., Boullay, P., & Mercurio, D. (2004). TEM study of cation-deficient-perovskite related $\text{AnB}_{n-1}\text{O}_{3n}$ compounds: The twin-shift option. *Journal of Solid State Chemistry*, 177(4–5), 1188–1196. <https://doi.org/10.1016/j.jssc.2003.10.024>

Voitic, G., & Hacker, V. (2016). Recent advancements in chemical looping water splitting for the production of hydrogen. *RSC Adv.*, 6(100), 98267–98296. <https://doi.org/10.1039/C6RA21180A>

Wang, W., Tadé, M. O., & Shao, Z. (2015). Research progress of perovskite materials in photocatalysis- and photovoltaics-related energy conversion and environmental treatment. *Chemical Society Reviews*, 44(15), 5371–5408. <https://doi.org/10.1039/c5cs00113g>

Wang, Z., Tan, S., Xiong, Y., & Wei, J. (2018). Effect of B sites on the catalytic activities for perovskite oxides $\text{La}_{0.6}\text{Sr}_{0.4}\text{Co}_x\text{Fe}_{1-x}\text{O}_{3-\delta}$ as metal-air batteries catalysts. *Progress in Natural Science: Materials International*, 28(4), 399–407. <https://doi.org/10.1016/j.pnsc.2018.03.002>

Zhu, J., Li, H., Zhong, L., Xiao, P., Xu, X., Yang, X., Zhao, Z., & Li, J. (2014). Perovskite oxides: Preparation, characterizations, and applications in heterogeneous catalysis. *ACS Catalysis*, 4(9), 2917–2940. <https://doi.org/10.1021/cs500606g>

Zhu, X., Li, K., Neal, L., & Li, F. (2018). Perovskites as Geo-inspired Oxygen Storage Materials for Chemical Looping and Three-Way Catalysis: A Perspective. *ACS Catalysis*, 8(9), 8213–8236. <https://doi.org/10.1021/acscatal.8b01973>

2 Experimental

In this chapter the methodologies, techniques and experimental systems used in this study will be introduced. These include sample preparation and post synthesis treatment, characterisation techniques and the experimental setups and procedures employed and designed for material processing and testing.

2.1 Introduction

This study revolves around the design, modification, characterization and testing of exsolved perovskite systems as catalysts/ oxygen carrier materials aiming to gain insight on the factors which lead to their activity and improve their performance. As nanostructured materials become more and more complicated and the diversity of their application grows, the selection of synthesis routes and techniques for their efficient study and characterisation has become a complex challenge (Mourdikoudis et al., 2018). Based on the studied material, the strengths and limitations of each method chosen must be assessed and more importantly how the techniques used can be combined in order to extract the information needed. Given the complexity of the systems studied here, the development of a strategic methodology for their systematic and efficient study is of utmost importance in order to be able to fabricate the designed systems and assess the relationship between their structure and properties.

The first challenge to be surpassed is the fabrication of the designed systems. There is an array of methods developed for the preparation of such metal oxide systems, ranging from fairly straight forward solid-state routes that involve mixing of powder reactants and heating to produce the desired product, to solution-based techniques which are based in mixing reagents in a solution and promise lower synthesis temperatures and times (Danks et al., 2016). Both approaches have been successfully employed for the production of metal oxide systems of varying complexity (Kousi et al., 2021), however the ultimate factor for the selection of a synthesis route is its ability to consistently and efficiently produce the desired material. Here, methods from both the solid state and the solution state chemistry are employed to produce the perovskite systems studied. For the fabrication of A-site deficient exsolvable perovskite systems, precise control of the stoichiometry is required. In view of this, a solid-state route was selected for their synthesis but modified in order to ensure homogeneity of the precursor mixture via several mixing steps (Neagu, 2012). The modified route coupled with the use of high purity precursors lead to the development of dependable method via which the A-site deficient systems could be produced. For the synthesis of simpler stoichiometric perovskite systems with less components, the sol-gel method was employed due to its small number of steps and low temperatures for the production of the desired product.

Post synthesis, the first important step is to determine if the produced sample has the chemical and structural properties that was designed to have and if these properties are consistent throughout the material. To answer all the above questions, X-ray diffraction (XRD), which is one of the most widely used laboratory characterisation techniques was employed. The wide theoretical background of the technique allows for the identification of unknown crystalline phases, qualitative and quantitative analysis of the samples. Coupled with the analytical tools developed such as the structure refinement method, XRD is one of the most powerful techniques for the study of crystalline samples. In addition, XRD can be employed for the study of the materials *in situ*, where the structural interactions between its constituents can be investigated under reaction conditions. In view of the above capabilities of the method and considering the aims of this study XRD was an indispensable tool, implemented throughout the experimental process.

The next important thing to consider is the samples high degree of tailorability which allow the modification of their micro- and nano- structure. This introduces changes in their structure, chemistry and morphology varying over different length scales. These changes play a key role on the material's performance. In view of this, the technique selected should be effective in probing these changes on and below the materials surface. For this, SEM was employed. Via SEM and abundance of information can be obtained regarding the topography of the surface of produced samples, allowing observation of the changes in both the materials nano- and micro-structure. Manipulation of samples, such as cleaving them in order to expose the bulk also allowed to expose and study the bulk of materials. The availability of EDX also made this technique attractive for the quick examination of the surface composition. SEM image analysis was an extremely important part of this study which was used for verifying that the design principles followed were successful and for correlating sample characteristics with activity.

Shifting the focus to under the surface the technique of choice was TEM. Through this, single nanoparticles where able to be observed located on, near and under the surface of the system. This powerful technique provided valuable information about the nanoparticle and host matrices and their crystallographic alignment which were key for extracting information about their relationship.

Targeted characterisation in order to study specific properties of the system was also essential. For the study of the oxygen capacity of the systems, TGA was employed allowing the measurement of the system's oxygen uptake with a high accuracy, something that would not be possible buy simply monitoring the gas consumption by the sample. For more in detail analysis of the composition of bimetallic nanoparticles XPS was employed which proved essential for uncovering the alloying nature of the exsolved nanoparticles.

Finally, efficient gas analysis was paramount for studying the changes in performance of the samples when employed for the conversion of methane to syngas. For this, mass spectrometry was utilised due to the fast data acquisition speed, accuracy and availability since the reactants and products studied are all detectable by the technique.

The findings of all the techniques and methods described above where combined throughout this study leading to the successful fabrication and investigation of the developed systems which ultimately lead to gaining valuable insight on this new class of composite materials. Details on the working principles of techniques utilised, apparatus used, and information about data analysis carried out in this study follow.

2.2 Material preparation and processing

2.2.1 *Modified Solid state synthesis*

The method of choice for the synthesis of the exsolved perovskite systems developed in this study is a modified solid-state route. The method is described here for the synthesis of the $\text{La}_{0.8}\text{Ce}_{0.1}\text{Ni}_{0.4}\text{Ti}_{0.6}\text{O}_3$ as the model composition and the steps involved are briefly illustrated in Figure 2.1.

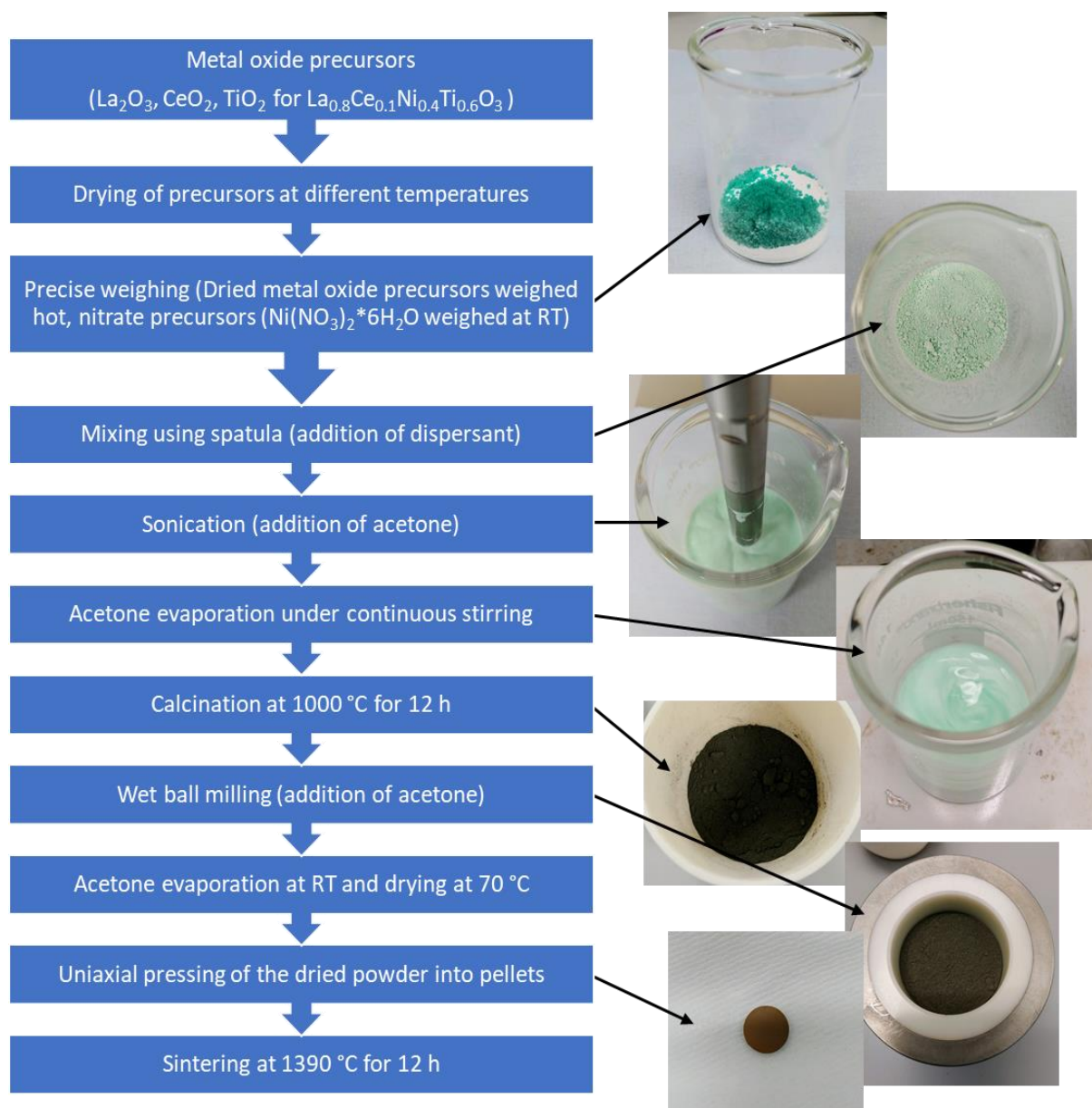


Figure 2.1 Flow chart and pictures of the modified solid state synthesis route.

High purity precursors, in this case oxides (La_2O_3 , CeO_2 , TiO_2) and nitrates ($\text{Ni}(\text{NO}_3)_2 \cdot 6\text{H}_2\text{O}$), were used in the appropriate stoichiometric ratios. In order to remove moisture/hydroxides, metal oxides were dried at different temperatures depending on the nature of the precursor (CeO_2 and TiO_2 at $400\text{ }^\circ\text{C}$ and La_2O_3 at $800\text{ }^\circ\text{C}$) for 3 hours and then cooled down to approximately $300\text{ }^\circ\text{C}$. Weighing of the dried precursors was done immediately after their removal from the furnace, while hot, into a heat resistant beaker. Once all dried precursors have been weighed in the appropriate stoichiometric ratio and the mixture has reached ambient temperature, the rest of the precursors, in this example $\text{Ni}(\text{NO}_3)_2 \cdot 6\text{H}_2\text{O}$, are also weighed in the same beaker. The powders were mixed thoroughly with a spatula before acetone and a small amount ($\sim 0.05\text{ wt. }%$) of a non- aqueous polyester/polyamide copolymer dispersant (Hypermer KD1 by CRODA Advanced Materials) were added. Using an ultrasonic probe (Hielscher UP200S), the mixture was then sonicated in order to break down

agglomerates and homogenise the mixture until a stable dispersion has formed. Sonication of the mixture with the addition of the dispersant produces a fine, stable dispersion with better homogeneity than that produced from typical powder mixing by mortar and pestle used in the traditional solid-state synthesis. Post sonication, the beaker was left at room temperature under constant stirring to ensure homogenization, for the acetone to be evaporated. The dry mixture was then transferred from the beaker to a ceramic (alumina) crucible and calcined at 1000 °C for 12 h in order to decompose carbonates, remove adsorbed water and kickstart the perovskite phase nucleation. Post calcination, the powder was left to cool down to RT inside the box furnace at a rate of 5 °C min⁻¹. The cooled calcined powder was then transferred into a planetary ball mill cup, mixed with a small amount of acetone and zirconia balls as the milling media, and wet milled for 2 h at 200 rpm in order to break down agglomerates formed during the calcination. Post milling the acetone was left to evaporate at room temperature and the resulting powder was transferred to a drying oven (70 °C) to dry completely. The milled powder was then stored in airtight vials ready for further processing. The powder was then pressed into pellets in order to ensure homogeneity of the resulting perovskite structure, which were fired at 1350 -1400 °C for 12 h and left to cool to RT inside the furnace with a cooling rate of 5 °C min⁻¹. The sintered pellets were further processed by crushing in an agate mortar and the resulting powder was sieved to the desired particle size of 80-160 µm.

2.2.2 Pellet processing

For the fabrication of porous pellets, the milled powder was mixed with a pore-former, Glassy carbon spherical powder, 0.4-1.2 micron, type 1 by Alfa Aesar (Figure 2.2). The powder and the required amount of pore former, depending on the target porosity to be achieved, were added into a mortar along with acetone and mixed well using a pestle. The acetone was left to evaporate at room temperature before the dry powder was transferred to a drying oven to dry completely. The resulting powder mixture was then pressed and fired at high temperatures (1350-1400°C) to produce the porous perovskite pellet. The spherical glassy carbon used as pore former was selected due its particle size being similar to that of the ball milled powder and this way uniform pore distribution and size could be achieved.

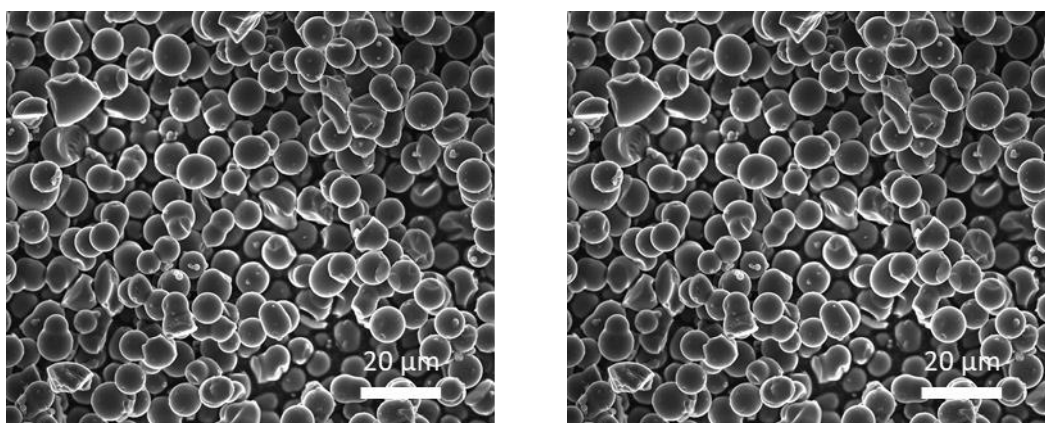


Figure 2.2 SEM micrographs of the Glassy carbon spherical powder, 0.4-1.2 micron, type 1.

2.2.3 *Sample pre-treatment*

In order to produce powder samples with exsolved nanoparticles and varying particle characteristics, the sieved to the required grain size powder was reduced at various temperatures and for different time duration (900-1000 °C for 0-30 h) in a controlled atmosphere tubular furnace under a continuous flow of dry 5% H₂/He ($p_{O_2} \sim 10^{-20}$ atm). The reducing gas was supplied by a compressed gas cylinder at a flow rate of 25 mL min⁻¹ regulated by a ball-float flowmeter and heating and cooling rates of 5 °C min⁻¹ were used. In order to eliminate inconsistencies in the partial pressure of the reducing gas as a result of different trace amounts of moisture in different gas cylinders, a moisture trap was installed in line before the reduction furnace. Prior to reduction, the system was evacuated using a pump and then flushed and purged with the reducing gas for 1 hour in order to ensure all air was removed.

Prior to testing the reduced-exsolved powders were oxidised in static air at 600 °C for 1 h with heating and cooling rates of 5 °C min⁻¹.

2.2.4 *Pechini sol-gel method*

The Sol-gel Pechini method was employed for the synthesis of the stoichiometric perovskite system used as reference material in this study (Danks et al., 2016). High purity metal nitrate precursors in stoichiometric ratios, in this case La(NO₃)₃·6H₂O, Sr(NO₃)₂ and Mn(NO₃)₃·4H₂O, were added to a beaker followed by citric acid (Sigma Aldrich 791725) and ethylene glycol (Sigma Aldrich 324558) in molar ratios to the total cations present of 1:1 and 1.2:1 respectively. 400 mL of deionized H₂O was added to the beaker, and the solution was stirred until all components have fully dissolved and a clear solution has been achieved. The solution was then transferred to a 10 L beaker to be dried at 75 °C for 24 hours. The orange dry gel formed after the drying process was lightly crushed using a mortar and pestle before being transferred into an alumina crucible to be calcined in air at 1050 °C for 18 hours. The resulting powder was then crushed and sieved and particle sizes between 80 and 160 μm were selected.

2.3 Characterisation methods and techniques

2.3.1 *Powder X-ray diffraction*

X-ray powder diffraction is among the most widely applied non-destructive techniques developed for the study of the atomic and molecular structure of different crystal phases of solid materials. As the name suggests, the sample is in a powder form, consisting of fine grains of crystalline material. The method records the scattered intensity of an X-ray beam diffracting from the sample as a function of angle. From the resulting pattern, valuable information regarding the composition and the crystal structure of the sample can be drawn.

Powder X-ray powder diffraction is employed for the identification of unknown crystalline materials and qualitative and quantitative analysis, including identification of the crystal structure, crystallite size and lattice strain. When X-rays hit matter, different absorption and scattering effects can take place. Due to the periodic nature of a crystalline structure, when the sample is irradiated with x-rays, constructive or destructive interference of the scattered radiation may occur, resulting in a characteristic diffraction pattern which can be used to investigate the structure of the material. The method is based on the diffraction of X-rays by

the atomic planes of the sample and the angle that these diffractions take place (Hübschen et al., 2016).

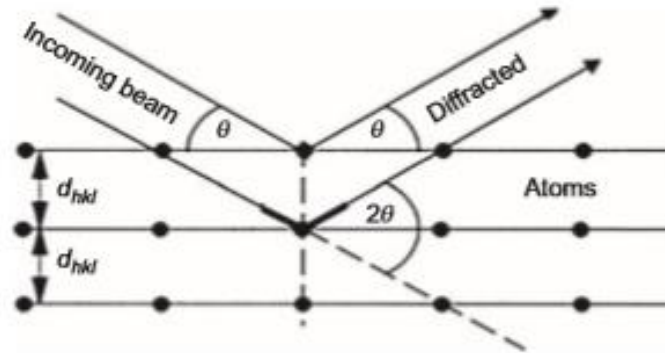


Figure 2.3: **Diffraction of X-rays from the lattice planes of a crystalline material (Hübschen et al., 2016).**

The X-ray beam is directed to the solid at an angle (θ) and X-rays are scattered elastically from the electrons of the atoms found in the crystal lattice. When the X-ray reflection waves produced are in phase, there is a constructive interference scattered by an angle 2θ (diffraction angle). These waves are collected and analysed through an X-ray detector to produce the diffraction pattern of the material. The XRD phenomenon can be illustrated geometrically (Figure 2.3) and is interpreted by Bragg's law (Eq. 2.1).

$$2 d \sin\theta = n \lambda \quad (\text{Eq. 2.1})$$

where n is the order of diffraction, λ is the wavelength of the incident X-ray beam in nm, d is the lattice spacing in nm and θ is the angle of the diffracted beam in degrees ($^\circ$). Qualitative analysis of the crystal phases can be carried out by determining the distances d between the planes through Bragg's law (Eq. 2.1) since d spacing is unique for every crystal structure. As a result, by comparing the d spacing of the peaks calculated and the d spacing of known crystal phases found in literature, it is possible to identify the crystal phases of the material. XRD is not limited to qualitative analysis, quantitative analysis can be carried out for the detection and calculation of the relative amount of secondary phases present in an impure sample, while other information such as calculation of the unit cell parameter and determination of the crystallite size and strain of the sample are possible. Lattice parameters, space group, chemical composition, macro-stress, and qualitative phase analysis can be investigated by the peak positions. Peak intensity provides valuable information regarding crystal structure (atomic positions, temperature factor or occupancy) as well as texture and quantitative phase analyses can be carried out. Finally, peak shape can be investigated for information regarding sample broadening contributions such as micro-strains and crystallite size (Hübschen et al., 2016). Even more information can be extracted via XRD by employing Rietveld refinement. In this a proposed model of a crystal structure is calculated by fitting a theoretical XRD pattern on the one obtained experimentally. This way the crystal structure of the material can be visualised, and further information can be extracted for the sample (Behrens & Schlögl, 2012).

The basic configuration of a typical Powder XRD instrument is presented in Fig. 2.3. The instrument is comprised of an X-ray generator (tube), an array of slits, a goniometer, a sample stage, a monochromator and a detector. X-rays are generated in the X-ray tube by the collision of electrons on a metal target (typically Cu) emitted by a tungsten filament and accelerated at high voltage. The generated X-rays hit the powder sample which is packed in a sample holder that is located at the centre of the goniometer, at different angles causing them to diffract and be collected by the detector.

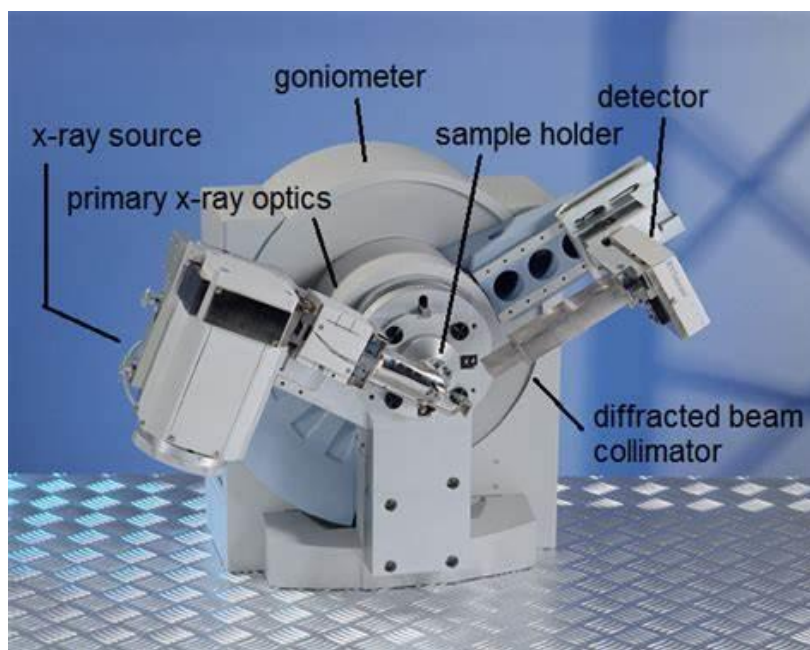


Figure 2.4 **Components of a typical powder diffractometer** (photo courtesy of Malvern-PANalytical B.V.).

X-ray diffraction patterns were collected at room temperature using a PANalytical X'Pert Pro Multipurpose diffractometer (MPD) fitted with an X'Celerator (RTMS detector). The XRD patterns obtained were analysed with STOE WinXPOW software in order to probe the crystal structure of the systems.

2.3.2 *Synchrotron In situ and operando XRD at ESRF*

Aiming to get further insight regarding the structural and compositional changes that the material undergoes during the redox process *in-situ* and operando X-ray diffraction experiments were conducted at the European Synchrotron Facility (ESRF). Multiple operando experiments were carried out and over 50 samples from different stages of the process were scanned in capillaries. The in-situ x-ray diffraction experiments were carried out on ID22 of the European Synchrotron Research Facility. The source for ID22 is an in-vacuum undulator that is located on a curve of the 844 m circumference of ESRF's electron particle accelerator that operates at an energy of 6 GeV. The source is capable of producing X-rays with energies ranging from 6 keV to 80 keV. The generated beam passes through a monochromator before hitting the sample and reaching the diffractometer. The diffractometer consists of nine silicon 111 crystals, with very small acceptance angle that acts as a filter for the removal of rays that are not parallel to the detectors. The filtering crystals along with the detectors are mounted

on a rotational stage that can move through the 2θ angle allowing the recording of peaks in the range of 0 to 25° . The geometry of the nine-detector system fan-like geometry allowing a large selection of 2θ angles to be recorded while the stage is moving in small increments. The X-ray energies produced in ID22 are optimal for such experiments since high energies are required in order to overcome the sample size and penetrate through reactor and samples in order to reach the detector while avoiding the lanthanum K edge of 39 keV. In addition, the high flux of x-rays allows for the rapid and with high precision determination of the peak structure, while the high-quality analyser crystals provide the high resolution needed, producing sharp peaks, making the monitoring of small shifts in peak positions possible. Peak shift, is of great importance for this project since it is expected to occur as the material is reduced and oxidized without changing phase, allowing the monitoring of the peak evolution before the phase change occurs where a new peak is formed. The evolution of peak splitting due to phase changes can also be detected.

In order to be able to run *in situ* experiments with a working reactor bed, certain system design parameters and limitations must be taken into consideration. The reactor system used was designed specifically to allow for such experiments and is described in detail in sub chapter 1.1.8. The particularity of this system is that a custom vertical split furnace, provided from IGI systems, is employed (Figure 2.5a). This furnace has a thin vertical window on either side, allowing the sample that is placed in the reactor to be 'visible' to the X-rays. Despite, the furnace being open to the environment through the slit, an isothermal zone of 20 cm ($\pm 10^\circ\text{C}$) is achievable at the maximum operating temperature of 1000°C . The reactor used is a quartz tube with a diameter on the order of 5 mm, which for a conventional area detector is a big limitation as diffraction from the front and the back of the reactor would cause broadening of the beam dimming the monitoring of fine peak shape changes and peak shifts impossible. ID22 is one of the few facilities in the world that can produce X-rays with enough flux at the required X-ray energy and has the analyser resolution necessary for this experiment. For the experiments in this study all samples were in powder form and a radiation energy of 38 keV (wavelength 0.35448 Å) was used. Samples were also scanned at room temperature by loading powders in 0.5 mm capillaries (Figure 2.5) and scanned at 2θ angles ranging from 0 to 40° , with an average acquisition time of 10 min. Scan time for each scan was 30 s, scanning at 2θ angles ranging from 0 to 20° .

All XRD data presented in this thesis is synchrotron data, unless stated otherwise in the figure caption. In-house XRD was used for day-to-day analysis and data is not presented.

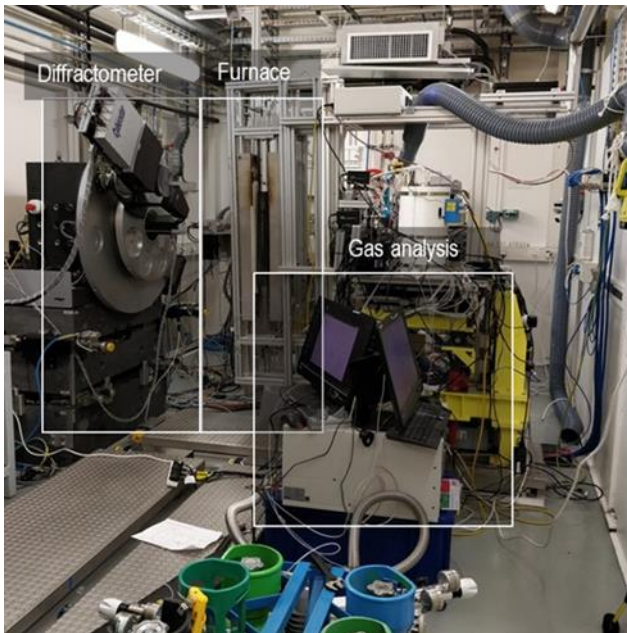
a**b**

Figure 2.5 **Photographs from ESRF.** a) Reactor system set up at ESRF. b) Capillaries loaded with powdered samples used for room temperature scans.

2.3.3 *Scanning electron microscopy*

Scanning Electron Microscopy (SEM) was the main technique employed for the analysis of the sample's surface characteristics and microstructure. In a Scanning Electron Microscope, a highly focused beam of electrons is generated and targeted to the sample that is placed inside a vacuum chamber. The electron beam is focused to a spot and as the sample is scanned, signals are emitted and collected by detectors. A typical SEM comprises of an electron gun (electron source and accelerating anode), electromagnetic lenses to focus the beam of electron, a vacuum chamber housing the specimen stage and an array of detectors to collect the signal emitted from the specimen (Figure 2.6).

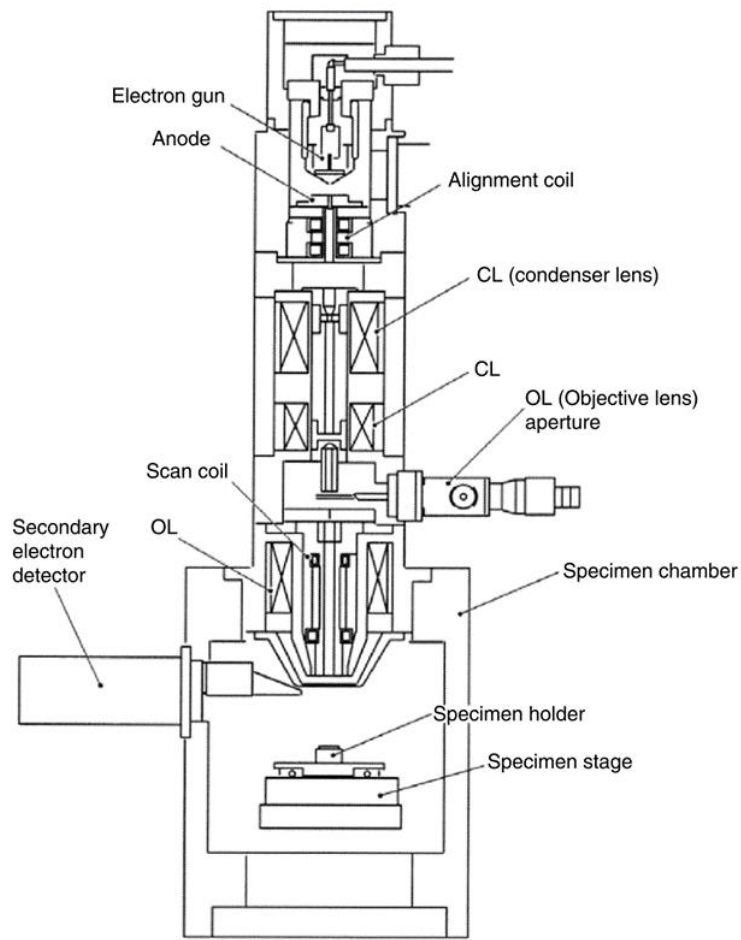


Figure 2.6 **Schematic of a typical Scanning Electron Microscope (SEM) (Zhou & Lin, 2007).**

Image formation is the result of that acquisition of these signals produced from the interaction between beam and specimen. Interactions are divided into two major categories: elastic interactions and inelastic interactions. When a beam of electrons hits a sample, the electron can either pass through the solid without losing energy (transmitted primary electrons), be adsorbed by the solid, or produce a signal, as a result of their interaction with the solid. The key signals emitted are scattered primary electrons (electrons that scatter without any loss of energy), secondary electrons (electrons emitted from the interaction of the beam with the sample's atoms), backscattered electrons (scattered electrons with 180° direction change) and X-rays. In SEM, the signals collected from the secondary electrons and the backscattered primary electrons are collected and combined to form an image (Hübschen et al., 2016). Elastic scattering of electrons by the atomic nuclei of the sample results in backscattered electrons (BSE) which are used for generating images based on Z-contrast which can be used for determining the compositional homogeneity of the specimen. Inelastic scattering of electron by the atomic nuclei of the sample results in secondary electrons, which are used to provide topographical information about the sample's surface and provide information about the surface texture and roughness. Inelastic scattered electrons by sample atoms result in the emission of X-rays from lower sample depths and can be used for analysing the chemical composition of the sample through a method called Energy Dispersive X-ray spectroscopy (EDX). Finally, Auger electrons produced by inelastic scattering with sample atoms near the

surface can be utilised for surface chemical analysis (Zhou & Lin, 2007). The different signals emitted by electron-specimen interactions and the regions within the specimen where the signals are generated are summarised in Figure 2.7.

A FEI Helios Nanolab 600 and a Tescan Vega 3LMU fitted with a Bruker XFlash® 6 | 30 were used in this work. The SEM were operated under high vacuum and with voltage ranging from 1 to 30 kV. Powder samples were mounted on SEM specimen stubs using carbon adhesive tabs with aluminium foil core and conductive silver paint in order to increase electric conductivity and minimise sample charging during the image acquisition process. Particle and microstructure characteristics were calculated using the image analysis software ImageJ.

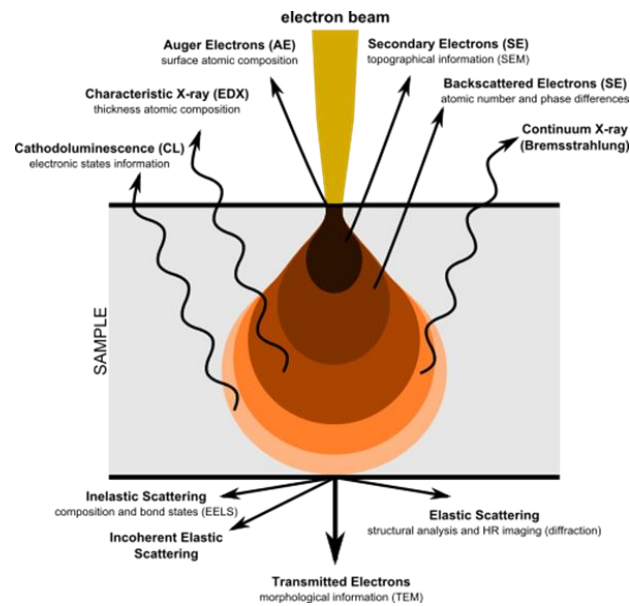


Figure 2.7 Schematic representation of the different signals produced by electron-specimen interactions and regions within the specimen where the signals are generated (Image courtesy of ThermoFisher Scientific).

2.3.4 Transmission electron microscopy

Transmission electron microscopy is the technique employed here for the analysis of the sample's internal microstructure. In contrast to SEM where image is generated based on scattered electrons, TEM utilises electron transmitting through the specimen. The image produced is a result of electrons collected which have passed through the 'electron transparent', thin specimen (less than 100 nm). Structural and chemical analysis can be carried out on the same sample across length scales ranging from the atomic level up to 100 μm (Hübschen et al., 2016).

A TEM is typically comprised of an electron gun, probe-forming lenses and apertures, a specimen holder, image-forming lenses and apertures, electron detectors and a vacuum system (Che & Védrine, 2012). Electrons are generated by the electron gun located at the top of the microscope column. The electron beam travels along the column in vacuum where an array of condenser lenses magnifies it and controls its size before being directed to the sample. The beam goes through the electro transparent sample and an image is created by the objective lenses, projector lenses and a fluorescent screen.

The TEM micrographs in this study were obtained on a JEOL JEM-2100 system.

2.3.5 *Thermogravimetric analysis*

Thermo-gravimetric analysis (TGA) is a technique that allows recording of the mass loss (reduction, drying etc.) or gain (oxidation, adsorption etc.) of a material with high precision. The changes in mass are recorded versus temperature and time under a certain gas atmosphere. Depending on the heating regimes and gas atmospheres used, TGA can provide insight about materials characteristics such as oxygen capacity, redox and thermal stability and reaction kinetics.

A typical TGA is mainly comprised of a high precision balance with a crucible where the sample is loaded. The crucible resided into a sealed furnace with programmable temperature through which heating and cooling rates can be controlled. A gas feed system is connected to the furnace through which the reaction atmosphere can be altered.

TGA analysis in this study was conducted using a Rubotherm dynTHERM system. For the oxidation- weight gain experiments a weighted amount of the sample (500 mg) was introduced into the TGA crucible, and the gas flow rate was regulated at 200 mL min⁻¹. The sample was heated up in 20% O₂/ He to 600 °C, dwell for 3 h, and subsequently cooled to RT.

2.4 Experimental setups

2.4.1 *Mini reactor setup for temperature programmed experiments*

This setup was used for all Temperature Programmed Reduction (TPR), Temperature Programmed Oxidation (TPO) and few-cycle chemical looping experiments carried out at Newcastle University, aiming to investigate the material's reactivity to methane, redox properties and anti-coking features. The rig, presented in Figure 2.8, briefly comprises of a quartz reactor tube, a furnace, a series of mass flow controllers and a mass spectrometer for gas analysis. Manual ball valves were used for gas switching.

The reactor used is a quartz tube with a fixed quartz frit of no. 3 porosity, measuring 6mm in diameter, 1.55 mm in wall thickness and 30 cm in length. The reactor tube is connected to the system through a series of Swagelok Ultra-Torr vacuum fittings and held in a vertical furnace forming a sealed fixed-bed reactor. The Ultra-Torr fittings house a closed end tube which allows temperature measurement in the catalyst bed by a type K thermocouple which is placed in the centre of the bed housed in a closed end quartz tube threaded though the torr fittings.

Feed gas flow rates is set manually via mass flow controllers connected to control boxes and a pressure gauge is used to monitor any pressure changes during operation. Back flow preventers (BFP) are installed throughout the system as an additional safety measure in order to prevent unwanted backflowing and mixing of gasses in the system.

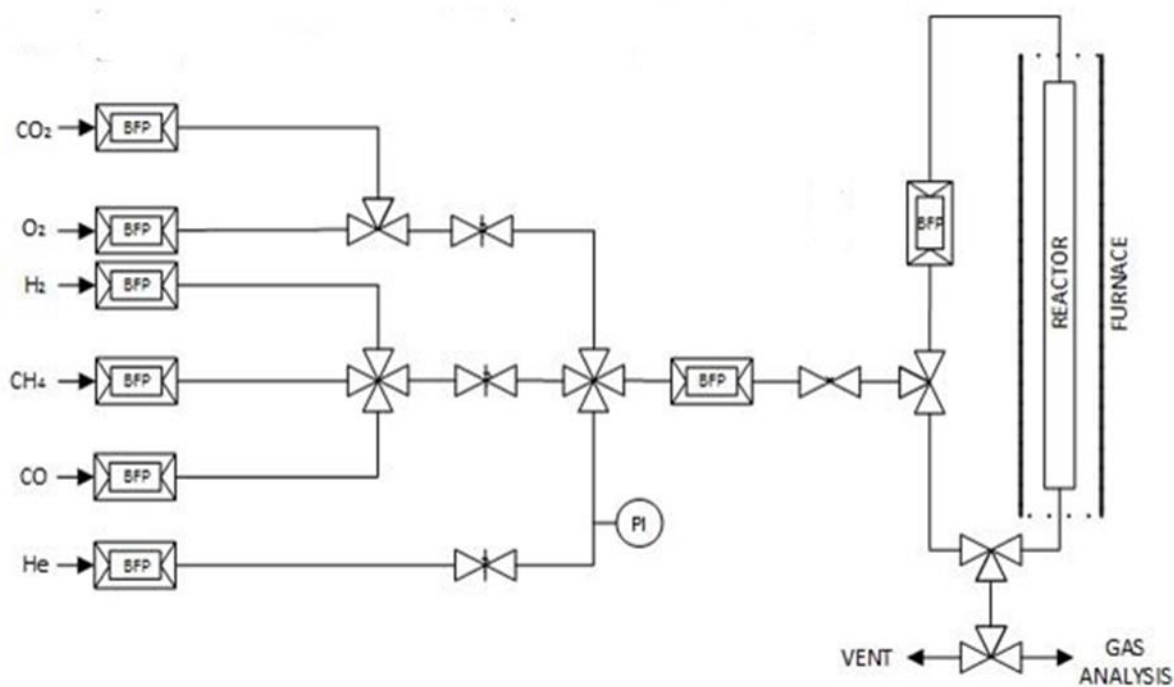


Figure 2.8: **Flow diagram of the mini-reactor setup.**

2.4.2 Automated fixed bed Integral reactor system

This system was employed for the long-term chemical looping experiments at Newcastle University and for the *in-situ* X-ray diffraction experiments on beam line ID22 at the European Synchrotron Research Facility (ESRF).

Briefly, the system presented in Fig. 7 mainly comprises of a 1.6 m long quartz reactor tube with a diameter of 5 mm, a vertical furnace, a mass spectrometer (Hiden Analytical QGA, HAS-301-1291), a liquid filled permeation tube and furnace (HW), a set of 7 computer-controlled mass flow controllers (SLA5850, Brooks Instrument), a series fully automated 4-way valves and pressure transducers (PG309-100GV, Omega).

The flow system consists of 9 automated 4-way valves supplied by VICI (Valco Instruments Co. Inc.) which allow gas direction switching. During the experiment, flow of all reactive gases is continuous and gas direction to and from the reactor is governed by switching of the valves which are controlled via software. Feed gas flow rates to the system are set and regulated by 7 mass flow controllers connected to high pressure cylinders containing the gasses. The mass flow controllers are connected to the main computer software through which their set points are controlled. Via the same software a gas shut off solenoid valve attached to their outlet is also controlled ensuring that the flow of gas will be terminated when the flow rate through the mass flow controllers is set to zero, since on their own the mass flow controllers are not able to act as an on/off valve. Additionally, the solenoid valves ensure that the flow is terminated in the event of an interlock shutdown in the case of a system failure due to loss of connection for more than 5 minutes. Pressure transducers were used for pressure monitoring in various points throughout the system and Pressure indicators (PI) were used for manually

balancing the pressure in the system and leak testing. In order to avoid pressure heads developing through the system, needle valves were installed to the end of vent lines and before gas analysis in order to ensure that pressure drop throughout the system was consistent regardless of the gas flowing. Two pressure relief valves designed to fail at 5 barg were installed at the end of the reactor outlet line and at the end of the main vent line in order to ensure safe operation in the case of needle valve failure (clogging). During the experiment, the local bed temperature was recorded with a K-type thermocouple placed in contact with the quartz reactor tube.

The reactor used was a quartz tube with an internal diameter of 4mm, wall thickness of 2mm and 140 cm in length. The reactor was connected to the system using Ultra Torr fittings. The powder sample was packed into the reactor between two quartz wool plugs which kept the bed in place. Additionally, two quartz rods of smaller diameter were placed inside the reactor, on either side of the bed and in direct contact with the quartz wool plugs, in order to minimize the dead volume in the reactor and assist with preventing the bed from moving during gas switching.

All metal (stainless steel) piping which were involved with H₂O flow were wrapped in heating lines in order to ensure that the H₂O remained in vapour form and prevent condensation in the system. Condensation in the lines would lead to inconsistent moisture content reaching the reactor and the gas analysis system, compromising the experimental results.

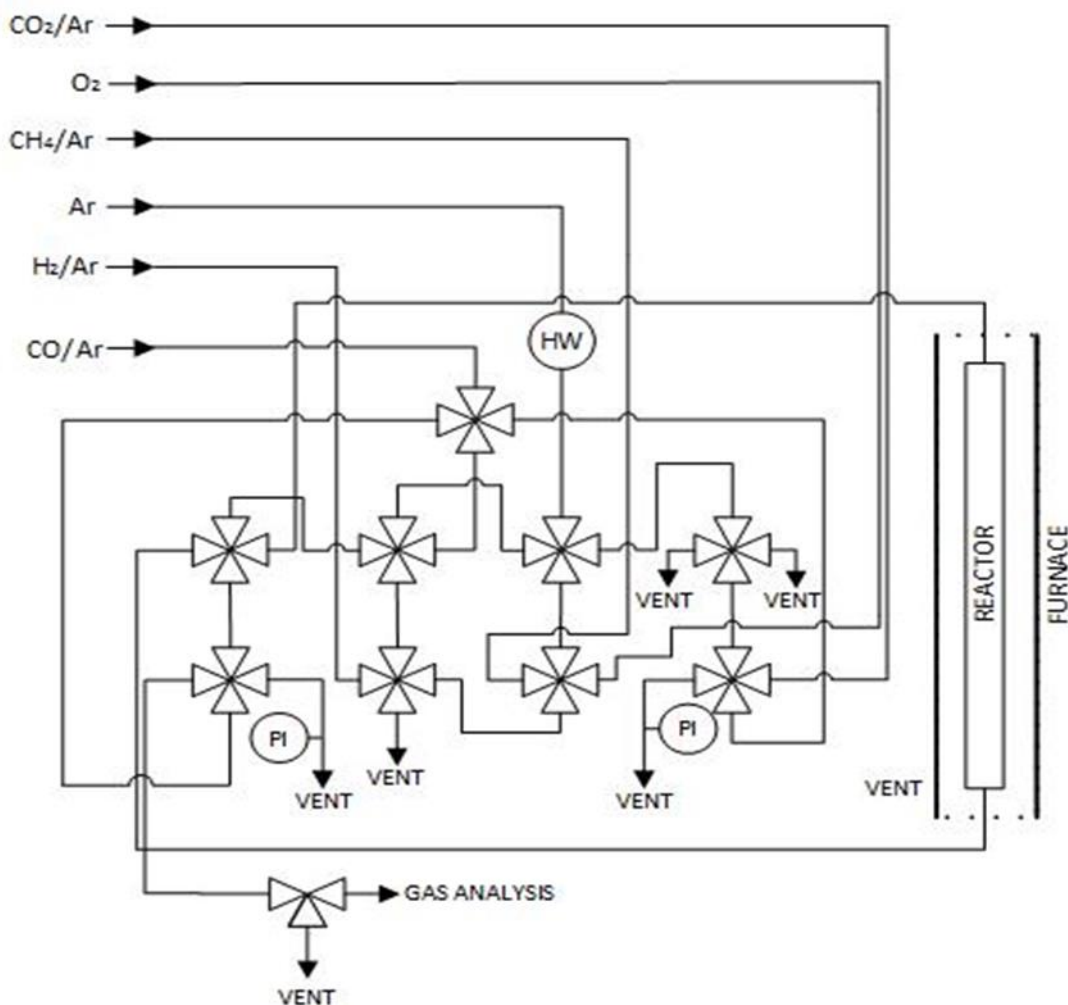


Figure 2.9: Flow diagram of the automated fixed bed integral reactor system.

2.4.3 Gas analysis

Gas analysis for all experiments carried out in this study was performed using a quadrupole mass spectrometer working with electron impact ionisation, a quadrupole mass filter and a secondary electron multiplier detector (Hiden Analytical QGA, HAS-301-1291).

Mass spectrometry is one of the most powerful methods for the detection and characterization of compounds. In a typical MS procedure, the sample (gaseous, solid or liquid) transferred to the ion source of the mass spectrometer to be ionized by bombarding it with electrons. These ions are then separated according to their mass to charge ratio, by accelerating them and passing them through an electric or magnetic field. Ions with different mass-to-charge ratios will suffer different amounts of deflection crashing at different points on the detector, this way allowing their identification. Mass spectrometers must operate at low pressures (10^{-3} - 10^{-9} Torr), created by vacuum-pumping systems. This is essential as it prevents collisions between the ions and background molecules which would compromise the mass analysis (Lever et al., 2005). A simplified layout of a mass spectrometer is shown in Figure 2.10.

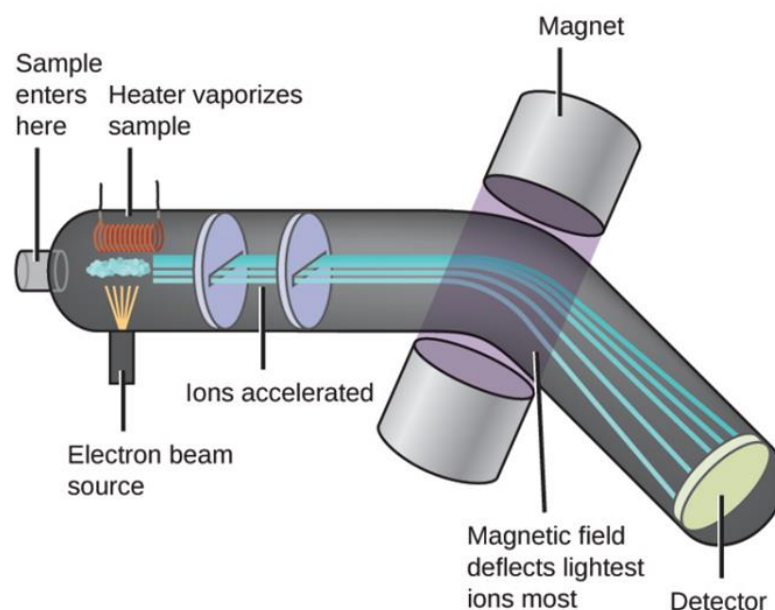


Figure 2.10 **Simplified layout of a mass spectrometer (Flowers et al., 2015).**

The system used in this study has an input stream flow rate to 20 ml/ min and an inlet pressure of 1 bar. A high sampling rate is achieved by using a Secondary Electron Multiplier (SEM) detector, which allows for small ion currents to be detected by amplifying the ion signals.

During all experiments in this study CH_4 , O_2 , H_2 , CO and CO_2 were continuously monitored (at $m/z = 15$ (CH_4), 32 (O_2), 2 (H_2), 28 (CO) and 44 (CO_2)) through the mass spectrometer's heated capillary line. The mass to charge ratio of ions measured was converted to gas concentrations via calibration.

Calibration was conducted by periodically feeding known concentrations (5%) of CH_4 , O_2 , H_2 , CO and CO_2 , in a balance of He and He as a zero gas into the mass spectrometer to obtain calibration factors, cracking factors (for CO_2 into CO) and the background current. Calibrations with all calibration gases and the zero gas were performed before and after each experiment. In the case of long term (multiple day) experiments calibration was also conducted during the experiment. The corrected mass to charge ratio current for all gases was a calibration factor multiplied by the difference between the recorded signal and the background signal, minus any cracking signal from other species on that particular mass to charge ratio channel.

2.5 Experimental procedures

2.5.1 Temperature programmed reduction

For the temperature programmed reduction experiments a weighted amount of sample (150 mg) was loaded in the reactor and purged in situ with He at RT. TPR profiles were obtained from RT to 750 °C with a heating rate of 5 or 10 °C min^{-1} (depending on the reactor setup where the experiment was conducted) under a constant flow of reducing gas mixture of 5% CH_4/He flowing at 50 mL min^{-1} at atmospheric pressure. The reactor outlet was analysed by a mass spectrometer (Hiden Analytical QGA, HAS-301-1291). Calibration of the gases was conducted using known concentrations (5%) of CO , CO_2 , H_2 , O_2 and CH_4 prior to each

experiment using the reactor bypass line. Integration of the MTPR signals allowed for the calculation of the total amount of gases consumed and produced.

2.5.2 Temperature programmed oxidation

Temperature programmed oxidation (TPO) experiments were performed either for monitoring the oxidation of the material or for measuring the carbon deposition after methane conversion experiments. For the oxidation monitoring experiments 80 mg of samples was loaded in the reactors and purged in situ with He at RT. For measuring the deposited carbon post TPR experiments, a weighted amount of the used sample (~80mg) was used.

Temperature was increased from RT to 750 °C at a rate of 5 or 10 °C min⁻¹ (depending on the reactor setup where the experiment was conducted), under a constant flow of 5% O₂/He used as the oxidising gas mixture, flowing at 50 mL min⁻¹ at atmospheric pressure. Temperature was kept at 750 °C until the O₂ (CO₂) signal reached the baseline. O₂, CO₂ and CO signals at the outlet of the reactor were continuously monitored by a mass spectrometer (Hiden Analytical QGA, HAS-301-1291). Integration of the TPO signals allowed for the calculation of carbonaceous deposits.

2.5.3 Chemical looping cycling experiments

In order to determine the stability of the systems under redox cycling, experiments with repeated oxidation/reduction cycles were performed. The cycling was carried out at atmospheric pressure and in various temperatures (depending on the experiment) ranging from 550 to 650 °C (determined from the activation profile of the tested sample). After the sample was loaded, the reactor was flushed with He, flowing at 30 mL min⁻¹ and the temperature was then raised at the required value with a heating rate of 5 °C min⁻¹. After the temperature has stabilised, the sample was subjected to multi-cycle isothermal reduction under 5% CH₄/He and isothermal oxidation under 5% O₂/He with inlet flow rates ranging from 30 to 50 mL min⁻¹. Reduction and oxidation half cycle duration varied depending on the experiment. Between half-cycles the reactor was purged with inert gas (He) in order to avoid mixing of the two reactant streams. Calibration of the gases was conducted using known concentrations (5%) of CO, CO₂, H₂, O₂ and CH₄ prior to each experiment using the reactor bypass line. For long term cycling experiments calibration was also done during the experiment after every 15 cycles completed using the reactor bypass line while flowing inert gas through the reactor.

2.6 Data processing

2.6.1 Gas analysis data

For the calculation of conversions, product selectivity, carbon deposition and oxygen capacity for the gas analysis data, the following equations were used.

$$N_{CO} = \int_R (y_{CO})_{outlet} n dt \quad (\text{Eq. 2.1})$$

$$N_{CO_2} = \int_R (y_{CO_2})_{outlet} n dt \quad (\text{Eq. 2.3})$$

$$N_C = \int_O (y_{CO_2})_{outlet} n dt + \int_O (y_{CO})_{outlet} n dt \quad (\text{Eq. 2.4})$$

$$N_{CH_4} = \int_R (y_{CH_4})_{outlet} n dt \quad (\text{Eq. 2.5})$$

Where the letter under the integral denotes the reduction step (R for TPR or half-cycle) or the oxidation step (O for TPO or half-cycle). N_{CO} , N_{CO_2} are the total moles of CO, CO₂, produced, respectively, during the reduction step and N_{CH_4} is the total moles of unreacted CH₄ (measured at the outlet of the reactor). n is the total molar flow rate corresponding to each experiment, m is the mass of sample.

Conversion of methane (C_{CH_4} , %) was calculated by the following equation:

$$C_{CH_4} = \frac{N_{CO} + N_{CO_2} + N_C}{N_{CO} + N_{CO_2} + N_C + N_{CH_4}} \cdot 100 \quad (\text{Eq. 2.6})$$

Product selectivity (%) was calculated by the following equations:

$$S_{CO} = \frac{N_{CO}}{N_{CO} + N_{CO_2} + N_C} \cdot 100 \quad (\text{Eq. 2.7})$$

$$S_{CO_2} = \frac{N_{CO_2}}{N_{CO} + N_{CO_2} + N_C} \cdot 100 \quad (\text{Eq. 2.8})$$

$$S_C = \frac{N_C}{N_{CO} + N_{CO_2} + N_C} \cdot 100 \quad (\text{Eq. 2.9})$$

Carbon deposition ($\text{mg}_{\text{carbon}}/\text{g}_{\text{sample}}$) was calculated by the integration of the curve of CO₂ after TPO experiments. Complete absence of CO meant that the oxidation of carbon lead only to total combustion products.

$$c = \frac{M_C}{m} N_C \quad (\text{Eq. 2.10})$$

Where c is the deposited carbon and M_C is the molar mass of carbon.

Oxygen capacity (mol O/mol of perovskite) was calculated by the following:

$$\zeta_C = (2N_{CO_2} + N_{CO}) \cdot \frac{M_P}{m} \quad (\text{Eq. 2.11})$$

$$\zeta_G = \frac{m_f - m}{m} \cdot \frac{M_P}{M_O} \quad (\text{Eq. 2.12})$$

$$\zeta_X = \frac{f_{Ni}}{M_{Ni}} \cdot \frac{M_P}{f_P} \quad (\text{Eq. 2.13})$$

Where ζ_C , ζ_G and ζ_X correspond to the oxygen capacity (expressed as moles of O per moles of perovskite) calculated from TPR, TGA and X-ray diffraction Rietveld refinement, respectively. M_P, M_O, M_{Ni} are the molar masses of the perovskite, oxygen and nickel, respectively. m is the sample weight used in the respective experiments. For the TGA experiment, m_f is the final weight of the sample. f_{Ni} and f_P are the weight fractions of the respective species as calculated via Rietveld refinement.

2.6.2 XRD data analysis and Rietveld refinement

The XRD patterns obtained were analysed with STOE Win XPOW software in order to determine the crystal structure and cell parameters.

Rietveld refinement was performed using FullProf software. Rietveld refinement maps variables to multiple structural parameters and minimizes the difference between the calculated and experimentally obtained XRD patterns corresponding to the proposed model of the crystal structure. Diffraction peaks were fitted using a pseudo-Voigt profile. The parameters refined include scale factors, background polynomial parameters or linear interpolations between a set of background points with refinable heights, unit cell parameters, peak profile parameters u , v , w , and η (Lorentz-Gaussian distribution), zero-shifted atomic positions, and site occupancies.

2.6.3 Image analysis

Image processing and analysis in this study was carried out using ImageJ software (Rueden et al., 2017). Particle analysis was done using the *Analyze Particles* plugin (Rueden et al., 2017) through which particles on the image were identified and their surface area and total number was returned. Using their area measurement and assuming spherical nanoparticles, the average diameter size s was determined, and particle population P was calculated by dividing the number of identified particles on the analysed area of the image (A). Assuming spherical nanoparticles, the exsolved Ni atoms per area N_{Ni} were calculated with Eq. 2.14.

$$N_{Ni} = \frac{\sum_{\text{Particles}} \frac{1}{6} \pi s^3 \cdot \frac{\rho(\text{Ni}) \cdot N_A}{M(\text{Ni})}}{A} = \frac{\sum_{\text{Particles}} \frac{1}{6} \pi s^3 \cdot 91.42 \text{ nm}^{-3}}{A} \quad (\text{Eq. 2.14})$$

References

- Behrens, M. & Schlögl, R. (2012) 'X-Ray Diffraction and Small Angle X-Ray Scattering', *Characterization of Solid Materials and Heterogeneous Catalysts: From Structure to Surface Reactivity, Volume 1&2*, 2pp. 609–653.
- Che, M. & Védrine, J.C. (2012) *Characterization of Solid Materials and Heterogeneous Catalysts: From Structure to Surface Reactivity, Volume 1&2*. Vol. 1–2.

- Danks, A.E., Hall, S.R. & Schnepf, Z. (2016) 'The evolution of "sol-gel" chemistry as a technique for materials synthesis', *Materials Horizons*, 3(2), pp. 91–112.
- Flowers, P., Theopold, K., Langley, S.F. & Robinson, W.R. (2015) *Chemistry*. Vol. 1. Openstax Rice University.
- Hübschen, G., Altpeter, I., Tschuncky, R. & Herrmann, H.G. (2016) *Materials Characterization Using Nondestructive Evaluation (NDE) Methods*. Vol. 3. Elsevier Ltd.
- Kousi, K., Tang, C., Metcalfe, I.S. & Neagu, D. (2021) 'Emergence and Future of Exsolved Materials', *Small*, 17(21), .
- Lever, A.B.P., McCleverty, J.A. & Meyer, T.J. (2005) *COMPREHENSIVE COORDINATION CHEMISTRY II - From Biology to Nanotechnology Volume 2: Fundamentals: Physical Methods, Theoretical Analysis, and Case Studies*.
- Mourdikoudis, S., Pallares, R.M. & Thanh, N.T.K. (2018) Characterization techniques for nanoparticles: Comparison and complementarity upon studying nanoparticle properties, *Nanoscale*, 10(27), pp. 12871–12934.
- Neagu, D. (2012) *Materials and Microstructures for High Temperature Electrochemical Devices through Control of Perovskite Defect Chemistry*. [Online].
- Rueden, C.T., Schindelin, J., Hiner, M.C., DeZonia, B.E., Walter, A.E., Arena, E.T. & Eliceiri, K.W. (2017) 'ImageJ2: ImageJ for the next generation of scientific image data', *BMC Bioinformatics*, 18(1), pp. 1–26.
- Zhou, W. & Lin, Z. (2007) *Scanning Microscopy for Nanotechnology*.

3 Development and investigation of a system with exo-/ endo-nanoparticles for the conversion of methane to syngas

In this chapter the methodology for designing and producing perovskite systems with exo-endo- particles is introduced. The produced composite system is studied and emergent properties stemming from the unique relationship of its components are investigated. Gas analysis coupled with in-situ and operando X-ray techniques, TGA and SEM are employed providing insight on the systems enhanced capabilities. The system is applied and studied, under reaction conditions, for the conversion of methane and as oxygen carrier for Chemical looping partial oxidation of methane showcasing its applicability and superior performance. The results presented in this chapter have been published in (Kousi, Neagu, & Metcalfe, 2020) and the report is referenced throughout.

3.1 Introduction

Through the literature review carried out in the first chapter of this study, it becomes apparent that dispersing active metallic nanoparticles on the surfaces of supports is key for controlling the surface reactivity of materials employed in a plethora of catalytic and energy conversion technologies. However, what if it was possible to develop systems where nanoparticles were not only dispersed on their surface but also in their bulk? When attempting to visualise and design such materials two main questions arise: how can they be synthesised efficiently and what will be the involvement of the subsurface characteristics, if any, on the material's properties and performance? A similar concept was investigated by Kim and collaborators in a study where gold nanoparticles were assembled together with a perovskite oxide resulting in a nanocomposite with enhanced oxygen ion transport and oxygen reduction capability. This was determined to be a result of the strained perovskite oxide lattice induced by the gold nanoparticles (Kim et al., 2019). Under the same broad concept, noble metallic nanoparticles have been embedded within other inorganic crystal lattices leading to improved electronic transport in a similar manner to that of substitutional doping (Cargnello et al., 2015). Therefore, it has been shown that metallic nanoparticles embedded in various non-metallic supports can potentially lead to advanced materials that can be tailored through strain engineering, allowing control of various properties such as electron, oxide- ion and thermal transport (Greeley et al., 2004; Wu et al., 2019; Choi et al., 2019), catalytic activity (Greeley et al., 2004; Strasser et al., 2010; Wang et al., 2019; Jalili et al., 2011; Escudero-Escribano et al., 2016) and magnetic properties (Lu et al., 2012).

However, developing such systems is still a challenge, as is controlling nanoparticles characteristics and dispersion. This is mainly due to the current approach used for their synthesis which usually involves assembling the metallic clusters with the non- metallic host, which limits the range of combinations that can be used to metals which are usually noble and hosts that do not chemically interact during the preparation process (Kim et al., 2019; de Rogatis et al., 2010). As a result, this greatly limits the type of composite nanomaterials and structures that can be produced. A method like redox exsolution can be promising for such an application since the metals that are to form the embedded phase can be initially dispersed within the host matrix as atoms in a solid solution and precipitate out of it, upon exsolution, forming the nanoparticles. Exsolution has already opened new horizons for many material-related processes, providing an advanced toolset that leads to the creation of well dispersed, confined particles on the surface of an oxide supports (Reader is referred to Chapter 1). The surface exsolved nanoparticles exhibit enhanced resistance to carbon deposition and agglomeration owing to their partly submerged - well anchored nature (Figure 3.1a) as well as increased activity stemming from strain (Neagu et al., 2017, 2015). Due to these characteristics, such materials have received increased interest and have been successfully employed in both catalytic and electrochemical processes (Liu et al., 2016; Irvine et al., 2016; Kwak et al., 2018; Kwon et al., 2017; Zubenko et al., 2017; Gao et al., 2017; Thalinger et al., 2016; Zhu et al., 2016).

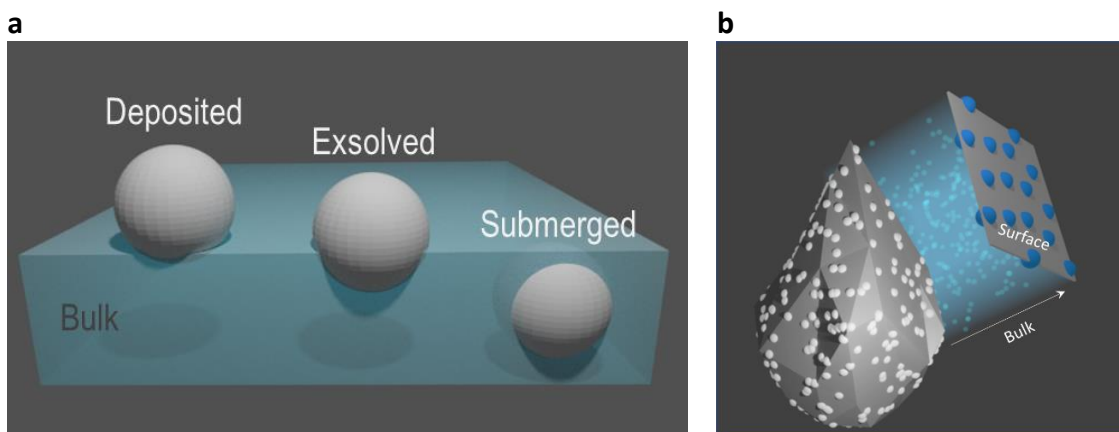


Figure 3.1 Models of systems with particles with different levels of immersion. a) Deposited, surface-exsolved and submerged-exsolved particles as produced by different preparation techniques. b) Model of the proposed composite system with exo-/endo- nanoparticles (Kousi, Neagu, Bekris, et al., 2020).

Here, the focus is expanded from only the surface to the bulk, and the possibility of controllably exsolving nanoparticles under the surface of materials is examined. The exsolution concept is evolved with the aim to grow submerged particles (endoparticles) in perovskite oxides of 100–150 nm particle size (Figure 3.1b). Design parameters are employed for the composition of the perovskite oxide aiming to promote endoparticle exsolution. The resulting composite system's characteristics are investigated and the effect of strain due to endoparticle formation on the system's properties and performance is assessed. The relationship between the composite system's components is revealed and its enhanced activity is showcased by employing it for the challenging selective conversion of methane to syngas. Finally, the applicability and durability of the material is illustrated as it is employed as oxygen carrier for the partial oxidation of methane via Chemical Looping (CLPO).

3.2 Developing a perovskite system with endogenous nanoparticles

For the creation of systems with endogenous nanoparticles, the first step is to employ a set of design principles for the composition and develop a methodology that will effectively promote particle exsolution in the bulk rather than the surface. For the system's composition, a titanate-based perovskite is selected due to its relatively low cation transport (Miyoshi & Martin, 2009) so that the local particle nucleation is promoted instead of the fast mobilisation of the exsolvable anions to the surface. An A-site deficiency is introduced along with a high B-site substitution to promote exsolution and enhance the tendency of metal nucleation in the perovskite lattice. In the composition developed here, the B-site is doped with 0.4 Ni in $\text{La}_{0.8}\text{Ce}_{0.1}\text{Ni}_{0.4}\text{Ti}_{0.6}$ which is equivalent to a 10 wt.% doping of Ni. The reduction temperature and/or duration at which exsolution occurs are also increased in order to overcome the high energy barriers caused by strain and oxide reconstruction around the particle (Gao et al., 2016; Oh et al., 2015) that limit nucleation and growth within the oxide lattice.

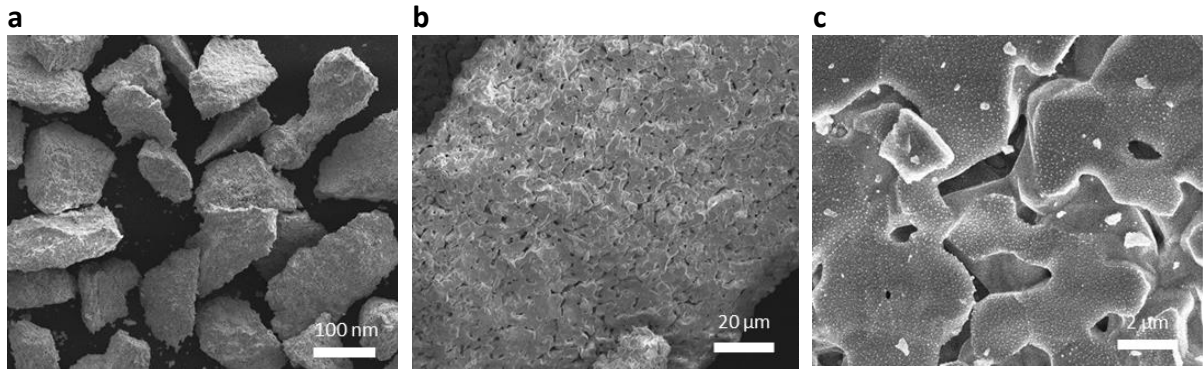


Figure 3.2 **SEM micrographs of powdered $\text{La}_{0.8}\text{Ce}_{0.1}\text{Ni}_{0.4}\text{Ti}_{0.6}\text{O}_3$.** (a) Powder grains after sieving with a particle size of 80-160 μm , (b) Detail of the surface of the powder presented in (a) and (c) Powder surface decorated with exsolved Ni nanoparticles

The perovskite samples are synthesised via the modified solid-state synthesis route described in detail in Chapter 2. The mixed precursors are pressed into pellets and sintered at 1390 $^{\circ}\text{C}$ in order to form the perovskite phase before being crushed and sieved into a powder with a particle size of 80-160 μm (Figure 3.2 a,b). This powder is used throughout this study for all characterisation and testing. Exsolved samples are produced by reducing the $\text{La}_{0.8}\text{Ce}_{0.1}\text{Ni}_{0.4}\text{Ti}_{0.6}\text{O}_3$ perovskite powder in 5% H_2/Ar atmosphere in varying conditions (Figure 3.2c).

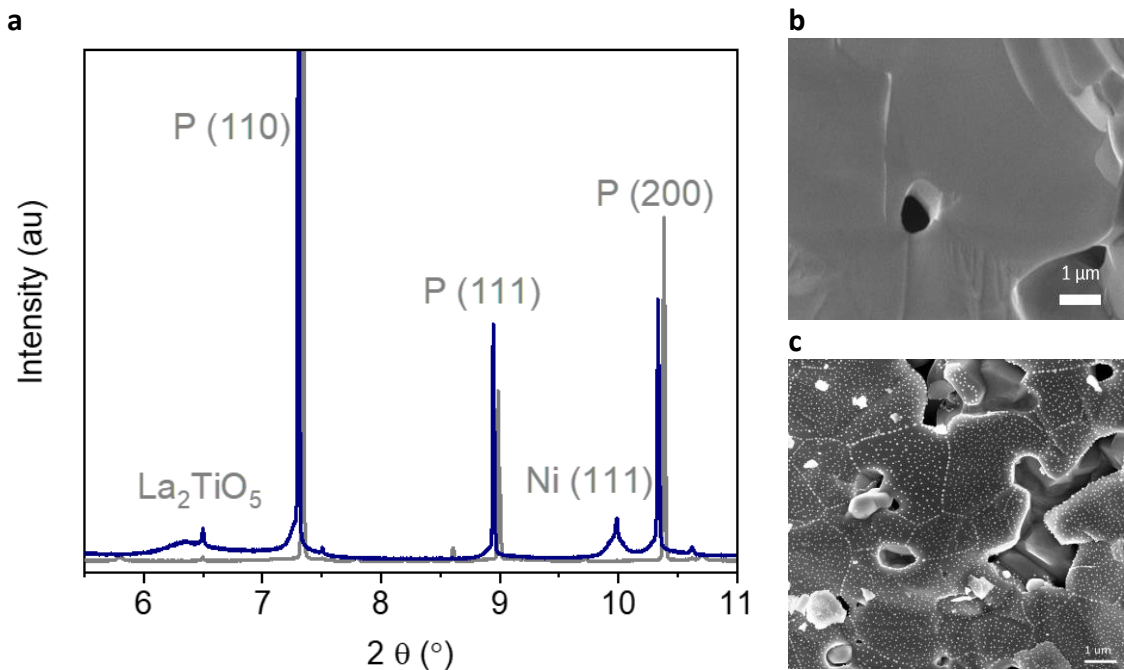


Figure 3.3 **Room temperature Synchrotron XRD patterns and SEM micrographs of the synthesised $\text{La}_{0.8}\text{Ce}_{0.1}\text{Ni}_{0.4}\text{Ti}_{0.6}\text{O}_3$.** a) XRD patterns of the systems in as-prepared state (grey) and post exsolution at 1000 $^{\circ}\text{C}$ for 10 h in 5% H_2/Ar atmosphere (navy). b) and c) SEM images of the surface of the system: (b) Before exsolution and (c) after exsolution.

The structure of the perovskite is examined via powder X-ray diffraction in as-prepared state (after sintering) as well as after the exsolution process has occurred (post reduction at 1000°C for 10h in 5% H₂/Ar atmosphere) and presented in Figure 3.3. The resulting perovskite displays a high degree of crystallinity as illustrated by the sharp peaks in the X-ray diffraction patterns. From the SEM and TEM micrographs presented in Figure 3.4 **SEM and TEM images of the La_{0.8}Ce_{0.1}Ni_{0.4}Ti_{0.6}O₃ system.** (a) Surface of the perovskite after exsolution (b) Cross section of a near surface area of the perovskite after exsolution with endo- and exo- particles visible. Line added to highlight the edge between surface and bulk. (c) TEM image of the bulk in near surface region before exsolution (d)-(e) TEM images of the bulk after exsolution in near surface (d) and only bulk region (e) where embedded nanoparticles are visible (f) TEM images of the perovskite lattice before (left) and after exsolution (right) with lattice models superimposed illustrating the expansion of the perovskite unit cell after endoparticle formation (Kousi, Neagu, Bekris, et al., 2020). It is illustrated that the selected conditions successfully lead to systems with homogeneously dispersed metallic particles on their surface and bulk in a controlled manner. The successful exsolution is also reflected in the XRD pattern obtained post exsolution in which a main perovskite phase, a Ni metal phase and a reflection associated with La₂TiO₅ are identified. The La₂TiO₅ phase forms as a result of the high extent of exsolution achieved with almost all of the substituted Ni being exsolved. This is confirmed by the calculations following. The expected extent of exsolution can be calculated via a mass balance during exsolution.

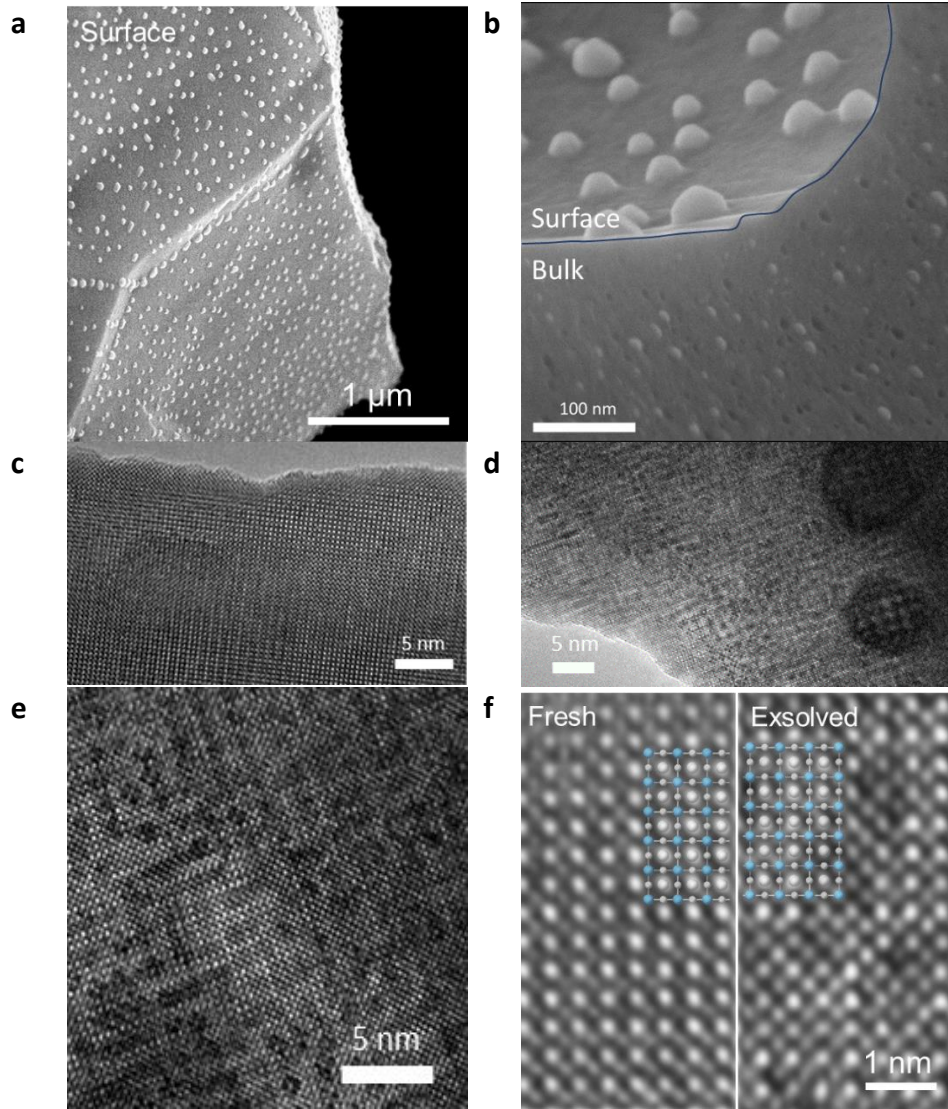


Figure 3.4 **SEM and TEM images of the $\text{La}_{0.8}\text{Ce}_{0.1}\text{Ni}_{0.4}\text{Ti}_{0.6}\text{O}_3$ system.** (a) Surface of the perovskite after exsolution (b) Cross section of a near surface area of the perovskite after exsolution with endo- and exo- particles visible. Line added to highlight the edge between surface and bulk. (c) TEM image of the bulk in near surface region before exsolution (d)-(e) TEM images of the bulk after exsolution in near surface (d) and only bulk region (e) where embedded nanoparticles are visible (f) TEM images of the perovskite lattice before (left) and after exsolution (right) with lattice models superimposed illustrating the expansion of the perovskite unit cell after endoparticle formation (Kousi, Neagu, Bekris, et al., 2020).

For the exsolution of e moles of Ni, the following stoichiometry coefficients can be derived:



Where:

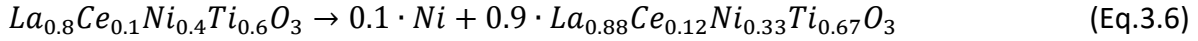
$$a = 0.1 \cdot (11 - 20e) \quad (\text{Eq.3.2})$$

$$b = 0.1 \cdot (-1 + 10e) \quad (\text{Eq.3.3})$$

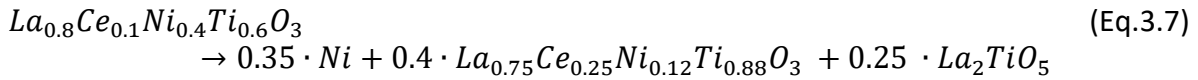
$$x = \frac{1}{(11 - 20e)} \quad (\text{Eq.3.4})$$

$$y = \frac{2 \cdot (-2 + 5e)}{(-11 + 20e)} \quad (\text{Eq.3.5})$$

e is assumed to be $e \leq 0.1$ as this is the amount of A-site deficiency so:



So, 0.1 Ni out of the total 0.4 which was substituted in the B-site is expected to be exsolved and no La_2TiO_5 formation is expected in an only surface exsolution scenario. Here however, from the quantification results from Rietveld refinement (Figure 3.6) it is derived that under the reduction conditions employed, the exsolution of a significantly higher fraction of Ni (e) was achieved. So here $e = 0.35$ which leads to:



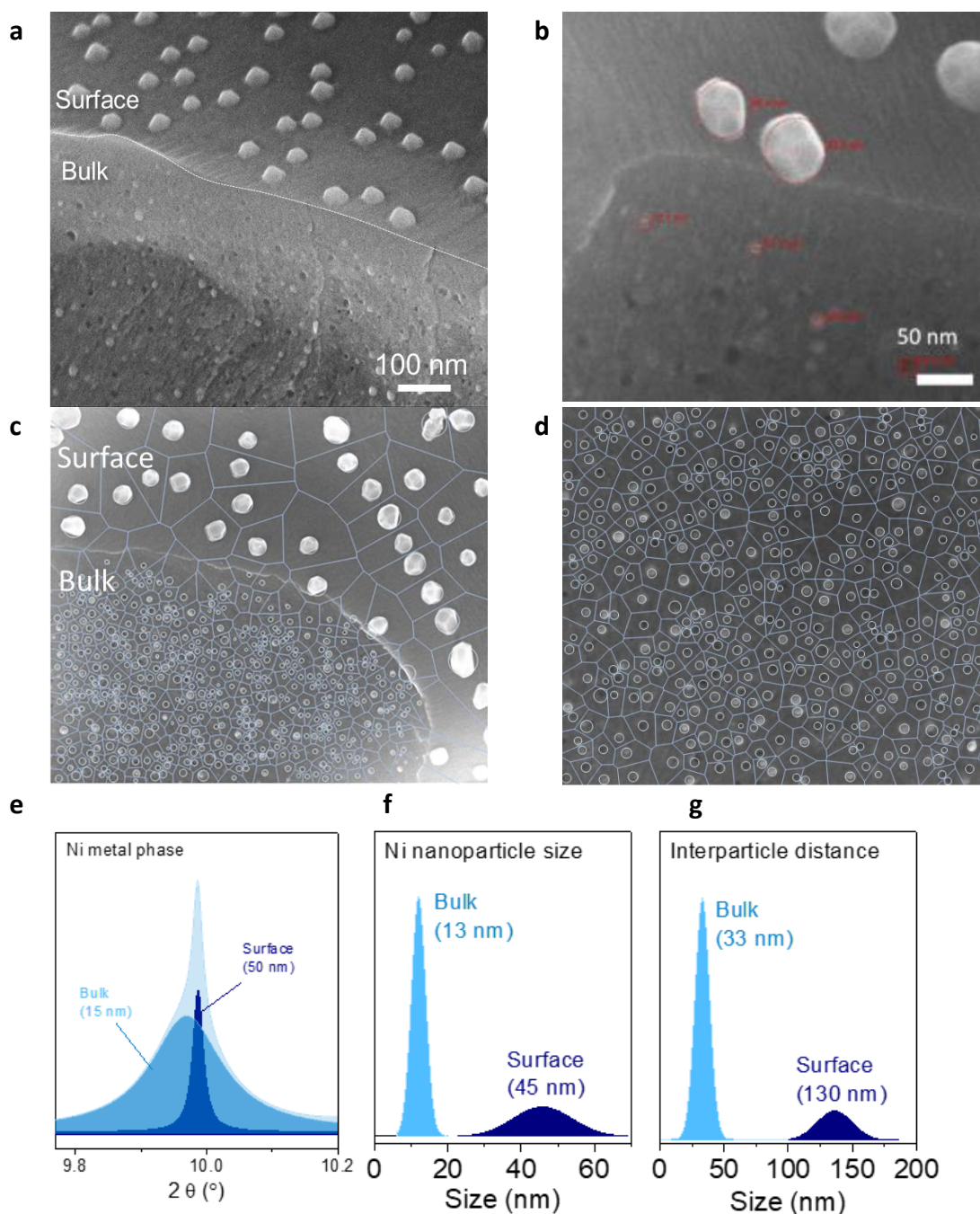


Figure 3.5 Investigation of surface (exo-) and bulk (endo-) exsolved particles. a) Cross-section SEM revealing exo- and endo- particles and their differences in size and population **b)** Measurement of particles on the surface and bulk in near-surface region **(c)-(d)** Voronoi tessellation of the perovskite based on the proximity of exsolved particles. SEM images with Voronoi diagrams superimposed of a **(c)** near-surface region with both endo- and exo-particles are visible **(d)** bulk region containing only endoparticles **e)** Deconvoluted Ni metal peak from the synchrotron XRD diffractogram presented in Figure 3.3 into the contributing surface and bulk particles via Rietveld refinement **f)** Ni metal particle size distribution of **(a)** calculated via image analysis. **g)** Domain size distribution calculated by image analysis on the Voronoi diagram in **(d)** (Kousi, Neagu, Bekris, et al., 2020).

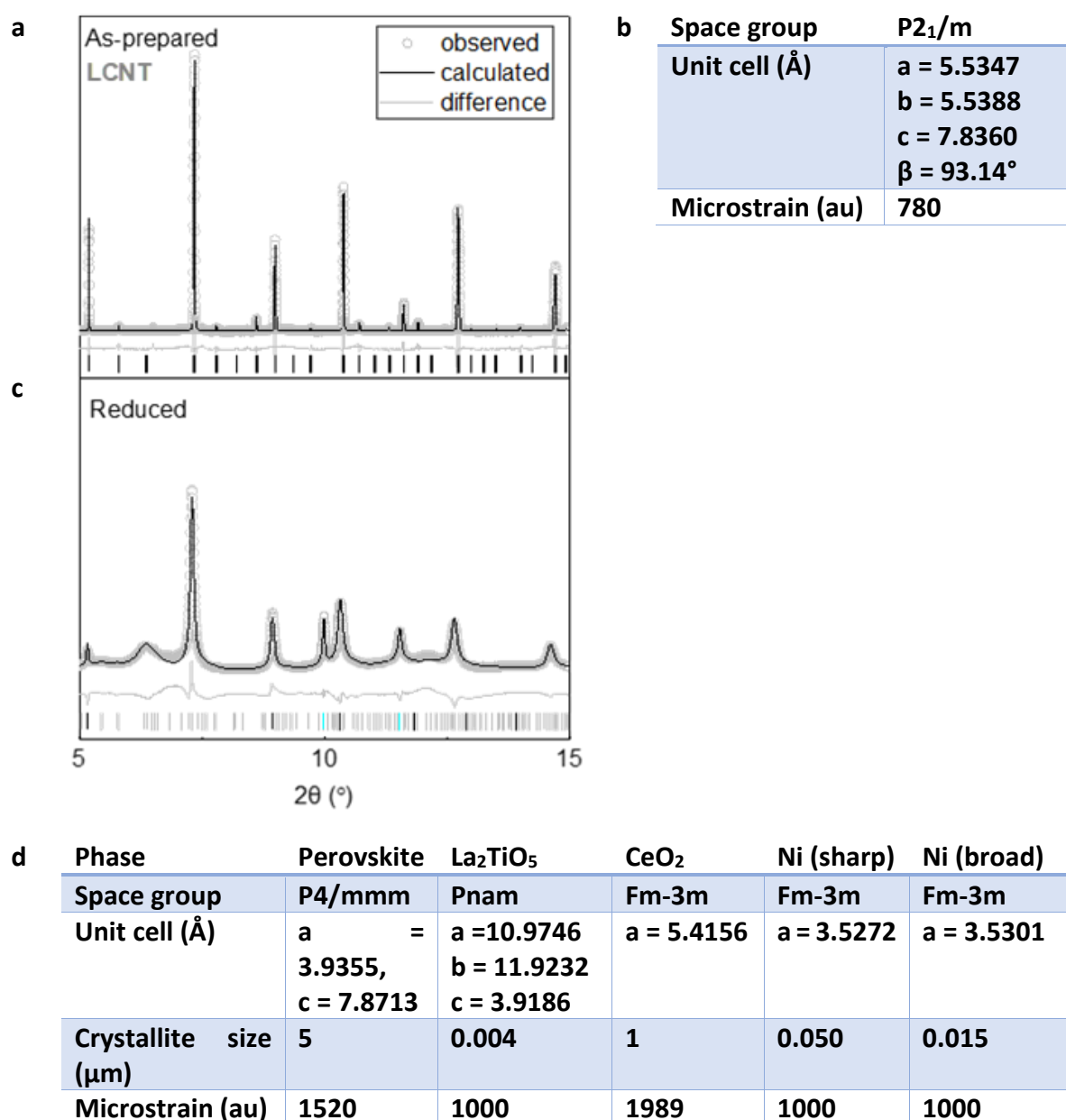
As shown from the above calculations, approximately 0.35 Ni out of the total 0.4 that was substituted in the B-site has been exsolved and for this extreme degree of exsolution, the formation of La_2TiO_5 observed in the XRD is expected. It should be noted that although, via the employed conditions, exsolution of more than 3 times higher than the normally expected was achieved, it still happened in a control manner as highlighted by the XRD, SEM and TEM analysis (Figure 3.3 and Figure 3.4 **SEM and TEM images of the $\text{La}_{0.8}\text{Ce}_{0.1}\text{Ni}_{0.4}\text{Ti}_{0.6}\text{O}_3$ system.** (a) Surface of the perovskite after exsolution (b) Cross section of a near surface area of the perovskite after exsolution with endo- and exo- particles visible. Line added to highlight the edge between surface and bulk. (c) TEM image of the bulk in near surface region before exsolution (d)-(e) TEM images of the bulk after exsolution in near surface (d) and only bulk region (e) where embedded nanoparticles are visible (f) TEM images of the perovskite lattice before (left) and after exsolution (right) with lattice models superimposed illustrating the expansion of the perovskite unit cell after endoparticle formation (Kousi, Neagu, Bekris, et al., 2020).).

Further investigation of the exsolved system via SEM reveals that the particles exsolved on the surface and bulk display big differences in their size and population (Figure 3.5 a,b). The particles exsolved in the bulk are much smaller than their surface exsolved counterparts with diameters of 13 vs 45 nm respectively. This is believed to be linked to the strain that is associated with growing particles in the bulk which are expected to grow smaller according to theoretical calculations which project that the lattice is more likely to accommodate for smaller particles (Gao et al., 2016; Oh et al., 2015). Further analysis confirms this as it unveils more differences in the unit cell parameters and degree of strain of the two and is discussed in depth in the following subchapter. Additionally, the endoparticles exhibit a much higher population at 1000 vs 100 particles μm^{-2} , respectively.

Due to this extremely high population density the bulk exsolved nanoparticles are in nanoscale proximity of each other thus maximising the exerted strain induced on the perovskite lattice. The interparticle distance is calculated from a Voronoi tessellation of their spatial arrangements and determined to be of the same order of size as the particles at approximately 13 and 33 nm, respectively. By comparing the surface and bulk exsolved Ni particles to standard Ni metal (3.5168 Å) it is found that the exo- particles are strained by 0.29% (3.5272 Å), while the endoparticles are, as expected, even more strained at 0.37% (3.5301 Å). Microstrain is also induced on the perovskite matrix ABO_3 from the high particle population of the bulk particles which is found to be roughly twice as high as compared to that of the initial perovskite (Figure 3.6). This is also visualised by the peak broadening in Figure 3.3a and quantified via Rietveld refinement of the as-prepared and reduced/ exsolved samples (Figure 3.6).

The difference in size and population of exo- and endo- nanoparticles is also showcased in the shape of the Ni peak obtained by the X-ray synchrotron diffraction pattern (Figure 3.3a). The peak is deconvoluted and found to consist of a sharp tip and a broad base curve. The sharp tip is assigned to the larger, surface exsolved particles while the broader peak to the smaller, bulk-exsolved particles (Figure 3.5e). The assignment of the peaks was done by chemically removing (etching with HNO_3) the exo-particles and comparing the resulting XRD

diffraction pattern of the etched sample to that of the original. The resulted XRD pattern of the etched sample was identical to that of the un-etched sample but focusing on the Ni peak was found that the sharp peak was missing, thus indicating that the sharp peak is representative of the presence of particles on the surface. This analysis is presented and discussed in depth in the following chapter where the effects of the systems characteristics on activity are discussed (Subchapter 4.3). X-ray data were also quantified by Rietveld refinement revealing the overall system's degree of exsolution is approximately 8 wt. % Ni metal which corresponds to almost all of the substituted Ni being exsolved with 0.35 mol Ni per mol rABO₃ being exsolved (Figure 3.6, Appendix A). 85% of the exsolved Ni corresponds to the particles in the bulk. The system can be visualised to be comprised of 1 wt.% of 45 nm Ni particles on its surface and 7 wt.% of 13 nm Ni particles present in the bulk. The high ratio of endo- to exo-particles highlights that the set of the design principles introduced during the design stage successfully led to enhanced particle formation in the bulk as opposed to the surface.



Wt. %	46.1	45.2	0.4	1.3	7.0
--------------	-------------	-------------	------------	------------	------------

Figure 3.6 Rietveld refinement of the fresh (a,b) and reduced-exsolved (c,d) samples. For (a) wR = 17% and (c) wR=18% (Appendix A) (Kousi, Neagu, Bekris, et al., 2020).

From the analysis above, it is showcased that the methodology developed here enables the production of composite perovskite-metal particle systems with nanoparticles on the surface and in the bulk. The systems developed are self-nanostructured with the nanoparticles emerging upon exsolution after strategic compositional design and exsolution conditions selection and self-strained due to the extent of exsolution and the highly populated from particles bulk. These characteristics make the system promising for exhibiting emergent properties such as enhanced bulk oxygen storage and transport which can enable the connection between the buried bulk particles and the gas stream and eventually leading to enhanced functionality (Cho et al., 2016; MacManus-Driscoll et al., 2008).

3.3 Controlling material strain and oxygen exchange by controlling the release of endoparticles

Having observed the microstrain induced on the perovskite matrix ABO_3 as a result of the high population of endoparticles, a series of experiments is designed aiming to investigate microstrain development and its effect on the systems oxygen capacity and transport capabilities. The first objective is attempting to control microstrain by controlling the conditions in which the reduction of the material takes place, as through this it is possible to control the extent of exsolution and characteristics. By employing different protocols such as different reduction temperatures and/or durations the overall degree of exsolution of the embedded metal can be controlled as well as resulting particle characteristics such as size, interparticle distance and population. To prove this, a series of samples was prepared ranging from a sample that exhibited only surface exsolved particles, to samples with increasingly higher content of exsolved metal nanoparticles in their bulk. To produce the said samples the materials were reduced at 900 °C for 0, 10 and 30 h and at 1000 °C for 10 h. As illustrated by the SEM micrographs in Figure 3.7 the chosen reduction conditions successfully lead to samples with different surface and bulk particle characteristics. In detail, from the SEM photos it is revealed that all samples have exsolved surface nanoparticles while the submerged nanoparticle content increases from none to progressively higher (Figure 3.7). Further study of the surface via SEM reveals that the interparticle distance is controlled by the reduction temperature, with the distance between nanoparticles being smaller at lower temperatures, while the size of the nanoparticles is controlled by the duration, with nanoparticles growing bigger with increasing time (Figure 3.7).

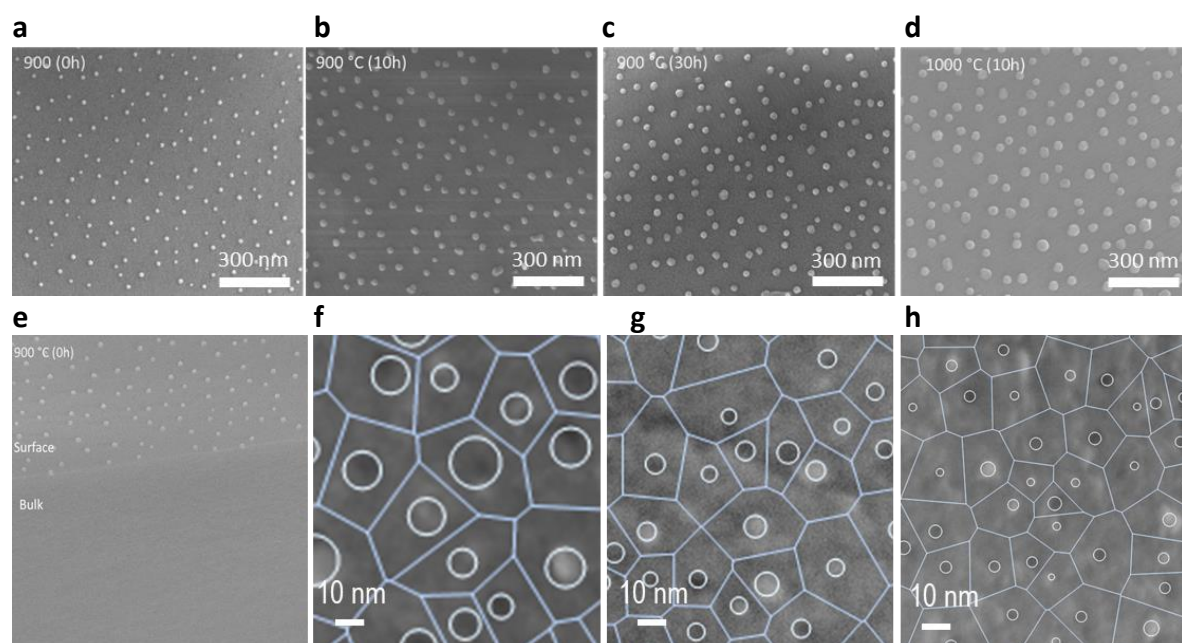


Figure 3.7: SEM micrographs of samples reduced at 900 °C for 0, 10 and 30 h and at 1000 °C for 10 h. (a)-(d) Overview of surface exsolved particles, (e) View of the surface and bulk of the sample reduced at 900 °C for 0 h where endoparticles did not form (f)-(h): Submerged nanoparticles with superimposed Voronoi tessellation of their spatial arrangement of the samples presented in b, c and d (Kousi, Neagu, Bekris, et al., 2020).

By analysing the phase and microstructure of the resulting samples via XRD, it is confirmed that particles in the bulk can actually form at reduction temperatures as low as 900 °C, provided that the reduction duration is enough, as showcased by the growing Ni peak (Figure 3.8a, b). Quantification of the peak via Rietveld refinement reveals that in all cases the overall weight fraction of the endoparticles surpasses that of the surface particles as calculated and compared in Figure 3.8c as Ni_S and Ni_B . The size of the submerged nanoparticles across the prepared samples varies from ~ 3.5 to ~ 6.5 and to ~ 13 nm, while the corresponding interparticle distance ranges from ~ 20 to ~ 25 and to ~ 33 nm, respectively (Figure 3.8c). While bulk nanoparticles exhibit extreme variations across the samples it should be noted that the difference in exoparticle size and population of the corresponding samples is significantly smaller (Figure 3.7).

Aiming to gain a better understanding on the effect of these parameters on oxygen capacity and oxygen exchange, the oxygen uptake of the different samples is measured as they are being oxidised under the same conditions. Since the surface exsolved particles have similar characteristics across all samples, and more importantly their weight fraction is much smaller than that of the bulk exsolved ones, it is assumed that surface exchange kinetics are similar. Thus, any difference observed on the oxygen uptake experiments will be a result of the relative oxygen diffusivities within the bulk. The experiments are conducted in a TGA and the results are presented in Figure 3.8d. The sample with only surface particles exhibits a very low oxygen capacity and exchange rate which is characteristic of such perovskite titanate systems. On the other hand, both oxygen capacity and oxygen exchange are significantly higher for the bulk exsolved systems and increase even higher as the embedded metal content increases. At

the same time, the temperature on which oxygen exchange initiates decreases as endoparticle content increases revealing that both oxygen capacity and exchange ability are improved by the presence of particles in the bulk.

The effects observed above are quantified by fitting the oxygen uptake data with a logistic function (Eq. 3.8) which is characteristic of such oxidation processes and by plotting the corresponding oxygen capacity (ζ_G , mol O per mol perovskite) and time constants (τ , h⁻¹) associated with oxygen exchange rate (Figure 3.8c).

$$wt = \frac{w}{1+e^{\tau(t-t_s)}} \quad (\text{Eq. 3.8})$$

As expected, by comparing Ni_B and ζ_G on the resulting figure the oxygen capacity of the samples increases proportionally with the exsolved metal content. However, when comparing Ni_B and τ it appears that the oxygen exchange rate does not correlate with the endoparticle content, but rather it seems to be much more strongly related to parameters such as size and interparticle distance of the bulk particles and in particular their ratio as illustrated by τ and s/d in Figure 3.8c. However, this is not something not expected, as such parameters are usually closely related and indicative to the strain that the particles exert on the host lattice. Nevertheless, by plotting the oxygen exchange data in an Arrhenius plot it is revealed that the activations energies recorded here are characteristic of perovskite oxide systems, but with the values being closer to values reported for perovskites with oxide-ion diffusivities higher than titanates (De Souza, 2015). This observation suggests that although the perovskite appears to still be responsible for oxygen exchange mediation between endo- and exo- particles, its oxygen transport ability has been augmented by the strain introduced to the lattice by the bulk exsolved nanoparticles.

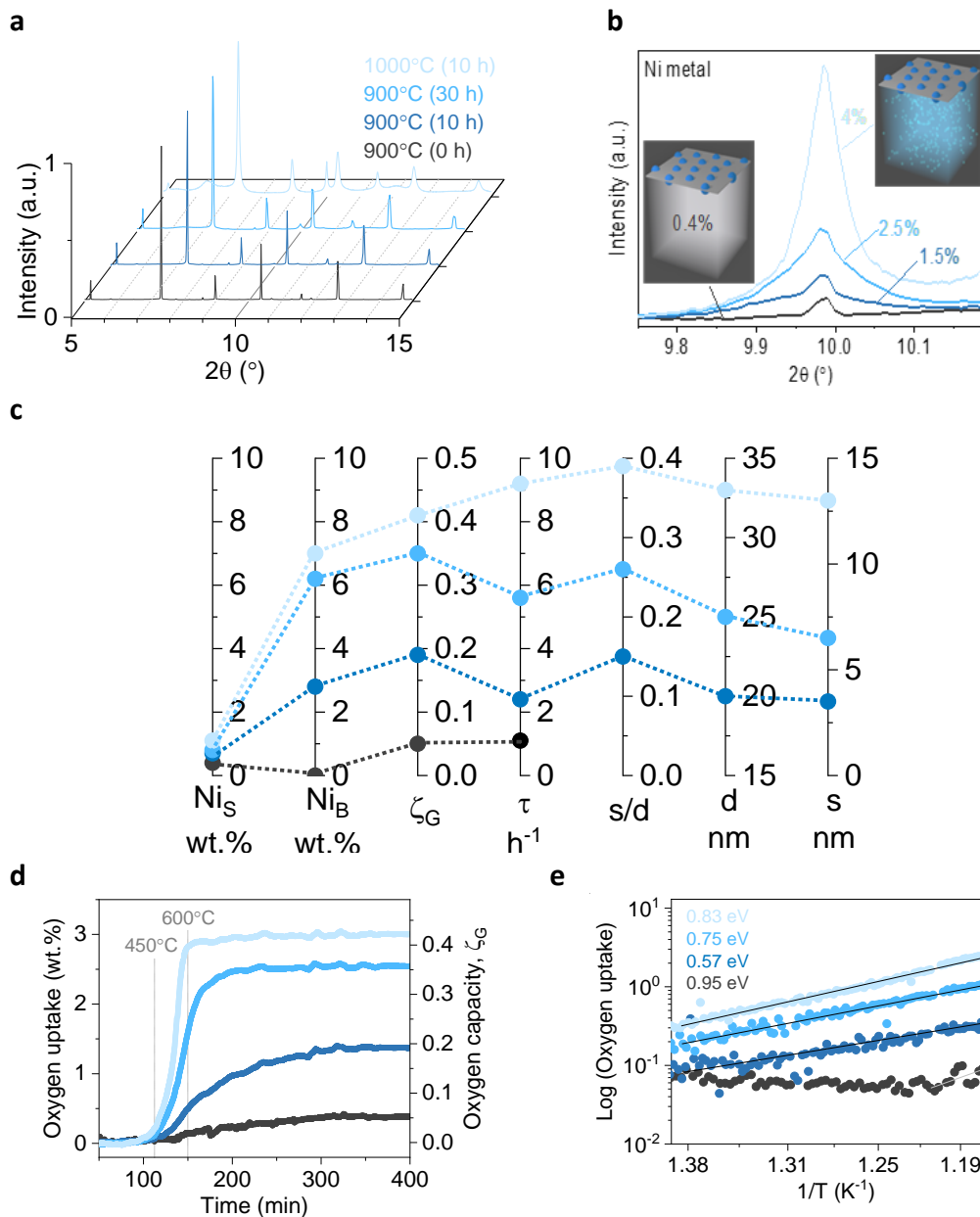


Figure 3.8: Controlling bulk exsolution, strain and oxygen capacity and exchange. a) Synchrotron XRD diffractograms of samples reduced at 900 °C for 0 h (dark grey), 10 h (dark blue) and 30 h (blue) and at 1000 °C for 10 h (light blue). b) Detail of the diffractogram presented in (a), focusing on the Ni peak and corresponding total (surface and bulk) Ni content (wt.%) calculated via Rietveld refinement. c) Parallel axes plot for the systems presented in (a) for the Ni metal content at the surface (Ni_S , wt.%) and in the bulk (Ni_B , wt.%) both calculated via Rietveld refinement of the data from (a), oxygen capacity (ζ_G , mol O per mol of perovskite), time constant of oxygen exchange calculated by fitting the data shown in (d) with a logistic function (Eq. 3.8) (τ , h^{-1}), ratio of the average endoparticle diameter (s) and average interparticle distance between endoparticles (d), average endoparticle diameter (s , nm) and average distance between neighbouring bulk particles (d , nm, Figure 3.7). d) Oxygen uptake from the oxidation experiment via TGA and corresponding oxygen capacity (mol O per mol of perovskite) as a function of time, up to a temperature of 600 °C, for the samples presented in (a). e) Arrhenius plot corresponding to the data presented in (d) and calculated activation energy for oxygen transport (Kousi, Neagu, Bekris, et al., 2020).

3.4 Further increase of strain through reversible oxygen incorporation

Having witnessed the effect strain can have on the oxygen capacity and exchange capabilities of the system, the next objective was to attempt to augment this effect in view of further improving performance. This is achieved by exploiting the different redox expansion rates of the perovskite and Ni phases (Yuan et al., 2019). Post oxidation, the Ni lattice expands by approximately 15% due to oxygen incorporation. However, when the perovskite phase is oxidised oxygen is incorporated in the oxygen vacancies of the perovskite resulting to an almost negligible alteration of the lattice dimensions. These are then dominated by the charge of the B-site ions which increases, leading to an overall contraction of the unit cell of <1% (Bishop et al., 2014).

In order to gain better understanding of the process, the extent of the oxygen re-incorporation and its effect to the strain of the perovskite lattice, the oxygen uptake is monitored via gas composition analysis as a function of temperature while also monitoring the structure of the perovskite in real time via synchrotron X-ray. Subsequent Rietveld refinement of the synchrotron data allows the extraction of information about the structural changes of the perovskite matrix that is then correlated to the gas composition data and presented in Figure 3.9. As temperature rises from room temperature (RT) to ~400 °C the system (perovskite and Ni particles) only appears to undergo thermal expansion with the two phases behaving as two individual phases as it becomes evident by their thermal expansions. The expansion of Ni was consistent with reported values of $1.34 \times 10^{-5} \text{ }^\circ\text{C}^{-1}$ and the expansion of the rABO_3 matrix was $0.94 \times 10^{-5} \text{ }^\circ\text{C}^{-1}$, which is as well characteristic of reported similar systems (Villars & Hulliger, n.d.; Neagu & Irvine, 2010). At 400 °C, the Ni metal phase starts to oxidise as illustrated by the decrease of its fraction from 8 to 4 wt.% and close to 550 °C the expansion of the unit cell of the perovskite appears to happen at a faster rate as indicated by the increase in the slope. Interestingly, this is not the behaviour one would expect as the residual perovskite lattice, at this point, is expected to contract as it is being oxidised (Bishop et al., 2014; Moreno et al., 2014). Therefore, it is concluded that for this to happen the lattice expansion from Ni to NiO should account for the lattice expansion of the perovskite observed. Thus, it appears that the two phases of the system previously acting individually are now connected. In addition, at the same temperature range, the degree of macrostrain in the perovskite matrix increases approximately 6 times Figure 3.9d while the crystal and grain structure is maintained (Figure 3.10). Upon reaching 600 °C the process has concluded and further increase in temperature does not appear to cause any further changes in the structure.

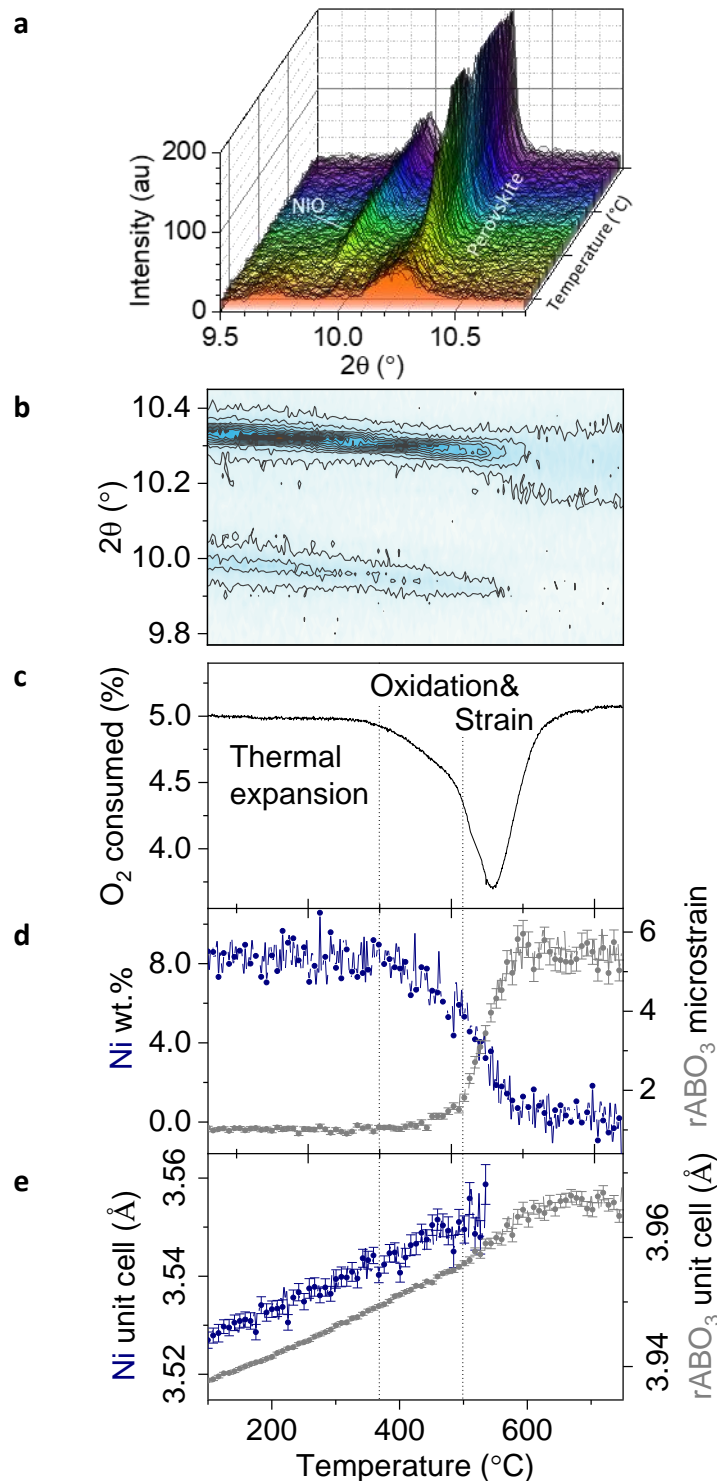


Figure 3.9 **Increasing strain levels to unlock oxygen ion exchange.** **a)** Synchrotron XRD data acquired during the temperature programmed oxidation of a system with submerged nanoparticles presented in 3D plot as a function of diffraction angle, time, and scan number. **b)** XRD data from (a) presented in a 2D plot as a function of diffraction angle, time, and corresponding temperature. **c)** O₂ (%) consumption during experiment(a). **d–e)** structural information calculated from (a) by Rietveld refinement showing: **d)** Ni metal content and rABO₃ microstrain (relative to the initial, reduced state value) as a function of time and temperature and **e)** Unit cell parameter of the Ni metal and rABO₃ phase as a function of time and temperature (Kousi, Neagu, Bekris, et al., 2020).

Post oxygen re-incorporation the sample was analysed via XRD revealing that all the Ni metal had been successfully converted to NiO while still retaining its socketed nature as presented in (Figure 3.9d, Figure 3.10b), while the La_2TiO_5 phase was found to remain unchanged (Figure 3.10a), and the crystallographic alignment between the bulk particles and the perovskite was preserved (Figure 3.10c). It should be noted here that the high increase in microstrain achieved by this process is maintained during the following redox cycles causing an increase of 15% of the oxygen exchange time constant τ .

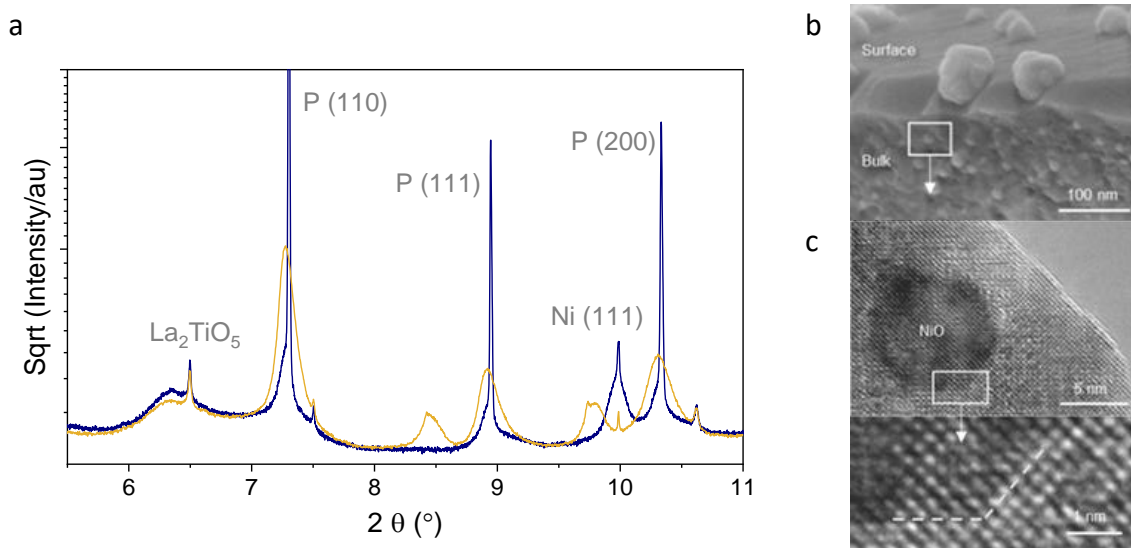


Figure 3.10 **Structure and surface of the system post increasing strain via oxygen incorporation by a temperature programmed oxidation experiment.** **a)** Room temperature synchrotron XRD diffractograms of the system before (navy) and after (yellow) the TPO showing the change in the Ni and perovskite peaks while the La_2TiO_5 remains unchanged. **b)** SEM image of a cross section of the sample after the TPO **c)** TEM image and detail of the sample after post oxidation highlighting the crystallographic alignment between perovskite host and a NiO endoparticle. The dotted line follows the perovskite-particle interface.

It is concluded that via the methodology developed a system with submerged nanoparticles was successfully created exhibiting enhanced oxygen capacity largely stemming from its submerged nanoparticles, the presence of which also leads to enhanced oxygen exchange abilities as a result of the strain they induce in the perovskite lattice.

3.5 Employing an exsolved system with endo- exo- nanoparticles for methane activation

Aiming to demonstrate the advanced capabilities of the developed exo- endo- system it is employed for the activation of methane. The performance of the low surface area ($\sim 1 \text{ m}^2 \text{ g}^{-1}$) exo- endo- system is compared, on a weight basis, to that of a high surface area ($\sim 100 \text{ m}^2 \text{ g}^{-1}$) Ni/ Al_2O_3 sample, state of the art for methane conversion (Papadopoulou et al., 2012), with similar loading of overall metal particles (10 wt.%, $\sim 8 \text{ nm}$ size) as synthesised and calculated via Rietveld refinement of its XRD pattern (Figure 3.11). The large difference in surface area between the two samples stems from the fact that in the bulk-exsolved system, as discussed above, most nanoparticles are in the bulk, while on the deposited sample all metal is located on its surface. Methane conversion and product selectivity are continuously monitored as a function of temperature and the resulting MTPR profiles are presented in Figure 3.12.

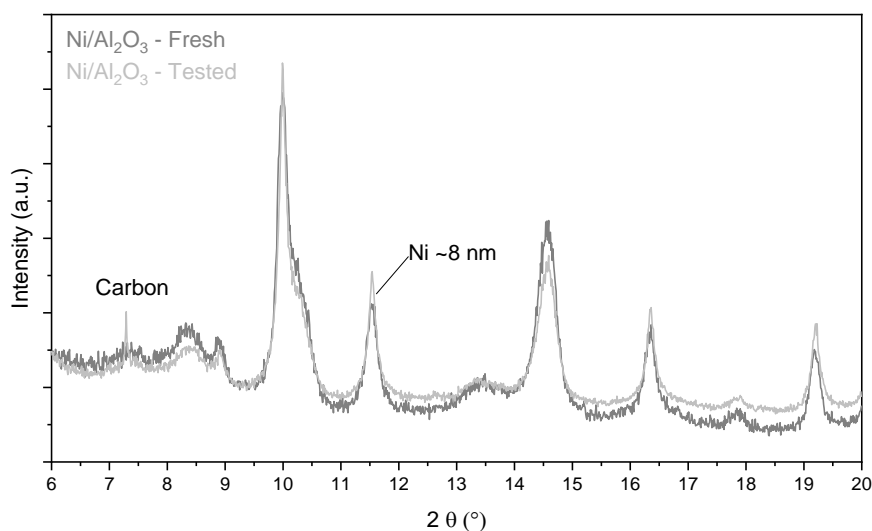


Figure 3.11 Room temperature synchrotron XRD diffractogram of Ni/Al₂O₃ before (Fresh) and after (Tested) being employed for the activation of methane.

The endo/exo- system activates methane at 550 °C with an activation profile comprised of a sharp consumption peak followed by a broader one at 600 °C, in a narrow temperature window. Product selectivity is high consisting of syngas, with the desirable for synthetic fuel production (Pakhare & Spivey, 2014), H₂:CO ratio of 2:1 (Figure 3.12a, b). The activation profile of the Ni/Al₂O₃ sample is similar although methane activation commences 50 °C higher despite its large surface area and thus abundance of active sites. Additionally, the reference sample's selectivity suffers greatly with only the first peak of its profile corresponding to gaseous products and its second peak, which spreads for over 100 °C, corresponding to methane cracking (Figure 3.12b). This is determined to be a result of the converted NiO to Ni metal particles, acting as sites for carbon deposition after their reduction from the reactant CH₄ stream (Papadopoulou et al., 2012). This is not observed in the Ni-rABO₃ system as this mechanism is suppressed due to the socketed and aligned nature of the surface exsolved Ni nanoparticles. This is consistent with previous reports where coke formation was found not to occur on exsolved nanoparticles exposed in hydrocarbon environments (Neagu et al., 2015). Overall, the bulk-exsolved sample was found to be highly selective towards syngas with a selectivity reaching 87% while the reference Ni/Al₂O₃ exhibited 88% selectivity towards carbon deposition (Figure 3.12b). Carbon deposition was further examined by oxidising the tested samples and monitoring the release of CO₂ via temperature programmed oxidation (TPO) (Figure 3.13). The difference between the two samples is striking with the deposited carbon on the Ni/Al₂O₃ sample beginning to oxidise to CO₂ from 300 °C in the form of three peaks (Figure 3.13a). These peaks are determined to correspond to three different types of carbon deposited and upon quantification of the total deposited species it, deposition is calculated to be 98 mg_{carbon}/mg_{sample} (Figure 3.13b). On the other hand, and as expected, the exsolved sample shows no carbon deposition.

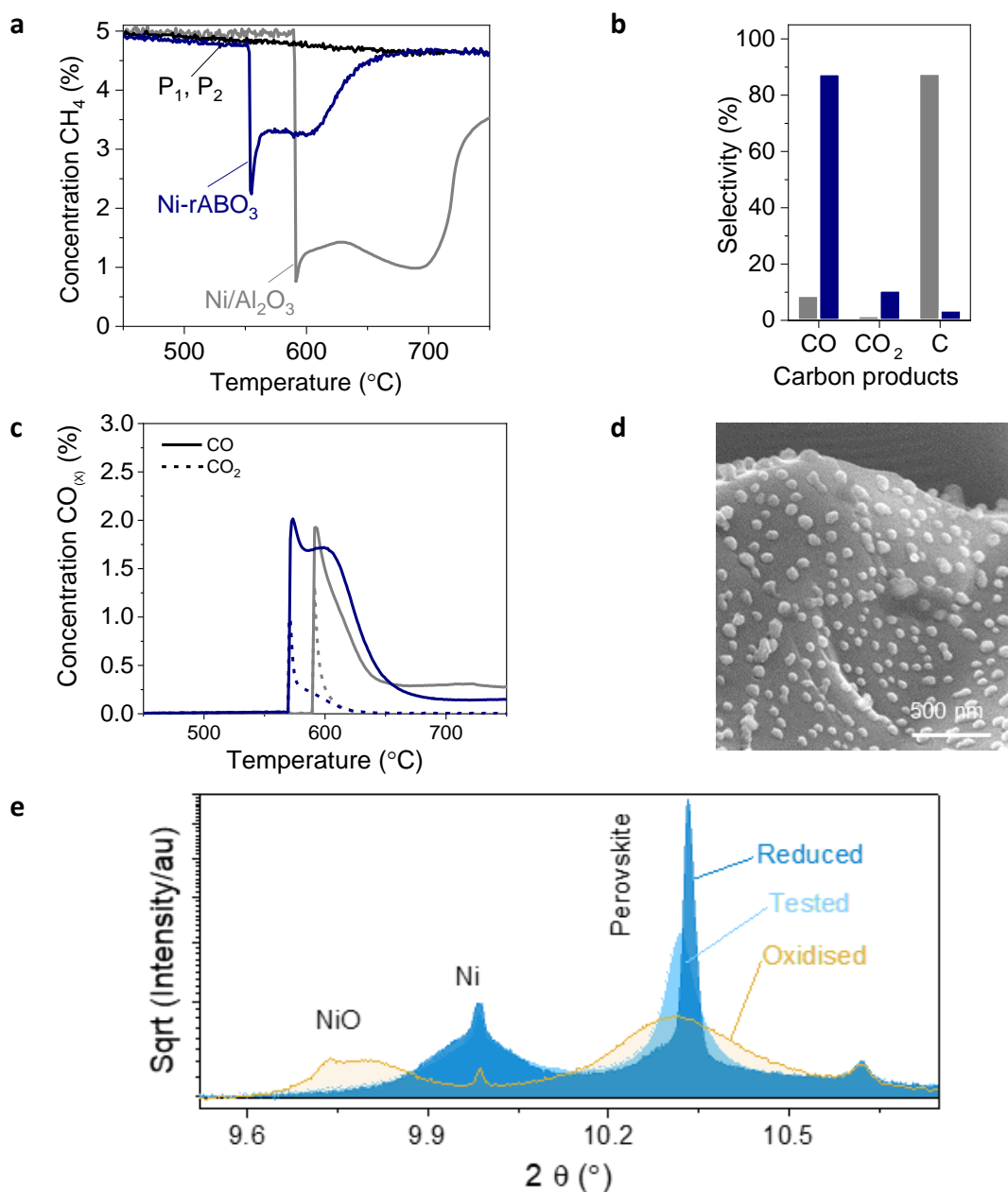


Figure 3.12 **Employing a system with exo-/endo- particles for the activation of methane.** a) Methane consumption as a function of temperature (MTPR) for various systems (150 mg of sample tested): Ni/Al₂O₃ (grey) (SSA ~ 100 m²/g), system with exo-/endo- exsolved particles, Ni-rABO₃ (navy) (SSA ~ 1 m²/g) containing nanoparticles exsolved on the surface and in the bulk, and P1 and P2 (black), representing a sample with only surface particles and one with only bulk particles (all surface particles were removed via etching), respectively. (b) Selectivity to carbon containing products corresponding to the experiment described in (a). (c) Carbon containing products produced during the experiment described in (a). (d) SEM image of the surface of the exsolved sample after the experiment described in (a), (e) Room temperature XRD data for Ni-rABO₃ at different stages: fresh (reduced/exsolved), post oxidation (before testing) and after testing for CH₄ activation in the TPR experiment described in (a).

The excellent performance of the exo/ endo system is assumed to be a result of its components and their ability to work synergistically. Aiming to deconvolute the contribution

of each component of this composite system, two new samples are produced. These samples are variants of the submerged system with the first having its surface nanoparticles removed and its bulk nanoparticles preserved while the second having only surface nanoparticles. The system with only bulk particles exhibited no activity (P_1 in Figure 3.12a), demonstrating that surface nanoparticles are essential for enabling methane activation. The system with only surface nanoparticles was also found to be inactive in the examined temperature window (P_2 , Figure 3.12a) proving that surface nanoparticles alone are not sufficient for promoting methane conversion since due to the absence of bulk exsolved nanoparticles the materials oxygen capacity is low. However, in Ni-rABO₃'s case where both surface and bulk particles are present, the two appear to work synergistically with the bulk NiO particles being actively involved in the catalytic transformation of CH₄, being converted to Ni metal, even though they are located as deep as tens of μm under the surface. This is showcased via XRD as presented in Figure 3.12f where the Ni and NiO peaks of the sample are compared between its oxidised state (before testing) and after. The NiO peak is shown to disappear as the Ni peak forms again after testing, to the same levels it was after its reduction, prior its oxidation. Moreover, it is calculated that the NiO to Ni phase change is responsible for 85% of the conversion to oxygenated products, with the rABO₃ support being responsible for the rest due to its oxygen capacity. More importantly, due to its highly strained nature the rABO₃ matrix is able of mediating oxygen transfer between the submerged particles and their surface counterparts which are responsible for CH₄ activation. This is also confirmed by comparing the activity of systems with a varying bulk nanoparticle content in the next chapter where conversion is found to increase with increasing bulk nanoparticle content and consequently strain as discussed in detail in Chapter 4. As presented above, when reduced, Ni nanoparticles strain expansively, while when oxidised, as when employed for methane conversion, it is the perovskite that is strained expansively as the unit cell parameter of the NiO is $\sim 7\%$ larger than that of the perovskite. This expansive (referred to as tensile in the cited report) strain has been reported to augment oxygen exchange ability (Markus et al., 2013). Furthermore, the oxygen vacancy content of the perovskite oxide is also enhanced due to the presence of the embedded nanoparticles which can also lead to improved oxygen exchange. The oxygen capacity of the perovskite (ζ_p) can be calculated by subtracting the, calculated from Rietveld refinement, oxygen capacity of the surface and bulk particles (ζ_x), from the oxygen capacity of the entire system (endo-, exo- particles and perovskite host) calculated by TGA (ζ_G). For the system used here (maximum endoparticle content) the calculated oxygen capacity of its components are: $\zeta_G=0.41$ $\zeta_x=0.31$ $\zeta_p=0.10$ while for a system with no endoparticles the corresponding values are: $\zeta_G=0.05$ $\zeta_x=0.0.1$ $\zeta_p=0.04$. This reveals that the oxygen vacancy concentration of the perovskite is increased by a factor of 2.5 as a result of endoparticle formation. Besides oxygen capacity and more importantly, upon submerged particle formation the strain of the perovskite increases by a factor of 2 and by a factor of 6 after the first oxygen incorporation. This shows that the main factor which contributes towards the augmented oxygen transport observed is strain.

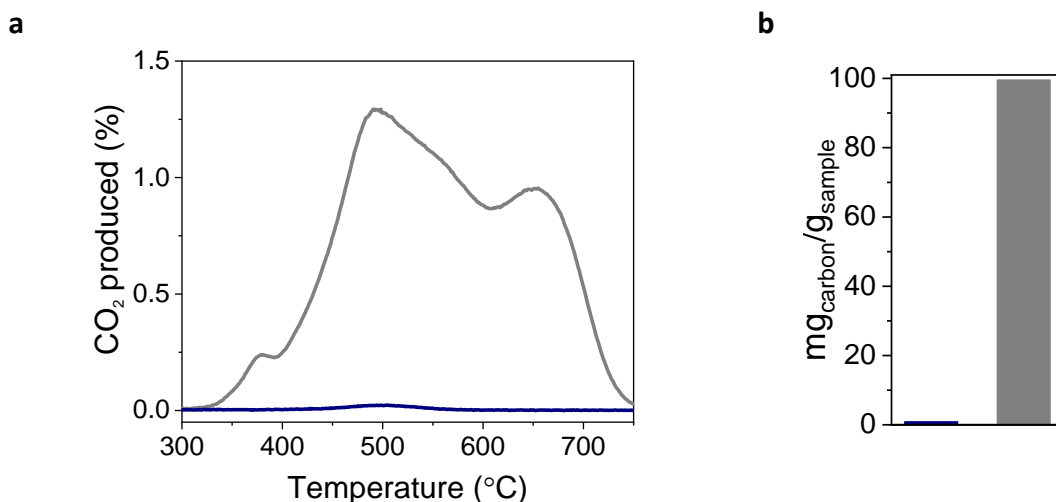


Figure 3.13 Carbon deposition after the MTPR experiment described above, measured by temperature programmed oxidation of Ni/rABO₃ (Navy) and Ni/Al₂O₃ (Grey). **a**) CO₂ produced during the oxidation of the deposited carbon as a function of temperature, revealing the amount and type of carbon. **b**) Quantified released carbon from the two systems (Kousi, Neagu, Bekris, et al., 2020).

It is thus concluded that the exo/endo-system developed here behaves kinetically as if all its NiO nanoparticles are on the surface, but because in fact they are buried in the perovskite bulk, the oxygen release happens in a controlled manner leading to the highly selective production of syngas observed (Mihai et al., 2012).

3.6 Operando mechanistic insight of methane conversion with an exo/endo- exsolved system
 Aiming to gain a deeper insight on the contribution of the different components of the system under reaction conditions, the methane activation process is monitored operando. Gas composition is analysed continuously and combined with real time structural information as obtained via Rietveld refinement of obtained synchrotron X-ray data (Figure 3.14). Post analysis the process is divided into five distinct stages (Figure 3.14b, c). From room temperature (RT) to 500°C the system is undergoing thermal expansion with the thermal expansion coefficients of the two phases (rABO₃ and NiO) appearing not to be correlated at $\sim 1.06 \times 10^{-5} \text{ } ^\circ\text{C}^{-1}$ for rABO₃ and $\sim 1.29 \times 10^{-5} \text{ } ^\circ\text{C}^{-1}$ for NiO (Neagu & Irvine, 2010). In the following stage, at $\sim 550 \text{ } ^\circ\text{C}$, methane activation commences, and the sharp methane activation peak is found to coincide with the decrease of the NiO fraction from ~ 10.3 to 9 wt.%. This decrease corresponds to the amount of NiO that has been calculated to be on the surface. This indicates that the first sharp peak of the activation profile is correlated to the surface particles of the system and this is also confirmed by the previous observation made above of a similar sharp peak in the profile of Ni/Al₂O₃ as well as in literature on similar exsolved samples where all Ni particles were present on the surface (Otto et al., 2019). In depth analysis and discussion on the methane activation profile of such exsolved system will follow in the next chapter. At the same time, the unit cell parameter of the perovskite matrix also increases rapidly, characteristic of the rABO₃ being reduced by methane. This is assumed to be facilitated by the now formed Ni metal surface particles, as they have been fully reduced from NiO at this point after reacting with methane, but with the O²⁻ ions now supplied by the perovskite (Eq. 3.8).

This supply of O^{2-} ions to the Ni particles creates vacancies in the perovskite lattice (Eq. 3.9) which, in turn, act as hopping sites for oxygen transport to the surface. At the same time, the unit cell of the perovskite is expanded due to the release of electrons in the lattice which decrease the oxidation state of the B-site ions (Eq. 3.10) resulting in the observed sharp increase of the unit cell parameter.



The third observed stage stretches across a 50 °C temperature window for 10 minutes, with the unit cell parameter of the perovskite remaining relatively unchanged while the NiO endoparticles are now being gradually reduced and converted to Ni. The CH_4 converted during this stage yields almost pure syngas with the previously reported 2:1 $H_2:CO$ ratio and showcased again in Figure 3.14b. However, the behaviour of the unit cell parameter of the perovskite (remaining almost constant) is interesting, since one would expect that it should actually keep increasing due to the perovskite being reduced further and if not from that a rise should have been observed only due to thermal expansion. This indicates that the lattice contraction resulting from the transition of 15% NiO to Ni is so great that it actually affects the perovskite lattice and compensate for is thermal expansion to the point that it negates it making the unit cell parameter appear as remaining constant. Thus, the components of the system now appear to work as a unit rather than individually (as indicated by their uncorrelated thermal expansions) as they were in the 1st stage of the process. The fourth stage begins at the point where all the submerged NiO has been converted. At this point an increase larger than the one observed in the 1st stage of the process is observed in the slope of the unit cell of the perovskite, implying that the perovskite is now being reduced as well as thermally expand and contributes to the conversion of the final amount of methane. Upon completion of the conversion, the slope of the unit cell parameter of the $rABO_3$ returns to values corresponding to only thermal expansion.

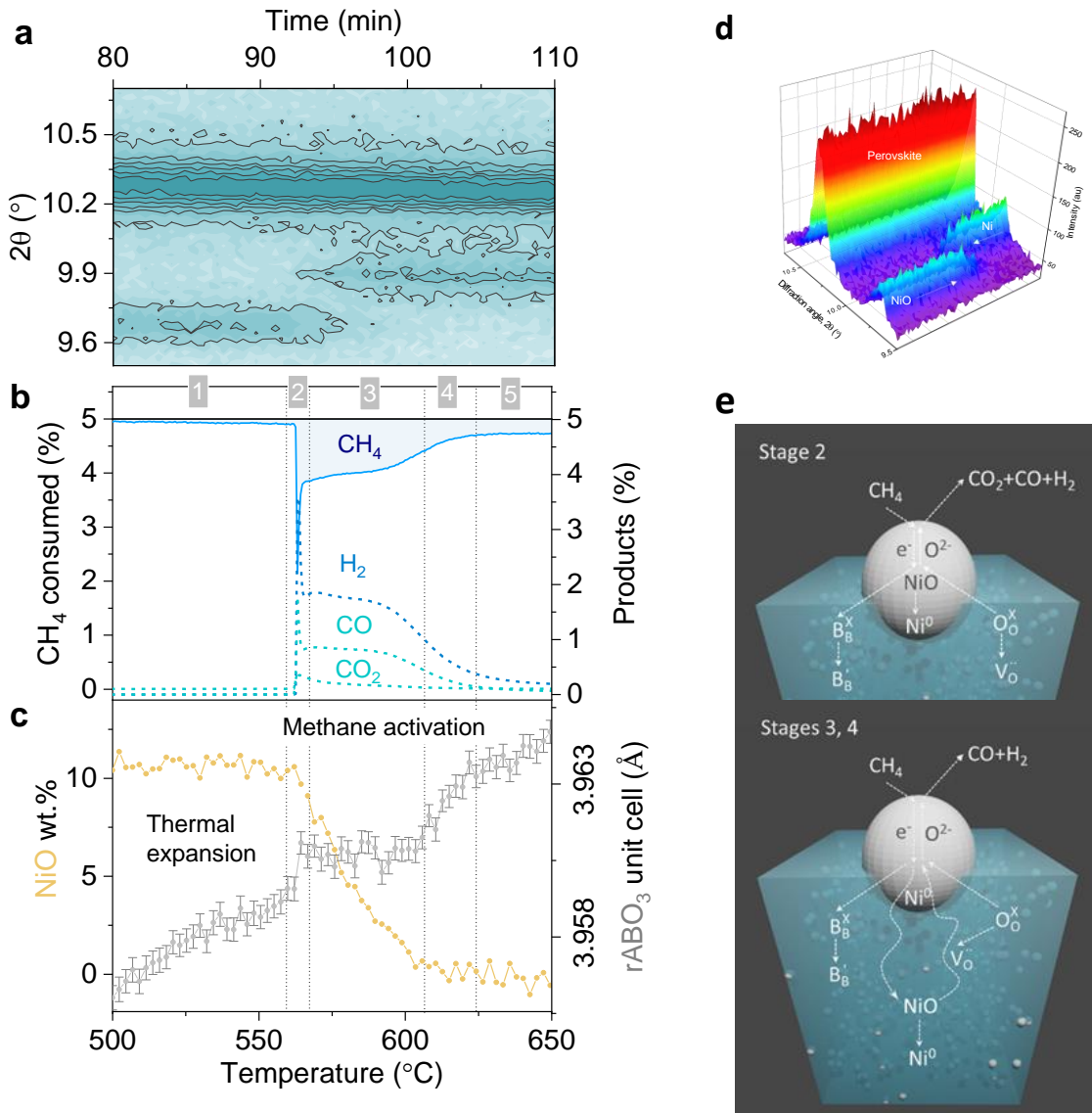


Figure 3.14 **Operando insight into the mechanism of methane conversion with a system with exo-/endo-nanoparticles.** a) Synchrotron XRD data of the system acquired during the temperature programmed reduction under 5% CH₄ in 2D, as a function of diffraction angle, time and corresponding temperature (presented in (c)); the plot is aligned with (b) and (c). b) CH₄ conversion to H₂, CO₂, CO products during the TPR experiment described in (a). c) NiO content and perovskite unit cell parameter calculated by Rietveld refinement of the data presented in (a) and plotted as a function of time (presented in (a)) and temperature. d) XRD data of (a) presented in 3D showcasing the transition of NiO to Ni during the TPR experiment described in (a). e) Schematic of the methane conversion mechanism corresponding to the stages identified during the experiment described in (a) (Kousi, Neagu, Bekris, et al., 2020).

3.7 Operando mechanistic insight of methane conversion via chemical looping partial oxidation with an exo/endo- exsolved system

In view of the applicability of the system as an oxygen carrier, the catalytic redox performance and structure is investigated operando during isothermal cycling (Figure 3.15). The cycling temperature selected is at 650 °C, as this was the temperature at the end of the activation window as observed in the previous experiment Figure 3.14b. The system is cycled between

CH₄ and O₂ with the reduction cycle being 10 min while the oxidation cycle 5 min. The system is found to be capable of operating reversibly, transitioning between the two cycles while retaining highly selective yields, remaining coke free and showing no signs of degradation such as cracks which often occur under cycling conditions (Figure 3.19d). Rietveld refinement of the data reveals that the oxidation of the system happens in less than 1 minute, while its reduction is slower, taking approximately 6 min to complete (Figure 3.15). Moreover, from the phase analysis presented in Figure 3.17 and Figure 3.15a,c it is unveiled that the endoparticles do not redissolve into the perovskite during their oxidation, as they cycle between their reduced and oxidised state, as the fraction of the NiO remains the same and equal to its starting value even after consecutive redox cycles. It should also be noted here that it is also found that the perovskite matrix strain remains the same throughout cycling and to the same levels created by the first oxidation (Figure 3.15).

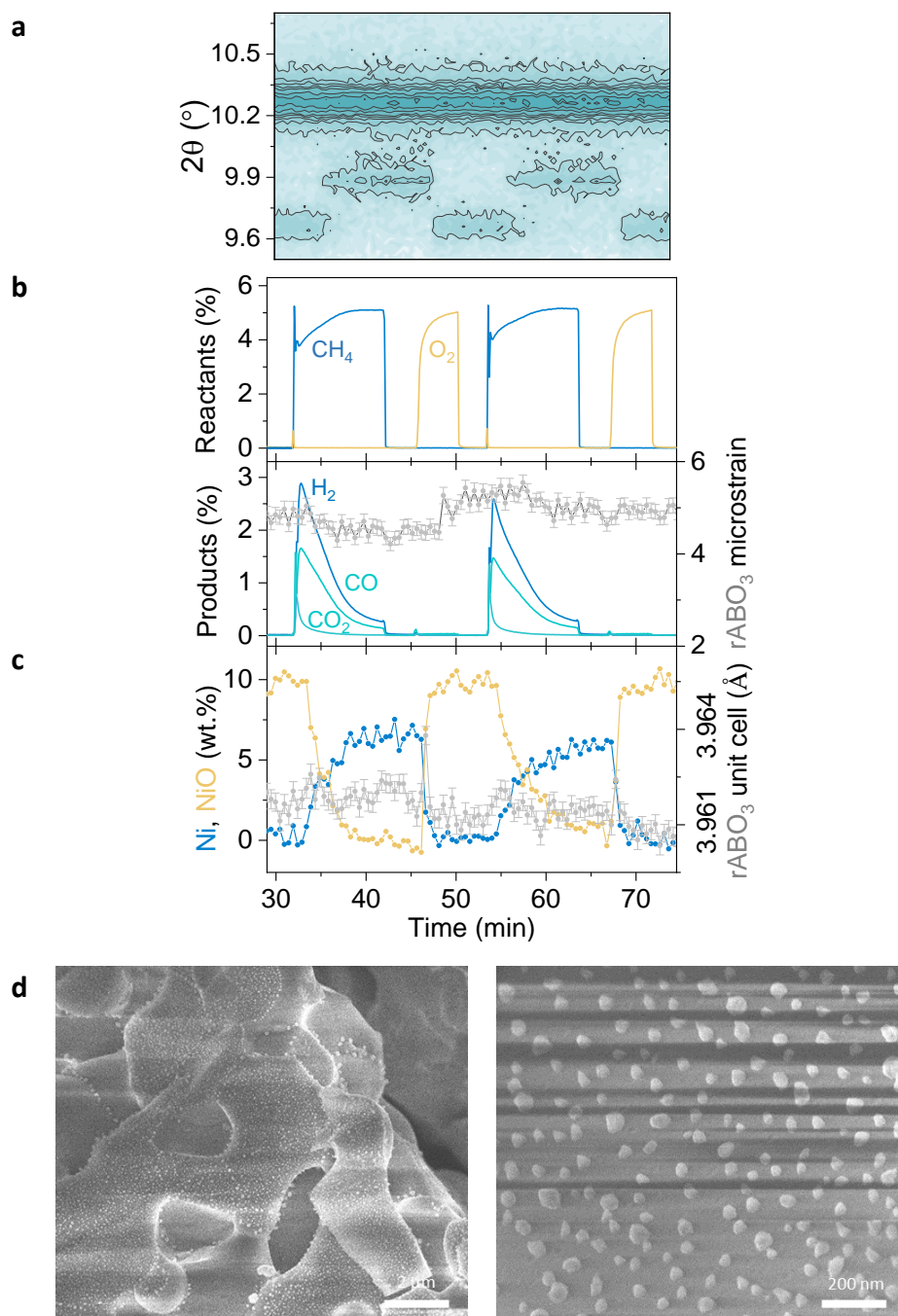


Figure 3.15 **Operando insight into the mechanism of methane conversion via chemical looping partial oxidation with a system with exo-/endo-nanoparticles.** a) Synchrotron XRD pattern of the system in operando under cycling between redox feeds of 5% CH₄ and 5% O₂ at 650 °C. b) Composition of reactants (CH₄ and O₂) and products (H₂, CO, CO₂) obtained by gas analysis at the outlet during cycling experiment described in (a) and microstrain of rABO₃ during cycling calculated from Rietveld refinement, c) Calculated Ni and NiO wt.% and rABO₃ unit cell during cycling, d) SEM micrographs of the micro- and nano- structure of the sample post cycling (Kousi, Neagu, Bekris, et al., 2020).

Having proved the system's cycling ability at low temperatures, experiments were conducted aiming to compare the exsolved system's performance to that of a more traditional/ non-exsolved perovskite based OCM. For this, the Pechini sol-gel method was employed for the

synthesis of $\text{La}_{0.8}\text{Sr}_{0.2}\text{MnO}_3$ (LSM821) aiming to utilise Mn's reactivity against methane to achieve a comparable performance. LSM821 was successfully synthesised, crushed and sieved to the desired particle size of 80-160 μm and pre-treated under similar condition to those of the exsolved system. Reduction was done in 5% H_2/Ar at 900°C and oxidation in Air at 600 °C. The produced sample displayed a more porous microstructure to that of the exsolved system which is considered beneficial (Figure 3.16c). Upon testing via TPR the sample appears to start activating methane at low temperatures with conversion increasing as temperature increases but remaining low overall. Additionally, selectivity is found to be poor, with methane being converted almost exclusively to CO_2 initially and selective conversion commencing at much higher temperatures. TPO conducted post reaction also reveals carbon deposits on the sample while, most importantly, SEM images of the surface post testing reveal significant degradation of the material after just one redox cycle (Figure 3.16d). In view of all the above, and the fact that cycling for LSM821 to be selective should commence in much higher temperatures, the enhanced performance of the exo/ endo- system is showcased and further comparison with the exsolved between the two systems under cycling conditions was not pursued.

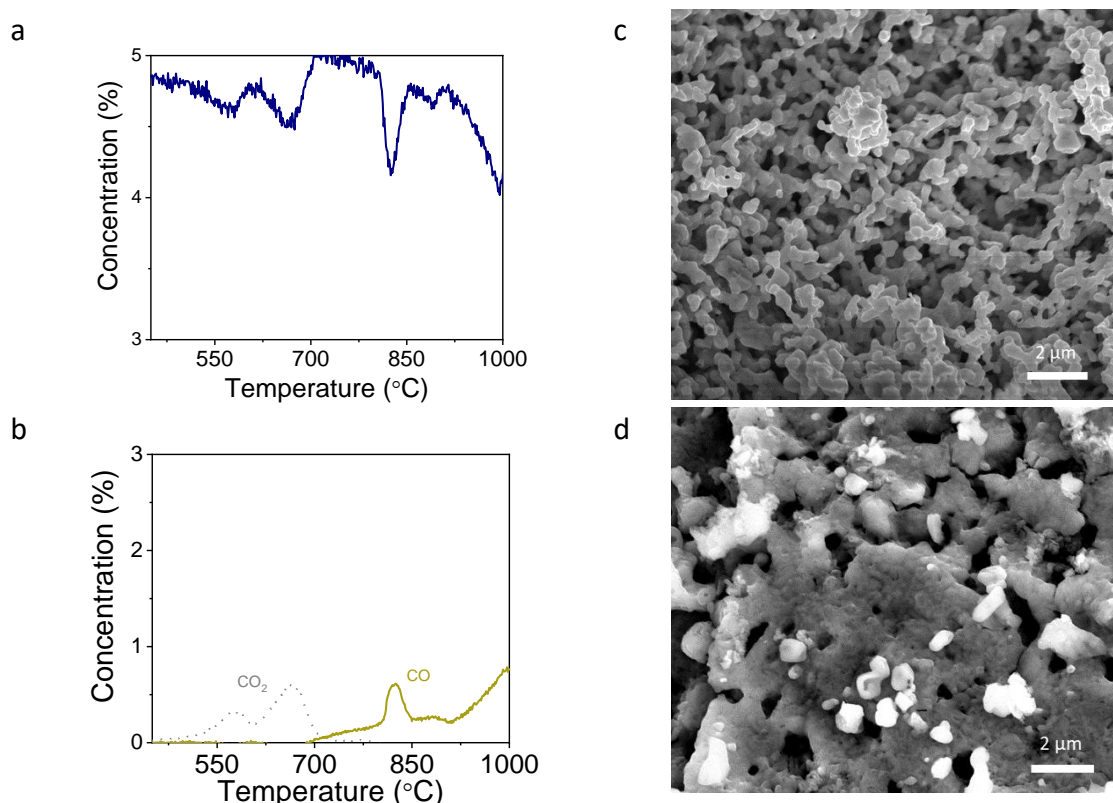


Figure 3.16 $\text{La}_{0.8}\text{Sr}_{0.2}\text{MnO}_3$ (LSM821) employed for the conversion of methane. a) Methane consumption and b) selectivity to carbon products against temperature. Sample microstructure c) before testing and d) after testing.

3.8 Application of the developed exo/endo- exsolved system as an oxygen carrier for the partial oxidation of methane via chemical looping

Having investigated the short-term cycling ability of the system the next step in order to showcase its true potential as an oxygen carrier, is employing it in a series of experiments for the chemical looping partial oxidation of methane (CLPO). The system is tested under varying

conditions aiming to determine suitable operating conditions (Figure 3.18). 150 mg of material is loaded into the reactor in its oxidised state and cycled between feeds of 5% CH₄/He and 5% O₂/He. Two temperatures are selected for testing (570 and 650 °C) corresponding to the middle and end of the activation window, respectively, as observed in the TPR experiments above. The cycling time was also varied (5- 10 min half cycles, 5 min half cycles presented in Figure 3.17) aiming to extract more information on its effect on the system's activity and selectivity as function of contact time.

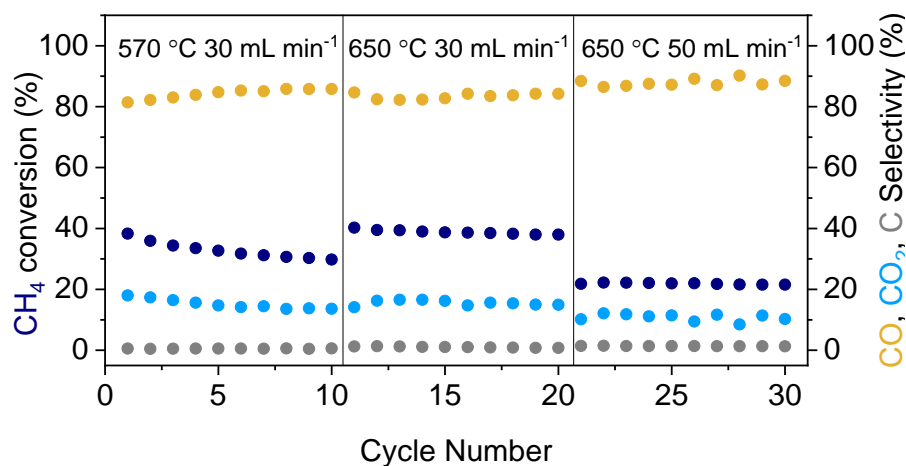


Figure 3.17 **Survey of Chemical looping partial oxidations cycling conditions.** Conversion (left axis) and selectivity (right axis) as a function of cycle number, using an endo-/exo- particle system at different temperatures and flow rates. 150 mg of sample were used and cycled between 5% CH₄/He and 5% O₂/He (Kousi, Neagu, Bekris, et al., 2020).

The system is found to remain highly selective regardless the operating temperature with the selectivity to CO varying from 80 to 90% between the two. This is not surprising since selectivity was determined to stem from the endogenous particles which in both conditions remain accessible and thus able to mediate selectivity. The overall conversion appears to increase at higher temperatures and with longer contact times. Across all experiments the sample remains coke free with the selectivity to carbon deposition being lower than 1%.

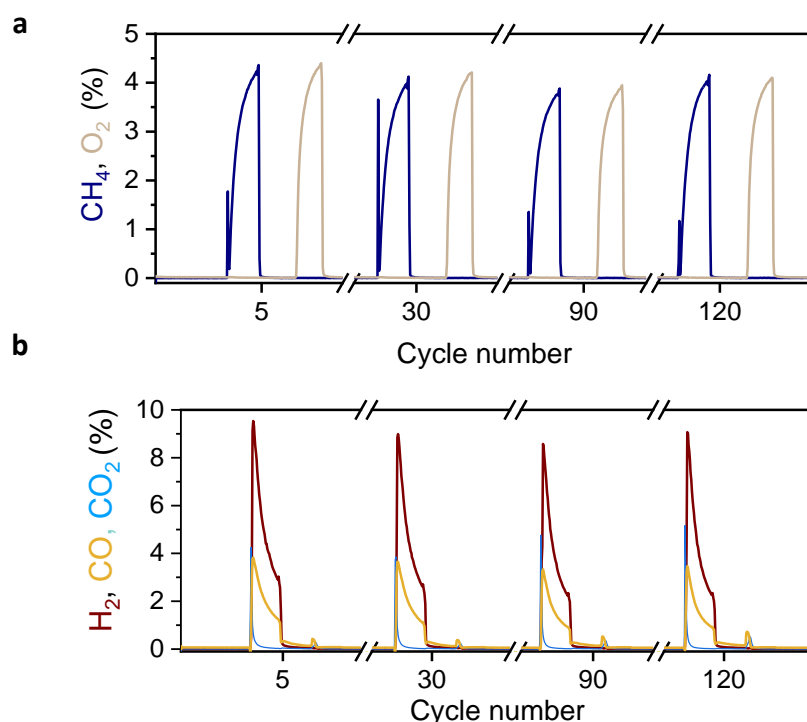


Figure 3.18 Long term stability test of a system with exo/endo-particles employed for the conversion of methane via chemical looping partial oxidation at 570 °C using 300 mg of sample, over 130 cycles. a) Conversion of reactants and b) product selectivity as a function of cycle number.

Aiming to test the stability of the system under long-term cycling, double the amount of sample is used (300 mg) and the experimental conditions are set at 570 °C and 30 mL min⁻¹ (NTP). Selectivity remains stable for over 130 cycles at over 80%. Overall conversion starts at 70% and stabilises at 55% after 90 cycles (Figure 3.19a) while carbon deposition is kept under 1% throughout the experiment (Figure 3.19c). Selectivity to products also remains high and stable throughout the experiment with overall production dropping slightly, consistent with the observed drop in conversion (Figure 3.19b, c). Post cycling the microstructure of the system is examined via SEM. Overall, the system's microstructure remains intact after 130 cycles and its nanoparticles both exo- and endo- are retained (Figure 3.19d- f). It observed that the average size of submerged nanoparticles increases by approximately 10% while smallest nanoparticles of diameter under 5nm seem to have disappeared (Figure 3.19 g,e). Comparing the systems performance to that of materials in literature under similar mass to flow ratios, the system developed here is found to achieve similar conversion and selectivity but at temperatures of 300 °C lower and over a longer number of cycles showcasing the systems enhanced performance and stability (Zeng et al., 2018; Dai et al., 2006; Zhu et al., 2018).

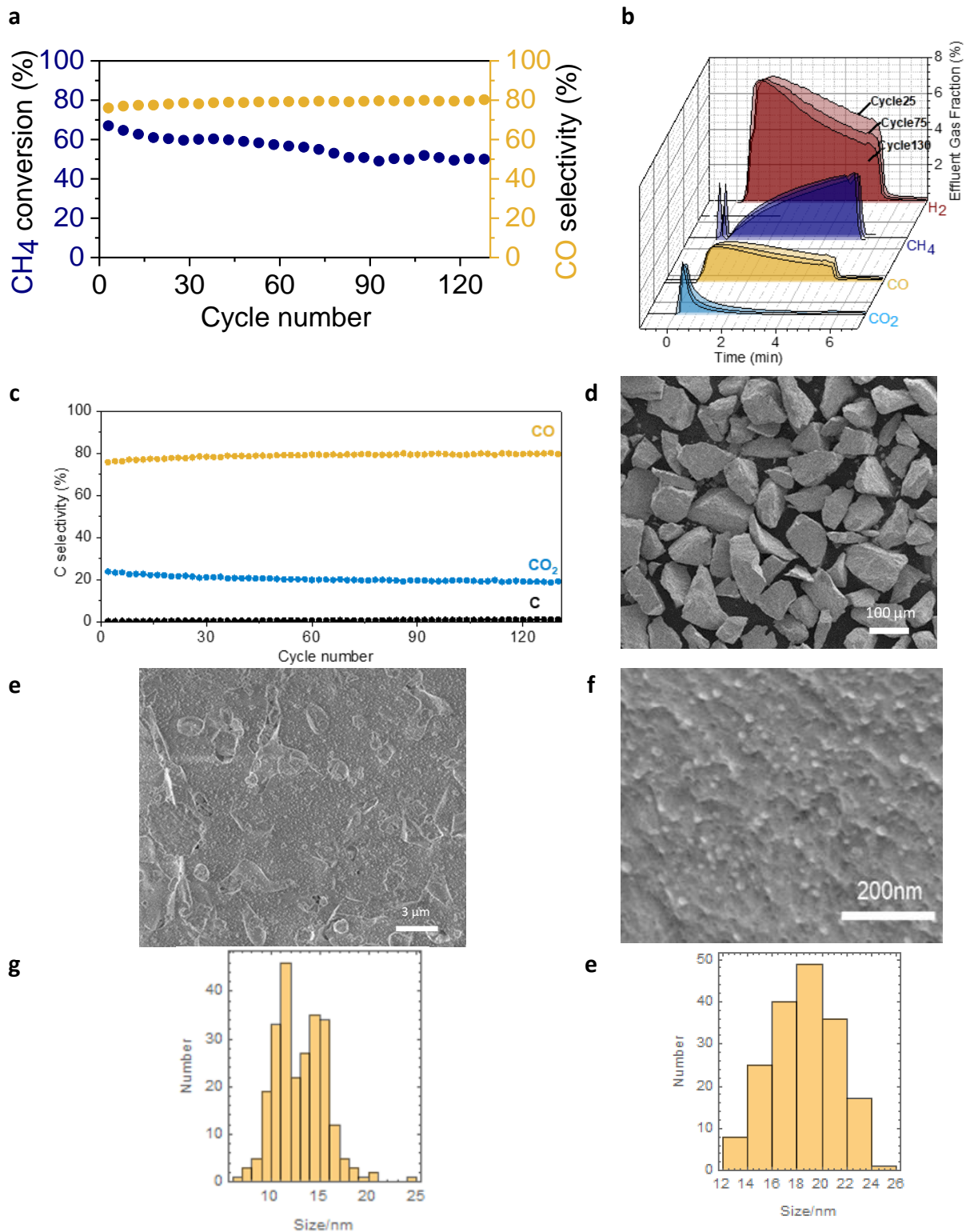


Figure 3.19 Long-term cycling of a system with exo-/endo- particles for the conversion of methane via Chemical Looping partial oxidation using 300 mg of sample, over 130 cycles. a) CH₄ conversion and selectivity to CO against cycle number. b) Difference in consumption of reactants and selectivity to all products between cycles 25, 75 and 130, c) Selectivity to carbon products against cycle number.

d-f) SEM micrographs of the micro- and nano- structure of the sample post 130 cycles, d) Microstructure of the sample intact, e) exoparticles and f) endoparticles preserved post 130 cycles with the nanoparticles preserved. Particle size distribution before (g) and after (f) cycling in their oxidized state (Kousi, Neagu, Bekris, et al., 2020).

3.9 Conclusions

The results presented in this chapter showcase the capability of growing endogenous metallic nanoparticles within a perovskite matrix in a controllable manner. The exsolution concept is employed and evolved to grow homogenous metallic nanoparticles throughout the bulk of a perovskite oxide host. High degrees of exsolution were achieved leading to a system where almost all the embedded metal was exsolved to form homogenous particles with high dispersion. The endogenous nanoparticles were at nanoscale proximity to each other resulting to a highly strained metal and host. This leads to a composite with an enhanced oxygen exchange ability where even the deepest submerged nanoparticles can be accessed by the gas phase as they are found to be connected to the surface via nanodomains formed due to the high levels of induced strain. This is consistent with previous studies reporting that strain enhances oxygen capacity and exchange (Greeley et al., 2004). It is demonstrated that the endoparticles can also undergo repeated cyclic, redox transformation, transitioning between their metal and metal oxide state which allows them to act as accessible submerged oxygen reservoirs in the nanoscale while the composite maintains its integrity and the nanoparticles are protected against agglomeration and other deactivation mechanisms. The combined high oxygen transport and high oxygen capacity observed coupled with their durability makes these materials attractive for application in a plethora of energy conversion processes where oxygen storage and cyclability are essential such as thermochemical solar to fuel (Michalsky et al., 2015), redox flow batteries (Xu et al., 2011) and chemical looping (Metcalf et al., 2019). The applicability of the system is showcased by employing it for the challenging process of methane activation and conversion (Tang et al., 2014; Christian Enger et al., 2008) with the system exhibiting superior performance managing to convert methane with high selectivity to syngas at lower temperatures to that of the state of the art material with the same loading. Finally, the system is employed as an oxygen carrier for the conversion of methane via chemical looping partial oxidation (CLPO) where the materials cyclability and redox durability are illustrated with methane being selectively converted to syngas for over 130 cycles.

Such strain-enhanced oxygen transport ability and catalytic could revolutionise many fields which are discussed in the final chapter of the thesis. Following our analysis and observations in this chapter the next chapter targets the deconvolution of the effect of the different components of the system on its performance aiming on providing insight on how these systems can be tailored in order to allow their rational design depending on the technology and transformation of interest.

References

Bishop, S.R., Marrocchelli, D., Chatzichristodoulou, C., Perry, N.H., Mogensen, M.B., Tuller, H.L. & Wachsman, E.D. (2014) Chemical expansion: Implications for electrochemical energy storage and conversion devices. *Annual Review of Materials Research*. 44 (February), 205–239.

- Cargnello, M., Johnston-Peck, A.C., Diroll, B.T., Wong, E., Datta, B., Damodhar, D., Doan-Nguyen, V.V.T., Herzing, A.A., Kagan, C.R. & Murray, C.B. (2015) Substitutional doping in nanocrystal superlattices. *Nature*. 524 (7566), 450–453.
- Cho, S., Yun, C., Tappertzhofen, S., Kursumovic, A., Lee, S., Lu, P., Jia, Q., Fan, M., Jian, J., Wang, H., Hofmann, S. & MacManus-Driscoll, J.L. (2016) Self-assembled oxide films with tailored nanoscale ionic and electronic channels for controlled resistive switching. *Nature Communications*. 7.
- Choi, E.M., Di Bernardo, A., Zhu, B., Lu, P., Alpern, H., Zhang, K.H.L., Shapira, T., Feighan, J., Sun, X., Robinson, J., Paltiel, Y., Millo, O., Wang, H., Jia, Q. & MacManus-Driscoll, J.L. (2019) 3D strain-induced superconductivity in $\text{La}_2\text{CuO}_{4+\delta}$ using a simple vertically aligned nanocomposite approach. *Science Advances*. 5 (4), 1–11.
- Christian Enger, B., Lødeng, R. & Holmen, A. (2008) A review of catalytic partial oxidation of methane to synthesis gas with emphasis on reaction mechanisms over transition metal catalysts. *Applied Catalysis A: General*. 346 (1–2), 1–27.
- Dai, X.P., Li, R.J., Yu, C.C. & Hao, Z.P. (2006) Unsteady-state direct partial oxidation of methane to synthesis gas in a fixed-bed reactor using AFeO_3 (A = La, Nd, Eu) perovskite-type oxides as oxygen storage. *Journal of Physical Chemistry B*. 110 (45), 22525–22531.
- Escudero-Escribano, M., Malacrida, P., Hansen, H.M., Vej-Hansen, U., Velazquez-Palenzuela, A., Tripkovic, V., Schiøtz, J., Rossmeisl, J., Stephens, I.E.L. & Chorkendorff, I. (2016) Dering That Can Enable the Engineering of Material Properties Through Spontaneous Ordering of Nanoparticles. *Science*. 352 (6281), 73–76.
- Gao, Y., Chen, D., Saccoccio, M., Lu, Z. & Ciucci, F. (2016) From material design to mechanism study: Nanoscale Ni exsolution on a highly active A-site deficient anode material for solid oxide fuel cells. *Nano Energy*. 27499–508.
- Gao, Y., Wang, J., Lyu, Y.Q., Lam, K. & Ciucci, F. (2017) In situ growth of Pt_3Ni nanoparticles on an A-site deficient perovskite with enhanced activity for the oxygen reduction reaction. *Journal of Materials Chemistry A*. 5 (14), 6399–6404.
- Greeley, J., Krekelberg, W.P. & Mavrikakis, M. (2004) Strain-induced formation of subsurface species in transition metals. *Angewandte Chemie - International Edition*. 43 (33), 4296–4300.
- Irvine, J.T.S., Neagu, D., Verbraeken, M.C., Chatzichristodoulou, C., Graves, C. & Mogensen, M.B. (2016) Evolution of the electrochemical interface in high-temperature fuel cells and electrolyzers. *Nature Energy*. 1 (1), 1–13.
- Jalili, H., Han, J.W., Kuru, Y., Cai, Z. & Yildiz, B. (2011) New insights into the strain coupling to surface chemistry, electronic structure, and reactivity of $\text{La}_{0.7}\text{Sr}_{0.3}\text{MnO}_3$. *Journal of Physical Chemistry Letters*. 2 (7), 801–807.
- Kim, S.J., Akbay, T., Matsuda, J., Takagaki, A. & Ishihara, T. (2019) Strain Effects on Oxygen Reduction Activity of Pr_2NiO_4 Caused by Gold Bulk Dispersion for Low Temperature Solid Oxide Fuel Cells. *ACS Applied Energy Materials*. 2 (2), 1210–1220.
- Kousi, K., Neagu, D., Bekris, L., Papaioannou, E.I. & Metcalfe, I.S. (2020) Endogenous

- Nanoparticles Strain Perovskite Host Lattice Providing Oxygen Capacity and Driving Oxygen Exchange and CH₄ Conversion to Syngas. *Angewandte Chemie - International Edition*. 59 (6), 2510–2519.
- Kousi, K., Neagu, D. & Metcalfe, I.S. (2020) Combining Exsolution and Infiltration for Redox, Low Temperature CH₄ Conversion to Syngas. *Catalysts*. 10 (5), 468.
- Kwak, N.W., Jeong, S.J., Seo, H.G., Lee, S., Kim, Y.J., Kim, J.K., Byeon, P., Chung, S.Y. & Jung, W.C. (2018) In situ synthesis of supported metal nanocatalysts through heterogeneous doping. *Nature Communications*. 9 (1), 1–8.
- Kwon, O., Sengodan, S., Kim, K., Kim, G., Jeong, H.Y., Shin, J., Ju, Y.W., Han, J.W. & Kim, G. (2017) Exsolution trends and co-segregation aspects of self-grown catalyst nanoparticles in perovskites. *Nature Communications*. 8 (May), 1–7.
- Liu, S., Liu, Q. & Luo, J.L. (2016) Highly Stable and Efficient Catalyst with in Situ Exsolved Fe-Ni Alloy Nanospheres Socketed on an Oxygen Deficient Perovskite for Direct CO₂ Electrolysis. *ACS Catalysis*. 6 (9), 6219–6228.
- Lu, P., Wu, X., Guo, W. & Zeng, X.C. (2012) Strain-dependent electronic and magnetic properties of MoS₂ monolayer, bilayer, nanoribbons and nanotubes. *Physical Chemistry Chemical Physics*. 14 (37), 13035–13040.
- MacManus-Driscoll, J.L., Zerrer, P., Wang, H., Yang, H., Yoon, J., Fouchet, A., Yu, R., Blamire, M.G. & Jia, Q. (2008) Strain control and spontaneous phase ordering in vertical nanocomposite heteroepitaxial thin films. *Nature Materials*. 7 (4), 314–320.
- Markus, K., Zhuhua, C., Wen, M., Bilge, Y., Herbert, H. & Jurgen, F. (2013) Tensile Lattice Strain Accelerates Oxygen Surface Exchange and Diffusion in La_{1-x}Sr_xCoO_{3-δ} Thin Films. *ACS Nano*. 7 (4), 3276–3286.
- Metcalfe, I.S., Ray, B., Dejoie, C., Hu, W., de Leeuwe, C., Dueso, C., García-García, F.R., Mak, C.M., Papaioannou, E.I., Thompson, C.R. & Evans, J.S.O. (2019) Overcoming chemical equilibrium limitations using a thermodynamically reversible chemical reactor. *Nature Chemistry*. 11 (7), 638–643.
- Michalsky, R., Botu, V., Hargus, C.M., Peterson, A.A. & Steinfeld, A. (2015) Design principles for metal oxide redox materials for solar-driven isothermal fuel production. *Advanced Energy Materials*. 5 (7), 1–10.
- Mihai, O., Chen, D. & Holmen, A. (2012) Chemical looping methane partial oxidation: The effect of the crystal size and O content of LaFeO₃. *Journal of Catalysis*. 293175–185.
- Miyoshi, S. & Martin, M. (2009) B-Site cation diffusivity of Mn and Cr in perovskite-type LaMnO₃ with cation-deficit nonstoichiometry. *Physical Chemistry Chemical Physics*. 11 (17), 3063–3070.
- Moreno, R., Zapata, J., Roqueta, J., Bagués, N. & Santiso, J. (2014) Chemical Strain and Oxidation-Reduction Kinetics of Epitaxial Thin Films of Mixed Ionic-Electronic Conducting Oxides Determined by X-Ray Diffraction. *Journal of The Electrochemical Society*. 161 (11), F3046–F3051.

- Neagu, D. & Irvine, J.T.S. (2010) Structure and Properties of $\text{La}_{0.4}\text{Sr}_{0.4}\text{TiO}_3$ Ceramics for Use as Anode Materials in Solid Oxide Fuel Cells. *Chemistry of Materials*. 22 (17), 5042–5053.
- Neagu, D., Oh, T.S., Miller, D.N., Ménard, H., Bukhari, S.M., Gamble, S.R., Gorte, R.J., Vohs, J.M. & Irvine, J.T.S. (2015) Nano-socketed nickel particles with enhanced coking resistance grown in situ by redox exsolution. *Nature Communications*. 6.
- Neagu, D., Papaioannou, E.I., Ramli, W.K.W., Miller, D.N., Murdoch, B.J., Ménard, H., Umar, A., Barlow, A.J., Cumpson, P.J., Irvine, J.T.S. & Metcalfe, I.S. (2017) Demonstration of chemistry at a point through restructuring and catalytic activation at anchored nanoparticles. *Nature Communications*. 8 (1), 1855.
- Oh, T.S., Rahani, E.K., Neagu, D., Irvine, J.T.S., Shenoy, V.B., Gorte, R.J. & Vohs, J.M. (2015) Evidence and Model for Strain-Driven Release of Metal Nanocatalysts from Perovskites during Exsolution. *Journal of Physical Chemistry Letters*. 6 (24), 5106–5110.
- Otto, S.K., Kousi, K., Neagu, D., Bekris, L., Janek, J. & Metcalfe, I.S. (2019) Exsolved Nickel Nanoparticles Acting as Oxygen Storage Reservoirs and Active Sites for Redox CH_4 Conversion. *ACS Applied Energy Materials*. 2 (10), 7288–7298.
- Pakhare, D. & Spivey, J. (2014) A review of dry (CO_2) reforming of methane over noble metal catalysts. *Chemical Society Reviews*. 43 (22), 7813–7837.
- Papadopoulou, C., Matralis, H. & Verykios, X. (2012) 'Catalysis for alternative energy generation', in L. Gucci & A. Erdöhelyi (eds.) *Catalysis for Alternative Energy Generation*. [Online]. Springer US. pp. 57–127.
- de Rogatis, L., Cargnello, M., Gombac, V., Lorenzut, B., Montini, T. & Fornasiero, P. (2010) Embedded phases: A way to active and stable catalysts. *ChemSusChem*. 3 (1), 24–42.
- De Souza, R.A. (2015) Oxygen Diffusion in SrTiO_3 and Related Perovskite Oxides. *Advanced Functional Materials*. 25 (40), 6326–6342.
- Strasser, P., Koh, S., Anniyev, T., Greeley, J., More, K., Yu, C., Liu, Z., Kaya, S., Nordlund, D., Ogasawara, H., Toney, M.F. & Nilsson, A. (2010) Lattice-strain control of the activity in dealloyed core-shell fuel cell catalysts. *Nature Chemistry*. 2 (6), 454–460.
- Tang, P., Zhu, Q., Wu, Z. & Ma, D. (2014) Methane activation: The past and future. *Energy and Environmental Science*. 7 (8), 2580–2591.
- Thalinger, R., Gocyla, M., Heggen, M., Dunin-Borkowski, R., Grünbacher, M., Stöger-Pollach, M., Schmidmair, D., Klötzer, B. & Penner, S. (2016) Ni-perovskite interaction and its structural and catalytic consequences in methane steam reforming and methanation reactions. *Journal of Catalysis*. 33726–35.
- Villars, P. & Hulliger, F. (eds.) (n.d.) *SrTiO₃ rt thermal expansion: Datasheet from "PAULING FILE Multinaries Edition -- 2012" in SpringerMaterials* (https://materials.springer.com/isp/physical-property/docs/ppp{_}2eb81b8d8d45f48d22c3a950e7acc800).
- Wang, L., Zeng, Z., Gao, W., Maxson, T., Raciti, D., Giroux, M., Pan, X., Wang, C. & Greeley, J. (2019) Tunable intrinsic strain in two-dimensional transition metal electrocatalysts.

Science. 363 (6429), 870–874.

- Wu, Y., Chen, Z., Nan, P., Xiong, F., Lin, S., Zhang, X., Chen, Y., Chen, L., Ge, B. & Pei, Y. (2019) Lattice Strain Advances Thermoelectrics. *Joule*. 3 (5), 1276–1288.
- Xu, N., Li, X., Zhao, X., Goodenough, J.B. & Huang, K. (2011) A novel solid oxide redox flow battery for grid energy storage. *Energy and Environmental Science*. 4 (12), 4942–4946.
- Yuan, K., Lee, S.S., Cha, W., Ulvestad, A., Kim, H., Abdilla, B., Sturchio, N.C. & Fenter, P. (2019) Oxidation induced strain and defects in magnetite crystals. *Nature Communications*. 10 (1), 1–10.
- Zeng, L., Cheng, Z., Fan, J.A., Fan, L.S. & Gong, J. (2018) Metal oxide redox chemistry for chemical looping processes. *Nature Reviews Chemistry*. 2 (11), 349–364.
- Zhu, X., Li, K., Neal, L. & Li, F. (2018) Perovskites as Geo-inspired Oxygen Storage Materials for Chemical Looping and Three-Way Catalysis: A Perspective. *ACS Catalysis*. 8 (9), 8213–8236.
- Zhu, Y., Zhou, W., Ran, R., Chen, Y., Shao, Z. & Liu, M. (2016) Promotion of Oxygen Reduction by Exsolved Silver Nanoparticles on a Perovskite Scaffold for Low-Temperature Solid Oxide Fuel Cells. *Nano Letters*. 16 (1), 512–518.
- Zubenko, D., Singh, S. & Rosen, B.A. (2017) Exsolution of Re-alloy catalysts with enhanced stability for methane dry reforming. *Applied Catalysis B: Environmental*. 209711–719.

4 Deconvolution of the effect of micro- and nano-structure on the performance of exsolved perovskite systems with exo-/endo- particles

In this chapter the effects of the different components of an exo/endo- particle system on its activity is investigated and deconvoluted. Methodologies for creating microstructurally and nanostructurally tailored systems are implemented and the samples are tested for the activation for methane. By selectively modifying system's characteristics their effect on performance is uncloaked. The findings of this study provide insight on how exo-/endo-particle systems perform and can be rationally designed to improve performance and tailor selectivity.

4.1 Introduction

From the results presented in Chapter 3, it is evident that exo/ endo- composite nanoparticle perovskite systems exhibit a combination of unique emergent properties stemming from the synergistic relationship of their components that allow them to outperform traditional materials. However, as with any new class of materials and especially when such degree of tailorability is possible (Neagu et al., 2019, 2017; Papaioannou et al., 2018), understanding the direct contribution of the components of the system on its performance is key for allowing application driven material development (van Deelen et al., 2019; Sie & Krishna, 1998). Although the effect of submerged particles on enhancing overall redox and catalytic performance has been demonstrated in subchapter 3.5 (Kousi, Neagu, Bekris, Papaioannou, et al., 2020), their direct contribution on the system's reactivity remains to be studied systematically. Additionally, the role of other components of the system such as exo-particle presence and changing of the support's microstructure remain a mystery.

In this chapter, the highly tuneable nature of the exsolved systems is demonstrated and methodologies are developed for the production of samples with tailored characteristics. The selective modification of each component of the system (exoparticles, endoparticles and microstructure) allows for the deconvolution of its effect on the system's performance as it is employed for the conversion of methane to syngas. The involvement of bulk nanoparticles is demonstrated by creating a series of samples with increasing submerged particle content and monitoring the changes in activity while correlating it with findings presented in Chapter 3. The role of surface nanoparticles is deconvoluted by creating samples that have their surface nanoparticles gradually removed. Finally, the effect of modifying the microstructure on activity is investigated by studying systems with varying porosity, revealing the critical effect microstructure has on surface exsolution and in extent on the system's activity and selectivity.

4.2 Probing the effect of endo- nanoparticles on activity

Aiming to provide insight on the effect of submerged nanoparticles on the systems performance towards CH₄ conversion to syngas, systems with progressively higher amount of exsolved of Ni nanoparticles in the bulk are developed and tested. The systems are produced by following the methodology presented in subchapter 3.3 which involved modifying reduction conditions (temperature and time under stream). This allows control over the system's surface particle characteristics (size and population) (Neagu et al., 2013; Otto et al., 2019) and more importantly the gradual release of nanoparticles in the bulk (Kousi, Neagu, Bekris, Papaioannou, et al., 2020). By employing this design principle, four samples with increasing bulk particle content ranging from a system without submerged nanoparticles to systems with a progressively higher submerged particle content are created. The systems studied are identical to those presented in Chapter 3 and thus, their characteristics and properties are expected and found to be the same as the ones reported before. Endo- and exo- particle generation following different reduction regimes is observed via SEM imaging. The expected 3D models and the SEM images of the corresponding exsolved sample's surface and bulk are presented in Figure 4.1 showcasing, once again, that the methodology developed successfully leads to samples with increasing endoparticle content. The increasing content of exsolved Ni metal in the form of endoparticles is also illustrated via the evolution of the Ni

peak observed in the XRD diffractograms of the samples (Figure 4.2b). From the quantification of these peaks (not presented for brevity as has been presented in subchapter 3.3) the overall Ni exsolution in wt% is also calculated (Figure 4.2c) while further image analysis allows the calculation of exsolved endo- and exo- particle characteristics (Figure 4.2d).

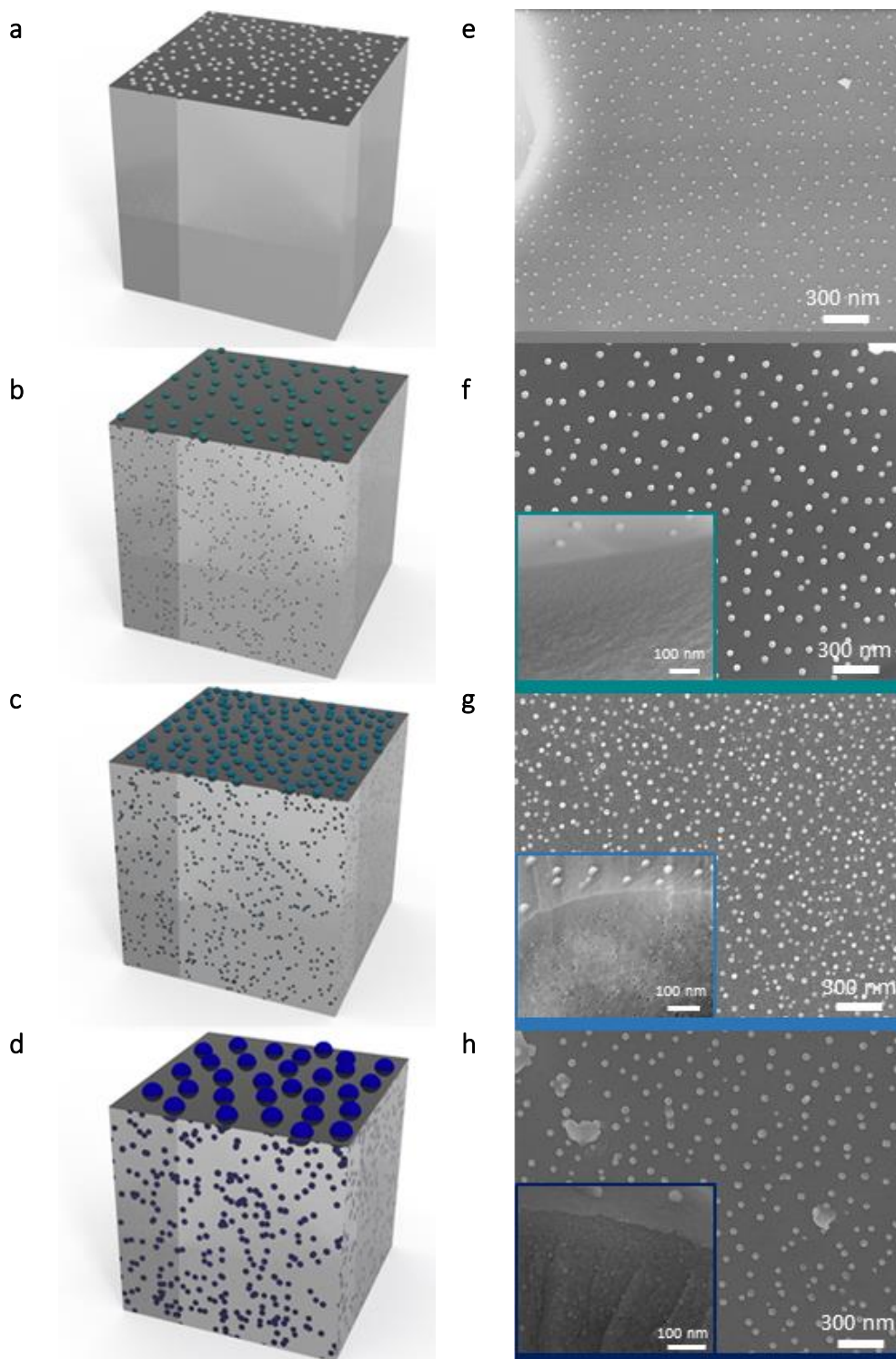


Figure 4.1 **Systems with gradually increasing endoparticle content.** (a)-(d) 3D models of systems with increasing nanoparticle content in the bulk. (e)-(h) Corresponding SEM micrographs of the surface and bulk of the systems illustrated in (a)-(d). Gradual release of

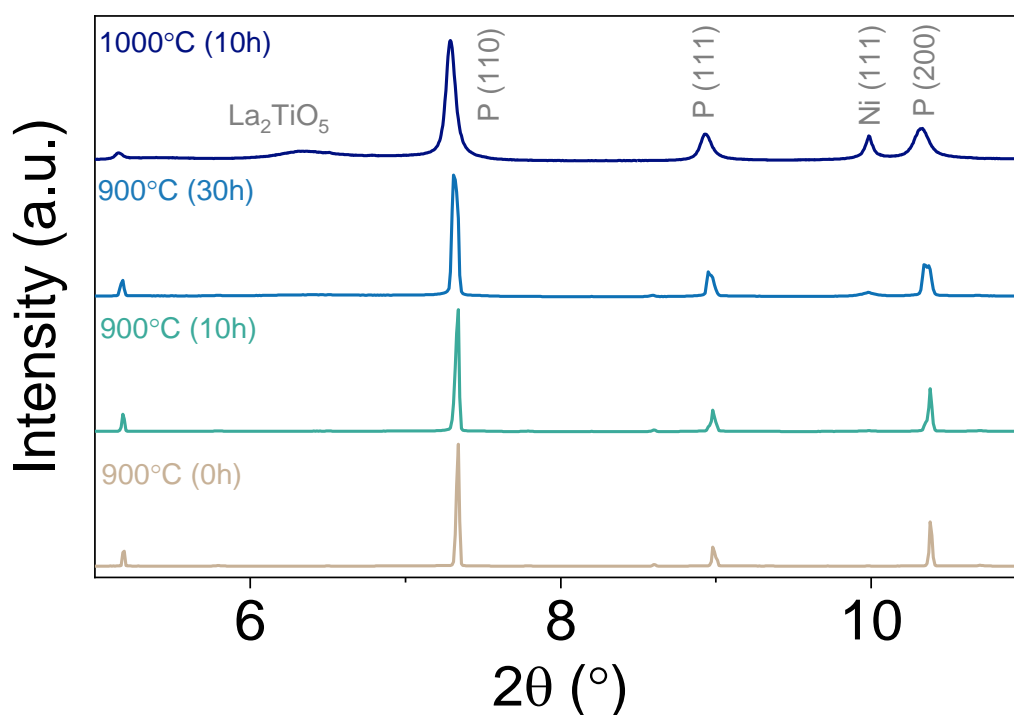
nanoparticles in the bulk was achieved by reducing the $\text{La}_{0.8}\text{Ce}_{0.1}\text{Ni}_{0.4}\text{Ti}_{0.6}\text{O}_3$ perovskite in 5% H_2/Ar atmosphere: at 900 °C for 0 h (a, e, grey), 10 h (b, f, teal) and 30 h (c, g, light blue) and at 1000 °C for 10 h (d, h, navy blue).

The difference between surface and bulk nanoparticle characteristics is once again striking across all samples with the particles generated in the bulk being much smaller in size but exhibiting a very high population. This is illustrated in both the 3D models (Figure 4.1 a-d) and the corresponding SEM micrographs of the system's surface and bulk (Figure 4.1 e-h) and verified by the calculated particle size (Figure 4.2d) via image analysis. The observed increase in particle generation is confirmed by monitoring the total extent of exsolution via XRD phase analysis and it is quantified via Rietveld refinement. The XRD patterns of the samples reduced at different conditions are presented in Figure 4.2a and the Ni phase evolution shown in detail in Figure 4.2b. Increasing reduction temperature and time the main perovskite peak appears to broaden (P(110) in Figure 4.2a), evidence of the perovskite lattice becoming gradually strained as a result of the increasing amount of exsolution in the bulk. This is verified by the evolution of the Ni phase peak that intensifies as the exsolved Ni phase increases (Figure 4.2b). Quantification of the peak reveals that the Ni wt.% content of the perovskite increases dramatically from 0.4 wt. % for the system with only surface nanoparticles to 8 wt. %, which corresponds to approximately 80% of the Ni in the lattice being exsolved (0.33 of the 0.4 doped), yet still occurs in a controlled manner. This high degree of exsolution also results in the perovskite phase being highly strained. Further examination of the Ni peak also reveals that it consists of a sharper tip and a broader base peak, which is characteristic for systems with submerged nanoparticles and have been assigned to particles on the surface and bulk, respectively (Kousi, Neagu, Bekris, Papaioannou, et al., 2020). The effect of nanoparticle formation in the bulk is also apparent from the increasing oxygen capacity of the systems with higher exsolved Ni content. TGA measurements presented in subchapter 3.4 reveal that the exsolved Ni nanoparticles act as oxygen reservoirs with the system with only surface nanoparticles exhibiting an oxygen capacity of 0.6 O wt.% which increases gradually for systems with higher exsolved Ni content in the bulk, ultimately reaching 3 O wt. %.

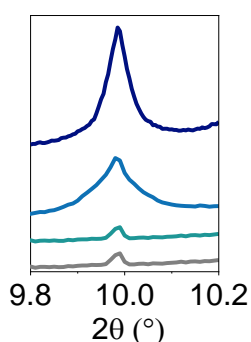
From the results presented above, it is evident once again that system's properties are significantly improved as exsolved nanoparticle content in the bulk and overall Ni exsolution increases inducing strain to particles and host. In order to determine how this improvement reflects on the systems' reactivity, the systems are employed for the conversion of methane and the activation process and selectivity are monitored as a function of temperature (Figure 4.3). The system with only surface nanoparticles appears almost inactive up to 700 °C probably due to its low oxygen content as a result of the overall small percentage of Ni exsolved. Upon bulk nanoparticle formation, some activity is observed at 750 °C with the overall conversion of methane remaining low. As overall exsolved Ni content increases the performance of the system is enhanced dramatically with the activation temperature shifting by 80 °C. Given that the two samples had similar surface particle characteristics in terms of size (Figure 4.2c), as they were reduced at the same temperature, this shift in activity cannot be attributed to surface particle characteristics and this illustrates that the enhanced performance observed stems from what lies in the bulk. The two samples have drastically different submerged

nanoparticle content and as a result the sample reduced for longer not only exhibits higher Ni particle content which act as oxygen reservoirs but more importantly has become highly strained leading to the enhancement of its overall reactivity. As determined in subchapter 3.5, the induced strain, now connecting the endoparticles with the surface, makes the oxygen stored in the submerged nanoparticles available to the reaction, allowing faster oxygen exchange from the bulk to the surface which drives CH₄ conversion at lower temperatures. This is confirmed by the fourth system which has the higher overall amount of Ni exsolved and in extent the higher strain, which drives the activation temperature even lower and overall conversion higher as showcased by its consumption curve (Figure 4.3).

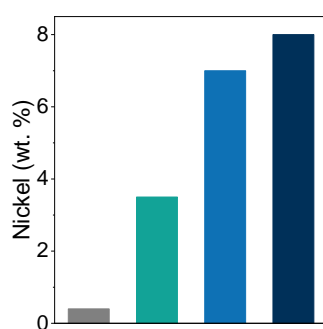
a



b



c



d

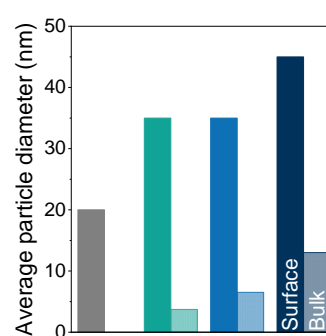


Figure 4.2 **Structure and characteristics of the developed exo-/ endo- systems with progressively higher endoparticle content presented in Figure 4.1.** a) Room temperature synchrotron X-ray patterns of the systems after reduction in different conditions. b) XRD pattern detail of the Ni peak evolution form (a) as the extent of exsolution in the bulk increases. c) Extent of exsolution expressed as increasing exsolved Ni (wt%) content from the quantification of the Ni peak presented in b via Rietveld refinement. d) Average size of exo- and endo- nanoparticles.

The activation profile across all samples has the form of a sharp consumption peak followed by a second broader one, characteristic of such Ni containing systems as reported in Chapter 3 and in literature (Kousi, Neagu, Bekris, Papaioannou, et al., 2020; Kousi, Neagu, Bekris, Cali, et al., 2020; Otto et al., 2019; Kousi et al., 2021; Kousi, Neagu, & Metcalfe, 2020) with the two peaks becoming more pronounced as reactivity is augmented. Selectivity to syngas remains high across all samples yielding syngas with a H₂/CO ratio of 2:1 and only traces of CO₂ produced. Carbon deposition is also minimal, as quantified in subchapter 3.5 for the most active sample (1000 °C (10h)), hence the potentially more susceptible coke formation. It should be noted here, that in previous reports on similar exsolved systems a decrease in selectivity and even carbon formation on systems reduced at high temperatures has been reported and attributed to the poor anchorage and bad interaction between particle and support as a result of the extreme reduction conditions (Otto et al., 2019; Kousi, Neagu, & Metcalfe, 2020). This is not observed here with the nanoparticles remaining well socketed and no carbon deposition occurring even on the sample reduced in the most extreme conditions, thus retaining one of the fundamental advantages of the submerged exsolved systems which combine resistance against poison mechanisms offered by the anchored surface nanoparticles (Papaioannou et al., 2019) coupled with the controlled oxygen release from the bulk (Kousi, Neagu, Bekris, Papaioannou, et al., 2020).

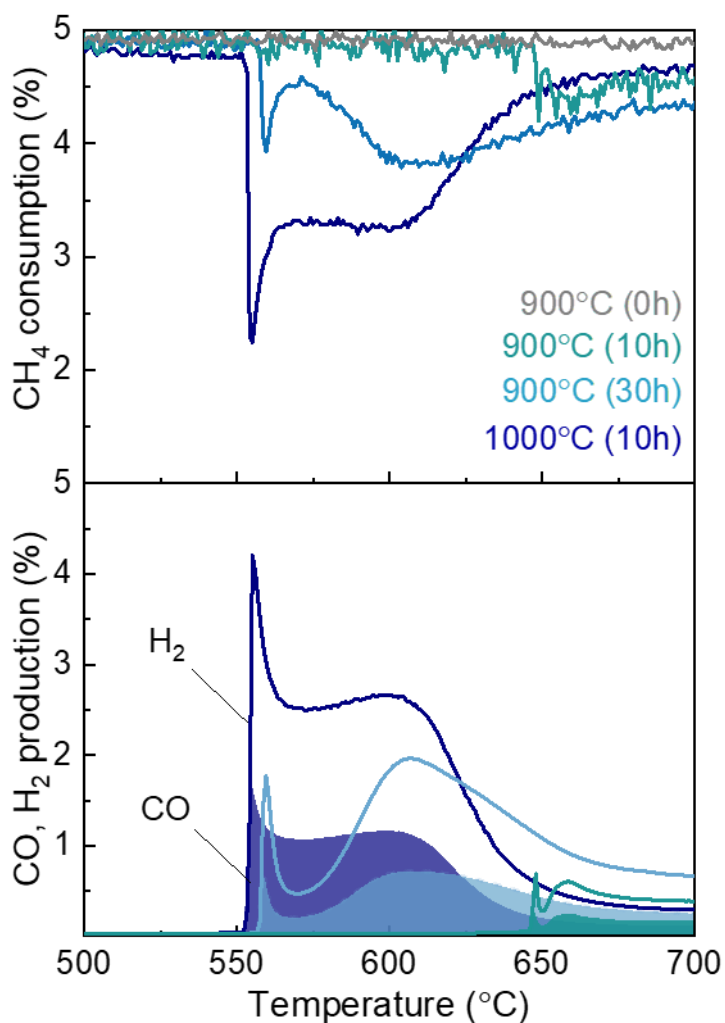


Figure 4.3 **Activity of endo-/exo- systems with progressively higher endoparticle content against methane.** Methane conversion and selectivity to syngas as a function of temperature.

From this investigation becomes evident that endoparticles play a major role in enhancing an exsolved system's performance as a result of the induced strain developed in the perovskite lattice due to the high extent of exsolution. The presence of submerged nanoparticles in the transformation is determined to be critical since the non-endoparticle containing equivalent system is seemingly inactive in the examined temperature window. As systems with a higher content of submerged particles are employed, activity is improved dramatically and due to the small changes in surface particle characteristics, it becomes clear that the observed improvement can only arise from changes occurring in the bulk.

It is demonstrated that controlled release of nanoparticles in the bulk can be achieved by tuning reduction conditions and that the generation of such nanoparticles play a pivotal role in improving the systems redox properties and performance. Overall activity increases as the extent of exsolution increases leading to higher conversions at lower temperatures without compromising selectivity.

4.3 Deconvoluting the role of surface nanoparticles on the material's activity

As it has become evident that developments in the bulk drastically alter the system's properties and performance, the next question that arises is what is the involvement, if any, of exoparticles in the activation process. In the results presented till now, both in subchapter 3.5 and subchapter 4.2, although surface particle characteristics change among samples with increasing extent of exsolution/ endoparticle content, changes have not been found to be important neither in the system's overall oxygen capacity (as their fraction is much smaller to that of the endoparticles, reader referred to subchapter 3.2) nor in increasing reactivity as the overall increase in performance seems to be underpinned by endoparticle development. Before attempting to deconvolute the effect of specific exoparticle characteristics, their overall involvement in the activation process is assessed. To achieve that, the most reactive system is employed and variants of it that have their surface nanoparticles gradually removed while the ones in the bulk are preserved are prepared and tested. Samples are reduced at 1000 °C for 10 h aiming to produce highly active systems with high endo-particle density and overall degree of exsolution as demonstrated before. Post reduction, the exsolved powdered samples are treated with HNO₃ aiming to remove the Ni exoparticles via chemical etching (Figure 4.4a-b). Post etching, the systems are oxidised at 600 °C for 1 h in air, before their performance against methane is tested.

The effect of HNO₃ on exoparticles is demonstrated in Figure 4.4 where SEM micrographs and XRD analysis of a sample before (Reduced) and after treatment (Etched) are presented. From the SEM overview of the surface, it is showcased that post etching all exoparticles have been successfully removed while in higher magnifications and focusing in areas where the bulk has been exposed, it is illustrated that endoparticles were preserved as they did not come in contact with the acid. The full removal of exoparticles is also visible by the change on the XRD diffractogram of the sample before and after etching (Figure 4.4c, d). In first sight the two diffractograms appear the same, which is expected since the structure of the sample was not modified, but upon closer examination of the Ni peak (Figure 4.4c) it is revealed that post treatment the sharp peak has disappeared. This assigns the sharp tip of the Ni peak to surface nanoparticles, since it vanished upon removal of the exoparticles, and the broader base to the endoparticles which post treatment remain unaltered. This analysis of the two extreme samples (with all exoparticles present and all removed) was also used for the peak assignment discussed in subchapter 3.5).

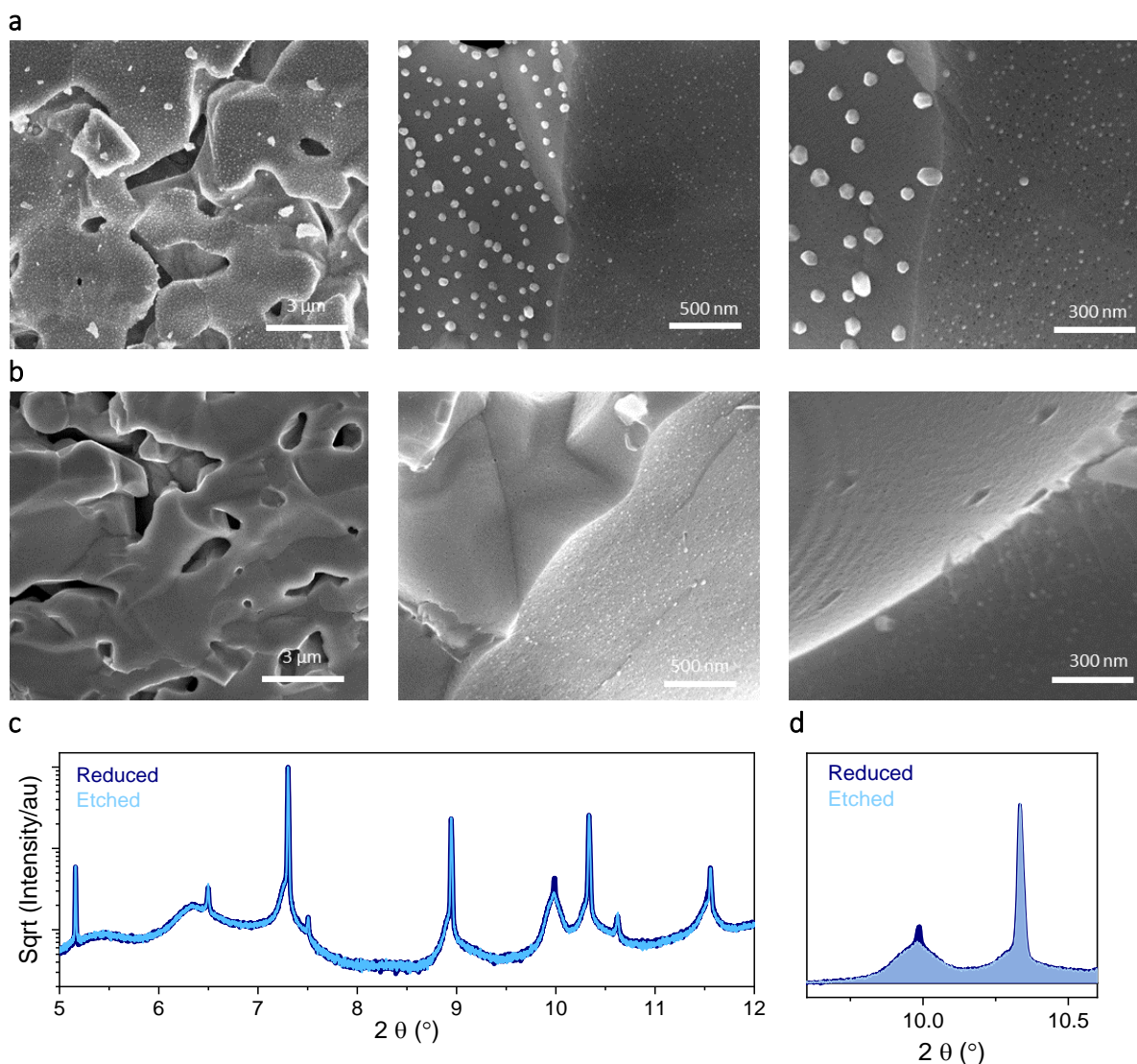


Figure 4.4 **Removal of exoparticles by chemical etching.** (a)-(b) SEM images of a sample with exo- and endo- exsolved particles a) before and b) after removal of surface particles by chemical etching while particles in the bulk remain intact. c) Synchrotron XRD diffractograms of the samples before (Reduced) and after (Etched) etching, d) Detail of the Ni peak from (c) illustrating the absence of a sharp tip on the diffractogram of the etched sample.

However, aiming to further study the involvement of exoparticles on activity, here more samples are created and tested. By varying etching conditions (HNO_3 concentration and contact time), three variants of the system that exhibit different surface particle characteristics are produced (Figure 4.5). The first system has its surface nanoparticles completely removed (Fully etched-grey in Figure 4.5) leaving behind deep pits on the surface of the perovskite in their place exposing their socketed nature (Neagu et al., 2015). Consequently, the surface of the sample is left barren of active sites. As a result, the sample is virtually inactive (Fully etched in Figure 4.6) signifying the importance of surface nanoparticles, since without their presence CH_4 activation is not possible and furthermore the oxygen stored in the bulk is not accessible. In view of this, it is confirmed that the system's activity is a result of the synergistic contribution of surface and bulk nanoparticles where both components are

essential for methane activation as surface nanoparticles act both as active sites and ‘bridges’ connecting the endoparticles with the reacting stream for oxygen transport.

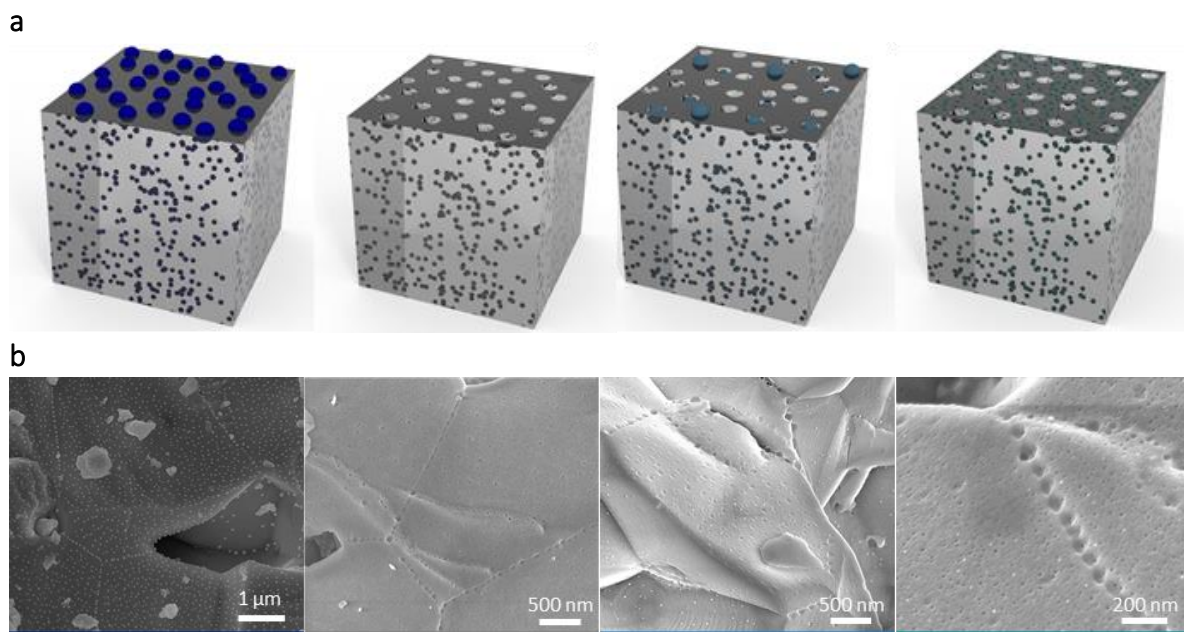


Figure 4.5 **Systems designed for deconvoluting the effect of exo-particles on activity.** (a) 3D models of systems with their surface nanoparticles gradually removed while the ones in the bulk remain intact. System will all exoparticles (navy blue) present, system with all exoparticles removed (grey), system with few exoparticles removed (light blue) and systems with all exoparticles removed but etched to the point where endoparticles are exposed on the surface (teal) (b) Corresponding SEM micrographs of the model systems illustrated in (a).

Without particle presence on the surface, the bulk particles are inaccessible to gas stream and the catalytic transformation cannot occur. Aiming to extract more information about this relationship, the second system has its surface nanoparticles partially removed (Partially-etched/ light blue in Figure 4.5) by reducing its contact time with the acid. The remaining Ni nanoparticles on the surface appear to be able maintain the capability of the system to activate methane with the activation temperature remaining the same but with the sharp consumption peak now being suppressed (Figure 4.6). This experimentally assigns the first sharp peak and consequently activation temperature to the exo-particles while implying that this peak is dependent on the total amount of Ni exsolved on the surface, as it has been calculated by Retvield refinement in Chapter 3. Taking it one step further a fourth sample was prepared where surface nanoparticles have been completely removed and the perovskite surface has been slightly etched to the point that the tip of some submerged Ni nanoparticles start being exposed on the surface. The surface of the resulting sample (Over-etched/ teal in Figure 4.5) is populated by the exposed bulk nanoparticles. The system’s activity seems to adopt a similar profile as the unetched sample but with the activation temperature now pushed towards higher values. The formation of the sharp peak is evident of the nickel nanoparticles now being exposed to the stream as it is expected from the insight gained from the results above. The shift in the activation temperature indicates that although the relationship between surface and bulk has been restored via the presence of bulk

nanoparticles on the surface, now the active sites have decreased overall, and the oxygen transport is not being facilitated as effectively as through their bigger surface-exsolved counterparts.

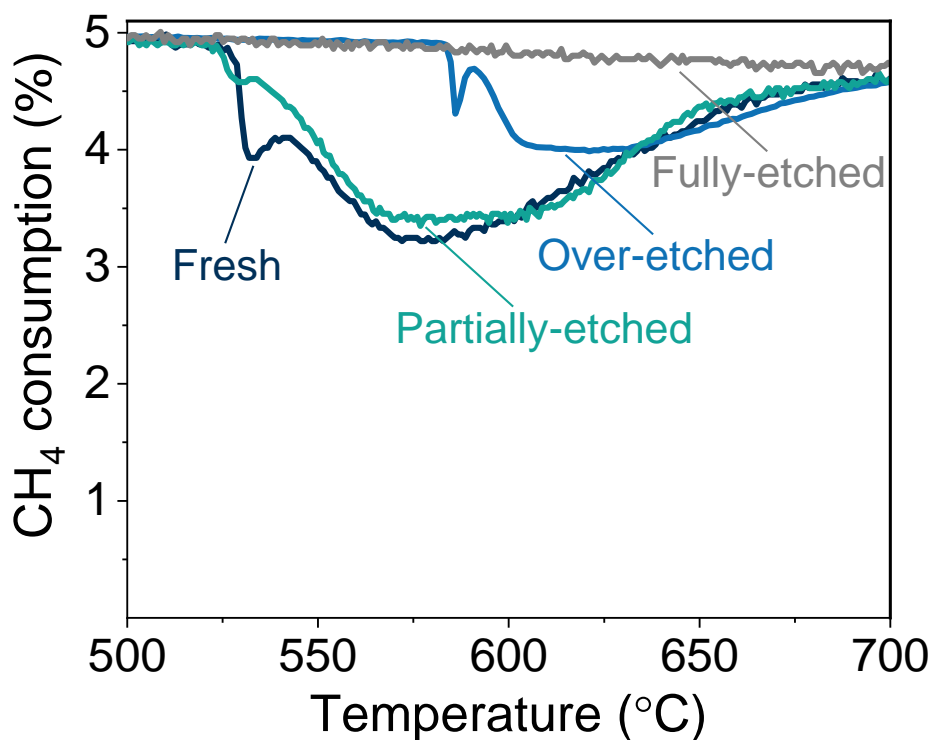


Figure 4.6 **Involvement of exoparticles on the activity of systems with exo-/ endo-particles.** Methane activation profiles of the systems presented in Figure 4.5.

Although surface nanoparticle contribution to the system's oxygen capacity is small, as calculated by Rietveld refinement in subchapter 3.4, their presence on the surface is found to be paramount for the system's performance. It is proven that the first activation peak observed in the methane activation profiles of the submerged systems is directly associated with the amount of Ni available on the surface and in direct contact with the reactive stream while the second one is associated with the particles in the bulk.

4.4 Elucidation of the effect of microstructural modification on the system's performance

Modification of the microstructural characteristics of the catalyst support has been proven critical for the performance of catalysts since it can lead to major shifts in activity and product selectivity stemming from the changes in the structure, surface-related chemical properties of the material and different particle-support interactions (T. et al., 1998; Peng et al., 2018). In traditional deposited and impregnated catalysts increased porosity of the support is highly desirable since mass transfer can improve and more surface is available for the active phase to be dispersed leading to greater active surface area, subsequently leading to enhanced activity (Ashik et al., 2017; Kung & Ko, 1996; Parlett et al., 2013; Mitchell et al., 2013). The same hypothesis can be made for the case of exsolved systems as a more porous microstructure can be expected to lead to higher activity since, in principle, due to the higher surface area now available, more nanoparticles can be exsolved. Additionally, while porosity increases, perovskite grain size decreases thus the distance through which the exsolvable

anions have to migrate in order to reach the surface is minimized, possibly allowing for even higher degree of surface and exsolution to be achieved (Otto et al., 2019). However, for the more complex exsolved systems with exo- and endo- particles studied here since particle nucleation also occurs in the bulk, the effect of microstructural modifications is expected to be more complex.

Higher overall extent of exsolution may be achieved with more anions exsolving and due to the small grain size oxygen transfer from within the bulk may be quicker, but also bulk nanoparticle formation may be suppressed since surface exsolution could be favourable, impeding particle nucleation in the bulk. Furthermore, in exsolution there are more parameters to be considered since surface exsolution itself is complex and very closely linked to the microstructure of the perovskite support. Reports have shown that when perovskites undergo thermal treatments, such as sintering, surfaces exposed to air develop a different composition from the bulk which is A-site rich, henceforth referred to as “native surface” (Neagu et al., 2013; Kyriakou et al., 2019), and this transformation has been found to occur even in perovskites that have been compositionally designed to be A-site deficient, like the ones employed here. This “native surface”, due to its A-site rich chemical composition suppresses exsolution and hinders particle formation. As a result, such surfaces tend to yield fewer nanoparticles which also have different characteristics than those exsolved from their A-site deficient counterparts. Therefore, the outside surface of the pellet and the surface of pores forming during the sintering process are native surfaces and are expected, upon reduction, to have a much lower particle population. On the other hand, the A-site deficient surfaces- “cleaved surfaces” that are formed by exposing the sintered pellet’s bulk via crushing it to a powder, are expected to exhibit higher particle population. To visualise this, two SEM micrographs of prepared systems with different porosities are presented in Figure 4.7. The striking difference in particle nucleation between the two surfaces is showcased in both images with the two areas (native and cleaved) displaying very different particle populations. The surface of pores (native) hardly exhibits any nucleation while the cleaved areas are densely populated. Additionally, from the comparison of the two photos it is illustrated that as the material becomes more porous, its available for exsolution surface area is dominated by that of the pores (native). This results into a sample with a large fraction of areas with extremely low population and a small percentage of areas where particle formation is very high. This invalidates the hypothesis that a higher porosity will automatically lead to increased surface exsolution but rather indicates that the higher activity reported for porous exsolved perovskite systems (Otto et al., 2019; Kousi, Neagu, Bekris, Cali, et al., 2020) is a result of various other factors.

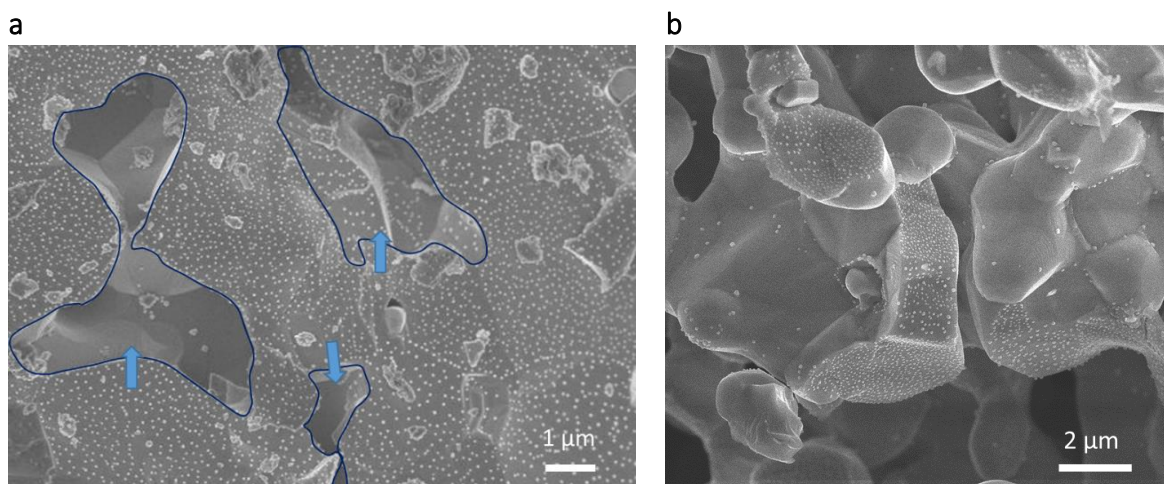


Figure 4.7 Surface exsolution on exo/endo- particle perovskite systems with different porosity. a) Overview of a dense perovskite system with pore surfaces exhibiting limited exsolution highlighted, b) Overview of a perovskite system with high porosity where pore surfaces are dominant, showcasing the difference between exoparticle characteristics exsolved on native (A-site rich) and cleaved surfaces (A-site deficient).

Aiming to investigate these factors samples with increasing porosity are developed, and the changes observed in activity and product selectivity are correlated with the nature of the exsolved nanoparticles formed. To achieve this, increasing amounts of pore former are mixed with the calcined powder before it is pressed into pellets and sintered (reader referred to the experimental chapter). The organic pore former burns off during the high temperature sintering process leaving behind pores throughout the pellet. Post sintering, the pellets are crushed and sieved in order to obtain powders with the desired 80-160 μm grain size and create randomly cleaved surfaces. All samples are then reduced in 5% H_2/Ar atmosphere at 1000 $^\circ\text{C}$ for 10 h. After reduction, the system's nano- and micro-structure is examined via SEM before being oxidized in air at 600 $^\circ\text{C}$ for 1 h and tested. Overviews and detail of the surface of samples with increasing porosity are presented in Figure 4.8, showcasing that through this methodology materials with tailored microstructure can be produced. Once again, it can be seen how increasing porosity the surface of pores occupies a larger fraction of the materials surface area (Figure 4.8b).

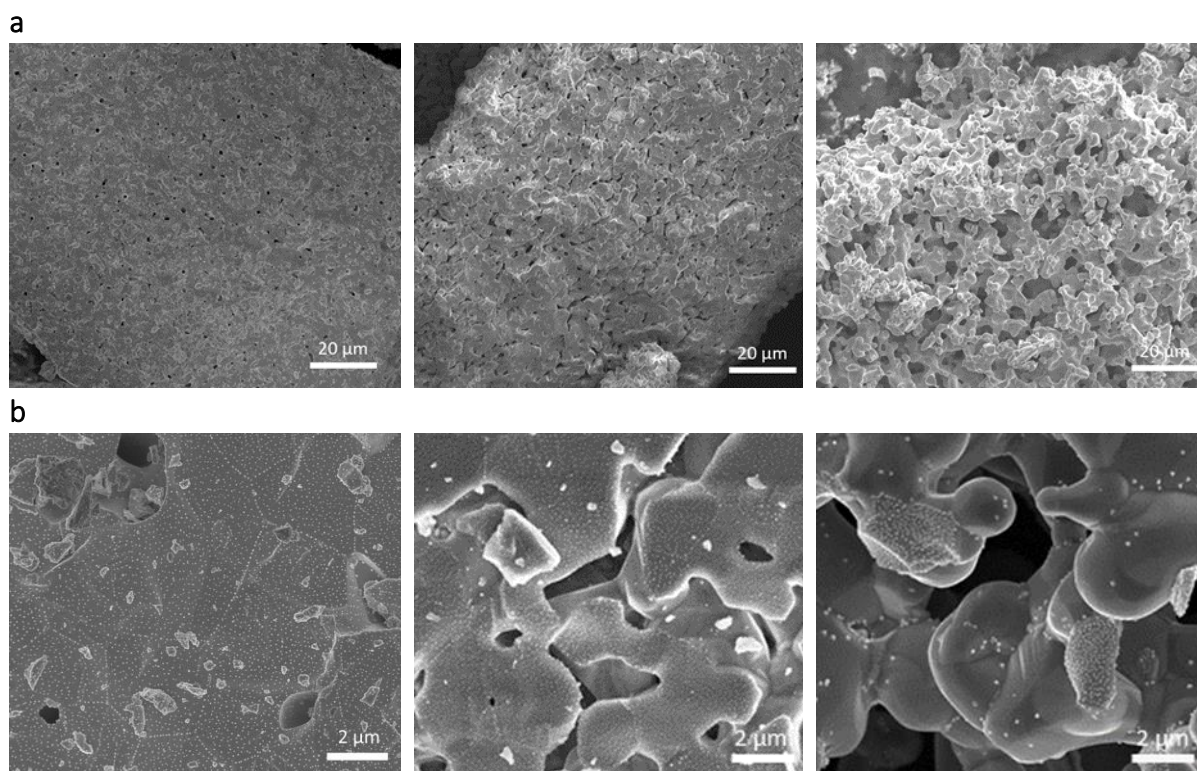


Figure 4.8 **Exo/endo- particle exsolved systems with varying porosities.** a) Overviews of perovskite grains with increasing porosity. b) Morphology of the surface the systems presented in (a) with pores occupying larger percentage of the materials surface area as porosity increases.

Since all pre-treatment conditions, except pore former content, are the same for all samples, the differences observed in particle characteristics and catalytic performance should only be the effect of the microstructural tuning. For this investigation, all types of nanoparticles exsolved in the system are considered since they exhibit very different characteristics. The particles, namely: nanoparticles exsolved on pores (exoparticles, on native surface), on cleaved surfaces (exoparticles, on surfaces created after crushing the pellet to produce the powder grains) and within the bulk (endoparticles, in the bulk of the powder grains which are exposed by manually crushing the powder grains to be brought for SEM analysis) and the differences between them are displayed in Figure 4.9.

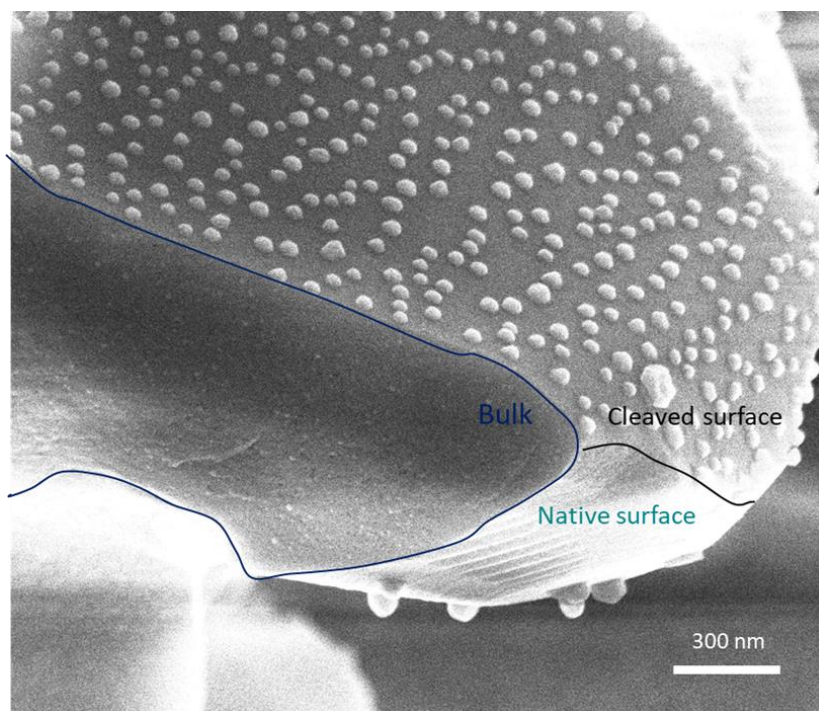


Figure 4.9 **Exsolved particle characteristics in different regions of an exo/endo- particle system.** Endoparticles exsolved in the Bulk (navy blue) and exoparticles exsolved on a cleaved surface (black) and on a native surface (teal).

On the SEM micrograph presented above (Figure 4.9), the three different regions available for exsolution in an exo/ endo-particle system and the particles exsolved on them exhibiting different characteristics are captured on a single image. The striking difference between endoparticles and exoparticles has been investigated and discussed extensively already. However here, the different characteristics of the particles exsolved on the native surface can be seen in detail. The particles are bigger than the ones exsolved on cleaved surfaces but more importantly much fewer in population as expected from the analysis discussed above. Hence, due to native surfaces occupying only a small fraction of the surface available for exsolution and in extent the even smaller fraction of the native surface-exsolved particles, make their contribution on activity negligible. However, although the native surface-exsolved particles do not play an important role, the native surface itself, acting as an exsolution inhibitor, can be pivotal for activity especially since pore surface becomes more dominant with increasing porosity (Figure 4.8b).

By examining images of higher magnification, the phenomenon of exsolution inhibition in porous samples becomes even more profound (Figure 4.10). The images compare a sample with low relative porosity (~6%) against a highly porous sample of approximately 40% relative porosity. The surface of the less porous sample (Figure 4.10a) is uniformly decorated with exoparticles with high population and the pores only occupy a small fraction of its microstructure. On the contrary, exsolution of the exposed surfaces of the porous sample is limited with the surface available for exsolution being mainly that of the pores. As a result, surface exsolution is hindered with the native surface of the pores being sparsely occupied by non-uniformly exsolved nanoparticles, while the few cleaved surfaces are extremely highly

populated, especially considering the size of the nanoparticles. This is not surprising since, as described above, the native surface acts as a release barrier for exsolution and the cleaved areas seem to act as release points for exsolution to occur, leading to increased nucleation and growth in a small area. Particle nucleation in the bulk remains high which is expected and considered to also be an additional factor due to which nucleation in the pore surface was so low, since it seems that bulk nanoparticle formation was favoured (Figure 4.9). In addition, the grain size of the two samples can be distinguished from the hierarchical particle exsolution across the grain boundaries, which as expected, become smaller as porosity increases.

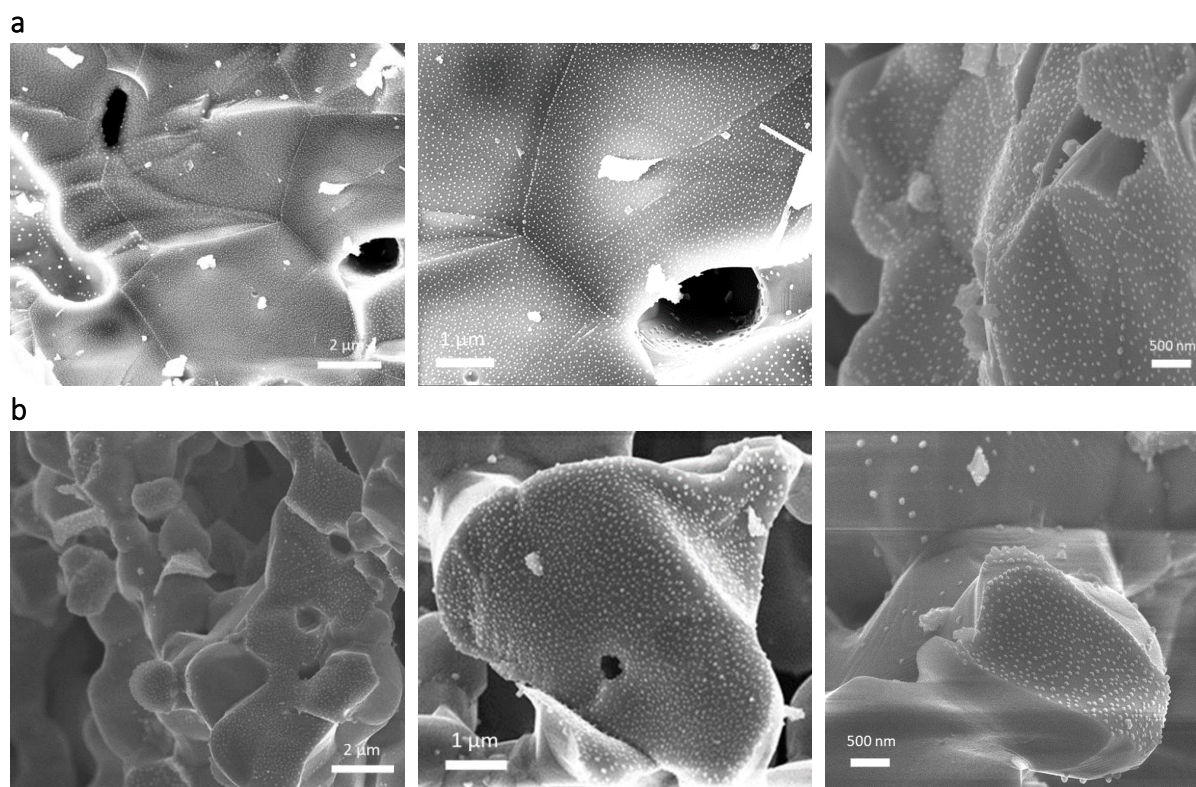


Figure 4.10 Comparison of exoparticle exsolution between samples with different porosities. Increasing magnification from left to right. a) Sample with low porosity exhibiting uniform exsolution across its surface and large grain size. b) Highly porous sample with smaller grains and non-uniform exsolution across its surface, which consists of areas with extremely high and extremely low particle population.

In order to systematically study the evolution of the above observations and their effect on the materials activity, six systems with increasing porosity are developed. Their characteristics are quantified via image analysis through which samples' relative porosity, average exoparticle diameter, population, grain size and Ni atoms present on the surface are calculated (Figure 4.11). Image analysis was conducted by examining over five photos and different areas for each system in order to minimise errors. Ni atoms μm^{-2} are used here in order to reveal the actual number of possible active sites on the materials surface, since a high population number does not necessarily lead to a high overall active site density since this high populated may be a very small fraction of the surface of the material as it has been already demonstrated for highly porous samples. As expected, grain size (burgundy in Figure 4.11a) decreases with porosity increase. In the denser sample, population is high which causes

exoparticles to remain smaller in size. The high population combined with the low fraction of low-populated porous areas leads to a high surface coverage but due to the small nanoparticle size, the overall Ni exsolved per μm^2 of the surface is not the highest recorded. As samples become more porous particle population drops and remains between 60 to 65 nanoparticles μm^{-2} across a 18 % increase in porosity. This is the result of exoparticles now growing bigger by approximately 10 nm. However, bigger exsolved particles do not lead to higher amount of Ni atoms exsolved as the lower population of cleaved areas and more importantly the increasing fraction of low-populated pores lead to a drop in Ni exsolved atoms μm^{-2} . This however stabilises across a range of 6 % porosity increase through which particles grow bigger and population drops. As samples become more porous particle population increases dramatically while particle size reduces but this is not representative of the sample as it is revealed from the number of Ni atoms exsolved that plummet. This is because the now extremely highly populated areas with big nanoparticles are not present throughout the sample surface but rather, as presented in the SEM micrographs above (Figure 4.10b), are localised and represent a small fraction of it as the majority is now occupied pores.

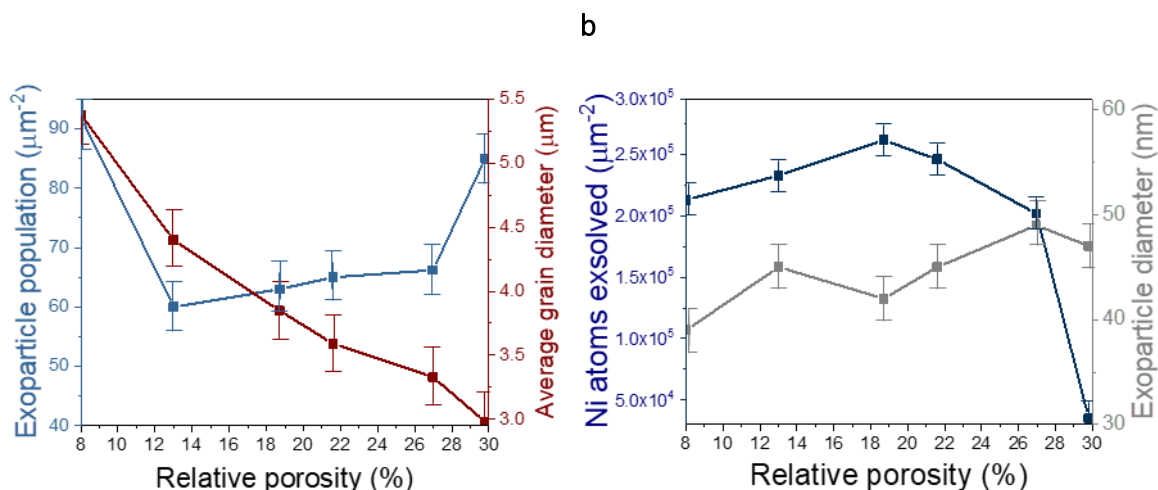


Figure 4.11 **Characteristics of exo/endo-particle systems with increasing porosity.** Quantification of a) Exoparticle population and grain size, b) Ni atoms exsolved on the surface and exoparticle size.

The effect of such disparities between exoparticle characteristics, grain size and more importantly overall active Ni atoms exsolved on the surface is evident on the sample's activity. The dense samples appear to activate methane at higher temperature and their activation profile consist of a pronounced sharp peak closely followed by the second broader peak. As porosity increase the sharp peak becomes gradually smaller while the activation temperature shifts 100 °C lower. Additionally, the two peaks become more separated as though surface methane activation and oxygen supply from the bulk happen in steps expanding this way the activation window which for the most active sample spans across 200 °C. The observed shrinkage of the first peak is attributed to the gradually fewer surface nanoparticles available as a result of the less cleaved areas due to pore area increase, while the broadening of the second peak indicates that conversion is dictated by nanoparticles in the bulk. It seems that at this point, an optimal ratio between surface nanoparticles and bulk has been achieved

which comprises of enough surface nanoparticles to lead to low temperature activation and provide effective connection with the bulk for the oxygen reservoirs to be accessed. As samples become more porous the activation temperature climbs back at higher values while the sharp activation peak becomes again more pronounced. This is attributed to the structure becoming compromised exposing some of the nanoparticles in the bulk to the stream, but with them not being enough to activate methane effectively or to regulate oxygen transfer from the bulk probably due to their poor anchorage. The adverse effect of high porosity becomes even more evident as for the most porous sample the activation temperature is comparable to that of the dense one but with the two peaks almost merging and conversion spanning over a small temperature window. As before, but now in a more extreme manner the microstructure has been compromised and comprises of a few well anchored surface nanoparticles which are not enough to activate methane at lower temperatures and as a result the now exposed bulk nanoparticles trigger the transformation but without being able to act as efficient oxygen bridges with the bulk to regulate oxygen exchange, the release happens rapidly, and the conversion is completed within 50 °C.

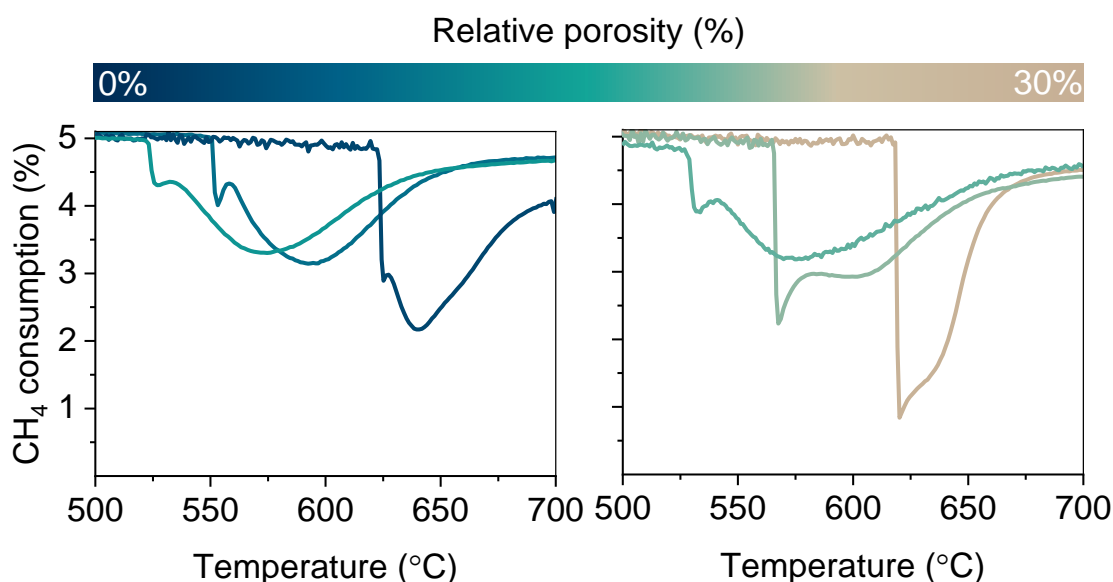


Figure 4.12 **Elucidation of microstructural modification effects on the performance of systems with exo/ endo- nanoparticles.** Methane activation profiles of exo/ endo- particle systems with increasing relative porosity.

Given the extreme effect of microstructural modification on particle characteristics, activity and performance, the final question to be answered is what the effect of such modifications on product selectivity is. In order to determine this, H₂ production as well as the carbon products are monitored for samples with increased porosity. As illustrated in Figure 4.13, overall high selectivity to syngas is observed across all samples. However, looking closely at the carbon products CO₂ production appears to originate and follow the first sharp consumption peak. From previous investigation presented above, the first peak was directly associated with surface particles, hence the overall CO₂ production is due to the surface particles driving the reaction in full oxidation due to the rapid release of oxygen. However,

during the second peak when oxygen release is mediated through the bulk, CO₂ production is minimal. As expected, samples with more exposed particles on the surface lead to higher CO₂ production and this way a direct correlation can be established between the nature of the exposed particles and the CO₂ produced. This effect is even more pronounced in the highly porous sample where due to the microstructure being compromised more bulk nanoparticles are exposed to the stream leading to higher undesirable CO₂ production. Overall, it appears that a trade-off relationship is present linking surface/exposed to the stream nanoparticles with the activation temperatures and selectivity making the microstructural modification of these systems challenging.

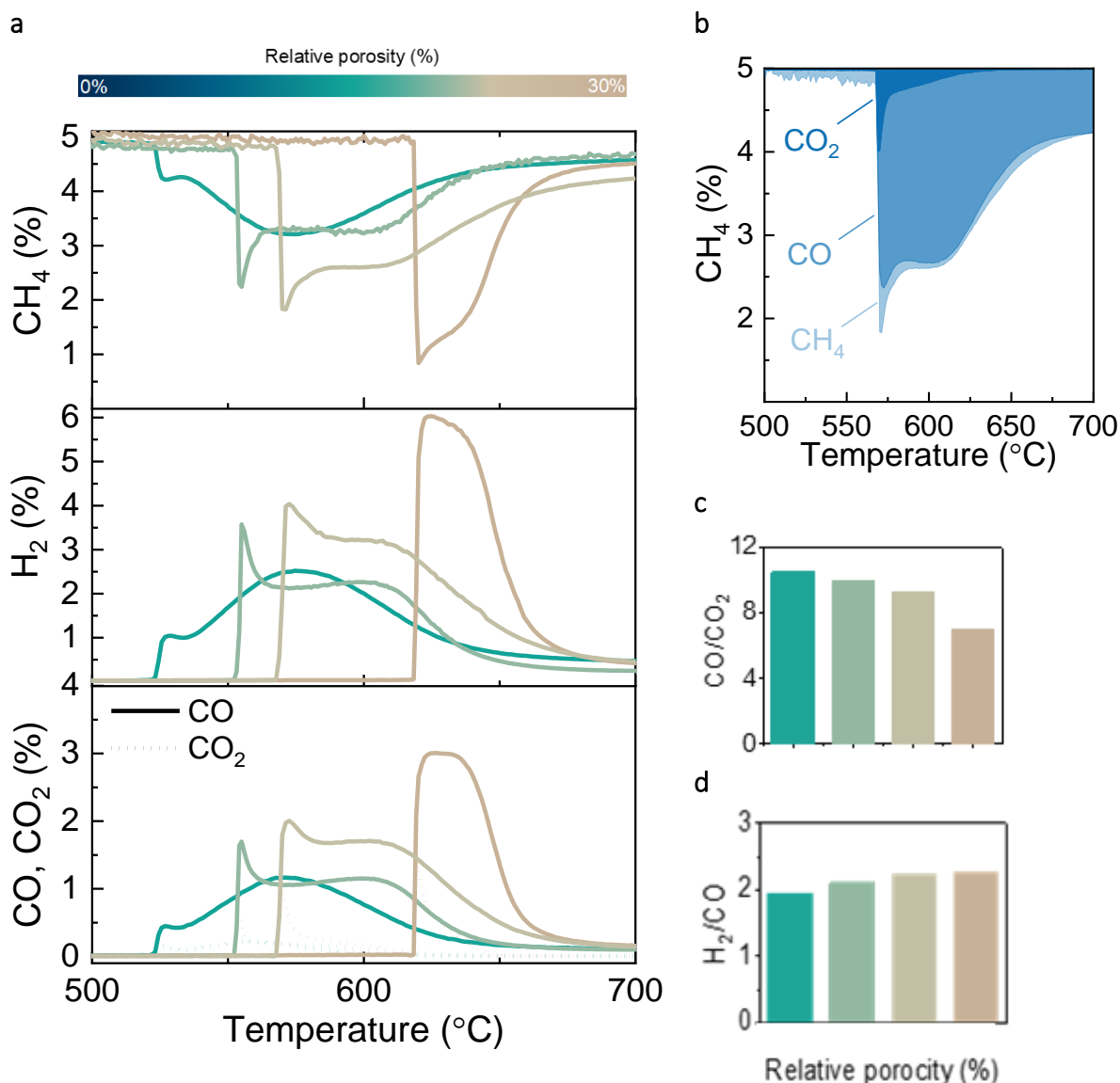


Figure 4.13 **Effect of microstructural modifications on product selectivity.** a) Methane conversion and product selectivity of systems with increasing relative porosity. b) Schematic of the conversion of methane to products. (c) Variation of CO/CO₂ and H₂/CO ratios as a result of microstructural modification.

4.5 Conclusions

Aiming to provide insight on the factors that dictate the activity of composite exsolved perovskite systems with endo- and exo- nanoparticles, in this study the $\text{La}_{0.8}\text{Ce}_{0.1}\text{Ni}_{0.4}\text{Ti}_{0.6}\text{O}_3$ perovskite system capable of exsolving Ni nanoparticles on its surface and bulk for the conversion of methane to syngas. We demonstrate the means to control the release of nanoparticles in the bulk by tuning reduction conditions and assess the detrimental effect submerged nanoparticles have on activity enhancement as a result of the overall higher degree of exsolution which leads to increased oxygen capacity and reactivity stemming from the strain induced in the perovskite lattice allowing fast oxygen exchange between surface and bulk. We examine the direct effect of particles in the bulk and particles on the surface on activity showcasing the importance of surface nanoparticles for the catalytic transformation. Modification of the materials porosity is found to be directly linked with exsolution directly affecting surface nanoparticle characteristics which in turn can have variable effect on reactivity. The effect of microstructural modification and to an extent surface particle modification is also determined to have a direct effect on product selectivity shifting the ratio of syngas produced depending on the characteristics of nanoparticles present on the surface. Nevertheless, the various modified systems exhibit excellent selectivity to syngas overall with CO_2 production being limited under 10 % across all samples tested while H_2/CO ratio revolves around the desirable 2:1 mark. Overall, the effect of bulk and surface nanoparticles is deconvoluted providing valuable insight on how perovskite system activity and yield can be enhanced by taking advantage of the high tailor ability of the systems. The findings of this work provide valuable information for the rational design of such systems for their employment for target applications and products.

References

- Ashik, U.P.M., Wan Daud, W.M.A. & Hayashi, J. ichiro (2017) A review on methane transformation to hydrogen and nanocarbon: Relevance of catalyst characteristics and experimental parameters on yield. *Renewable and Sustainable Energy Reviews*. 76 (March), 743–767.
- van Deelen, T.W., Hernández Mejía, C. & de Jong, K.P. (2019) Control of metal-support interactions in heterogeneous catalysts to enhance activity and selectivity. *Nature Catalysis*. 2 (11), 955–970.
- Kousi, K., Neagu, D., Bekris, L., Calì, E., Kerherve, G., Papaioannou, E.I., Payne, D.J. & Metcalfe, I.S. (2020) Low temperature methane conversion with perovskite-supported: exo / endo -particles. *Journal of Materials Chemistry A*. 8 (25), 12406–12417.
- Kousi, K., Neagu, D., Bekris, L., Papaioannou, E.I. & Metcalfe, I.S. (2020) Endogenous Nanoparticles Strain Perovskite Host Lattice Providing Oxygen Capacity and Driving Oxygen Exchange and CH_4 Conversion to Syngas. *Angewandte Chemie - International Edition*. 59 (6), 2510–2519.
- Kousi, K., Neagu, D. & Metcalfe, I.S. (2020) Combining Exsolution and Infiltration for Redox, Low Temperature CH_4 Conversion to Syngas. *Catalysts*. 10 (5), 468.
- Kousi, K., Tang, C., Metcalfe, I.S. & Neagu, D. (2021) Emergence and Future of Exsolved

Materials. *Small*. 17 (21), .

- Kung, H.H. & Ko, E.I. (1996) Preparation of oxide catalysts and catalyst supports - A review of recent advances. *Chemical Engineering Journal and the Biochemical Engineering Journal*. 64 (2), 203–214.
- Kyriakou, V., Neagu, D., Papaioannou, E.I., Metcalfe, I.S., Sanden, M.C.M. Van De & Tsampas, M.N. (2019) Applied Catalysis B : Environmental Co-electrolysis of H₂O and CO₂ on exsolved Ni nanoparticles for efficient syngas generation at controllable H₂ / CO ratios. *Applied Catalysis B: Environmental*. 258 (February), 117950.
- Mitchell, S., Michels, N.L. & Pérez-Ramírez, J. (2013) From powder to technical body: The undervalued science of catalyst scale up. *Chemical Society Reviews*. 42 (14), 6094–6112.
- Neagu, D., Kyriakou, V., Roiban, I.L., Aouine, M., Tang, C., Caravaca, A., Kousi, K., Schreur-Piet, I., Metcalfe, I.S., Vernoux, P., Van De Sanden, M.C.M. & Tsampas, M.N. (2019) In Situ Observation of Nanoparticle Exsolution from Perovskite Oxides: From Atomic Scale Mechanistic Insight to Nanostructure Tailoring. *ACS Nano*. 13 (11), 12996–13005.
- Neagu, D., Oh, T.S., Miller, D.N., Ménard, H., Bukhari, S.M., Gamble, S.R., Gorte, R.J., Vohs, J.M. & Irvine, J.T.S. (2015) Nano-socketed nickel particles with enhanced coking resistance grown in situ by redox exsolution. *Nature Communications*. 6.
- Neagu, D., Papaioannou, E.I., Ramli, W.K.W., Miller, D.N., Murdoch, B.J., Ménard, H., Umar, A., Barlow, A.J., Cumpson, P.J., Irvine, J.T.S. & Metcalfe, I.S. (2017) Demonstration of chemistry at a point through restructuring and catalytic activation at anchored nanoparticles. *Nature Communications*. 8 (1), 1855.
- Neagu, D., Tsekouras, G., Miller, D.N., Ménard, H. & Irvine, J.T.S. (2013) In situ growth of nanoparticles through control of non-stoichiometry. *Nature Chemistry*. 5 (11), 916–923.
- Otto, S.K., Kousi, K., Neagu, D., Bekris, L., Janek, J. & Metcalfe, I.S. (2019) Exsolved Nickel Nanoparticles Acting as Oxygen Storage Reservoirs and Active Sites for Redox CH₄ Conversion. *ACS Applied Energy Materials*. 2 (10), 7288–7298.
- Papaioannou, E.I., Neagu, D., Ramli, W.K.W., Irvine, J.T.S. & Metcalfe, I.S. (2019) Sulfur-Tolerant, Exsolved Fe–Ni Alloy Nanoparticles for CO Oxidation. *Topics in Catalysis*. 62 (17–20), 1149–1156.
- Papaioannou, E.I., Neagu, D., Ramli, W.K.W., Irvine, J.T.S. & Metcalfe, I.S. (2018) Sulfur-Tolerant , Exsolved Fe – Ni Alloy Nanoparticles for CO Oxidation. *Topics in Catalysis*. 0 (0), 0.
- Parlett, C.M.A., Wilson, K. & Lee, A.F. (2013) Hierarchical porous materials: Catalytic applications. *Chemical Society Reviews*. 42 (9), 3876–3893.
- Peng, R., Li, S., Sun, X., Ren, Q., Chen, L., Fu, M., Wu, J. & Ye, D. (2018) Size effect of Pt nanoparticles on the catalytic oxidation of toluene over Pt/CeO₂ catalysts. *Applied Catalysis B: Environmental*. 220462–470.
- Sie, S.T. & Krishna, R. (1998) Process development and scale up: II. Catalyst design strategy. *Reviews in Chemical Engineering*. 14 (3), 159–202.

T., K., H., G., R., H. & J., R. (1998) Preparation of catalysts VII : proceedings of the 7th International Symposium on Scientific Bases for the Preparation of Heterogeneous Catalysts, Louvain-la-Neuve, Belgium, September 1-4, 1998. *Preparation of Catalysts VII*. 1. 807–815.

5 Development and testing of an exsolved perovskite system with exo/endo-nanoparticles for low temperature methane activation

In this chapter the methodologies developed, and insight gained on exo/endo-particle systems are employed for the design of a new composition that will have the ability to drive CH₄ activation temperature even lower. To achieve this, cobalt is incorporated in the previously designed system aiming to increase the surface reactivity of the material as well as increase the oxygen transport through the bulk. The new system's characteristics are tuned according to previous findings and its performance for methane activation is tested. The results presented have been published and this chapter is based on (Kousi, Neagu, Bekris, Cali, et al., 2020).

5.1 Introduction

Up to this point in this study, it has been demonstrated that the exsolution concept can be controlled to produce composite systems with particles on the surface as well as in the bulk leading to materials with increased reactivity. This, led to materials with the ability to convert methane to syngas selectively at much lower temperatures than their supported equivalents with similar loading (Kousi, Neagu, Bekris, Papaioannou, et al., 2020). Employment of the systems as oxygen carriers for the conversion of methane via chemical looping showcased their applicability for the technology while further study of variants of the system has proved that such systems are reproducible, and their emergent properties can be exploited further. Furthermore, insight has been gained on the involvement of the system's components on its performance and the ability to tune the materials performance via microstructural and nanostructural tailoring has been investigated.

In this chapter, the methodologies and strategy for creating and tuning these systems are employed for the creation of a system with even higher reactivity targeted for its application against methane conversion and as an OCM for the low temperature and coke free methane conversion to syngas. This will serve as a proof of concept that the findings of this study can be employed for the production of even more reactive systems for targeted applications. Here, the system is developed for tackling the long sought after in energy conversion applications problem of lowering the temperature at which methane is converted to valuable products while maintaining selectivity, thus eliminating the need for product separation despite the conversion taking place at moderate conditions (Cui et al., 2018). Aiming to produce a system with even better performance, the endogenous-exsolution concept is employed once again, but for the production of a more reactive system both the surface reactivity of the material as well as its oxygen transport through the bulk should be increased. To achieve this, cobalt (Co) is incorporated in the previously designed systems as Co has been shown to improve oxide-ion transport in perovskites (Shao & Halle, 2004). Furthermore, experimental and computational studies have shown that mixed Co-Ni spinel oxides have the ability to activate methane at much lower temperatures than individual Ni or Co oxides due to the local crystallographic and electronic structure characteristics (Tao et al., 2015; Horlyck et al., 2018; Xu et al., 2016; Lim, Cho, Yang, M. H. Engelhard, et al., 2015; Wu et al., 2019; Zeng et al., 2019; Feng et al., 2018). Additionally, as demonstrated here in Chapter 4 and in simpler surface exsolved systems in literature, increasing the porosity of the samples can lead to the enhancement of their surface reactivity and oxygen diffusion (Tang et al., 2019; Kousi, Neagu, & Metcalfe, 2020). The newly designed system's characteristics and performance are investigated and compared to that of the system studied above, showcasing the successful implementation of methods leading to a better performing system.

5.2 Design and exsolution of $\text{La}_{0.7}\text{Ce}_{0.1}\text{Co}_{0.3}\text{Ni}_{0.1}\text{Ti}_{0.6}\text{O}_{3-\delta}$

The design of the new system is based on the $\text{La}_{0.8}\text{Ce}_{0.1}\text{Ni}_{0.4}\text{Ti}_{0.6}\text{O}_{3-\delta}$ (referred to as LCNT in this chapter) system which has been the studied composition throughout this study. In order to modify the system for the exsolution of CoNi particles, 0.3 out of 0.4 of Ni is replaced with Co in the perovskite $\text{La}_{0.8}\text{Ce}_{0.1}\text{Ni}_{0.4}\text{Ti}_{0.6}\text{O}_{3-\delta}$ (LCNT). Following the design principles presented in subchapter 3.2 the A-site cation ratio is adjusted in order to compensate for the charge

difference between Co (2+/3+) and Ni (2+). This leads to the production of $\text{La}_{0.7}\text{Ce}_{0.1}\text{Ni}_{0.1}\text{Co}_{0.3}\text{Ti}_{0.6}\text{O}_{3-\delta}$ (LCNT). The new composition is synthesized by the modified solid-state method described in detail in sub-chapter 2.2.1 and the pellets are sintered at 1400°C where the perovskite phase is formed.

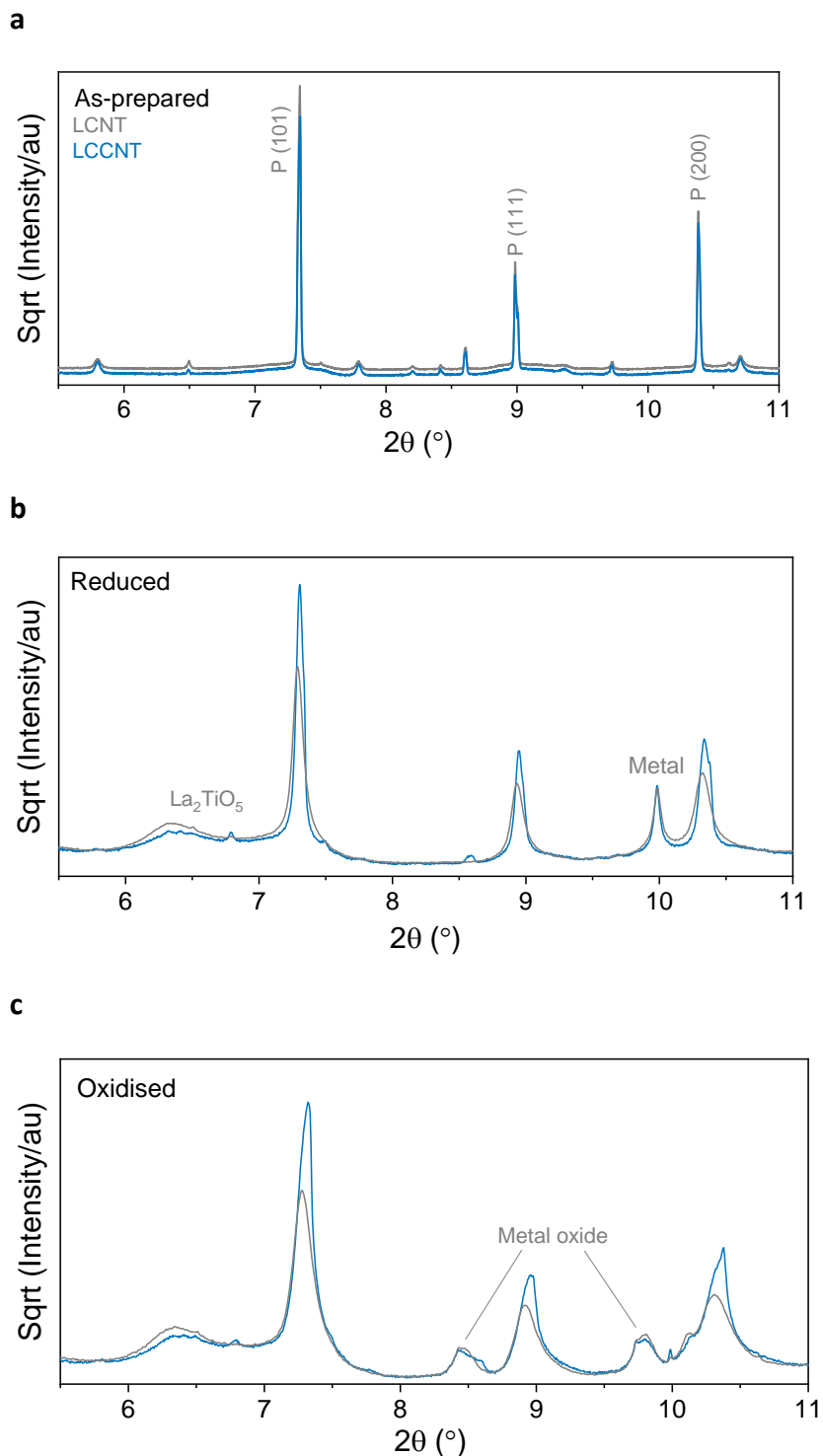


Figure 5.1 Room temperature synchrotron XRD patterns of the synthesized exo/endo-systems in as-prepared, reduced (exsolved) and oxidised stage. XRD patterns of the newly synthesised $\text{La}_{0.7}\text{Ce}_{0.1}\text{Ni}_{0.1}\text{Co}_{0.3}\text{Ti}_{0.6}\text{O}_{3-\delta}$ (LCCNT) system (blue) compared to those of the

$\text{La}_{0.8}\text{Ce}_{0.1}\text{Ni}_{0.4}\text{Ti}_{0.6}\text{O}_{3-\delta}$ (LCNT) system (grey) in as prepared (a), reduced (b) and oxidised stage (c).

The resulting pellets are crushed and sieved to produce powders with perovskite particle size of 80-160 μm and tested for purity via synchrotron X-ray diffraction and Rietveld analysis. The characteristics and performance of LCCNT are compared to those of LCNT here and throughout the study. The prepared powders are single phase, exhibiting high degree of crystallinity which are illustrated by the sharp peaks in the X-ray diffraction patterns presented in Figure 5.1. The powdered samples are then reduced under a 5% H_2/He stream at 1000 $^\circ\text{C}$ for 10 h in order to exsolve nanoparticles on and under the surface. The micro and nanostructure of the resulting exsolved samples are presented in Figure 5.2. It is demonstrated that the employed design principles successfully lead to the production of samples with exo/endo- nanoparticles with the expected characteristics. The surface-exsolved exsolved particles differ greatly in terms of size and population as compared to the ones exsolved in the bulk. Exoparticles are 40 nm in diameter while endo particles are much smaller at approximately 10 nm while their population is much higher. A comparison between the exo- and endo- particle size and population is presented in Figure 5.2d at a cross-section between surface and bulk.

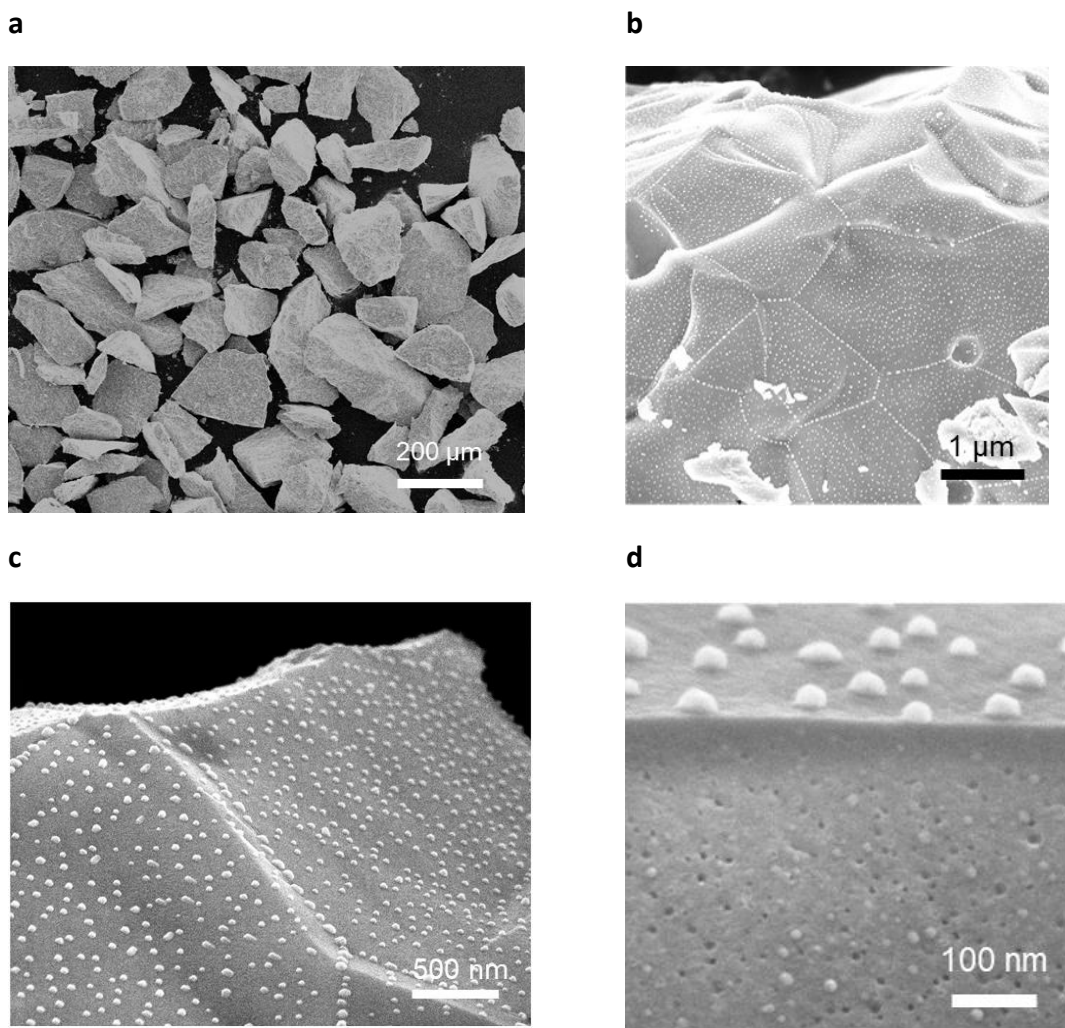


Figure 5.2 **SEM micrographs of $\text{La}_{0.7}\text{Ce}_{0.1}\text{Co}_{0.3}\text{Ni}_{0.1}\text{Ti}_{0.6}\text{O}_{3-\delta}$ (LCCNT)**. a) Overview of the sample grains (80-160 μm), b) overview and c) detail of the surface of the perovskite post reduction (exsolution) in 5% H_2/Ar atmosphere at 1000 $^\circ\text{C}$ for 10 h, d) cross-section view after exsolution revealing exo- and endo- particles and their different characteristics.

Phase analysis on the exsolved samples reveals that the high population and dispersion of bulk nanoparticles resulted in a decrease in the perovskite host crystallite size and an increase in its micro-strain by a factor of 2. The degree of exsolution was quantified by refining the XRD patterns acquired after the reduction treatment of the samples (Figure 5.1b and Figure 5.3). It was determined that the majority of the metal substituted in the perovskite lattice successfully exsolved. Approximately 0.3 was exsolved in the case of LCCNT and 0.33 in the case of LCNT out of the total 0.4 metal initially substituted in the lattice of the perovskite. This amounts to approximately 8 out of 10 wt.% of the total metal content substituted in the lattice of the perovskite. XRD analysis further reveals that post reduction reflections attributed to La_2TiO_5 had developed as a result of the extreme extent of exsolution. This has been observed before in Chapter 3 and once again is determined to be a spectator species with no real involvement to the exsolution or the activation process since it remains unchanged throughout the redox treatment process that the material has undergone. It should be noted that the two compositions are designed

so that the overall extent of exsolution is similar, thus allowing the deconvolution the chemical form nano- and micro structural effects on reactivity (Xu et al., 2016; Wu et al., 2019; Guerrero-Caballero et al., 2019).

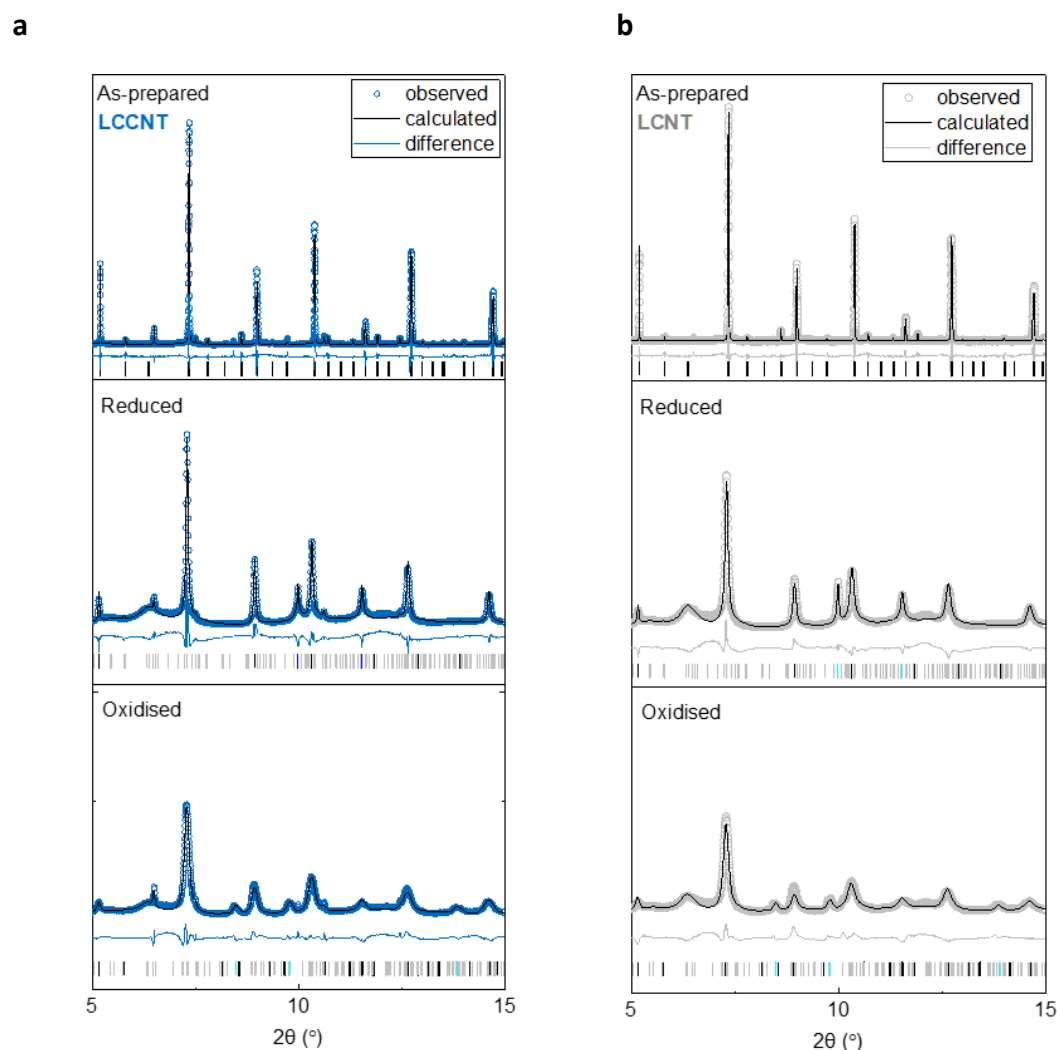


Figure 5.3 Phase analysis via Rietveld refinement of the synthesised exo/endo- systems. Room temperature synchrotron XRD patterns of a) LCCNT (blue) and b) LCNT (grey) in as-prepared, reduced and oxidised states.

Examination of the samples post oxidation reveals that all the metal phase is converted to the metal oxide phase. This is observed in the X-ray diffraction pattern (Figure 5.1b) and confirmed via the refinement analysis (Figure 5.3). Peak broadening is also observed for the perovskite which reveals a further increase in the microstrain of the host lattice, of a factor of 5 as compared to the reduced state. This is attributed to the high dispersion of the nanoparticles in the bulk and their chemical expansion as the transition from metal-to-metal oxide. Both LCNT and LCCNT samples adopt the same rock salt crystal structure following their oxidation. This indicated that both Ni and Co are present in a +2 oxidation state as Co would be expected to adopt a higher +3 oxidation state if a spinel type crystal structure was present. This is usually not expected since when Co metal is oxidised in air usually forms a $\text{Co}^{2+}/\text{Co}^{3+}$ spinel oxide

(Wang et al., 2016; Kessler et al., 1989). However, in this case it seems that this transformation was inhibited possibly due to the extensive strain which induced a compressive force onto the particles by the perovskite.

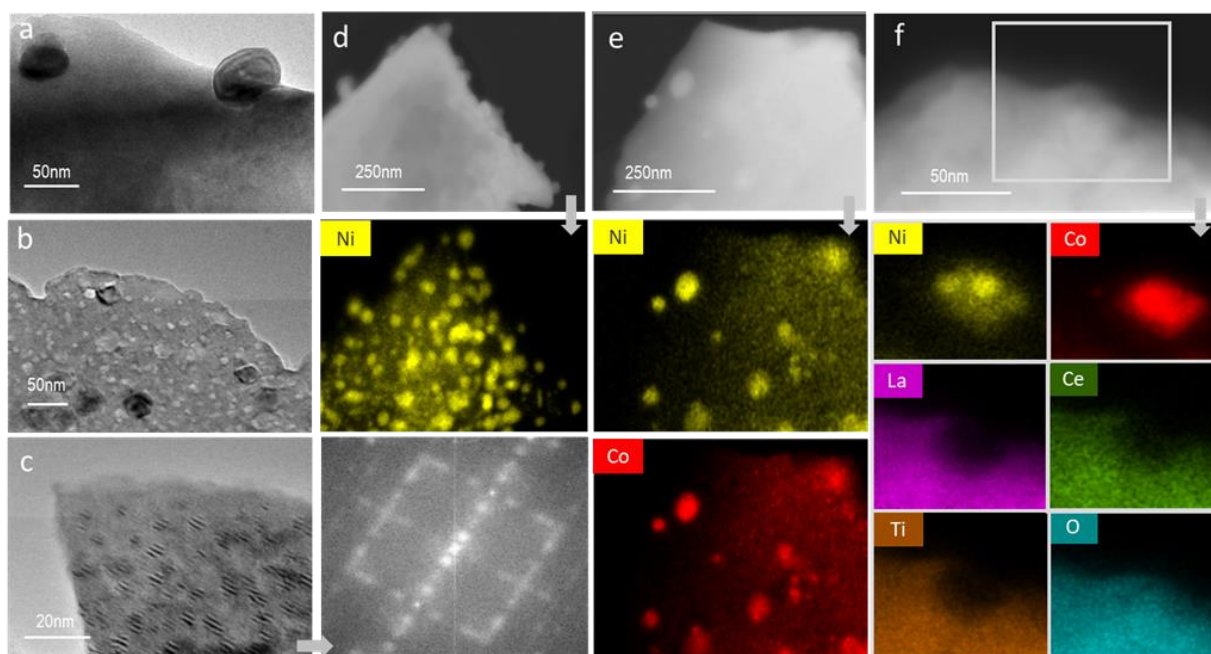


Figure 5.4 **Examination of the nanostructure of the Co and Ni-based samples via TEM.** a) Detail of a surface particle embedded in the perovskite matrix b) Overview of the perovskite matrix with exo- and endo- nanoparticles. c) Moire patterns, characteristic of the samples' morphology and FFT pattern. STEM images and corresponding EDX map of d) Reduced LCNT sample with mapping indicating the Ni exsolved particles. e) Reduced LCCNT sample demonstrating the presence of CoNi particles f) Oxidised LCCNT sample with a bimetallic particle with both Co and Ni components on the surface and demonstration of the socket in oxidised form by EDX mapping (Kousi, Neagu, Bekris, Cali, et al., 2020).

The existence of surface and subsurface nanoparticles, as well as their anchored nature is confirmed by further examining that materials microstructure via TEM (Figure 5.4). The endo particles appear to be in close proximity and surprisingly highly aligned crystallographically with the parent perovskite, forming a distinguishable Moire pattern (Figure 5.4c). This alignment, as determined earlier in this work (Chapter 3), is expected to facilitate the enhanced oxygen exchange between the submerged nanoparticles and the perovskite matrix. Additionally, the highly crystallinity of the prepared material is confirmed by the FFT patterns (Figure 5.4c) which indicate the existence of superlattice structures which are possibly linked with the La_2TiO_5 phase observed earlier (Figure 5.1b).

Study of the surface and bulk of the reduced LCCNT system was also done via EDX mapping (Figure 5.4d, e). Both exo- and endo-nanoparticles were found to consist of Ni metal of the LCNT sample and both Co and Ni homogeneously mixed throughout each particle for the LCCNT sample. The particles were also found to remain as mixed Co and Ni oxides after the oxidation of the sample, but with a tendency for Ni to segregate at the core of the particle but with Co

remaining more evenly dispersed through the particles. The deep anchorage of the particles is once again confirmed by further examination of the EDX images with La, Ce and Ti found to form a 'bay' shaped structure around the particles which contains Co, Ni and O. It should be highlighted that the socketed nature of the nanoparticles is retained even in their oxidised state, which, to the best of our knowledge, is believed to be the first time yet to be showcased so conclusively by EDX analysis.

5.3 Employment of the system for methane activation

The systems' reactivity against methane is investigated via temperature programmed reaction experiments. The conversion of methane and product selectivity of LCCNT are monitored and compared to that of the only Ni based exo/endo- exsolved system LCNT and a Ni/Al₂O₃ catalyst with high surface and similar loading of active metal by weight. The latter is considered the state-of-the-art material for various hydrocarbon-based transformations.

The newly developed LCCNT system's methane activation profile is characteristic of an exsolved material and as expected shares major similarities with that of the LCNT counterpart (Figure 5.5a). The perovskite appears to be able to mediate O transfer between the buried nanoparticle and the CH₄ stream, which is activated on the surface via the strained nanodomain network formed within the system due to the extensive exsolution in the bulk (Kousi, Neagu, Bekris, Papaioannou, et al., 2020). The activation temperature for both only Ni based samples (LCNT and Ni/Al₂O₃) is found to be identical at 580 °C but with the exo/ endo-particle system displaying higher resistance to carbon deposition and overall faster conversion as indicated by the CO₂ produced during the TPO experiment (Figure 5.5d, e) and the shorter temperature window through which the reaction takes place (Figure 5.5a), respectively. The activation window is also narrow for the NiCo- based sample which activates methane at the even lower temperature of 530 °C and with its activation profile consisting of a characteristic sharp peak followed by a broader one at 570 °C, again characteristic of exo/endo- particle systems. Selectivity is high with syngas being produced at the desirable for methanol production ratio of H₂:CO 2:1. For both exsolved systems selectivity to CO is high at 88% and 90% for LCNT and LCCNT, respectively while the Ni/Al₂O₃ system was 87% selective to carbon deposition. Overall, this showcases that doping of the LCNT system with Co and following the design principles developed in this study, successfully lead to a more reactive system with a methane activation temperature 50 °C lower, while syngas selectivity was maintained.

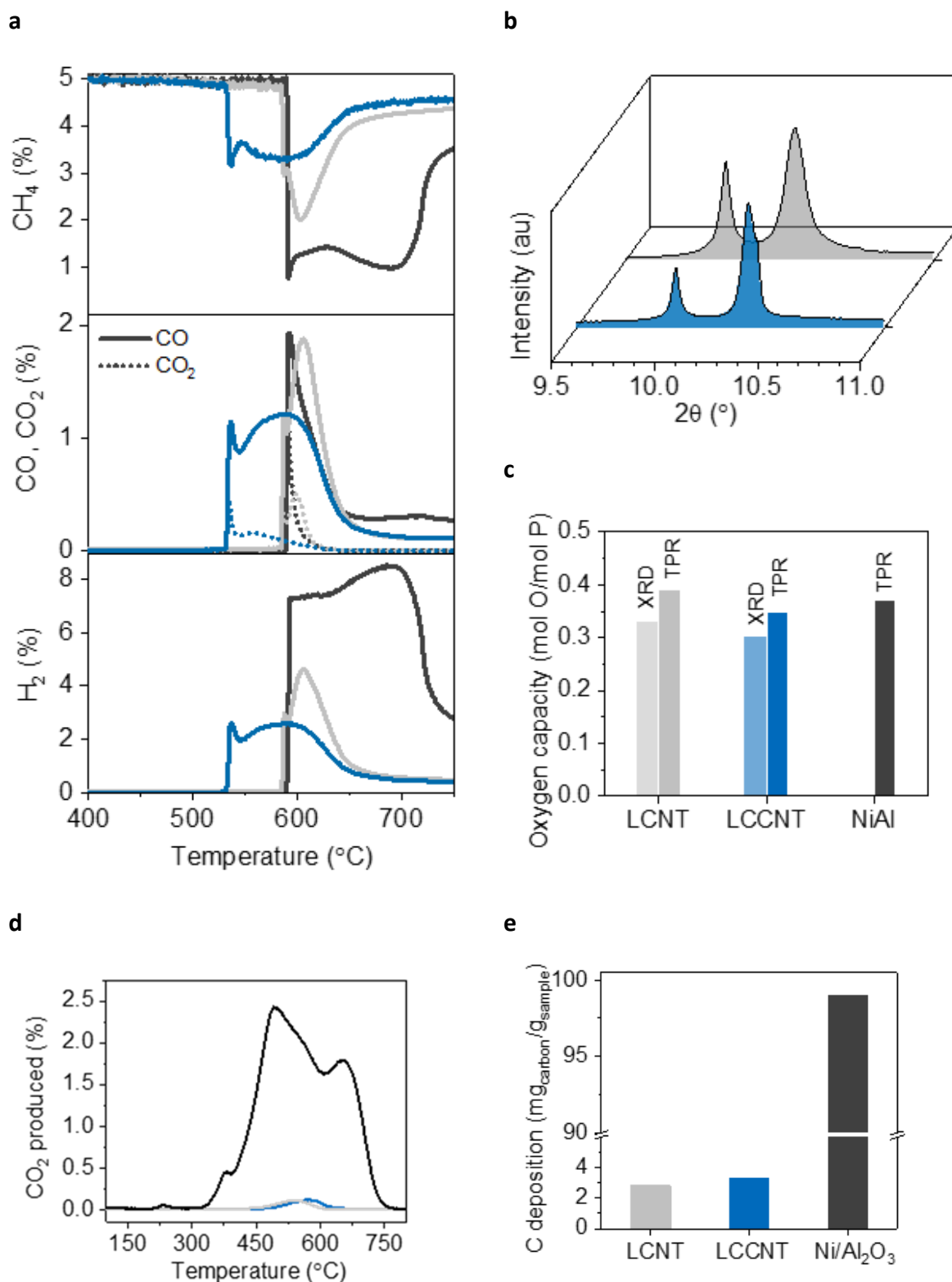


Figure 5.5 **Employment of the LCNT system for the activation of methane.** a) Consumption of methane and conversion to products (CO, CO₂ and H₂) for LCCNT, LCNT and Ni/Al₂O₃. b) X-ray diffraction patterns of LCCNT and LCNT. c) Calculated oxygen capacity of the two exsolved samples via the experiments described in a and Rietveld refinement. d) Temperature programmed oxidation experiment (TPO) following the activation experiment described in a.

e) Carbon deposition calculated by integration of the curves resulting from the TPO experiment presented in d (Kousi, Neagu, Bekris, Cali, et al., 2020).

The oxygen capacity of LCCNT is calculated via Rietveld refinement as well as via the TPR experiment (Figure 5.3 and Figure 5.5b, c). Interestingly, it is found that it is identical to that of LCNT which reveals that the observed increased reactivity is not a result of higher oxygen capacity but rather implies that it stems from synergistic effects between the mixed Co and Ni contained in the particles of the system (Guo et al., 2020). This behaviour has been demonstrated before in other catalytic processes, where employment of Ni-Co systems with high Co loadings lead to an increase in activity of more than one magnitude in different catalytic applications (Neagu et al., 2017; Lim, Cho, Yang, M. H Engelhard, et al., 2015). The claim that the activity enhancement observed here stems from the different chemistry of the particles is also supported by the fact that although activation starts at a lower temperature, the overall amount of methane converted is the same as that from LCNT despite the activation spanning over a longer temperature window. This indicates that the CoNi particles are more active, possibly due to the higher oxidation states they can achieve due to Co while the overall capacity of the system remains the same.

The systems resistance to carbon deposition is investigated by TPO carried out after the activation experiment. The two exsolved systems display similar type and amounts of deposited carbon (Figure 5.5d) which are quantified and found to be minimal (Figure 5.5e) showcasing the coke resistant nature of the exsolved exoparticles. When compared to that calculated of the state-of-the-art catalyst for methane conversion Ni/Al₂O₃, the results are more impressive as the coke deposited is quantified to be almost two orders of magnitude higher to that of the exsolved systems (3 vs 100 mg_{carbon}/g_{sample}) over a similar temperature range. From the TPO experiment assignment of the carbon type was also possible, as carbon was found to gasify at different temperatures ranging from 350 to 750 °C, which from literature are attributed to highly crystalline and fibrous profiles (Papadopoulou et al., 2012; Fan et al., 2009; Chen et al., 2005). The Ni/Al₂O₃ sample in particular exhibits three different kinds as indicated by the three peaks observed in the TPO experiment while only one is found to be present on the exsolved samples.

SEM analysis of the surface of both exsolved samples before and after testing illustrate that all particles remain well anchored, retaining their position and size after the redox cycle (Figure 5.6a). Photos of the LCCNT are presented which are also representative of the LCNT sample, whose surface after the redox transformation has been extensively studied in Chapter 3. Additionally, it is also found that the oxidised particles have been affected by the Kirkendall effect, which has been reported to be characteristic of exsolved Co nanoparticles (Neagu et al., 2017). This describes the formation of hollow-core nanoparticles upon oxidation due to the migration of metal ions outward instead of the diffusion of oxide ions inward. Additionally, the conclusions about carbon deposition reached above are confirmed as negligible amounts of deposited carbon are seen on the surface after testing, once again highlighting the high tolerance of exsolved particles against coking even at harsh conditions. The same cannot be said for the Ni/Al₂O₃ sample that displays high amounts of deposited carbon covering its surface.

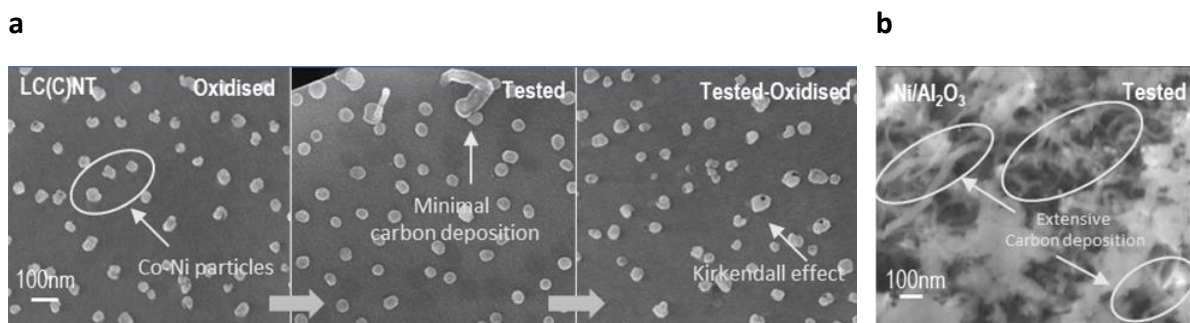


Figure 5.6 **SEM micrographs of tested samples.** a) SEM images of LCCNT, also representative of LCNT (hence LC(C)NT), before and after testing and after the carbon oxidation experiment after testing. b) Image of the Ni/Al₂O₃ sample after testing illustrating extensive carbon fibre formation on the surface of the sample (Kousi, Neagu, Bekris, Cali, et al., 2020).

Aiming to gain a better understanding on the effect Ni substitution of Ni has on the surface of the system and the particles themselves, both are examined via X-ray photoelectron spectroscopy before and after exsolution, oxidation and testing (Figure 5.7). The experiments were conducted by collaborators at Imperial College acknowledged in the acknowledgements section. It is revealed that the oxidation state and coordination environment of La, Ce and Ti for the Ni based sample (LCNT) remain unaltered throughout the redox transformation. La is found to be in its +3 oxidation state as indicated by a split of 4.6 eV between the main peak and its shake up satellite (Sunding et al., 2011), with Ti being in its +4 state. For Ce, the 3d spectra consist of only two peak pairs which correspond to the Ce 3d 4f²L (u0 and v0) and Ce 3d 4f¹L (u' and v') indicating that Ce is in its +3 oxidation state (Kotani et al., 1987; Pfau & Schierbaum, 1994). A small peak at the binding energy of 916.6 eV is also observed and found to correspond to the Ce 3d_{3/2} 4f⁰L (v'') in the +4 oxidation state, but overall it is concluded that Ce is found mainly in the +3 oxidation state (Figure 5.7a-c) and most likely these ions do not play an important role in the redox transformation. This is supported by the fact that the biggest change in oxidation state is found to occur for the Ni as observed in the Ni L₃M₄₅M₄₅ Auger spectra (Figure 5.7i). There, the vast majority of Ni which is in the form of NiO but also to as Ni(OH)₂ to some degree (Biesinger et al., 2012) in the as-prepared state, is observed to convert to its metallic state upon exsolution (Figure 5.7i). However, it should also be noted that some Ni²⁺ ions are expected to remain in the perovskite lattice since not all the Ni substituted in the perovskite matrix is actually exsolved (as found in sub-chapter 5.2 and subchapter 3.2). Once oxidised again, all Ni is converted to NiO and is present exclusively in this form before reverting back to Ni metal entirely after testing. The CoNi (LCCNT) system's behaviour is similar for the La, Ce, Ti and Ni components (Figure 5.7i) with Ni undergoing big redox changes while La, Ce and Ti remain unaltered during the redox transformation. Characteristically, Ni is found to behave the same as in the only Ni containing sample (LCNT) but here changes in Co are also observed. Initially, Co is found to be in its +2 oxidation state and converted to metal post reduction, with some Co²⁺ remaining in the perovskite matrix even after prolonged reduction. Post oxidation, Co is found in a similar to a Co₃O₄-type state being present in both +3 and +2 states. After testing where the sample was exposed to reducing conditions once again, almost all of Co converts to metal but again with some

remaining in Co^{2+} form, possibly in the perovskite matrix (Figure 5.7j). From the O 1s peak (Figure 5.7d, h) it is revealed that the coordination environment of O remains the almost unchanged, but the peaks appear to broaden at higher energies. This may be attributed to oxygen in a different environment, such as coordination to Co^{3+} and/or to surface hydroxyl groups. From this analysis it is revealed that the species that are actively involved in the redox transformation are Ni, which alternates between its +2 and metal state, and Co which cycles between its higher oxidation states of +3 and +2 and its metallic state. The ability of Co to reach and cycle between these slightly higher oxidation states could be part of the reason why activation of methane at a lower was achieved by the CoNi-based system.

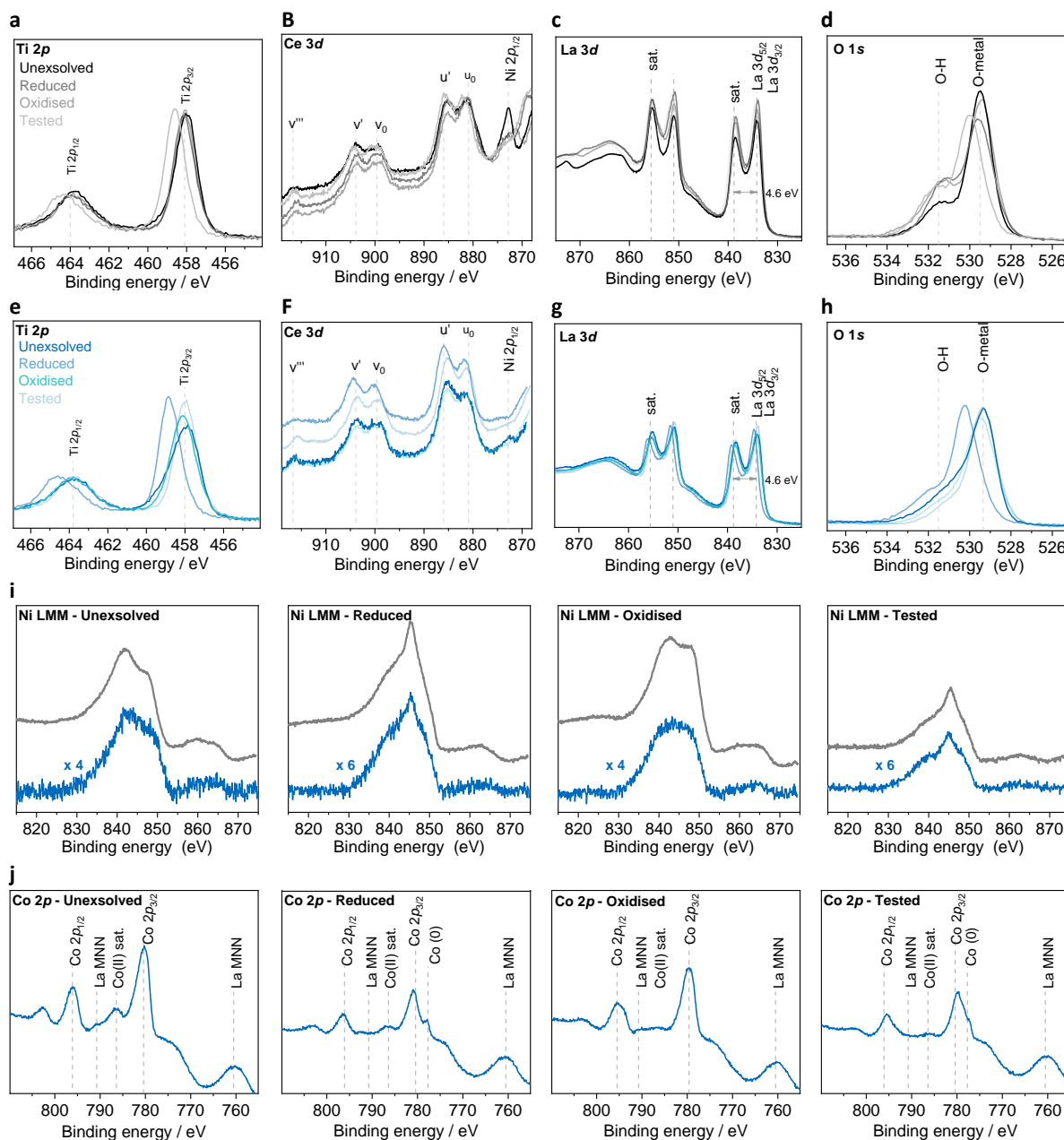


Figure 5.7 Surface analysis of the Ni and the Co-based exo/endo-particle systems via XPS. Core level XPS spectra for LCNT of **a.** Ti **b.** Ce **c.** La **d.** O₂. Core level XPS spectra for LCCNT of **e.** Ti **f.** Ce **g.** La **d.** O₂. **i.** Core level XPS spectra of Ni for the as-prepared (unexsolved), reduced

(exsolved), oxidised and tested LCNT system. **j.** Core level XPS spectra of Co for the as-prepared (unexsolved), reduced(exsolved), oxidised and tested LCCNT system (Kousi, Neagu, Bekris, Cali, et al., 2020).

5.4 Activity enhancement by microstructural modification

As demonstrated in Chapter 4 of this study, the activity of exo/ endo- particle systems can be enhanced by tuning the systems' microstructure. Without inflicting chemical changes on the surface and only by increasing the materials porosity, the grain size of the perovskite can be reduced leading to increasing the extent of surface exsolution since more ions can be drawn to the surface. Additionally, pore surface formation and cleaved surfaces can create an intricate combination of surfaces available for exsolution which if tuned can lead to an even higher number of active sites available on the surface. Hence, microstructural modification in turn is linked with exoparticle size characteristics (size and population) which were found to play a key role on the systems activity. If tailored, can lead to the generation of systems with a combination of smaller and higher in population catalytic sites available on the surface which are able to activate methane more effectively while also facilitating more efficient oxygen transport from the bulk.

Here the porosity of the LCCNT sample is increased by two approaches. Firstly, the sintering temperature where the perovskite is formed is reduced by 50 °C. This allows for a higher degree of porosity to be achieved as over-sintering is avoided, which in general leads to a less porous structure, while a single-phase material is still attainable. In addition, the methodology for controlling materials porosity described in Chapter 4 is employed. A pore former (glassy carbon) is mixed with the material before being pressed into pellets and sintered. Here, approximately 10 % of pore former is mixed which in combination with the lower sintering temperature (1350 °C in air) leads to a system with increased porosity. The relative porosity of the resulting material is measured via image analysis and determined to be approximately 20 %, which is a 15 % increase from the microstructurally unmodified material. The difference in porosity before and after tuning, as well as the difference inflicted in particle characteristics due to the modification are presented in Figure 5.8 a and b, respectively.

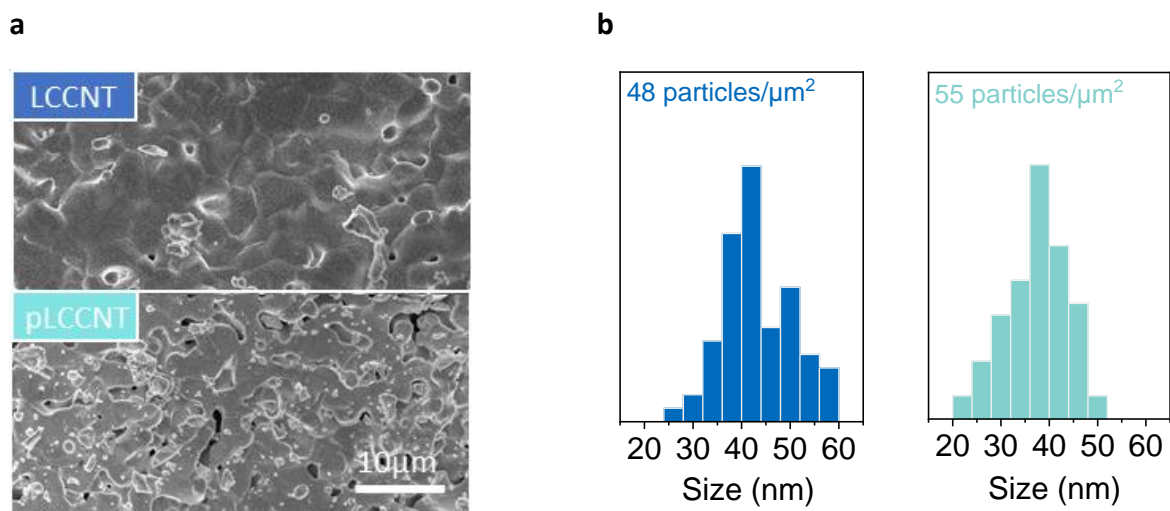


Figure 5.8 **Microstructural modification of the LCCNT exo/endo-particle system.** a) Overview of the sample before (blue) and after (teal) porosity enhancement. b) Particle size analysis of the exoparticles for the systems described in a.

The changes in the nanostructure of the system, as inflicted by the tuning of the microstructure, are also revealed via synchrotron X-ray analysis. The Ni peak corresponding to the reduced Ni nanoparticles is found to adopt the expected shape of a sharp peak combined with a broader one, as demonstrated before in this study, but for the modified sample the second peak appears to be much broader. This indicates that there is a bimodal distribution of nanoparticle size in the modified material while in the unmodified the particles appear to have a more uniform size (Figure 5.9b). Overall, however, as confirmed via particle analysis (Figure 5.8b), modifying the microstructure of the sample successfully lead to the exsolution smaller exoparticles under the same reduction conditions. The particle distribution of exoparticles for the pLCCNT appears to have shifted to lower values with the average particle diameter decreasing from 40 to 30 nm, accompanied by a slight increase in population. This combination of smaller and more numerous active sites on the materials surface, as demonstrated in Chapter 4, is expected to increase the reactivity of the sample by lowering the temperature in which methane is activated (Touahra et al., 2019; Akbarzadeh et al., 2019; Papadopoulou et al., 2012; Choudhary & Choudhary, 2008).

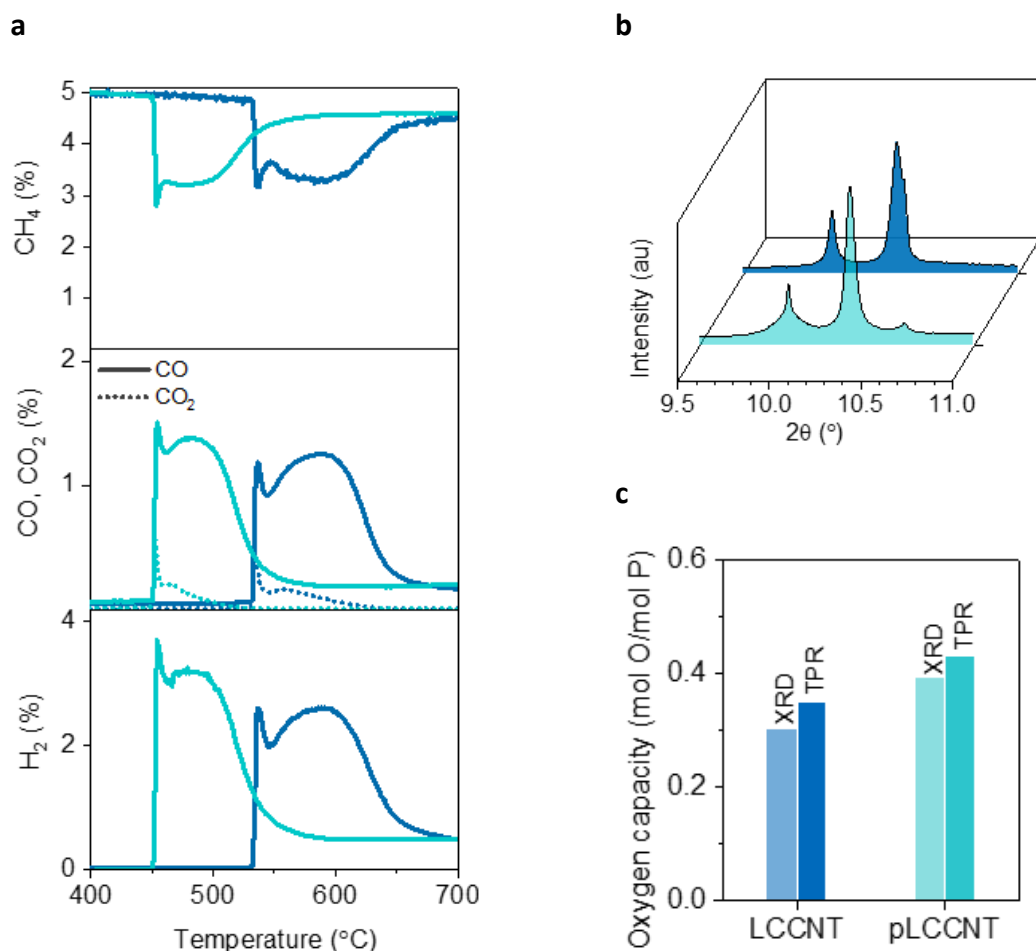


Figure 5.9 **Employing the microstructurally modified LCCNT system for methane conversion.**

a) Conversion of methane to syngas against temperature by the microstructurally modified (teal) and unmodified (blue) LCCNT systems. b) X-ray diffraction patterns revealing the change in microstructure and in turn nanostructure between the systems tested in a. c) Oxygen capacity of the two LCCNT systems calculated via refinement and the TPR experiment presented in a.

As expected, when the modified system was employed for the activation of methane (pLCCNT) it is found to activate methane at 450 °C, a temperature almost 80 °C lower than that of the original (unmodified) LCCNT system, while displaying similar oxygen capacity and selectivity (Figure 5.9a). In detail, selectivity over syngas remains high with a CO:CO₂ ratio higher than 9:1 and minimal carbon deposition across both samples, as confirmed by the carbon balance for the experiment which was more than 99 %. This performance is impressive, as for similar processes temperatures of around 900 °C are reported in literature for similar conversions and selectivity to be achieved (Dai et al., 2006). Similar performances have been reported in other studies with a similar goal of lowering the activation temperature of such processes but in noble metals were used to achieve them (Haribal et al., 2019). Furthermore, the increased porosity appears to have sped up oxygen exchange between the bulk and the gas phase since the methane activation window for pLCCNT stretches for 15 min, which is 3-4 min faster than the time the unmodified sample requires for achieving the same overall conversion. Although

the results presented here are impressive, as they result from a kinetic study, further optimization is needed in order for such systems to be applied in an industrial level. However, this demonstrates once again how microstructural tailoring of exo/ endo- systems can lead to a dramatic increase in their performance and opens new horizons for tuning these materials not only directly through their chemistry. Thus, microstructural control can be used to influence the nanostructure indirectly leading to emergent functionalities.

5.5 Application of the system as an OCM for the conversion of methane via Chemical Looping
Having tuned the system's performance, its applicability and long- term stability is tested by employing it as OCM for the Partial Oxidation of Methane via Chemical Looping (CLPO). The results from the TPR experiments presented above as well as literature reports on similar application are used for determining the operating conditions. Cycling is done at 550 °C and 30 mL min⁻¹ (NTP) of reactants are flown over 300mg of the material.

As presented in Figure 5.10a, conversion of methane stabilises fast and remains constant at 60%, while selectivity to CO is maintained at 80 % for 30 cycles. The fast stabilisation is interesting, as most OCMs applied for CL reported in literature exhibit a drop in activity and variable selectivity for the first 10-20 cycles before they stabilise or continue to decline, or a much higher temperature is required for achieving conversions similar to the ones observed here (Wong et al., 2017; Li et al., 2019). It is thus demonstrated that it is possible for endo/ exo- particle systems to be tuned to have a high initial performance and maintain it over long-term cycling. Additionally, no carbon deposition is found to take place throughout the experiment, despite the low temperature and high conversion, as no CO₂ is produced during the oxidation half cycle which would be indicative of deposited carbon being gasified (Figure 5.10b-d).

Analysis of the surface of the system via SEM after long-term testing reveals that the system shows minimal signs of degradation. From the overview images of the system no cracks are observed in the material showcasing the mechanical durability of its microstructure (Figure 5.10e). Furthermore, the nanostructure of the system also appears to remain almost intact, with most nanoparticles remaining well-socketed and showing minimal signs of agglomeration after the repeated redox cycling (Figure 5.10e). This was also confirmed by the conversion analysis (Figure 5.10a) where no decrease in activity or change in selectivity was observed by the 30th cycle, indicating that the components of the system remained unaltered and able to perform.

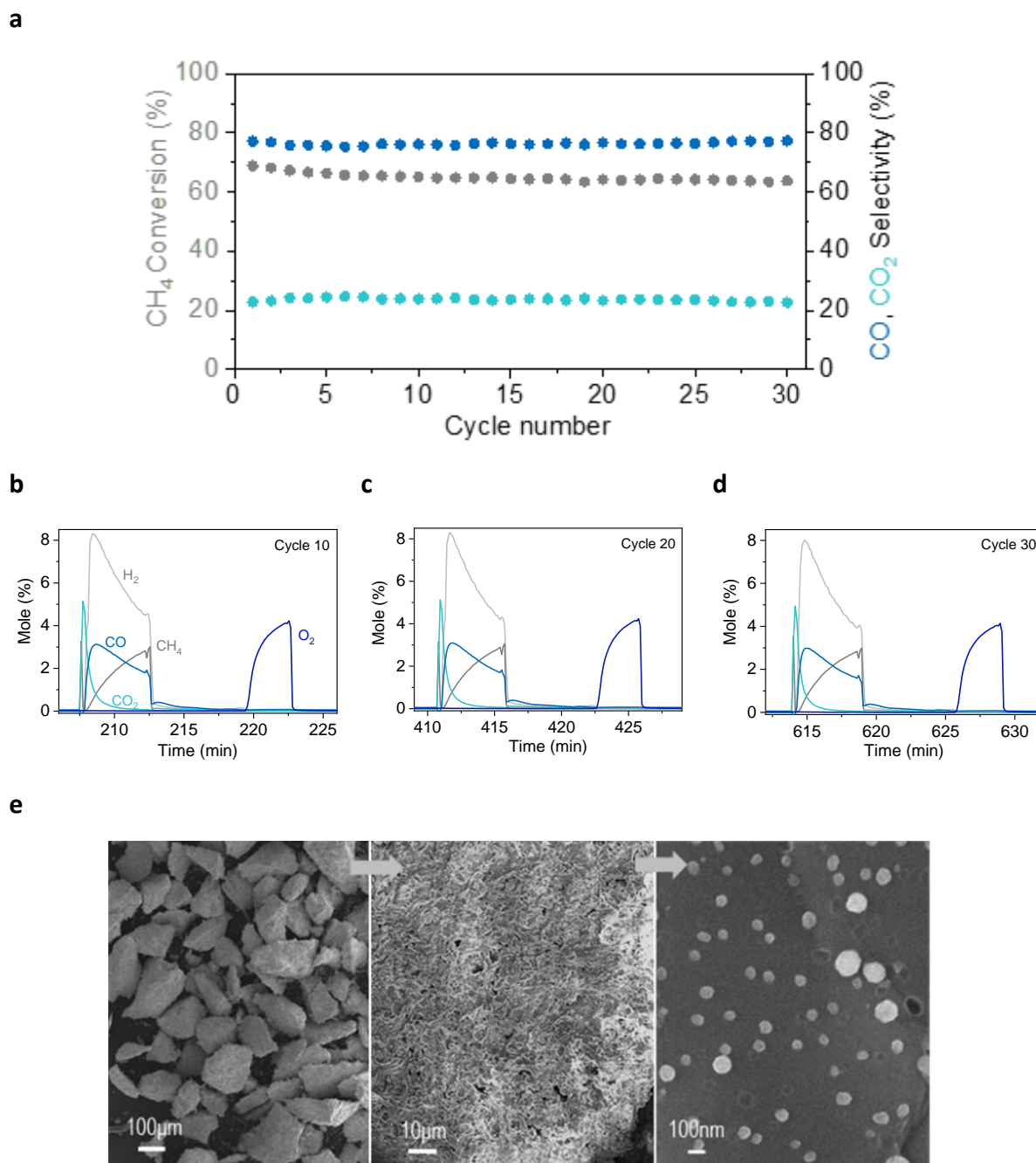


Figure 5.10 **Application of the pLCCNT exo/endo-particle system as OCM for the low temperature conversion of methane via Chemical Looping.** a) Conversion of methane and selectivity to carbon products (CO and CO₂) through cycling b) Outlet gas composition over time in the 10th cycle c. 20th cycle d. and 30th cycle e. SEM images of the surface of pLCCNT after the cycling experiment presented in a (Kousi, Neagu, Bekris, Calì, et al., 2020).

5.6 Conclusions

The methodologies developed and insight gained in previous chapters of this study were successfully applied for the creation of an exo/endo- particle perovskite system capable of exsolving NiCo nanoparticles for its targeted application of lowering the temperature at which

methane can be converted to useful products. While using a system with base metal nanoparticles the activation temperature was lowered from 600 °C to 450 °C. This was achieved by employing the design principles presented in Chapter 3 for doping the Ni system studied previously with Co, and by further tuning its microstructure according to the insight gained in Chapter 4.

The systems produced display a high degree of exsolution with a high fraction of the doped metal ions being exsolved as endoparticles embedded in their bulk. This leads to materials with a large oxygen capacity and emergent functionalities. In parallel, due to the well socketed nature of the exoparticles, the developed systems exhibit high tolerance against carbon deposition which is consistent with previous report in literature investigating systems with exsolved particles in hydrocarbon environments (Neagu et al., 2015). TEM and XPS analysis reveal that the exsolved particles are composed of a mixed Co-Ni oxide which leads to increased reactivity against methane. Modification of the microstructure of the system results to grain size decrease and intricate surface formation which in turn alters surface exsolution by making surface particles smaller in size and higher in population. This leads to decreasing the methane activation even further without compromising selectivity.

The system's applicability is further showcased by its employment as OCM for the conversion of methane via chemical looping. The tuned exo/endo-particle system is found to exhibit excellent stability for 30 cycles with high and selective conversion, which is achieved and stabilised from the first cycle and maintained throughout. The robustness and high oxygen capacity demonstrated, combined with high activity prove the suitability of such systems for redox cycling applications such as chemical looping but also make them promising candidates for technologies such as three-way catalysts and thermochemical solar to fuels conversion. Furthermore, the findings of this chapter demonstrate that the design principles, tuning methodologies developed in this study can be employed for the rational design of exo/ endo-particle systems with enhanced performance for targeted applications.

References

- Akbarzadeh, O., Mohd Zabidi, N.A., Abdul Wahab, Y., Hamizi, N.A., Chowdhury, Z.Z., Merican Aljunid Merican, Z., Rahman, M.A., Akhter, S., Shalauddin, M. & Johan, M.R. (2019) Effects of cobalt loading, particle size, and calcination condition on Co/CNT catalyst performance in Fischer-Tropsch reactions. *Symmetry*. 11 (1), 1–18.
- Biesinger, M.C., Lau, L.W.M., Gerson, A.R. & Smart, R.S.C. (2012) The role of the Auger parameter in XPS studies of nickel metal, halides and oxides. *Physical Chemistry Chemical Physics*. 14 (7), 2434–2442.
- Chen, L., Lu, Y., Hong, Q., Lin, J. & Dautzenberg, F.M. (2005) Catalytic partial oxidation of methane to syngas over Ca-decorated-Al₂O₃-supported Ni and NiB catalysts. *Applied Catalysis A: General*. 292295–304.
- Choudhary, T. V. & Choudhary, V.R. (2008) Energy-efficient syngas production through catalytic oxy-methane reforming reactions. *Angewandte Chemie - International Edition*. 47 (10), 1828–1847.

- Cui, X., Li, H., Wang, Y., Hu, Y., Hua, L., Li, H., Han, X., Liu, Q., Yang, F., He, L., Chen, X., Li, Q., Xiao, J., Deng, D. & Bao, X. (2018) Room-Temperature Methane Conversion by Graphene-Confined Single Iron Atoms. *Chem.* 4 (8), 1902–1910.
- Dai, X.P., Li, R.J., Yu, C.C. & Hao, Z.P. (2006) Unsteady-state direct partial oxidation of methane to synthesis gas in a fixed-bed reactor using AFeO_3 (A = La, Nd, Eu) perovskite-type oxides as oxygen storage. *Journal of Physical Chemistry B.* 110 (45), 22525–22531.
- Fan, M.S., Abdullah, A.Z. & Bhatia, S. (2009) Catalytic technology for carbon dioxide reforming of methane to synthesis gas. *ChemCatChem.* 1 (2), 192–208.
- Feng, Z., Du, C., Chen, Y., Lang, Y., Zhao, Y., Cho, K., Chen, R. & Shan, B. (2018) Improved durability of Co_3O_4 particles supported on SmMn_2O_5 for methane combustion. *Catalysis Science and Technology.* 8 (15), 3785–3794.
- Guerrero-Caballero, J., Kane, T., Haidar, N., Jalowiecki-Duhamel, L. & Löfberg, A. (2019) Ni, Co, Fe supported on Ceria and Zr doped Ceria as oxygen carriers for chemical looping dry reforming of methane. *Catalysis Today.* 333 (December 2017), 251–258.
- Guo, M., Cheng, Z., Liu, Y., Qin, L., Goetze, J., Fan, J.A. & Fan, L.S. (2020) Cobalt doping modification for enhanced methane conversion at low temperature in chemical looping reforming systems. *Catalysis Today.* 350 (June 2019), 156–164.
- Haribal, V.P., Wang, X., Dudek, R., Paulus, C., Turk, B., Gupta, R. & Li, F. (2019) Modified Ceria for “Low-Temperature” CO_2 Utilization: A Chemical Looping Route to Exploit Industrial Waste Heat. *Advanced Energy Materials.* 9 (41), 1–10.
- Horlyck, J., Lawrey, C., Lovell, E.C., Amal, R. & Scott, J. (2018) Elucidating the impact of Ni and Co loading on the selectivity of bimetallic NiCo catalysts for dry reforming of methane. *Chemical Engineering Journal.* 352 (June), 572–580.
- Kessler, T., Visintin, A., de Chialvo, M.R., Triaca, W.E. & Arvia, A.J. (1989) The development of a cobalt oxide spinel structure overlayer on cobalt electrodes. A modified electrode surface of electrocatalytic interest. *Journal of Electroanalytical Chemistry.* 261, 315–329.
- Kotani, A., Jo, T. & Parlebas, J.C. (1987) Many-body effects in core-level spectroscopy of rare-earth compounds. 37.
- Kousi, K., Neagu, D., Bekris, L., Cali, E., Kerherve, G., Papaioannou, E.I., Payne, D.J. & Metcalfe, I.S. (2020) Low temperature methane conversion with perovskite-supported: exo / endo - particles. *Journal of Materials Chemistry A.* 8 (25), 12406–12417.
- Kousi, K., Neagu, D., Bekris, L., Papaioannou, E.I. & Metcalfe, I.S. (2020) Endogenous Nanoparticles Strain Perovskite Host Lattice Providing Oxygen Capacity and Driving Oxygen Exchange and CH_4 Conversion to Syngas. *Angewandte Chemie - International Edition.* 59 (6), 2510–2519.
- Kousi, K., Neagu, D. & Metcalfe, I.S. (2020) Combining Exsolution and Infiltration for Redox, Low Temperature CH_4 Conversion to Syngas. *Catalysts.* 10 (5), 468.

- Li, T., Jayathilake, R.S., Taylor, D.D. & Rodriguez, E.E. (2019) Structural studies of the perovskite series $\text{La}_{1-x}\text{Sr}_x\text{CoO}_{3-\delta}$ during chemical looping with methane. *Chemical Communications*. 55 (34), 4929–4932.
- Lim, T.H., Cho, S.J., Yang, H.S., Engelhard, M.H. & Kim, D.H. (2015) Effect of Co/Ni ratios in cobalt nickel mixed oxide catalysts on methane combustion. *Applied Catalysis A: General*. 50562–69.
- Lim, T.H., Cho, S.J., Yang, H.S., Engelhard, M.H. & Kim, D.H. (2015) Effect of Co/Ni ratios in cobalt nickel mixed oxide catalysts on methane combustion. *Applied Catalysis A: General*. 50562–69.
- Neagu, D., Oh, T.S., Miller, D.N., Ménard, H., Bukhari, S.M., Gamble, S.R., Gorte, R.J., Vohs, J.M. & Irvine, J.T.S. (2015) Nano-socketed nickel particles with enhanced coking resistance grown in situ by redox exsolution. *Nature Communications*. 6.
- Neagu, D., Papaioannou, E.I., Ramli, W.K.W., Miller, D.N., Murdoch, B.J., Ménard, H., Umar, A., Barlow, A.J., Cumpson, P.J., Irvine, J.T.S. & Metcalfe, I.S. (2017) Demonstration of chemistry at a point through restructuring and catalytic activation at anchored nanoparticles. *Nature Communications*. 8 (1), 1855.
- Papadopoulou, C., Matralis, H. & Verykios, X. (2012) Utilization of Biogas as a Renewable Carbon Source: Dry Reforming of Methane. *Catalysis for Alternative Energy Generation*. 57–127.
- Pfau, A. & Schierbaum, K.D. (1994) The electronic structure of stoichiometric and reduced CeO_2 surfaces: an XPS, UPS and HREELS study. *Surface Science*. 321 (1), 71–80.
- Shao, Z. & Halle, S.M. (2004) A high-performance cathode for the next generation of solid-oxide fuel cells. *Nature*. 431 (7005), 170–173.
- Sunding, M.F., Hadidi, K., Diplas, S., Løvvik, O.M., Norby, T.E. & Gunnæs, A.E. (2011) XPS characterisation of in situ treated lanthanum oxide and hydroxide using tailored charge referencing and peak fitting procedures. *Journal of Electron Spectroscopy and Related Phenomena*. 184 (7), 399–409.
- Tang, C., Kousi, K., Neagu, D., Portolés, J., Papaioannou, E.I. & Metcalfe, I.S. (2019) Towards efficient use of noble metals: Via exsolution exemplified for CO oxidation. *Nanoscale*. 11 (36), 16935–16944.
- Tao, F.F., Shan, J.J., Nguyen, L., Wang, Z., Zhang, S., Zhang, L., Wu, Z., Huang, W., Zeng, S. & Hu, P. (2015) Understanding complete oxidation of methane on spinel oxides at a molecular level. *Nature Communications*. 6.
- Touahra, F., Chebout, R., Lerari, D., Halliche, D. & Bachari, K. (2019) Role of the nanoparticles of Cu-Co alloy derived from perovskite in dry reforming of methane. *Energy*. 171465–474.

Wang, H.Y., Hung, S.F., Chen, H.Y., Chan, T.S., Chen, H.M. & Liu, B. (2016) In Operando Identification of Geometrical-Site-Dependent Water Oxidation Activity of Spinel Co_3O_4 . *Journal of the American Chemical Society*. 138 (1), 36–39.

Wong, Y.J., Koh, M.K., Khavarian, M. & Mohamed, A.R. (2017) Investigation on cobalt aluminate as an oxygen carrier catalyst for dry reforming of methane. *International Journal of Hydrogen Energy*. 42 (47), 28363–28376.

Wu, Z., Yang, B., Miao, S., Liu, W., Xie, J., Lee, S., Pellin, M.J., Xiao, D., Su, D. & Ma, D. (2019) Lattice Strained Ni-Co alloy as a High-Performance Catalyst for Catalytic Dry Reforming of Methane. *ACS Catalysis*. 9 (4), 2693–2700.

Xu, L., Wang, F., Chen, M., Zhang, J., Yuan, K., Wang, L., Wu, K., Xu, G. & Chen, W. (2016) Carbon Dioxide Reforming of Methane over Cobalt-Nickel Bimetal-Doped Ordered Mesoporous Alumina Catalysts with Advanced Catalytic Performances. *ChemCatChem*. 8 (15), 2536–2548.

Zeng, D., Qiu, Y., Zhang, S., Ma, L., Li, M., Cui, D., Zeng, J. & Xiao, R. (2019) Synergistic effects of binary oxygen carriers during chemical looping hydrogen production. *International Journal of Hydrogen Energy*. 44 (39), 21290–21302.

6 Conclusions

In this chapter the main conclusions and thesis outcomes are discussed. It is also showcased how the thesis objectives outlined in Chapter 1 were met.

6.1 Conclusions

The results presented in this study demonstrate the successful targeted development and application of a new class of composite exsolved perovskite oxide systems that display emergent properties and enhanced performance for the conversion of methane via chemical looping. The design principles employed lead to the evolution of the exsolution concept allowing the creation of materials that are capable of extensive, homogenous, and controlled growth of metallic nanoparticles at nanoscale proximity in the system's bulk. It is found that the growth of such a high population of nanoparticles throughout the bulk of the oxide, induces strain in both phases of the system which leads to enhanced oxygen transport and exchange abilities while also increasing the system's overall reactivity. This is showcased by choosing to perform this study by employing a titanate perovskite oxide ($\text{La}_{0.8}\text{Ce}_{0.1}\text{Ni}_{0.4}\text{Ti}_{0.6}\text{O}_3$), which due to its low surface area and low oxygen exchange capability would be expected to underperform for such an application (Merkle & Maier, 2008). However, upon the formation of exo- and endo- metallic nanoparticles, it becomes highly active, producing synthesis gas with high selectivity and minimal carbon deposition at lower temperatures than conventional materials (Qin et al., 2018). Consistent with the objectives of the thesis, the materials developed display augmented oxygen storage and transport capabilities coupled with enhanced reactivity leading to their successful application as catalysts and oxygen carriers for the conversion of methane.

Through the methodology developed it is demonstrated that it is possible to increase the extent of exsolution and enable the controlled growth of a high population of nanoparticles not only on the surface but more importantly within the bulk of an oxide host. Exsolving such high fraction of the doped ions as metal, results to the increase of the systems overall oxygen storage capacity as the submerged particles act as nanoscale oxygen storage reservoirs. This increase in capacity is found to be one order of magnitude higher than that of conventional perovskites (Zhu et al., 2018). Furthermore, due to the extensive nanoparticle growth in the bulk, strain is induced in both metal nanoparticle's and host's lattice creating a series of nanodomains seamlessly connecting the embedded nanoparticles with the surface. This is found to drastically enhance the oxygen transport and exchange across the nanocomposite, with even the deepest submerged nanoparticles becoming accessible by the reactant gas phase and actively involved in the redox transformation. It is demonstrated that the endoparticles are also capable of undergoing cyclic redox transformation, transitioning between metal and metal oxide state, thus incorporating, and releasing oxygen repeatedly while the overall integrity of the material is maintained even after extensive cycling. The fact that endoparticles are submerged protects them from agglomeration while also allowing them to surpass other deactivation processes. At the same time the surface exsolved particles acting as active sites, exhibit enhanced durability against degradation and poisoning, owing to their socketed nature, while the overall integrity of the nanocomposite is maintained. This illustrates the applicability of such systems for the chosen challenging cyclic redox application of chemical looping methane reforming.

Having uncovered the emergent capabilities stemming from the formation of the endogenous nanoparticles, deeper insight is gained on the contribution of the system's components on its performance. The same Ni-doped composition is employed and by exploiting the high tunability of the systems, variants with different particle and structure characteristics are created and tested for the conversion of methane. By tuning the components of the system, a systematic investigation is carried out revealing what impact modifications in its nano and microstructure have on its reactivity. The key role of submerged nanoparticles on overall performance is showcased and the involvement of the exoparticle on activity and selectivity is uncloaked. Furthermore, the close relationship between exsolution and the systems microstructure is investigated and its pivotal role in the materials reactivity and selectivity is uncovered. Through the above investigation methods of tuning the system's characteristics are showcased and insight is gained on how such systems can be modified to tailor their performance according to their application.

Having gained insight on the systems performance, as a proof of concept, the principles and methodologies developed in this study are employed for the rational design of another exo-endo- titanate oxide system with even higher performance, capable of selectively converting methane at even lower temperatures while maintaining high selectivity and robustness under long term cycling. For this, the $\text{La}_{0.7}\text{Ce}_{0.1}\text{Co}_{0.3}\text{Ni}_{0.1}\text{Ti}_{0.6}\text{O}_3$ composition is designed and Ni-Co bimetallic endo- and exo- particles are successfully exsolved aiming to lower the activation temperature of methane even lower. The system's micro- and nano- structure are also tuned following the methodologies developed. Consistent with previous findings in this study the system is found to have a high extent of exsolution with a large fraction of the doped anions being exsolved in the bulk and acting as oxygen reservoirs thus leading to high oxygen capacity. This combined with the highly active exsolved Co-Ni nanoparticles and the tuned structure led to the successful activation of methane at 450°C which is remarkable for a non-precious metal system. Additionally, the particles exhibit high tolerance against deactivation by carbon deposits as expected. Further analysis of the chemistry of nanoparticles confirms their mixed Ni-Co composition is responsible for the observed high activity, while investigation of the modified microstructure showcases once again the strong link between micro- and nanostructure which upon tuning leads to increased reactivity. Furthermore, the system is able to operate cyclically converting methane via chemical looping reforming at an even lower temperature while selectivity is maintained and not showing any signs of degradation. The above findings showcase that the insight gained, and methodologies developed here can be successfully utilised for the rational design and tuning of composite exo-/endo- systems with tailored application driven capabilities.

Beyond the demonstration of the material's performance against methane activation and as an oxygen carrier in chemical looping, the combination of emergent properties and performance tunability showcased in this study make the exo-/endo- systems developed attractive for many other fields of research. Parallels can be drawn about the systems produced here and ones produced via substitutional doping due to their hierarchical nature (de Rogatis et al., 2010). In a similar way to which doping has enabled the control of a wide range of material properties, the methodology proposed here, has the potential of

revolutionising the production of hierarchically tailored nanostructured materials leading to emergent functionalities. These functionalities are found to stem from both chemical and physical alterations that occur on exsolved particles as well as the host lattice due to the local strain induced and due to the formation of new interfaces within the host lattice. This is not observed in classic deposition though, where only local chemical alterations on the structure are observed between the host and deposited species while the continuity between host and doped species is maintained. This difference found only when exsolving doped nanoclusters from within i.e. nanocluster ‘doping’ of oxides (Kousi et al., 2020) offer a new dimension for the creation materials with emergent capabilities that can be controlled via strain and interface engineering.

To conclude, the ability of exsolving such high fraction of the doped metal phase leading to increased oxygen capacity make such materials attractive for applications such as three-way catalysts. The enhanced oxygen transport via strain is of interest in fields such as oxide-ion transport membranes, electrodes and electrolytes. The demonstrated reversibility over long term cycling offers a novel method of stabilising nanocomposites (cermets) redox cycling applications (Zeng et al., 2018). Finally, the high dispersion of metal nanoparticles achieved could be of great interest for their application for the design of thermoelectric and magnetic materials. Finally, the unique combination of high oxygen transport, high oxygen storage capacity as well as redox robustness, makes these materials appealing for energy conversion technologies that rely on cyclic oxygen storage such thermochemical solar to fuel (Michalsky et al., 2015), redox flow batteries (Xu et al., 2011) and chemical looping (Metcalf et al., 2019).

References

- Kousi, K., Neagu, D., Bekris, L., Papaioannou, E.I. & Metcalfe, I.S. (2020) Endogenous Nanoparticles Strain Perovskite Host Lattice Providing Oxygen Capacity and Driving Oxygen Exchange and CH₄ Conversion to Syngas. *Angewandte Chemie - International Edition*. 59 (6), 2510–2519.
- Merkle, R. & Maier, J. (2008) How Is Oxygen Incorporated into Oxides? A Comprehensive Kinetic Study of a Simple Solid-State Reaction with SrTiO₃ as a Model Material. *Angewandte Chemie International Edition*. 47 (21), 3874–3894.
- Metcalf, I.S., Ray, B., Dejoie, C., Hu, W., de Leeuwe, C., Dueso, C., García-García, F.R., Mak, C.-M., Papaioannou, E.I., Thompson, C.R. & Evans, J.S.O. (2019) Overcoming chemical equilibrium limitations using a thermodynamically reversible chemical reactor. *Nature Chemistry*. (3), .
- Michalsky, R., Botu, V., Hargus, C.M., Peterson, A.A. & Steinfeld, A. (2015) Design Principles for Metal Oxide Redox Materials for Solar-Driven Isothermal Fuel Production. *Advanced Energy Materials*. 5 (7), 1401082.
- Qin, L., Guo, M., Liu, Y., Cheng, Z., Fan, J.A. & Fan, L.-S. (2018) Enhanced methane conversion in chemical looping partial oxidation systems using a copper doping modification. *Applied Catalysis B: Environmental*. 235143–149.

de Rogatis, L., Cargnello, M., Gombac, V., Lorenzut, B., Montini, T. & Fornasiero, P. (2010) Embedded phases: A way to active and stable catalysts. *ChemSusChem*. 3 (1), 24–42.

Xu, N., Li, X., Zhao, X., Goodenough, J.B. & Huang, K. (2011) A novel solid oxide redox flow battery for grid energy storage. *Energy and Environmental Science*. 4 (12), 4942–4946.

Zeng, L., Cheng, Z., Fan, J.A., Fan, L.S. & Gong, J. (2018) Metal oxide redox chemistry for chemical looping processes. *Nature Reviews Chemistry*. 2 (11), 349–364.

Zhu, X., Li, K., Neal, L. & Li, F. (2018) Perovskites as Geo-inspired Oxygen Storage Materials for Chemical Looping and Three-Way Catalysis: A Perspective. *ACS Catalysis*. 8 (9), 8213–8236.

7 Future work

In this chapter future projects stemming from the outcomes of this work are discussed.

7.1 Investigation of emergent material properties stemming from strain

As demonstrated extensively in this work, strain induced due to extensive endoparticles formation can lead to emergent functionalities which greatly enhance the systems redox performance and overall reactivity (Kousi, Neagu, Bekris, Papaioannou, et al., 2020). This project is aimed to further investigate the effect of induced strain via endo- particle formation on the oxidation ability of samples which can potentially lead to overcoming certain material's slow oxidation kinetics by reactants streams with lower pO_2 s. The findings of this study will provide insight on the effect of endo-particles and strain as a mean for the production of composite materials with enhanced redox kinetics that will be able to perform transformations under conditions that are thermodynamically unfavourable if the components of the system were used alone.

Planning and work on this project have already commenced. Powders have been synthesised and reduced at different temperatures in order to produce samples with a different extent of strain due to endoparticle formation. The reduced samples will be tested via temperature programmed and isothermal oxidation experiments in order to monitor their extent of oxidation under atmospheres with different pO_2 s ranging from air to water. Using the insight gained from this investigation, the materials are going to be tailored and tested for the activation of methane via chemical looping with varying oxidising agents with the goal of optimising them for chemical looping reforming of methane with water.

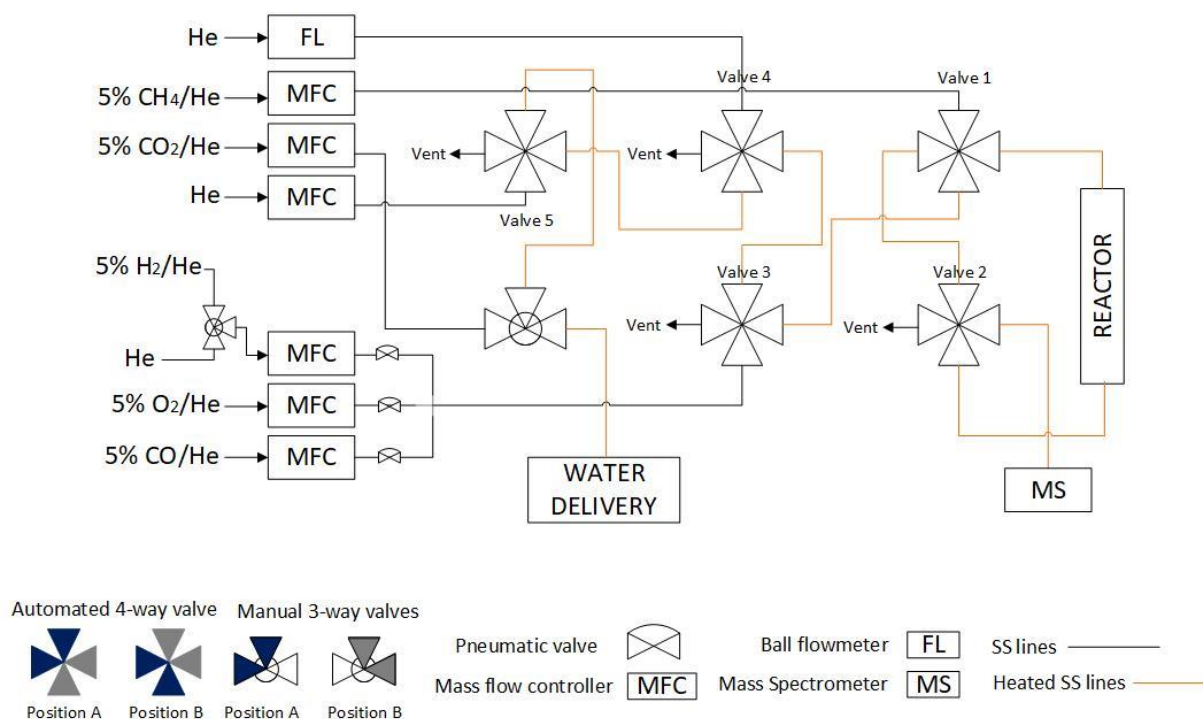


Figure 7.1 Flow diagram of the automated fixed bed and pellet reactor characterisation system.

For this project a new testing rig has been designed and is under its commissioning phase. The rig comprises of a flow system that allows automatic gas switching via automated 4-way valves, a furnace, adaptors that can house quartz reactors of different sizes and a water delivery system. The different reactor sizes will allow testing of powdered and pellet samples ranging from ~100 mg to ~ 2 g while the water delivery system allows for steam to be used as a reactant. The system is controlled via PC and can be programmed to run automated experiments with varying conditions, including cycling. Through use of buffer gasses and the integrated water delivery system, this rig will enable the testing of materials under varying pO_2 s and allow for short/ long-term cycling experiments under varying conditions.

7.2 Further studying of exoparticle involvement on the activation process and their synergistic relationship with endoparticles

As presented throughout this study, there is a strong relationship between endo- and exo-particles which is pivotal for the material's reactivity. This set of experiments is aimed to gain further understanding on this relationship and serve as a continuation of the deconvolution work presented in Chapter 5.

During this investigation, materials tested will not be in powder but rather in pellet form. This will allow to observe the phenomenon of exo/ endo- particle formation in pellets while also more importantly controlling the amount of exoparticle exsolution by modifying the pellet surfaces via polishing. This technique has been demonstrated before by (Neagu et al., 2019; Irvine et al., 2016) for the study of systems with only surface exsolution and employed as a way to produce samples with controlled uniform surface exsolution allowing for the studying and tracking of nanoparticle changes. Here, polishing specific areas of the pellet will effectively control exoparticle exsolution across samples while endoparticle formation will remain unaffected. By polishing more surfaces of the pellets, exoparticle formation will increase and the direct synergy between exoparticle and nanoparticle content on performance can be studied. Additionally, by altering the porosity of the pellets more insight will be gained about the effect of microstructure in pellet form.

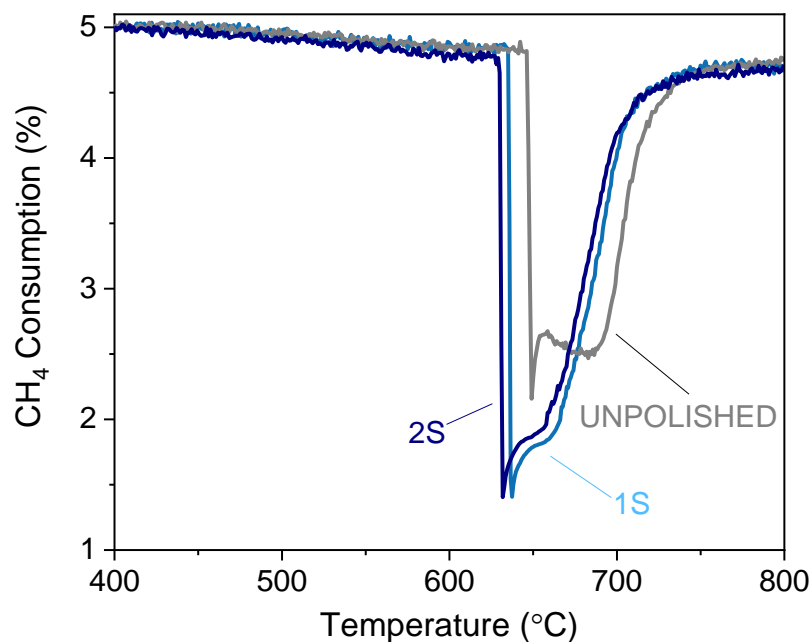


Figure 7.2 **Preliminary results of LCNT exo/ endo- systems in pellet form with increasing exoparticle content employed for the activation of methane.** Unpolished (grey) pellet with exoparticle formation suppressed, and systems with one surface (1S, light blue) and two surfaces (2S, navy blue) polished with gradually increasing exoparticle content while endoparticle content remains unchanged.

Pellets of the studied LCNT compositions with the same porosity have been produced and preliminary experiments have been conducted. Initial results are promising, showing an expected increase in activity as pellets with higher exoparticle content are tested (Figure 7.2). Three models were produced where the first had none of its surfaces polished, hence exoparticle formation was suppressed, while the other two had one and both surfaces polished, respectively, thus allowing for more uniform surface exsolution to occur. Due to equipment limitations the pellets tested until now were of small diameter (2 mm), and as a result only small increase in activity between the three samples, as more surface become available for surface exsolution, was observed. Nevertheless, the results observed are as expected and following the commissioning of the characterisation system presented in Figure 7.1, more experiments can commence with pellets of different geometries. This will allow for the further investigation of greater changes in activity due to exoparticle formation and will provide more information about the deconvolution of the activation curve of the samples. Furthermore, by comparing systems with varying porosities will also provide information about how exo/endo-systems can be modified in pellet form in order to increase robustness and control selectivity via microstructural tailoring.

7.3 Investigation of exsolved exo-/ endo- bimetallic particle systems with varying alloying particle composition

The exsolution of bimetallic nanoparticles has recently gained attention due to their enhanced performance in various applications stemming from synergistic effects that develop between the two co-exsolved metals (Sun et al., 2015; Tang et al., 2021). From the results presented in

Chapter 5 of this study, it is proven that bimetallic exsolution is possible for exo- /endo-nanoparticle systems with the resulting composite being highly reactive against methane (Kousi, Neagu, Bekris, Cali, et al., 2020). As a continuation of this work, this set of experiments aims to exsolve bimetallic exo- and endo- particles of different compositions and evaluate the effect of alloying particle composition on the materials properties and performance.

Different compositions of the original $\text{La}_{0.7}\text{Ce}_{0.1}\text{Co}_{0.3}\text{Ni}_{0.1}\text{Ti}_{0.6}\text{O}_3$ have been designed and synthesised where the ratio between the doped exsolvable Co:Ni varies, aiming to co- exsolve exo- and endo- particles with different Co:Ni composition. Powdered and pellet samples have been produced and processed. The pellet samples aim on the tracking of changes on specific nanoparticles during the different transformations as they occur from exposing the system in different conditions while the powdered samples will be studied under reaction conditions in a fixed bed reactor. The resulting systems will be employed for the activation of methane assessing their reactivity and the chemistry of the nanoparticles will be studied via TEM and XPS aiming to uncover the effect of varying particle composition on the system's performance.

7.4 Increasing the reactivity of exo-/ endo- particle systems by modifying exoparticle characteristics

Throughout this study the exsolution process was carried out by reducing samples in H_2 atmosphere successfully achieving a high degree of exsolution and producing exo/endo-exsolved samples decorated with spherical particles. However, recent studies have demonstrated that by altering the reduction atmosphere under which exsolution takes place it is possible to modify the shape of exsolved particles which can potentially lead to a tremendous increase in their reactivity (Neagu et al., 2019).

Aiming to investigate the feasibility of producing exo/endo- systems under different reduction atmospheres as well as the effect of such subsequent treatments on exoparticle characteristics and in extent system's performance, samples of the LCNT composition will be reduced and treated after post reduction, by different gas atmospheres (CO) and pO_2s (under vacuum). The resulting system's particle characteristics will be studied, and the systems will be employed for the activation of methane aiming to determine if such modification of the characteristics of surface exsolved particles can lead to emergent functionalities and enhanced performance. Furthermore, the resulting systems will be employed as OCMs for the conversion of methane via chemical looping aiming to investigate the exoparticle's durability under long-term cycling and any further enhancement of the materials redox ability due to changes in the synergistic relationship between surface and bulk.

References

- Irvine, J.T.S., Neagu, D., Verbraeken, M.C., Chatzichristodoulou, C., Graves, C. & Mogensen, M.B. (2016) Evolution of the electrochemical interface in high-temperature fuel cells and electrolyzers. *Nature Energy*. 1 (1), 1–13.
- Kousi, K., Neagu, D., Bekris, L., Cali, E., Kerherve, G., Papaioannou, E.I., Payne, D.J. & Metcalfe, I.S. (2020) Low temperature methane conversion with perovskite-supported: exo / endo -particles. *Journal of Materials Chemistry A*. 8 (25), 12406–12417.
- Kousi, K., Neagu, D., Bekris, L., Papaioannou, E.I. & Metcalfe, I.S. (2020) Endogenous

Nanoparticles Strain Perovskite Host Lattice Providing Oxygen Capacity and Driving Oxygen Exchange and CH₄ Conversion to Syngas. *Angewandte Chemie - International Edition*. 59 (6), 2510–2519.

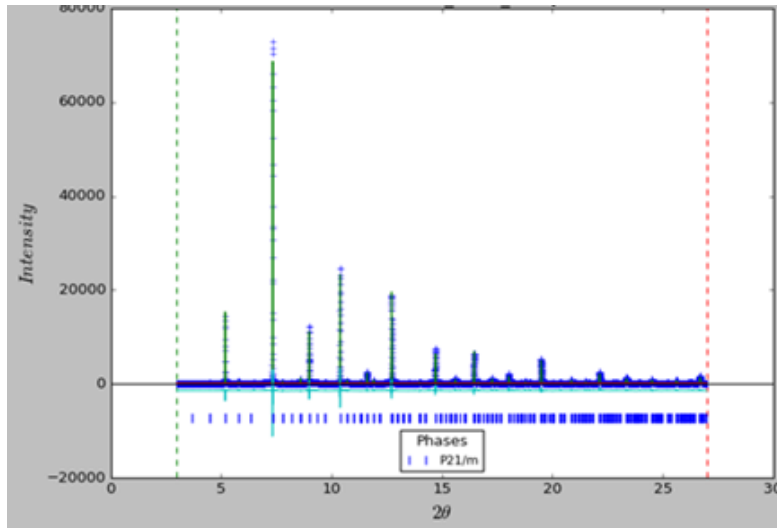
Neagu, D., Kyriakou, V., Roiban, I.L., Aouine, M., Tang, C., Caravaca, A., Kousi, K., Schreur-Piet, I., Metcalfe, I.S., Vernoux, P., Van De Sanden, M.C.M. & Tsampas, M.N. (2019) In Situ Observation of Nanoparticle Exsolution from Perovskite Oxides: From Atomic Scale Mechanistic Insight to Nanostructure Tailoring. *ACS Nano*. 13 (11), 12996–13005.

Sun, Y.F., Li, J.H., Cui, L., Hua, B., Cui, S.H., Li, J. & Luo, J.L. (2015) A-site-deficiency facilitated in situ growth of bimetallic Ni-Fe nano-alloys: a novel coking-tolerant fuel cell anode catalyst. *Nanoscale*. 7 (25), 11173–11181.

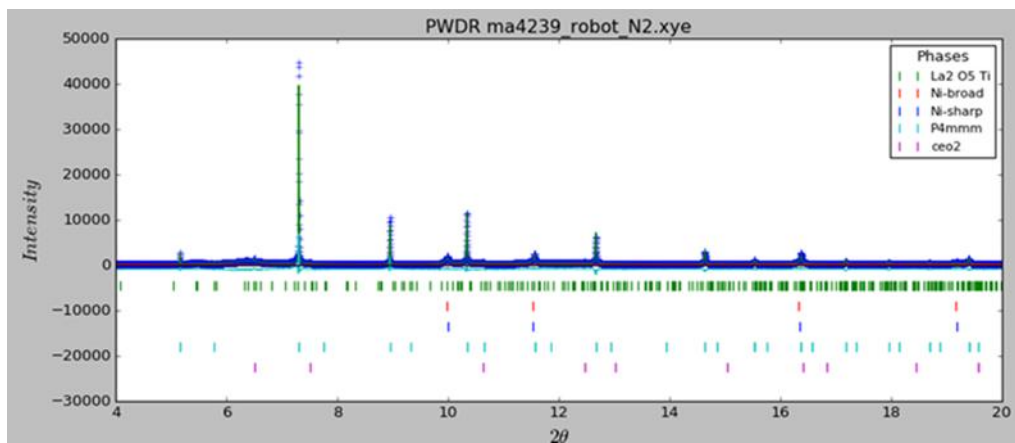
Tang, C., Kousi, K., Neagu, D. & Metcalfe, I.S. (2021) Trends and Prospects of Bimetallic Exsolution. *Chemistry - A European Journal*. 27 (22), 6666–6675.

Appendix A

a



b



Appendix A - 0.1 Rietveld refinement of the fresh (a,b) and reduced-exsolved (c,d) samples. For (a) wR = 17% and (c) wR=18% (Kousi, Neagu, Bekris, et al., 2020)

